



HAL
open science

Topological magnetic solitons in thin epitaxial films with reduced symmetry

Lorenzo Camosi

► **To cite this version:**

Lorenzo Camosi. Topological magnetic solitons in thin epitaxial films with reduced symmetry. Materials Science [cond-mat.mtrl-sci]. Université Grenoble Alpes, 2018. English. NNT : 2018GREAY012 . tel-01871292

HAL Id: tel-01871292

<https://theses.hal.science/tel-01871292>

Submitted on 10 Sep 2018

HAL is a multi-disciplinary open access archive for the deposit and dissemination of scientific research documents, whether they are published or not. The documents may come from teaching and research institutions in France or abroad, or from public or private research centers.

L'archive ouverte pluridisciplinaire **HAL**, est destinée au dépôt et à la diffusion de documents scientifiques de niveau recherche, publiés ou non, émanant des établissements d'enseignement et de recherche français ou étrangers, des laboratoires publics ou privés.

THÈSE

Pour obtenir le grade de

DOCTEUR DE LA COMMUNAUTÉ UNIVERSITÉ GRENOBLE ALPES

Spécialité : NANOPHYSIQUE

Arrêté ministériel : 25 mai 2016

Présentée par

Lorenzo CAMOSI

Thèse dirigée par **Jan VOGEL**, Directeur de Recherche
et codirigée par **Stefania PIZZINI**, Directrice de Recherche
préparée au sein du **Laboratoire Institut Néel**
dans **l'École Doctorale Physique**

Solitons Magnétiques Topologiques dans des couches minces epitaxiées à symétrie réduite

Topological Magnetic Solitons in thin epitaxial films with reduced symmetry

Thèse soutenue publiquement le **30 mai 2018**,
devant le jury composé de :

Monsieur ANDRE THIAVILLE

DIRECTEUR DE RECHERCHE, CNRS DELEGATION ILE-DE-FRANCE
SUD, Rapporteur

Monsieur STEPHANE ANDRIEU

PROFESSEUR, UNIVERSITE DE LORRAINE, Rapporteur

Monsieur STEFAN BLÜGEL

PROFESSEUR, INSTITUT PETER GRÜNBERG (PGI) ALLEMAGNE,
Président

Madame LILIANA BUDA-PREJBEANU

MAITRE DE CONFERENCES, GRENOBLE INP, Examineur

Monsieur OLIVIER FRUCHART

DIRECTEUR DE RECHERCHE, CNRS DELEGATION ALPES,
Examineur



Contents

1	Introduction	7
2	Introduction to the magnetism in C_{2v} systems	9
2.1	Magnetic materials and micromagnetic approximation	9
2.2	Symmetric exchange interactions	11
2.2.1	Direct exchange	11
2.2.2	Indirect exchange interaction	11
2.2.3	Micromagnetic formulation : one-dimensional model	12
2.2.4	Micromagnetic formulation : anisotropic exchange in a system with a C_{2v} symmetry	13
2.3	Dzyaloshinskii-Moriya interaction	15
2.3.1	Conditions and atomic formulations	15
2.3.2	Moriya model	15
2.3.3	Fert-Levy model	16
2.3.4	Interfacial DMI	17
2.3.5	Phenomenological interpretation of anisotropic DMI	17
2.3.6	DMI micromagnetic formulation in C_{4v} systems	19
2.3.7	DMI micromagnetic formulation in a C_{2v} symmetry system	20
2.4	Zeeman energy	22
2.5	Magneto-crystalline anisotropy energy	23
2.6	Dipolar energy	25
2.7	Magnetic response to an external magnetic field	27
2.7.1	Dynamic response: Landau-Lifshitz-Gilbert (LLG) equation	27
2.7.2	Magnetisation reversal	27
2.8	Curie temperature	31
3	Techniques and methods	33
3.1	UHV system: deposition and crystal characterisation	33
3.1.1	Riber chamber and Laser	33
3.1.2	Pulsed laser deposition	34
3.1.3	Molecular beam epitaxy (MBE)	37
3.1.4	Thin film epitaxial growth	37
3.1.5	RHEED	39
3.1.6	STM chamber	42
3.2	AFM	44
3.3	X-ray diffraction	45
3.4	Experimental techniques to determine the magnetic parameters	46
3.5	Magneto-optical effects	47
3.5.1	Wave propagation in a magnetic medium	47
3.5.2	Focused Kerr magnetometry	52
3.5.3	Kerr microscopy	53
3.5.4	BLS spectroscopy	56
3.6	Magnetic microscopy	59
3.6.1	XMCD-PEEM	59
3.6.2	MFM	61

4	Topological magnetic solitons	63
4.1	Topology	63
4.1.1	Topological number	63
4.1.2	Magnetic topological solitons	64
4.1.3	Berry phase and breaking of the time reversal symmetry	66
4.1.4	Emergent fields and topological Hall effect	68
4.1.5	Topological protection	70
4.2	Magnetic domain walls in isotropic matter	71
4.2.1	Competition between uniaxial anisotropy and exchange interaction	73
4.2.2	Role of the volume dipolar interaction	74
4.2.3	Role of the DMI	75
4.2.4	Effect of an in-plane magnetic field	76
4.3	Magnetic domain walls in C_{2v} symmetry systems	77
4.3.1	Role of anisotropic DMI with a C_{2v} symmetry	77
4.3.2	Role of the exchange interaction in a system with C_{2v} symmetry	79
4.3.3	Role of the biaxial anisotropy	80
4.3.4	Competition between in-plane anisotropy and volume dipolar interactions	80
4.3.5	Competition between anisotropic DMI and biaxial anisotropy	82
4.3.6	Role of an in-plane magnetic field along the easy axis of a system with C_{2v} symmetry	87
4.3.7	Review of magnetic domain walls in a C_{2v} symmetry system	89
4.4	2D topological solitons : skyrmions and anti-skyrmions	90
4.4.1	Micromagnetics of skyrmions	90
4.4.2	Skyrmion phase diagram	95
4.4.3	The topological soliton quality factor and stability	98
4.4.4	Micromagnetics of anti-skyrmions	100
4.4.5	Review on 2D topological solitons	106
5	Experimental results: magnetism in C_{2v} epitaxial systems	107
5.1	Materials for stabilizing isolated skyrmion	107
5.2	W\Co\Au and W\Co\Pt	108
5.2.1	Crystal relationships in epitaxial systems	108
5.2.2	Substrate preparation and characterisation	112
5.2.3	Growth parameters and crystal orientation	117
5.2.4	Crystal symmetry characterisation by GIXRD	120
5.2.5	Crystal surface characterisation by STM	121
5.3	Magnetic characterisation	123
5.3.1	Kerr magnetometry	123
5.4	DW motion	125
5.4.1	DW motion in systems with DMI	125
5.4.2	Creep regime	129
5.5	Kerr microscopy and DW motion	131
5.5.1	Creep regime	133
5.5.2	Regimes of the DW dynamics	136
5.5.3	Steady flow regime	137
5.5.4	DW dynamics review	140
5.6	Brillouin light scattering spectroscopy	141
5.6.1	Derivation of the effective DMI ($D_s^{(eff)}(\alpha)$)	143
5.6.2	Review on BLS spectroscopy measurements	144
5.7	Internal DW configuration and elliptical skyrmions	145
5.7.1	Conditions for skyrmion nucleation	146
5.7.2	MFM on nanopatterned W\Co\Au	148
5.7.3	XMCD-PEEM on W\Co\Au	149
5.7.4	Comments on the research of elliptical skyrmions in the W\Co\Au system	152
5.8	W\Co\Au-Pt solid solution	153
5.8.1	Growth of the Au-Pt _{solid solution}	153

5.8.2	Magnetic characterisation	154
5.8.3	MFM on W\Co\Au-Pt solid solution	156
5.8.4	XMCD-PEEM on W\Co\Au-Pt solid solution	159
5.8.5	Comments on the search of elliptical skyrmions in a W\Co\Au-Pt solid solution system	160
5.9	W\Fe\Co\Au	160
5.9.1	Growth and crystal characterisation	161
5.9.2	Magnetic characterisation and perspectives	162
6	Conclusions and perspectives	163
6.1	Conclusions	163
6.2	Perspectives	167

Chapter 1

Introduction

Skyrmions are two-dimensional topological solitons that appear in magnetism as chiral whirling vortex-like configurations (Fig. 1.1(a)). They present particle-like properties that are characterized by an integer topological charge. Skyrmions have been theoretically investigated [1, 2] and experimentally observed in bulk systems with B20 symmetry [3] and as metastable objects in ultra-thin magnetic films [4, 5, 6].

The chiral aspect of skyrmions and their stability arise from the presence of an antisymmetry exchange interaction, the Dzyaloshinskii-Moriya interaction (DMI). This interaction favors perpendicular alignment between neighbouring magnetic moments and can be found in systems with a lack of spatial inversion symmetry and spin orbit coupling. DMI manifests as a volume interaction in bulk materials with a lack of crystal inversion symmetry and as an interfacial interaction at the interface between magnetic materials and heavy metals.

DMI was theoretically predicted by Dzyaloshinskii [7] using symmetry arguments in bulk magnetic systems. Then Moriya [8] demonstrated the anti-symmetric spin coupling in systems with a lack of inversion symmetry, by including spin-orbit coupling in the super-exchange interaction. Fert and Levy [9] pointed out that high spin-orbit scattering centers can break the indirect exchange symmetry.

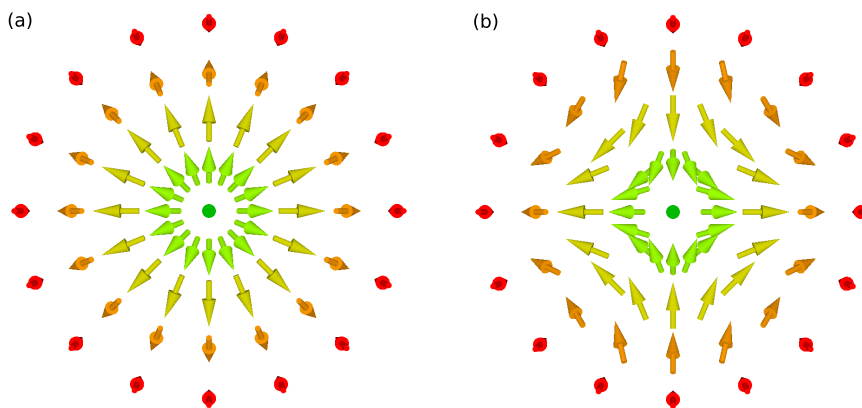


Figure 1.1: Artistic images of a skyrmion (a) and an anti-skyrmion (b) magnetic configuration

In this work, I try to answer to a fundamental question: Which is the relationship between the **crystal symmetry**, the **DMI symmetry** and the **topological solitons** in epitaxial magnetic thin films?

Skyrmions have an isotropic magnetic configuration and have been experimentally found in systems with isotropic magnetic interactions. Anisotropic magnetic interactions occur in systems with a reduced degree of symmetry, like in a crystal with C_{2v} symmetry, and they may lead to the stabilisation of new topological solitons, like **elliptical skyrmions** and **anti-skyrmions**.

The first are skyrmions with a non-cylindrical symmetry in anisotropic energy environments. The effect of spatially modulated exchange energy and magneto-crystalline anisotropy on the skyrmion shape has been theoretically analyzed [10, 11] and experimentally investigated [12] in ultra-thin films, while a distorted

skyrmion lattice [13] has been evidenced due to an anisotropic DMI in a mechanically-strained single-crystal.

Anti-skyrmions have been theoretically predicted in bulk systems where the D_{2d} and S_4 [1] symmetry induces an anisotropic DMI with inversion of chirality between perpendicular directions. They have been theoretically investigated as metastable states at an energy higher than the one of the skyrmion in ultrathin films with isotropic chirality [14] and in systems without DMI [15].

Anti-skyrmions (ASK) have been experimentally observed in a crystal with D_{2d} symmetry in a lattice configuration [16], but not yet in thin film systems as metastable isolated solitons. The reason is that most thin film systems showing DMI studied until now were polycrystalline, leading to the same sign and strength of the DMI in any in-plane direction. In order to stabilize ASK in thin films with perpendicular magnetisation, the sign of DMI has to be opposite along two in-plane directions of the film. This may occur in epitaxial thin films with a C_{2v} symmetry [17, 11, 18].

The work is organized into four chapters. The first two introduce the basic concepts, methods and approaches needed to try to answer to the questions posed at the beginning of this thesis:

- **Introduction to magnetism in C_{2v} symmetry systems**

First the magnetic interactions are introduced with several models. The magnetism is studied with the continuous micromagnetic approximation. The micromagnetic formulations of the interactions are derived from the atomic formulations. This approach allows to set a relationship between the crystal structure and symmetry and the micromagnetic formulations of interactions in systems with a C_{2v} symmetry.

- **Techniques and methods**

In this chapter the main experimental techniques used during this work are introduced. The main theoretical concepts needed to understand the physical phenomena on which these methods are based are explained. The techniques can be divided into three categories: crystal growth method and symmetry characterisation, magnetic characterisation and microscopy techniques.

The third and fourth chapters try to answer with theoretical and experimental approaches to the question of this thesis.

- **Topological magnetic solitons**

This chapter starts with a general introduction on topological solitons and on topological properties. Then one-dimensional and two-dimensional topological magnetic solitons are characterised and their topological properties discussed.

A micromagnetic approach is used that allows to start from the simplest one-dimensional soliton, the domain wall, and to add new interactions and symmetries step-by-step in order to characterise the stability conditions and the properties of skyrmions and anti-skyrmions. This approach allows to understand which topological soliton can be obtained as a function of the strength and of the symmetry of the magnetic interactions in systems with C_{2v} symmetry.

- **Experimental results on magnetism in thin films with C_{2v} symmetry**

In this chapter three different magnetic epitaxial systems with a C_{2v} symmetry are analysed:

- bcc(110) W \ hcp(0001) Co \ fcc(111) Au
- bcc(110) W \ hcp(0001) Co \ fcc(111) Au-Pt_{solid solution}
- bcc(110) W \ bcc(110) Fe \ hcp(0001) Co \ fcc(111) Au

The discussion for each material is divided into three parts according to the main questions of this work. First the growth conditions and the crystal quality and symmetry will be shown. Then the results of the magnetic characterisation will be discussed in order to understand the strength and symmetry of the anisotropic interactions. Finally the magnetic microscopy images of the magnetic configurations obtained on each system are reported.

Chapter 2

Introduction to the magnetism in C_{2v} systems

In this section the interactions that occur in magnetic systems will be introduced. A phenomenological discussion concerning the origin of the interactions is presented in the start of each section. This allows to understand under which conditions they occur and when they are relevant for the determination of the magnetic configurations. Then the energies of the interactions are formulated in the continuous micromagnetic approximation. The micromagnetic formulations, where it is possible, are calculated starting from the atomic interaction formulations in order to evidence the relationship between the symmetry of the crystals and of the interactions. For sake of simplicity the discussion is first developed for simple one-dimensional or isotropic systems, and then for systems with a C_{2v} symmetry; i.e. two-dimensional systems with two mirror planes perpendicular to the surface normal.

In a second part the response of the magnetisation to the presence of a magnetic field will be described and finally the Curie temperature in thin magnetic systems will be discussed.

The micromagnetic calculations developed in this section are the result of a collaboration with Stanislas Rohart from Laboratoire de Physique des Solides in Orsay (France).

2.1 Magnetic materials and micromagnetic approximation

A material is magnetic when it displays a magnetisation field \mathbf{M} . It arises from the competition between exchange energy and thermal fluctuations. Exchange energy is the interaction between neighbouring atoms that favors a collinear alignment of the atomic magnetic moments, whereas the thermal fluctuations induce disorder in the system. When thermal disorder dominates, the atomic magnetic moments cancel each other and no magnetisation field arises from the material. This condition occurs above a given critical temperature called Curie Temperature (T_C). Materials with a spontaneous magnetisation (M_s) are called ferromagnetic.

The atomic magnetic moments can be described as the sum of two effects:

- the *orbital magnetic moment* $\boldsymbol{\mu}$ arises from the electron's orbit around the nucleus. The orbital magnetic moment of the electron is proportional to its orbital angular momentum \mathbf{L} . In the Bohr model :

$$\boldsymbol{\mu}_L = \frac{e\mathbf{L}}{2m} = \frac{g_L\mu_B\mathbf{L}}{\hbar} \quad (2.1)$$

where \hbar is the reduced Plank constant, $g_L \simeq -1$ is the orbital g-factor and $\mu_B = e\frac{\hbar}{2m} = 9.27 \cdot 10^{-27} J/T$ is the Bohr magneton with e the electron charge and m its mass.

- the electrons own an intrinsic quantum magnetic moment. It is known as the *spin* \mathbf{S} and the resulting momentum reads:

$$\boldsymbol{\mu}_s = \frac{g_S\mu_B\mathbf{S}}{\hbar} \quad (2.2)$$

where the spin g-factor g_S is set to -2 according to Dirac's theory.

The net magnetic moment of an atom is thus the vectorial sum of the orbital and spin magnetic moments of all the electrons:

$$\boldsymbol{\mu}_J = \frac{g_J \mu_B \mathbf{J}}{\hbar} \quad (2.3)$$

where $\mathbf{J} = \mathbf{S} + \mathbf{L}$ and $g_J \approx \frac{3}{2} + \frac{S(S+1) - L(L+1)}{2J(J+1)}$.

This thesis is focused on the study of local magnetic textures $\mathbf{M}(\mathbf{r})$ in a ferromagnetic background. The physics that allows to describe these configurations occurs at the nanoscopic scale. In this range we are at the border between the classic and quantum regimes. $\mathbf{M}(\mathbf{r})$ will be described with a continuous model known as micromagnetism. In order to understand the limits of this approach the magnetic interactions will be described firstly in an atomic quantum model. Then the micromagnetic formulation will be derived starting from the quantum interactions.

The Micromagnetism approach is valid when two conditions are fulfilled :

- The magnetisation \mathbf{M} varies between two atomic sites sufficiently slowly to neglect the discrete nature of the magnetic moments. It is then described with a continuous function $\mathbf{M}(\mathbf{r})$.
- The system is far from the phase transition critical point. Therefore the thermal fluctuations are sufficiently low ($T \ll T_c$) (Sec. 2.8) to consider the magnetisation ($|\mathbf{M}| = M_s$) constant and uniform. The magnetisation can be divided in its norm and its direction. Defining the magnetisation unitary function $\mathbf{m}(r)$, $\mathbf{M}(\mathbf{r})$ reads :

$$\mathbf{M}(\mathbf{r}) = M \mathbf{m}(r) \quad (2.4)$$

2.2 Symmetric exchange interactions

In this section the symmetric exchange interactions are introduced. Considering two magnetic moments, the energy that describes this interaction is invariant when the two moments are switched. Antisymmetric exchange interactions will be introduced in the next section. Three different phenomena are considered and explained as origin of this interaction:

- direct exchange
- RKKY
- super-exchange

The micromagnetic expression of the exchange interaction is derived from the atomistic formulation, in two different cases, in order to evidence the relationship between the crystal structure and the micromagnetic exchange symmetry. First the exchange interaction is formulated using a simple one-dimensional model. This allows to focus on the differences between the atomistic and the micromagnetic model for understanding the conditions needed to allow performing this transformation. Then the exchange interaction is formulated in the particular case of a strained hcp (0001) surface. This surface has a C_{2v} symmetry and an anisotropic exchange interaction can be expected. These calculations allow to develop the micromagnetic model for studying the magnetic configurations in the experimentally studied systems.

2.2.1 Direct exchange

The exchange interaction is a quantum mechanical effect between identical particles. It arises when the wave function of indistinguishable particles overlap and they are subject to the exchange symmetry operation. In the case of electrons, which are fermions, the Pauli exclusion principle generates a repulsion between two identical states and tends to orient the electrons spins in the same direction. Indeed the combined state of fermion particles under symmetric operations displays an antisymmetric form. The lower energy state of this configuration is found when the spins of the two electrons are parallel. This phenomenon can be described by the Heisenberg model (spins are described in a three-dimensional space):

$$\mathcal{E}_{ex} = - \sum_{ij} J_{i,j} \mathbf{S}_i \cdot \mathbf{S}_j \quad (2.5)$$

where \mathbf{S}_i and \mathbf{S}_j are the spins associated to the electrons i and j and $J_{i,j}$ is the exchange constant. The short range nature, due to the overlap of the wavefunctions, allows to consider the sum \sum_{ij} only between the first neighbours.

2.2.2 Indirect exchange interaction

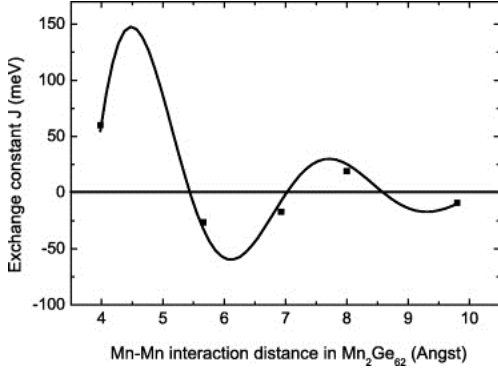
The exchange interaction can occur as an indirect phenomenon. It happens when the two studied wavefunctions do not directly overlap. The interaction is mediated by a third particle that overlaps its wavefunction with the two particles. In this thesis two kinds of indirect exchange interactions are presented:

- In metallic magnets a conduction electron can first interact with a magnetic particle and carry the magnetic moment information to a second one. This interaction is called **RKKY** from the name of the discoverers (Ruderman-Kittel-Kasuya-Yosida) [19]. The Hamiltonian of this interaction can be written as:

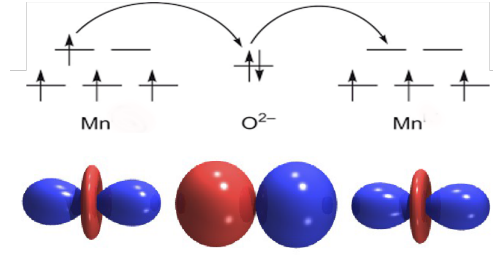
$$\begin{aligned} H(\mathbf{r}_{ij}) &= \sum_{ik} \frac{\boldsymbol{\mu}_i \cdot \boldsymbol{\mu}_j}{4} \frac{|\Delta k k|^2 m^*}{(2\pi)^3 r_{ij}^4 \hbar^2} [2kr_{ij} \cos(2\mathbf{k}\mathbf{r}_{ij}) - \sin(2\mathbf{k}\mathbf{r}_{ij})] \\ &= \sum_{ik} J_{i,k}^{RKKY}(\mathbf{r}) \boldsymbol{\mu}_i \cdot \boldsymbol{\mu}_j \end{aligned} \quad (2.6)$$

where \mathbf{r}_{ij} is the distance between the site i and j ; $\boldsymbol{\mu}_i$ is the magnetic momentum of atom i ; $\Delta k k$ shows the splitting of the electronic levels in the hyperfine configuration; m^* is the effective mass of the electrons in the conduction band and \mathbf{k} is the wave vector of the conduction electrons. The resulting $J_{i,k}^{RKKY}(\mathbf{r})$ is a space dependent quantity with an oscillatory behaviour (Fig. 2.1a)

- In insulating magnets an exchange effect can occur when a non-magnetic atom can share the same orbital with two magnetic atoms. The resulting exchange interaction is called **super-exchange** because of its long range character. It was first discovered in systems where two metallic transition atoms with localized $3d$ orbitals interact with each other through an intermediate ion p orbital. The interaction symmetry strongly depends on the symmetry of the overlapping orbitals. Kanamori [20] and Goodenough [21] formulated semi-empirical rules in order to determine the interaction symmetry using symmetry arguments. Anderson [22] discovered the fundamental role of the spin-orbit coupling in the superexchange interaction.



(a) [23] Dots: strength of the exchange interaction constant (J_n) between two Mn ions as a function of the Mn-Mn distance in $Ge_{1-x}Mn_x$. Solid line: theoretical trend of the RKKY interaction.



(b) Sketch of energy levels involved in the superexchange interaction between two d orbitals through a p orbital

2.2.3 Micromagnetic formulation : one-dimensional model

A simple 1D model helps to describe the exchange interaction formulation in the micromagnetic model. The discussion is expanded to general magnetic moments μ_i and μ_j . The magnetisation direction is described by the angle θ and the difference in direction between two neighbouring moments with $\delta\theta$:

$$\mathcal{E}_{ex} = -J|\mu|^2 \cos(\delta\theta) \quad (2.7)$$

For the micromagnetic conditions $\delta\theta$ is a continuous infinitesimal and the cosine can be expanded around θ_i :

$$\mathcal{E}_{ex} = -J|\mu|^2 \left[1 - \frac{(\delta\theta)^2}{2} \right] = \text{cost} + \frac{J|\mu|^2 a^2}{2} \left(\frac{d\theta}{dx} \right)^2 \quad (2.8)$$

where dx is the variation in the continuous space. The factor a is the distance between the moments a . It is small with respect to magnetic variations and the relation $a/dx = 1$ can be used.

In a 3D system with spherical symmetry the exchange energy density reads:

$$E_{ex} = A \sum_i \sum_j \left(\frac{\partial m_i}{\partial x_j} \right)^2 = A(\nabla \mathbf{m})^2 \quad (2.9)$$

where the magnetisation direction is described by $\mathbf{m}(\mathbf{r})$, \hat{i} and \hat{j} are versors of the 3D space and $A = (J^2/2a)$ is the exchange stiffness. When the spherical symmetry is broken the exchange interaction can be anisotropic and the relation between the atomic interaction and the micromagnetic one are more complex to derive.

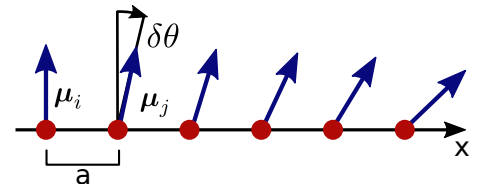


Figure 2.2: Expansion of exchange with θ to link discrete exchange to continuous theory.

2.2.4 Micromagnetic formulation : anisotropic exchange in a system with a C_{2v} symmetry

The exchange interaction in transition metals strongly depends on the distances between the atoms and thus on the crystal structure and symmetry. Therefore it is fundamental to develop a method that allows to formulate the micromagnetic exchange taking into account the atomic structure of the studied system.

In this part the micromagnetic exchange interaction is formulated starting from the atomistic one for the particular case of a strained hexagonal crystal. The crystal is described in Fig. 2.3 and the atomic exchange interaction reads:

$$\mathcal{E}_{ex} = \sum_{ij} \langle J_{ij} \rangle \mathbf{S}_i \cdot \mathbf{S}_j \quad (2.10)$$

where the sum \sum_{ij} is the sum over the nearest-neighbour bonds and the J_{ij} are the exchange parameters between the atoms i and j . Since the exchange constants depend strongly on the atomic distances one can consider $J_{01} = J_{01'} = J_1$ and $J_{02} = J_y$. If the studied magnetic configurations have a characteristic length larger than the interatomic distances one can pass to a continuous approach:

$$\mathcal{E}_{ex} = \frac{1}{2} \sum_i J_1 [(\mathbf{m}(\mathbf{r}_i) \cdot \mathbf{m}(\mathbf{r}'_1)) + (\mathbf{m}(\mathbf{r}_i) \cdot \mathbf{m}(\mathbf{r}_1))] + \frac{1}{2} J_y (\mathbf{m}(\mathbf{r}_i) \cdot \mathbf{m}(\mathbf{r}_2)) \quad (2.11)$$

The previous condition allows to develop the magnetisation $\mathbf{m}(\mathbf{r}_j)$ as the Taylor expansion of $\mathbf{m}(\mathbf{r}_i)$

$$\mathbf{m}(\mathbf{r}_j) = \mathbf{m}(\mathbf{r}_i) + a_j^{(x)} \frac{\partial \mathbf{m}(\mathbf{r}_i)}{\partial x} + a_j^{(y)} \frac{\partial \mathbf{m}(\mathbf{r}_i)}{\partial y} + \frac{1}{2} (a_j^{(x)})^2 \frac{\partial^2 \mathbf{m}(\mathbf{r}_i)}{\partial x^2} + \frac{1}{2} (a_j^{(y)})^2 \frac{\partial^2 \mathbf{m}(\mathbf{r}_i)}{\partial y^2} + \frac{1}{2} a_j^{(x)} a_j^{(y)} \frac{\partial^2 \mathbf{m}(\mathbf{r}_i)}{\partial x \partial y} \quad (2.12)$$

From the micromagnetic theory $|\mathbf{m}| = 1$ and $\mathbf{m} \cdot \partial \mathbf{m} = 0$. Hence it is possible to write $0 = \partial_x (\mathbf{m} \cdot \partial_x \mathbf{m}) = (\partial_x \mathbf{m})^2 + \mathbf{m} \cdot \partial_x^2 \mathbf{m}$ and the micromagnetic exchange energy reads:

$$\mathcal{E}_{ex} = \frac{1}{2} \sum_i \left(2J_1 (a_1^{(x)})^2 \right) \left(\frac{\partial \mathbf{m}(\mathbf{r}_i)}{\partial x} \right)^2 + \left(2J_1 (a_1^{(y)})^2 + J_y (a_2^{(y)})^2 \right) \left(\frac{\partial \mathbf{m}(\mathbf{r}_i)}{\partial y} \right)^2 \quad (2.13)$$

Then one can pass from the discrete sum \sum_i to the continuous integral $1/S \int dS$ with S the surface of the analyzed unit cell. Developing the sums and products one can obtain the micromagnetic expression of the exchange interaction in a strained hexagonal surface with C_{2v} symmetry:

$$\mathcal{E}_{ex} = \int A_x \left(\frac{\partial \mathbf{m}(\mathbf{r})}{\partial x} \right)^2 + A_y \left(\frac{\partial \mathbf{m}(\mathbf{r})}{\partial y} \right)^2 dS \quad A_x = \frac{1}{2} J_1 \cot \beta \quad A_y = \left(\frac{1}{2} J_1 + J_y \right) \tan \beta \quad (2.14)$$

where A_x and A_y are the two-dimensional micromagnetic exchange constants and they directly depend on the crystal structure through the angle β , that describes the deformation of the hexagonal crystal, and the constants J_1 and J_y . These two constants and their strength behaviour as a function of the distance are material dependent. Ab-initio calculations can be used to estimate their strength [24, 25] or they can be derived from experimental techniques [26, 27].

In order to understand the meaning of this formulation two extreme cases can be analyzed :

- Setting the angle $\beta = \pi/6$, the crystal becomes a **perfect hexagon**, J_1 and J_y can be set equal and the exchange energy becomes isotropic:

$$\mathcal{E}_{ex} = \int A \left[\left(\frac{\partial \mathbf{m}(\mathbf{r})}{\partial x} \right)^2 + \left(\frac{\partial \mathbf{m}(\mathbf{r})}{\partial y} \right)^2 \right] dS \quad A = \frac{\sqrt{3}}{2} J \quad (2.15)$$

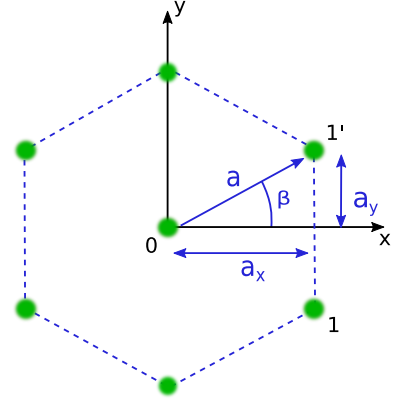


Figure 2.3: Sketch of a strained hcp (0001) surface

- Setting the angle $\beta = \pi/2$ the system becomes a monodimensional atomic chain, J_1 and J_y can be set equal and the exchange energy reads:

$$\mathcal{E}_{ex} = \int A \left(\frac{\partial \mathbf{m}(\mathbf{r})}{\partial y} \right)^2 dS \quad A = J \quad (2.16)$$

2.3 Dzyaloshinskii-Moriya interaction

In this section the Dzyaloshinskii-Moriya interaction (DMI) is introduced. In the first part a discussion is given concerning the origins of this interaction, the conditions for finding it and the systems in which it can be found. Two different models will be discussed:

- Moriya model
- Fert-Levy model

The Fert-Levy model is then used to give a phenomenological interpretation of the origin of the anisotropic DMI in thin films.

2.3.1 Conditions and atomic formulations

The Dzyaloshinskii-Moriya interaction is an antisymmetric exchange interaction that promotes a chiral non-collinear spin arrangement.

$$\mathcal{E}_{ij} = \sum_{ij} \mathbf{d}_{ij} \cdot \mathbf{S}_i \times \mathbf{S}_j \quad (2.17)$$

The atomic vector \mathbf{d}_{ij} sets the sign of the interaction and the chirality of the spin rotation. DMI occurs in systems with two fundamental properties:

- breaking of space inversion symmetry
- presence of spin-orbit coupling

The spin-orbit coupling plays a fundamental role. It allows to couple the spin and orbital magnetic moments. The orbital magnetic moment strongly depends on the system symmetry. The antisymmetric exchange interaction can be found in systems with a lack of spatial inversion symmetry. It was theoretically predicted by Dzyaloshinskii [28] using symmetry arguments in bulk magnetic systems. Then Moriya [8] demonstrated the anti-symmetric spin coupling in systems with a lack of inversion symmetry, by including spin-orbit coupling in the super-exchange interaction. Fert and Levy [9] pointed out that high spin-orbit scattering centers can break the indirect exchange symmetry. DMI can be found in bulk systems with a lack of structural inversion symmetry, in spin glasses or in thin film systems where the inversion symmetry is broken at the interface between magnetic atoms and a heavy metal with high spin-orbit coupling.

2.3.2 Moriya model

Moriya [8], using the Anderson model [22], studied the super-exchange interaction in systems with a high disorder. He was able to analytically derive the antisymmetric spin Hamiltonian theorized by Dzyaloshinsky [29] with symmetry arguments. The Anderson model considers one free $3d$ electron with its spin \mathbf{S} and moment \mathbf{p} in interaction with the ions of the magnetic crystal structure. He considered one-electron wave functions localized at the positions of magnetic (\mathbf{R}) and (\mathbf{R}') ions and orthogonal to each other. When the spin-orbit coupling is introduced these functions are not eigenfunctions of the spin component \mathbf{S}_z anymore.

The one-electron Hamiltonian can then written:

$$H = \frac{p^2}{2m} + V(r) + \frac{\hbar}{2m^2 c^2} \mathbf{S} \cdot [\nabla V(r) \times \mathbf{p}] \quad (2.18)$$

The gradient of potential generates an electric field $\nabla V(r) = \mathbf{E}$ that in the frame of the electron acts as a magnetic field \mathbf{B} . The exchange energy is calculated in second order perturbation with a combination of the annihilation and creation for the different spin states in the different sites. It reads:

$$E_{RR'} = J_{RR'}(\mathbf{S}(\mathbf{R}) \cdot \mathbf{S}(\mathbf{R}')) + \mathbf{d}_{RR'} \cdot (\mathbf{S}(\mathbf{R}) \times \mathbf{S}(\mathbf{R}')) + \mathbf{S}(\mathbf{R}) \cdot \Gamma_{RR'} \cdot \mathbf{S}(\mathbf{R}') \quad (2.19)$$

The first and the third terms are coefficients of the superexchange interaction. The second term is an antisymmetric exchange interaction, i.e. the Dzyaloshinski-Moriya interaction. Its intensity is proportional to the spin-orbit coupling, is strongly dependent on the crystal symmetry and it vanishes in crystals with inversion symmetry.

Moriya rules

Moriya developed some symmetry rules in order to set constraints on the direction of the $\mathbf{D}_{RR'}$ as a function of the crystal symmetries. The coupling between two ions in the crystal is then considered. The two ions 1 and 2 are located at the points A and B and the point bisecting the straight line AB is denoted by C. The following rules are obtained :

- When a center of inversion is located at C,

$$\mathbf{d} = 0 \quad (2.20)$$

- When a mirror plane perpendicular to AB passes through C,

$$\mathbf{d} \parallel \text{mirror plane or } \mathbf{d} \perp \overline{AB} \quad (2.21)$$

- When there is a mirror plane including A and B,

$$\mathbf{d} \perp \text{mirror plane} \quad (2.22)$$

- When a two-fold rotation axis perpendicular to AB passes through C,

$$\mathbf{d} \perp \text{two-fold axis} \quad (2.23)$$

- When there is an n-fold axis ($n \geq 2$) along AB,

$$\mathbf{d} \parallel AB \quad (2.24)$$

These conditions are called Moriya rules and are fundamental in the study of the DMI symmetry. Moreover they play a fundamental role in the derivation of the micromagnetic D constant in anisotropic systems.

2.3.3 Fert-Levy model

Fert and Levy [9] discovered that an antisymmetric exchange interaction can occur in magnetic transition metals in absence of inversion of crystal symmetry. It happens in the presence of non-magnetic impurities with high spin-orbit coupling. Conduction electrons with different spin directions are split in the scattering process with the non-magnetic impurities due to the presence of the spin-orbit coupling. In this process the inversion symmetry with respect to the midpoint between the two magnetic atoms is broken and the exchange has an antisymmetric component.

Fert and Levy [9] described this phenomenon considering the RKKY interaction between two magnetic ions and introducing the spin-orbit coupling in the scattering process with an impurity. They considered one-electron wave functions and performed a perturbation method with the following perturbing potential :

$$V = -\Gamma\delta(\mathbf{r} - \mathbf{R}_A)\mathbf{s} \cdot \mathbf{S}_A - \Gamma\delta(\mathbf{r} - \mathbf{R}_B)\mathbf{s} \cdot \mathbf{S}_B + \lambda(s)\mathbf{l} \cdot \mathbf{s} \quad (2.25)$$

where Γ describes the exchange interaction between the conduction electron spin (\mathbf{s}) and the magnetic ion spin \mathbf{S}_A (\mathbf{S}_B) in the position \mathbf{R}_A (\mathbf{R}_B). The term $\delta(s)\mathbf{l} \cdot \mathbf{s}$ describes the spin-orbit coupling. The symmetric component of this interaction corresponds to the RKKY interaction. The antisymmetric one takes the form:

$$H_{DM} = -V_1 \frac{\sin(\mathbf{k}_f \cdot (\mathbf{R}_A + \mathbf{R}_B + \mathbf{R}_{AB})) + (\pi/10)Z}{|\mathbf{R}_A \mathbf{R}_B \mathbf{R}_{AB}|} (\mathbf{R}_A \times \mathbf{R}_B) \cdot (\mathbf{S}_A \times \mathbf{S}_B) \quad (2.26)$$

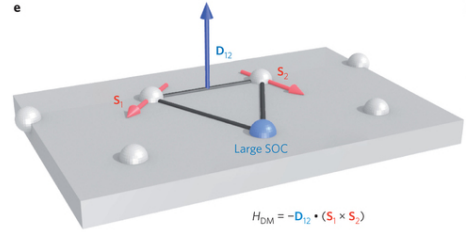


Figure 2.4: Sketch of the atoms that play a role in the DM interaction induced by non-magnetic impurities

where $V_1 = (135/32)(\lambda_d \Gamma^2 / E_F^2 k_F^3) \sin[(\pi/10)Z_d]$ is the perturbation potential for the conduction electron gas with λ_d the spin-orbit coupling constant for d electrons. \mathbf{R}_A , \mathbf{R}_B and \mathbf{R}_{AB} are respectively the positions of the two magnetic atoms and of the impurity; E_F and k_F are the energy and the wavelength of an electron at the Fermi surface and the term $(\pi/10)Z$ is the Fermi level phase shift induced by the interaction of the electron with the Z electrons in the magnetic material.

Notice that the DMI strongly changes as a function of the distance between the magnetic ions and the scattering point. The Fert-Levy model is valid for diluted impurities in a magnetic transition metal, but it is useful to phenomenologically understand the presence of DMI at the interface between a magnetic material and a heavy metal (ref) and the relation between the crystal symmetry and the anisotropic DMI [17, 18]

2.3.4 Interfacial DMI

The DMI can occur in thin magnetic films at the interface with a heavy metal. In these systems the breaking of the inversion symmetry arises from the presence of an interface and the spin-orbit coupling comes from the heavy metal. The antisymmetric exchange occurs in the first atomic layers of the magnetic material and the strength of the interaction scales therefore with the magnetic layer thickness.

Two kinds of micromagnetic DMI constants can be defined, D and D_s , where:

$$D = D_s/t \quad (2.27)$$

D is the micromagnetic DMI constant, D_s is the interface one and t is the film thickness. In order to calculate the atomic DMI vectors and the micromagnetic D strength for a given interface, ab-initio numerical calculations have been performed [30, 31].

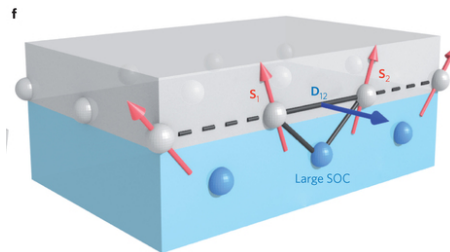


Figure 2.5: Sketch of the atoms that play a role in the DMI induced by the interface interaction between a heavy nonmagnetic metal and a magnetic thin film [32]

2.3.5 Phenomenological interpretation of anisotropic DMI

The DMI directly depends on the crystal symmetry of the studied interface. The relation between the crystal symmetry and the DMI symmetry has already been discussed [33, 34]. The authors analyzed systems with a C_{nv} symmetry, with $n \geq 3$ the number of mirror planes perpendicular to the surface, showing the presence of a microscopic isotropic DMI.

This section has the goal to phenomenologically explain the origin and the effects of the anisotropic DMI in systems with a C_{2v} symmetry. Firstly a phenomenological approach based on the Fert-Levy model will be used in order to understand the importance of the relative positions of the magnetic and the heavy atoms at the crystal interface (Sec. 2.3.3). Then the micromagnetic DMI formulation will be calculated for two different crystal geometries, C_{4v} and C_{2v} . The micromagnetic DMI is an averaged consequence of the atomic interactions. Hence in order to evidence the relation between the crystal symmetry and the micromagnetic DMI it is fundamental to analyze the atomic configuration and the symmetry of the interface between the magnetic and the heavy metal crystal. This analysis does not aim at the quantitative evaluation of DMI, but to illustrate how atomic DMI vectors \mathbf{d}_{ij} between atoms i and j at various atomic sites add up to yield global micromagnetic DMI constants along the main symmetry axes of the system.

The presence of anisotropic DMI in magnetic systems with C_{2v} symmetry can phenomenologically be understood considering the Fert-Levy three atoms model [9] described in Sec. 2.3.3. The strength and the sign of the interaction strongly depend on the geometry of the triangle composed by the ions and the

scattering point. Indeed the DMI vector ($\mathbf{d}(\mathbf{R}_1, \mathbf{R}_2, \mathbf{R}_{12})$) has its direction always parallel to the normal of the triangle and its sign depends on the triangle geometry. In order to understand this dependence two different cases can be analyzed. All the considerations will be extended to a two dimensional crystal where the \mathbf{d} out-of-plane components are averaged to zero. Hence all the analysis will be developed in a 1D approximation.

- We study the DMI sign and strength fixing the distance between the line connecting the magnetic atoms and the scattering point, which is kept centered in between the magnetic atoms (Fig. 2.6). The DMI strength in Fig. 2.6 is thus plotted as a function of the atomic distance R_{12} .

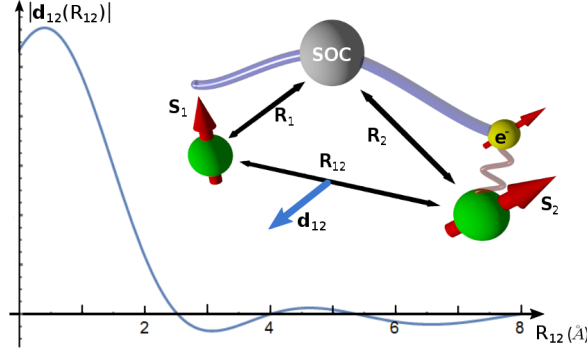


Figure 2.6: Plot of Eq. 2.26 as a function of the distance between the magnetic atoms \mathbf{R}_{12} in \AA . The y axis is normalized with respect to the constant V_1 . An artistic picture shows the configuration and the particles that play a role in the three atoms model for the DMI.

- We fix the position of the magnetic atoms and change the scattering point position in a line parallel to the line connecting the magnetic atoms. The DMI strength in Fig. 2.7 is thus plotted as a function of the distance r .

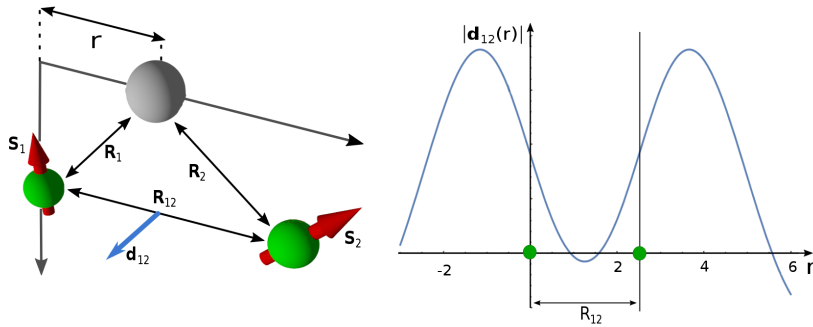


Figure 2.7: Plot of Eq. 2.26 as a function of the position of the scattering point \mathbf{r} . The y axis is normalized with respect to the constant V_1 . The distance between the magnetic ions is set equal to 3\AA .

In both the analysed cases \mathbf{k}_f is estimated from angle-resolved photoemission spectroscopy measurements performed by Moras et al. [35] on a Co/W(110) interface. The plots in Fig. 2.6 and 2.7 evidence the strong dependence of the DMI strength on the geometrical configuration. Indeed a change of the distance between the magnetic atoms and of the scattering point position drastically changes the interaction strength and can modify the DMI sign.

We consider the interface between a magnetic crystal and a heavy metal. In this stack the DMI arises from the interface with the high spin-orbit coupling metal that breaks the inversion symmetry. The Fert-Levy model can not be used to have a quantitative interpretation of DMI strength and sign because the interaction can not be reduced to a simple scattering phenomenon. On the other hand, we can use this

model as a phenomenological tool for determining the crystal symmetry class where it is possible to expect an anisotropic DMI. Indeed we can consider the relationship between the two-dimensional unit cells at the interface and take into account one by one the interactions between the magnetic ions with their closer scattering point independently one from the other.

We focus on the magnetic crystal and we consider the scattering points in the center of the bonds. In this approximation we can notice that a C_{2v} crystal allows an anisotropic interaction. Indeed in a rectangular crystal the difference in distance between the two crystallographic directions could induce a different strength and sign of the DMI vector. The same argument is not valid for higher symmetry classes like C_{3v} or C_{4v} . In these crystals an anisotropic DMI can only be obtained if the scattering points are placed in a different way with respect to the bonds between magnetic atoms.

2.3.6 DMI micromagnetic formulation in C_{4v} systems

In this section the derivation of an isotropic DMI energy in the micromagnetic approximation is performed. For sake of simplicity an interface with a C_{4v} symmetry is considered: a square magnetic crystal at the interface with a square crystalline heavy metal (Fig. 2.8).

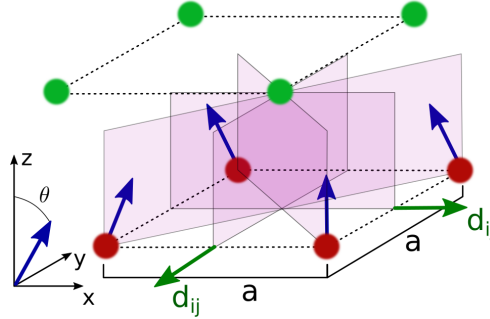


Figure 2.8: Sketch of magnetic moments (blue arrows) in a magnetic square lattice (red) with a C_{4v} symmetry. Four mirror planes (red) pass through the heavy atoms at the interface (green).

First the magnetic moments are replaced with the continuous magnetisation $\mathbf{m}(\mathbf{R})$. The DMI energy reads:

$$\mathcal{E}_{ij} = \sum_{ij} \mathbf{d}_{ij} \cdot [\mathbf{m}(\mathbf{R}_i) \times \mathbf{m}(\mathbf{R}_j)] \quad (2.28)$$

If the magnetisation changes slowly from \mathbf{R}_i to \mathbf{R}_j it is possible to expand the magnetisation around \mathbf{R} :

$$\mathcal{E}_{ij} = \sum_{ij} \mathbf{d}_{ij} \cdot [\mathbf{m}(\mathbf{R}) \times [\mathbf{m}(\mathbf{R}) + \mathbf{r}_{ij} \nabla \mathbf{m}(\mathbf{R})]] \quad (2.29)$$

The distance between the atoms can be set as $a = |\mathbf{r}_{ij}|$. The crystal presents two mirror planes passing through the heavy metal atoms. Then for the Moriya symmetry rules (see Sec. 2.3.2) the \mathbf{d}_{ij} are perpendicular to \mathbf{r}_{ij} and to the normal to the surface \mathbf{n} ($\mathbf{d}_{ij} = d(\mathbf{n} \times \mathbf{r}_{ij})$). The DM energy can be written:

$$\mathcal{E}_{DMI} = ad \left[\hat{y} \cdot \left(\mathbf{m} \times \frac{\partial \mathbf{m}}{\partial x} \right) - \hat{x} \cdot \left(\mathbf{m} \times \frac{\partial \mathbf{m}}{\partial y} \right) \right] \quad (2.30)$$

Developing the vectorial products the DMI energy density E_{DMI} reads:

$$\begin{aligned} E_{DMI} &= D \left[\left(\mathbf{m}_z \frac{\partial \mathbf{m}_x}{\partial x} - \mathbf{m}_x \frac{\partial \mathbf{m}_z}{\partial x} \right) + \left(\mathbf{m}_z \frac{\partial \mathbf{m}_y}{\partial y} - \mathbf{m}_y \frac{\partial \mathbf{m}_z}{\partial y} \right) \right] \\ &= D \left(\mathcal{L}_{xz}^{(x)} + \mathcal{L}_{yz}^{(y)} \right) \end{aligned} \quad (2.31)$$

with $D = \frac{d}{at}$ the micromagnetic DMI constant in J/m^2 . The convention of the Lifshitz invariants is used $L_{jk}^{(i)} = m_j \frac{\partial m_k}{\partial i} - m_k \frac{\partial m_j}{\partial i}$. This formulation is useful to describe the symmetry of a spin rotation promoted by the DMI. (i) indicates the direction in which the magnetisation is changing whereas (jk) describes the

plane where the magnetisation is rotating. In this simple case the DMI promotes an isotropic in-plane magnetisation modulation with the rotation plane parallel to the magnetisation change (Néel modulation). Defining θ as the angle between the magnetisation and \mathbf{n} and considering the circular symmetry the DMI energy density reads:

$$E_{DMI} = D \left(\frac{d\theta}{dr} \right) \quad (2.32)$$

where r is a radial coordinate. This energy formulation can be generalized to all isotropic magnetic systems. In case of anisotropic systems the discussion has to be performed for each crystal structure [34]

2.3.7 DMI micromagnetic formulation in a C_{2v} symmetry system

In this part the micromagnetic DMI will be calculated for an interface with a C_{2v} symmetry [17]. This calculation is developed in the specific interface geometry of the W bcc(110)\Co hcp (0001) interface. It allows to show the relationship between atomic vectors and micromagnetic parameters in the interface experimentally studied in this thesis (Sec. 5.2).

The Co/W superstructure is described in Sec. 5.2.3. In the Co/W superlattice the position of the W atoms with respect to the Co atoms changes from one Co unit cell to the next. Thus one can expect \mathbf{d}_{ij} vectors with different strengths and directions.

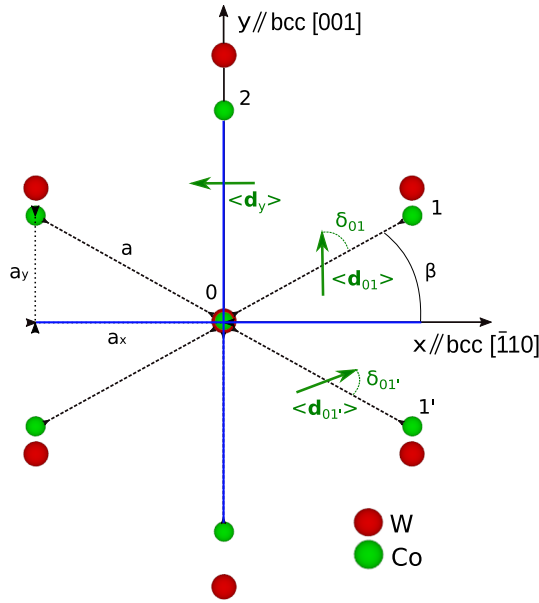


Figure 2.9: Sketch of the higher symmetry Co/W cell with the atomic DMI vectors (green) and the two symmetry planes (blue lines) of the C_{2v} symmetry.

Since the characteristic exchange length is larger than the super cell size, one can consider in this calculation only the higher symmetry cell. In Fig. 2.9 the higher symmetry Co/W cell with the $\langle \mathbf{d}_{ij} \rangle$ of the first neighbours are shown. The $\langle \mathbf{d}_{ij} \rangle$ vectors are the average of all the \mathbf{d}_{ij} for the same bonds on the superlattice.

The Moriya symmetry rules ([8]; Sec.2.3.2) allow to impose some constraints on the atomic $\langle \mathbf{d}_{ij} \rangle$ vectors. Indeed along the 02 bond the W atoms are aligned with the Co atoms and they belong to one of the mirror planes of the system. Then the $\langle \mathbf{d}_{02} \rangle$ will lie in the crystal plane perpendicular to its bond. Concerning the bonds 01' and 01, it is possible to define a two-fold symmetry axis passing through the W atom positions and perpendicular to these bonds. Hence the $\langle \mathbf{d}_{01'} \rangle$ and $\langle \mathbf{d}_{01} \rangle$ will lie in the plane perpendicular to the two-fold axis, i.e. within the crystal plane. The direction of these DMI vectors in the plane is defined

by two angles $\delta_{01'}$ and δ_{01} in Fig. 2.9. It is possible to write these vectors in the two-fold crystal framework:

$$\langle \mathbf{d}_{01'} \rangle = [\langle d_{01'} \rangle \cos(\delta_{01'} - \beta), \langle d_{01'} \rangle \sin(\delta_{01'} - \beta), 0] \quad (2.33)$$

$$\langle \mathbf{d}_{01} \rangle = [\langle d_{01} \rangle \cos(\delta_{01} + \beta), \langle d_{01} \rangle \sin(\delta_{01} + \beta), 0] \quad (2.34)$$

$$\langle \mathbf{d}_{02} \rangle = [-\langle d_y \rangle, 0, 0] \quad (2.35)$$

In a general two-dimensional system the DMI energy in the micromagnetic approach reads:

$$E_{DM} = - \int \left(D_{(xz)s}^{(x)} L_{xz}^{(x)} + D_{(yz)s}^{(y)} L_{yz}^{(y)} + D_{(yz)s}^{(x)} L_{yz}^{(x)} + D_{(xz)s}^{(y)} L_{xz}^{(y)} \right) dx dy \quad (2.36)$$

where $D_{(jk)s}^{(i)}$ are the surfacic DMI micromagnetic constants (in J/m) and $L_{jk}^{(i)}$ are Lifshitz invariants $L_{jk}^{(i)} = m_j \frac{\partial m_k}{\partial i} - m_k \frac{\partial m_j}{\partial i}$. The existence of this term $D_{(jk)s}^{(i)} L_{jk}^{(i)}$ is the signature that the DMI stabilizes a spin modulation where the j and k magnetic components change along the i direction. Along each direction the DMI stabilizes Bloch spirals ($D_{(xz)s}^{(y)} L_{xz}^{(y)}$ and $D_{(yz)s}^{(x)} L_{yz}^{(x)}$) and Néel cycloids ($D_{(xz)s}^{(x)} L_{xz}^{(x)}$ and $D_{(yz)s}^{(y)} L_{yz}^{(y)}$). In a C_{2v} symmetry system there are two mirror planes and the symmetry imposes that the magnetisation rotates in these planes [8]. Hence along the main axes of the system the DMI stabilizes only Néel cycloids and their energy can be formulated in the main axis coordinate system :

$$E_{DM} = - \int \left(D_{(xz)s}^{(x)} L_{xz}^{(x)} + D_{(yz)s}^{(y)} L_{yz}^{(y)} \right) dx dy \quad (2.37)$$

Eq. 2.37 shows that the DMI micromagnetic constants stabilizing Bloch spirals have to be zero. This evidence can be used to set new constraints on the atomic \mathbf{d}_{ij} vectors.

In order to understand how to set these constraints a general model can be developed to elucidate how to pass from the atomic \mathbf{d}_{ij} vectors to the micromagnetic $D_{(jk)s}^{(i)}$ constant for a system with different neighbours labelled with index k. Each bond can be characterized by the position of the Co atom \mathbf{a}_k and by a DMI vector \mathbf{d}_k . The atomic DMI energy in the first neighbours limit can be written:

$$E_{DM} = \frac{1}{2} \sum_i \sum_{k \in \text{NN}(i)} \mathbf{d}_k (\mathbf{m}_i \times \mathbf{m}_k) \quad (2.38)$$

where the summations are respectively performed on all atoms i and the nearest neighbours (NN) k of i . The case of large length magnetic configurations allows to describe the magnetisation in a continuous medium approach and to express \mathbf{m}_k as the Taylor expansion of \mathbf{m}

$$\begin{aligned} \mathbf{m}(\mathbf{r}_k) &= \mathbf{m}(\mathbf{r}_i) + (\mathbf{r}_k - \mathbf{r}_i) \cdot \hat{\mathbf{x}} \frac{\partial \mathbf{m}(\mathbf{r}_i)}{\partial x} + (\mathbf{r}_k - \mathbf{r}_i) \cdot \hat{\mathbf{y}} \frac{\partial \mathbf{m}(\mathbf{r}_i)}{\partial y} \\ &= \mathbf{m}(\mathbf{r}_i) + a_k^{(x)} \frac{\partial \mathbf{m}(\mathbf{r}_i)}{\partial x} + a_k^{(y)} \frac{\partial \mathbf{m}(\mathbf{r}_i)}{\partial y} \end{aligned} \quad (2.39)$$

then using Eq. 2.39 in Eq. 2.38, developing the vectorial and scalar products and using the formalism of the Lifshitz invariants, the DM energy can be written as :

$$E_{DM} = \frac{1}{2} \sum_{ik} a_k^{(x)} d_k^{(x)} L_{yz}^{(x)}(\mathbf{r}_i) - \sum_{ik} a_k^{(x)} d_k^{(y)} L_{xz}^{(x)}(\mathbf{r}_i) + \sum_{ik} a_k^{(y)} d_k^{(x)} L_{yz}^{(y)}(\mathbf{r}_i) - \sum_{ik} a_k^{(y)} d_k^{(y)} L_{xz}^{(y)}(\mathbf{r}_i) \quad (2.40)$$

Eq. 2.40 allows to calculate the micromagnetic DMI constant.

$$E_{DM} = \frac{1}{2} \sum_{ik} \left[a_k^{(x)} d_k^{(x)} L_{yz}^{(x)}(\mathbf{r}_i) - a_k^{(x)} d_k^{(y)} L_{xz}^{(x)}(\mathbf{r}_i) + a_k^{(y)} d_k^{(x)} L_{yz}^{(y)}(\mathbf{r}_i) - a_k^{(y)} d_k^{(y)} L_{xz}^{(y)}(\mathbf{r}_i) \right] \quad (2.41)$$

where S is the unit cell surface and the micromagnetic constants become:

$$D_{(xz)s}^{(x)} = \frac{1}{2S} \sum_k a_k^{(x)} d_k^{(y)} \quad D_{(yz)s}^{(y)} = -\frac{1}{2S} \sum_k a_k^{(y)} d_k^{(x)} \quad (2.42a)$$

$$D_{(xz)s}^{(y)} = \frac{1}{2S} \sum_k a_k^{(y)} d_k^{(y)} \quad D_{(yz)s}^{(x)} = -\frac{1}{2S} \sum_k a_k^{(x)} d_k^{(x)} \quad (2.42b)$$

Then if the analysed system has a C_{2v} symmetry $D_{(xz)s}^{(y)} = D_{(yz)s}^{(x)} = 0$ and this relation can be used to set the relation between the \mathbf{d}_{ij} vectors. For sake of simplicity in the following $D_{(xz)s}^{(x)}$ and $D_{(xz)s}^{(y)}$ constants are renamed respectively $D_s^{(x)}$ and $D_s^{(y)}$.

Now the micromagnetic D_s constants and their relation with the atomic \mathbf{d}_{ij} for the case of Co/W(110) can be found. Setting \mathbf{a}_k and \mathbf{d}_k in Eq. 2.42b equal to zero we obtain:

$$a \cos \beta \langle d_{01} \rangle \cos(-\beta + \delta_{01}) + a \cos \beta \langle d_{01'} \rangle \cos(\beta + \delta_{01'}) = 0 \quad (2.43)$$

$$- a \sin \beta \langle d_{01} \rangle \sin(-\beta + \delta_{01}) + a \sin \beta \langle d_{01'} \rangle \sin(\beta + \delta_{01'}) = 0 \quad (2.44)$$

Solving the system we find that $\langle d_{01} \rangle = \langle d_{01'} \rangle = d$ and $\delta_{01} = \pi - \delta_{01'}$. Hence the micromagnetic D_s constants become:

$$D_s^{(x)} = \frac{d \sin(\beta + \delta_{01})}{a \sin \beta} \quad (2.45)$$

$$D_s^{(y)} = \frac{2d}{a} \left[\frac{\cos(\beta + \delta_{01})}{\cos \beta} - \frac{d_y}{d} \frac{1}{\cos \beta} \right] \quad (2.46)$$

2.4 Zeeman energy

If a magnetic moment $\boldsymbol{\mu}$ is immersed in an external magnetic field a momentum of force is applied to turn it in the field direction. This phenomenon can be described by the Zeeman energy density:

$$E_Z = -\mu_0 \boldsymbol{\mu} \cdot \mathbf{H} \quad (2.47)$$

since the interaction is an external perturbation and does not depend on the relation between the magnetic moments in different points in space the micromagnetic form can be obtained replacing the magnetic moment with the magnetisation $\mathbf{M}(\mathbf{R})$:

$$E_Z = -\mu_0 \mathbf{M}(\mathbf{R}) \cdot \mathbf{H} \quad (2.48)$$

2.5 Magneto-crystalline anisotropy energy

The presence of a magnetic order can be described (see Sec. 2.2.1) using non-relativistic quantum mechanics. In this model the system free energy is independent on the magnetisation direction, i.e. the magnetic moments are free to orientate in all the space directions. In real systems the magnetisation lies in some preferred directions with respect to crystal axes or sample shape. This phenomenon can be introduced considering a relativistic correction of the electrons Hamiltonian. It introduces two effects that can break the isotropic characteristics of the magnetisation.

- The *relativistic correction to the kinetic energy*

$$E = \sqrt{\mathbf{p}^2 c^2 + m^2 c^4} = mc^2 + \frac{\mathbf{p}^2}{2m} - \frac{1}{8} \frac{(\mathbf{p}^2)^2}{m^3 c^2} + \dots \quad (2.49)$$

Where \mathbf{p} is the electron moment, m the electron mass and c the speed of light. In first approximation the third term in eq. 2.49 can be used to study the relativistic effects. This can be done using a perturbation theory with non-relativistic Hamiltonian. Since it depends on the crystal field $V(r)$ the resulting energy shift acquires an angular momentum dependence with the same symmetry as $V(r)$.

- The *spin-orbit coupling* describes the effect of the magnetic field that an electron feels when it moves in the crystal potential field $V(r)$.

$$-\boldsymbol{\mu} \cdot \mathbf{B} = \frac{e}{(mc)^2} \frac{1}{r} (\nabla V(\mathbf{r})) \mathbf{L} \cdot \mathbf{S} = \lambda \mathbf{L} \cdot \mathbf{S} \quad (2.50)$$

The introduction of this interaction splits the energy of electrons with different spins. This effect, as the previous, strongly depends on the crystal potential $V(\mathbf{r})$ and on its symmetry.

The effect of these phenomena is to lift the degeneracy of the spin orientation of the electrons in space and thus of the magnetisation. The probability to have the net magnetisation along some directions is bigger than along others. This is described by the magneto-crystalline anisotropy energy (MAE). It favours the alignment of magnetisation along specific axes or planes of the solid, called easy directions. The directions where this energy is maximized, are called hard axes.

A general expression of this energy density reads:

$$E_{mc} = \sum_i K_i f_i(\theta, \varphi) \quad (2.51)$$

where $f_i(\theta, \varphi)$ is a dimensionless function depending on the spherical coordinates and belongs to the same symmetry group as the magnetic crystal. K_i is the magneto-crystalline energy intensity.

The reversibility of this interaction involves the time-reversal symmetry of the energy; i.e. $f_i(\theta, \varphi)$ has only even terms. For example in cubic crystals the MCA energy density reads:

$$E_{mc} = K_1 s + K_2 p + K_3 p^2 + \dots \quad (2.52)$$

where $s = \alpha_1^2 \alpha_2^2 + \alpha_2^2 \alpha_3^2 + \alpha_1^2 \alpha_3^2$, $p = \alpha_1^2 \alpha_2^2 \alpha_3^2$ and α_i are the cosines of the magnetisation direction with respect to the cube axes.

Interface anisotropy

The presence of the interface with other materials or a surface adds an extra term to the magneto-crystalline anisotropy. The presence of surfaces and interfaces breaks the system's translational invariance. Then even the crystal field $V(r)$ symmetry is broken and a surface-interface MCA energy term can be expected. The total magneto-crystalline anisotropy energy density reads:

$$E_{MC} = E_{MC}^{(bulk)} + \sum_i \frac{K_i^{(s)}}{t} f_i(\theta, \varphi) \quad (2.53)$$

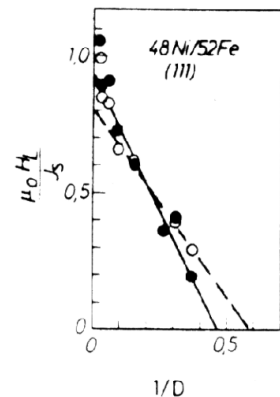


Figure 2.10: Historical example of the $1/t$ behaviour of the interfacial anisotropy in pitaxial 48Ni/52Fe (111) films [36]

where $K_i^{(s)} = K_s$ is the surface-interface magneto crystalline energy density. The $1/t$ term is introduced in order to consider the surface-interface nature. The magnetisation is influenced by this term only when the system thickness (t) is small making the surface effects relevant. It occurs generally in a thickness range up to a few nanometres.

Experimental studies confirm the $1/t$ law for the dependence of K_s on the thickness [36]. Moreover a tight-binding approach allowed to calculate the order of magnitude and the direction of K_s starting from the crystal structure [37]. A relation between the spin-orbit constant λ , the magnetic orbital moment difference between the easy and hard axis $\Delta\mu_L$, and the total MCA constant was found. In a uniaxial anisotropy case the energy per magnetic atom reads :

$$K \propto \frac{\lambda}{4\mu_B} \Delta\mu_L \quad (2.54)$$

Magneto-crystalline anisotropy in a system with C_{2v} symmetry

Eq. 2.51 shows that the magneto-crystalline anisotropy strongly depends on the crystal symmetry. A crystal with C_{2v} symmetry has two mirror planes perpendicular to each other and to the system plane (Fig. 2.11). Then one can expect a biaxial magneto-crystalline anisotropy with one axis in the sample plane (\hat{x}, \hat{y}) and one parallel to the system normal (\hat{z}). In these systems the magnetisation can be described using polar coordinates with the two angles θ and ϕ defined in Fig. 2.11.

The anisotropy energy density can be formulated:

$$E_a = (K_{\text{out}} - K_{\text{d}}) \sin^2 \theta - K_{\text{in}} \sin^2 \theta \cos^2 \phi \quad (2.55)$$

where K_{out} and K_{in} are the out-of-plane and the in-plane MCA constants. When the anisotropy constant K_{out} is positive and larger than K_{d} and K_{in} the system is magnetized out-of-plane with an extra easy axis in the plane. When the constant K_{in} is positive (negative) the \hat{x} direction is the in-plane easy axis (hard axis).

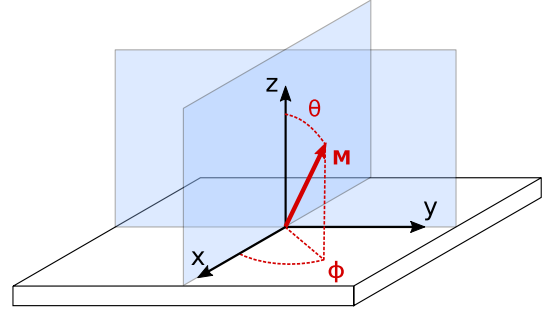


Figure 2.11: Sketch of the symmetry planes in a C_{2v} system (blue planes) and the frame used to describe the magnetisation in polar coordinates.

2.6 Dipolar energy

The dipolar or magnetostatic interaction arises from the mutual Zeeman interaction between all the dipoles in the volume of the magnetic material.

A single magnetic moment $\boldsymbol{\mu}_1$ generates a magnetic field:

$$\mathbf{H}(\mathbf{r}) = \frac{1}{4\pi r^3} \left(3 \frac{(\boldsymbol{\mu}_1 \cdot \mathbf{r})\mathbf{r}}{r^2} - \boldsymbol{\mu}_1 \right) \quad (2.56)$$

The mutual magnetostatic energy of the interaction with another magnetic moment $\boldsymbol{\mu}_2$ reads :

$$\mathcal{E}_d = \frac{1}{4\pi r^3} \left[3 \frac{(\boldsymbol{\mu}_1 \cdot \mathbf{r})(\boldsymbol{\mu}_2 \cdot \mathbf{r})}{r^2} - \boldsymbol{\mu}_1 \cdot \boldsymbol{\mu}_2 \right] \quad (2.57)$$

This two moments interaction allows to develop an easy model for understanding the effect of the dipolar interaction. For instance one can fix $\boldsymbol{\mu}_1$ in a given position and leave $\boldsymbol{\mu}_2$ free to rotate in a plane. In Fig. 2.12 a representation of the stray field produced by $\boldsymbol{\mu}_1$ is shown. The dipolar interaction is thus reduced when $\boldsymbol{\mu}_2$ is parallel to the stray field direction and generates a stray field that can perfectly superpose the one of $\boldsymbol{\mu}_1$. This magnetic configuration is called flux closure.

In the micromagnetic approximation the magnetic moments are described by the continuous magnetisation function $\mathbf{M}(\mathbf{r})$ and the magnetostatic energy takes the form:

$$\mathcal{E}_d = -\frac{\mu_0}{2} \int_V \mathbf{M}(\mathbf{r}) \cdot \mathbf{H}_d \, dV \quad (2.58)$$

where \mathbf{H}_d is the stray field and the 1/2 prefactor allows to not count twice the mutual Zeeman energy for each couple of moments. The direct solution of this equation is often impossible due to the self-consistent character of the interaction. Hence in this section different approaches to evaluate the dipolar interaction will be presented.

A possible approach consists in comparing the two Maxwell equations for the magnetic and electric fields:

$$\nabla \mathbf{E} = \frac{\rho}{\epsilon_0} \quad \nabla \mathbf{B} = 0 \quad (2.59)$$

where ρ is a volume charge density for the electrostatic field. Replacing \mathbf{B} by $\mu_0(\mathbf{M} + \mathbf{H})$:

$$\nabla \mathbf{H} = -\nabla \mathbf{M} = \rho_V \quad (2.60)$$

Hence one can consider the magnetisation divergence as a magnetic volume charge density (ρ_V) for the magnetic field \mathbf{H} . In a general system the magnetisation has singularities of \mathbf{M} at the surfaces. They can be considered as a magnetic surface charge density $\rho_s = \mathbf{M}(\mathbf{r}) \cdot \mathbf{n}$, where \mathbf{n} is the surface normal.

Using this formalism the magnetic stray field \mathbf{H}_d reads:

$$\mathbf{H}_d(\mathbf{r}) = \iiint_{dV} \frac{-\nabla \mathbf{M}(\mathbf{r} - \mathbf{u})}{4\pi |\mathbf{r} - \mathbf{u}|^3} d^3u + \oint_{dS} \frac{\mathbf{M} \cdot \mathbf{n}(\mathbf{r} - \mathbf{u})}{4\pi |\mathbf{r} - \mathbf{u}|^3} d^2u \quad (2.61)$$

Then substituting H_d in Eq. 2.58 and solving when it is possible the integral allows to calculate the dipolar energy.

Demagnetizing coefficient and local approximation

There are special classes of systems where the formulation of the dipolar energy takes an easy form due to the symmetry and the shape of the magnetic material. Considering a system with a uniform magnetisation $\mathbf{M}(\mathbf{r}) = M$ the average of the magnetic field generated by the magnetisation can be calculated:

$$\langle \mathbf{H}_d(\mathbf{r}) \rangle = -\mathbf{N} \cdot \mathbf{M} = -N_i M_i u_i \quad (2.62)$$

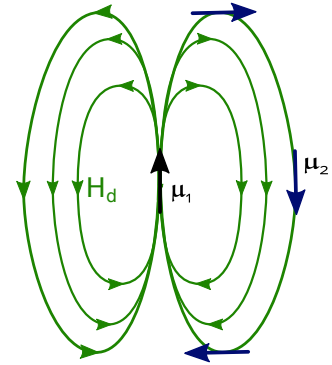


Figure 2.12: Sketch of the stray field (\mathbf{H}_d) produced by a magnetic moment $\boldsymbol{\mu}_1$ and three positions of the moment $\boldsymbol{\mu}_2$ that minimizes the dipolar energy.

\mathbf{N} is defined as the demagnetizing coefficients matrix and can be diagonalized in the u_i frame.

If the surface of a magnetic system is described by a polynomial equation of degree ≤ 2 , eq. 2.62 reads:

$$\mathbf{H}_d(\mathbf{r}) = -N_i M_i u_i \quad (2.63)$$

The values of the demagnetizing coefficients can be found with geometrical considerations and with the property $Tr(N_i) = 1$. Thus the dipolar energy density reads:

$$E_d = K_d \mathbf{m}^T \bar{\bar{\mathbf{N}}} \mathbf{m} \quad (2.64)$$

where $K_d = 1/2\mu_0 M s^2$.

The demagnetizing coefficients are the base of the local approximation. It is used in infinite 2D system where the stray field is locally normal to the system surface. Then the components of $\bar{\bar{\mathbf{N}}}$ are zero along the infinite directions and 1 along the surface normal and the dipolar energy reads:

$$E_d = K_d \sin^2 \theta \quad (2.65)$$

In systems with a MCA axis along the surface normal this effect is considered as a correction to the anisotropy that favours magnetisation in the system plane.

2.7 Magnetic response to an external magnetic field

In this section an introduction of the magnetisation response to an external magnetic field is introduced. Two different situations are described:

- The dynamic response will be studied in the macrospin approximation with the Landau-Lifshitz-Gilbert (LLG) equation.
- The static response for describing magnetisation reversal phenomena will be analysed with two different models as a function of the system disorder.

2.7.1 Dynamic response: Landau-Lifshitz-Gilbert (LLG) equation

The magnetisation dynamics under the application of an external magnetic field can be studied with a macrospin approximation, i.e. the magnetisation distribution is replaced by a single spin \mathbf{m} parallel to the direction of the magnetisation in the studied area. The magnetisation dynamics can thus be studied analysing the effect of the different torques generated by the external magnetic field \mathbf{B} . Moreover the effect of the different magnetic interactions on the macrospin can be introduced using the concept of effective magnetic field $\mu_0 \mathbf{H}_{\text{eff}} = -\delta E_{\text{tot}}/\delta \mathbf{m}$.

The dynamics of a macrospin is described by the Landau-Lifshitz-Gilbert equation:

$$\frac{d\mathbf{m}}{dt} = -\gamma \mathbf{m} \times \mathbf{H}_{\text{eff}} - \alpha \mathbf{m} \times \frac{d\mathbf{m}}{dt} \quad (2.66)$$

where γ is the electron gyromagnetic ratio and α is the damping parameter. The equation can be simplified considering the damping term as a second order effect ($\alpha \ll 1$) and replacing the $d\mathbf{m}/dt$ term of the damping part by the effect of the torques without damping:

$$\frac{d\mathbf{m}}{dt} = -\gamma \mathbf{m} \times \mathbf{H}_{\text{eff}} - \alpha \mathbf{m} \times (\gamma \mathbf{m} \times \mathbf{H}_{\text{eff}}) \quad (2.67)$$

In Sec. 5.4.1 this equation will be used to study the DW dynamics.

2.7.2 Magnetisation reversal

In this section, I discuss two easy models for a phenomenological interpretation of the magnetisation reversal upon the application of an external magnetic field.

The magnetic response can be described by the dimensionless tensor called susceptibility χ_{ij} :

$$M_i = \chi_{ij} H_j \quad (2.68)$$

where M_i and H_j are the magnetisation and magnetic field vectors. In ferromagnetic materials the typical static response to an external field has a hysteresis property and the plot of \mathbf{M} as a function of \mathbf{H} is called hysteresis loop.

Each model is based on strong approximations:

- The **Stoner-Wohlfarth** model considers that the magnetisation changes in a uniform and collinear way during the application of the external field. This is called the macrospin approximation.
- In the **Becker-Kondorski** model the magnetisation change is dominated by the creation and expansion of magnetic domains.

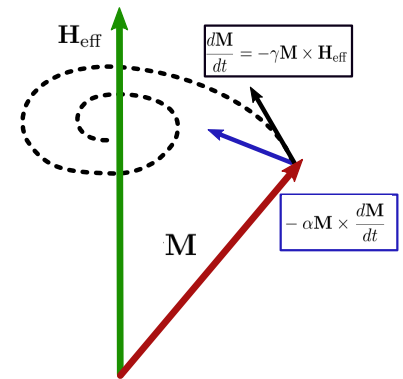


Figure 2.13: Sketch of the vectorial component of eq.5.8

Stoner-Wohlfarth model

The Stoner-Wohlfarth model is based on the hypothesis of uniform collinear magnetisation (macrospin). This is a really restrictive condition, but it helps to phenomenologically understand the magnetic order and to interpret the shape of the hysteresis loops.

An easy situation is considered: an uniaxial system with magnetisation M_s , volume V and total moment $M_s V$. The total energy under the application of an external magnetic field $\mathbf{B} = \mu_0 H$ with an angle θ_B from the easy axis can be written as:

$$\mathcal{E} = KV \sin^2 \theta - \mu_0 M_s H V \cos(\theta - \theta_B) \quad (2.69)$$

where θ is the angle between the magnetisation and the magnetic easy axis (Fig. 2.14).

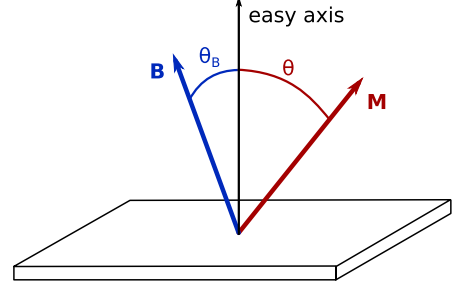


Figure 2.14: Sketch of the magnetic field \mathbf{B} and the macrospin magnetisation \mathbf{M} in a system with a volume V . θ and θ_B are respectively the angle between \mathbf{M} and the easy axis and between \mathbf{B} and the easy axis.

When the magnetic field is applied parallel to the easy axis but in the direction opposite to the magnetisation ($\theta = 0; \theta_B = \pi$), it promotes a magnetisation reversal. In dimensionless variables the system energy reads:

$$e = \frac{\mathcal{E}}{KV} \quad H_a = \frac{2K}{\mu_0 M_s} \quad h = \frac{H}{H_a} \quad (2.70)$$

where H_a is called the anisotropy field.

Hence the minimisation of $e(\theta)$ allows to find the energy minimum and the condition for the magnetisation switching. $\theta_+ = 0$ and $\theta_- = \pi$ are always equilibrium positions. For $h < 1$ an extra equilibrium position θ_b occurs. In that case θ_+ and θ_- are stable equilibrium positions, whereas θ_b is unstable. An energy barrier Δe prevents the magnetisation to reverse from the metastable state θ_+ towards the most stable state θ_- .

$$\Delta e = (1 - h)^2 \quad \Delta \mathcal{E} = KV \left(1 - \frac{H}{H_a}\right)^2 \quad (2.71)$$

For $h > 1$ only θ_+ and θ_- remain as equilibrium positions, respectively unstable and stable.

Then $h = 1 = h_{sw}$ is defined as the switching field; i.e when the system reaches this value an abrupt switching of magnetisation occurs. The energy barrier Δe and the unstable equilibrium point θ_b vanish and θ_- becomes the stable equilibrium point.

Fig. 2.15 shows the resulting hysteresis loop: the magnetisation remanence ($\mathbf{M}(\mathbf{H} = 0)$) is exactly one, the loop has a square shape and the coercivity field ($\mathbf{H}(\mathbf{M} = 0)$) equals the anisotropy field.

The calculation of the switching field can be generalized to an arbitrary value of θ_B and yields:

$$h_{sw}(\theta_B) = \left(\frac{1}{\sin^{2/3} \theta_B + \cos^{2/3} \theta_B} \right)^{3/2} \quad (2.72)$$

The resulting hysteresis loops are displayed in Fig. 2.15. They evolve from a perfectly square shape for the external field applied exactly along the easy axis direction ($\theta_B = 0$), to fully reversible with no remanence for the field applied exactly along a hard axis direction ($\theta_B = \pi/2$).

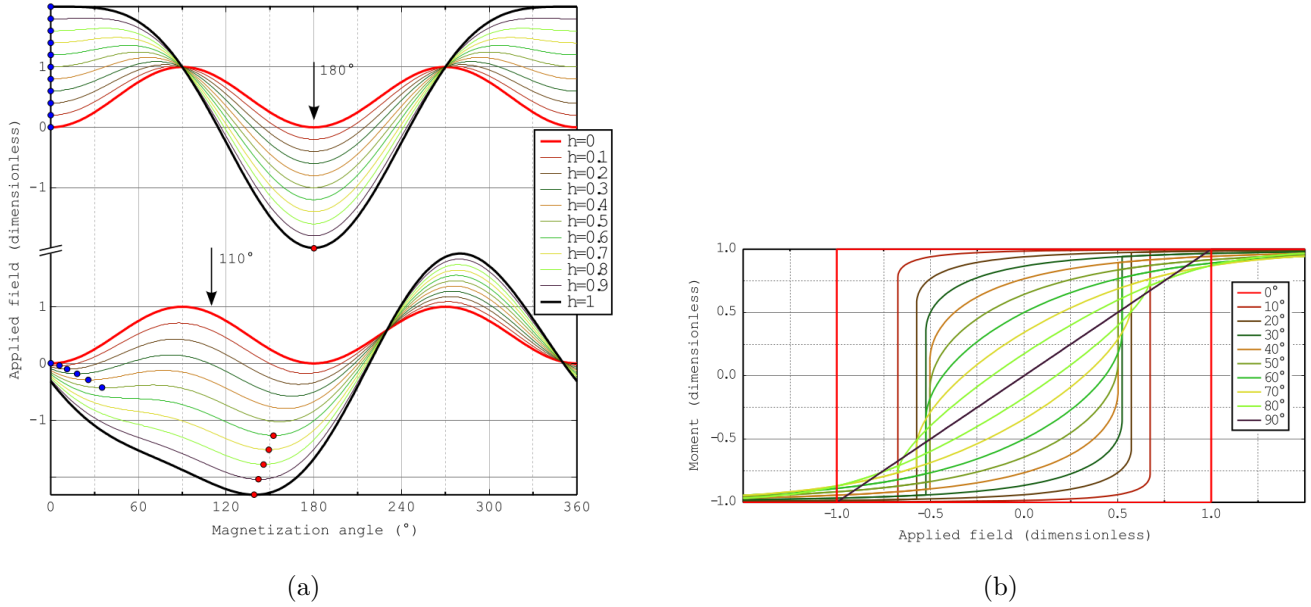


Figure 2.15: [38] (a) Energy profiles for increasing values of applied field, of a macrospin with uniaxial anisotropy. Profiles are drawn for the magnetic field applied along the easy axis ($\theta_B = \pi$, top) and along an intermediate angle ($\theta_B = 110^\circ$, bottom). For the latter, the series of profiles are slightly shifted vertically for clarity. The initial (resp. final) minima are marked with blue (resp. red) dots. (b) Hysteresis loops for various angles of applied field θ_B . Equal values for angles symmetric with respect to 45° are clearly evidenced.

Becker-Kondorski model

In order to easily understand this model, the expansion of a magnetic domain in a one-dimensional magnetic system is considered under application of an external magnetic field parallel to its magnetisation direction. Despite the strong approximation this model is useful for an interpretation of the magnetic response in systems with inhomogeneous magnetic properties.

Fig. 2.16(a) shows an example of a function $U(x)$ describing how the magnetic energy varies along the system. Note the presence of different energy minima. During the expansion of a magnetic domain the domain wall has the tendency to stop at these points (pinning points). The magnetisation distribution is described in Fig. 2.16(b). Two magnetic domains are considered: in the initial state $\mathbf{M} = +M_s$ for $x < x_0 - d$ and $\mathbf{M} = -M_s$ for $x > x_0 + d$ where x_0 is the center of the domain wall and $2d$ the domain wall width (Fig. 2.16).

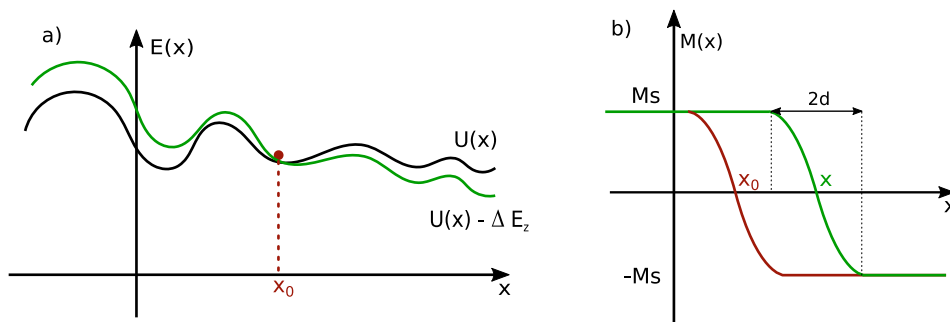


Figure 2.16: a) Energy distribution $U(x)$ and its change ($U(x) - \Delta E_z$) when a magnetic field is applied. b) Profile of the magnetisation before and after the application of a magnetic field

The changes of magnetic energy under the application of an external magnetic field can be calculated

studying the change of Zeeman energy :

$$\mathcal{E}_z = \int_{-\infty}^{+\infty} \mu \mathbf{M} \cdot \mathbf{H} dx \quad (2.73)$$

Hence it can be calculated as the subtraction between the energy of the initial and the final configurations, where the domain wall center is in the position x .

$$\mathcal{E}(x_0)_Z = \int_{-\infty}^{x_0-d} \mu \mathbf{M} \cdot \mathbf{H} dx + \int_{x_0-d}^{x_0+d} \mu \mathbf{M} \cdot \mathbf{H} dx + \int_{x_0+d}^{+\infty} \mu \mathbf{M} \cdot \mathbf{H} dx \quad (2.74)$$

and:

$$\mathcal{E}(x_0 + x)_Z = + \int_{-\infty}^{x_0-d} + \int_{x_0-d}^{x_0-d-x} + \int_{x_0-d+x}^{x+d-x} - \int_{x+d-x}^{x+d} + \int_{x+d}^{+\infty} \mu \mathbf{M} \cdot \mathbf{H} dx \quad (2.75)$$

The subtraction of the two equations is the Zeeman energy gain during the propagation:

$$\Delta \mathcal{E}_Z = -2\mu \mathbf{M} \cdot \mathbf{H} x \quad (2.76)$$

Hence when a magnetic field is applied the energy profile, shown in Fig. 2.16, is calculated as the sum of $U(x)$ and $\Delta \mathcal{E}_Z$:

$$\mathcal{E}(x) = U(x) - 2\mu \mathbf{M} \cdot \mathbf{H} x \quad (2.77)$$

The force $F(x)$ for propagating a DW is :

$$F(x) = -\frac{\partial \mathcal{E}(x)}{\partial x} = -\frac{\partial U(x)}{\partial x} + 2\mu \mathbf{M} \cdot \mathbf{H} \quad (2.78)$$

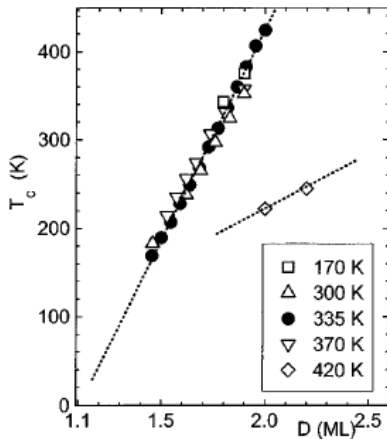
The magnetic domain expands and the magnetisation reverses when $\frac{dF(x)}{dx} = 0$. This condition is equivalent to the vanishing of the minimum of the energy profile in point x . Hence one can write an expression for the critical magnetic field \mathbf{H}_c needed for the domain expansion:

$$\mathbf{H}_c = \frac{1}{2\mu M} \frac{\partial U(x)}{\partial x} \frac{1}{\cos \theta} \quad (2.79)$$

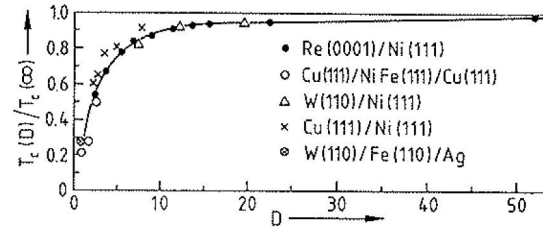
where θ is the angle between \mathbf{H} and \mathbf{M} .

This model can be used to describe the coercive field H_c in the study of magnetic hysteresis loops in systems affected by strong pinning effects. Notice that the critical field, phenomenologically connected with the coercive field, increases when θ increases, contrary to what was shown for the Stoner-Wohlfarth model (Fig. 2.15).

2.8 Curie temperature



(a) [39] Curie temperature as a function of Co thickness for different substrate deposition temperatures. The dashed line is a linear fit of the data with $T_s = 335\text{K}$



(b) Curie temperature as a function of the number of atomic layers (D) in various ultra-thin film materials [40]

The magnetic fluctuations due to finite temperature can reduce the spin correlations until a critical point called Curie Temperature (T_C) where the magnetic order is lost. At this value the system changes phase and transits from a ferromagnetic to a paramagnetic order.

Comparing the statistical expression for the thermal energy and the spin switching energy barrier allows to find a semiclassical expression for the Curie temperature:

$$T_C \propto \frac{2ZJ_{ij}}{3K_B} \quad (2.80)$$

where J_{ij} is the exchange energy constant and Z is the number of nearest neighbours. This model shows a direct correlation between the Curie temperature and the number of neighbours (Z). Then one can expect a reduction of T_C in thin film systems due to the reduction of Z . For instance in a thin film with N layers Z_N can be defined as an effective number of neighbours:

$$Z_N = Z + 2\frac{Z_s - Z}{N} \quad (2.81)$$

where Z_s is the number of nearest neighbours in a surface layer. Generally $Z_s < Z$ and the T_C decreases with a law $1/t$, where t is the sample thickness.

This easy model allows only a phenomenological interpretation. Indeed more complex models and experimental results given in Fig. 2.17b show a slow exponential behaviour of T_c as a function of the thickness [41, 39, 42, 43].

Chapter 3

Techniques and methods

In this chapter the experimental set-ups, the techniques and the methods used during this thesis research are described. First the Ultra-High-Vacuum (UHV) system that allows the sample growth with pulsed laser deposition (PLD) and molecular beam epitaxy (MBE) is described. The different epitaxial growth modes are discussed and two methods for a phenomenological understanding of the transition between them are presented. In this UHV system it is possible to perform *in-situ* crystal structure and topography characterisation during the growth with reflection high-energy electron diffraction (RHEED) and scanning tunneling microscopy (STM).

Then *ex-situ* techniques for the crystal characterisation are discussed. Grazing incidence X-ray diffraction (GIXD) is a synchrotron technique for the crystal characterisation whereas Atomic Force Microscopy (AFM) allows to study the surface topography.

In the third part a review of all the techniques needed for a complete characterisation of magnetic systems is given. In the fourth I describe X-ray magnetic circular dichroism photo-emission electron microscopy (XMCD-PEEM) and magnetic force microscopy (MFM). They allow to display the magnetisation distribution with a nano-scale resolution. Finally the code for performing micromagnetic simulations (OOMMF) and for the data analysis are shown.

3.1 UHV system: deposition and crystal characterisation

The UHV system in the "*pôle epitaxie*" in the Institut Néel, shown in Fig. 3.1, is composed of four different chambers connected with a tunnel that allows the transfer between the different set-ups and the load-lock chamber. A system of primary, turbo and ionic pumps guarantees ultra-high-vacuum in all the system. The experimental work presented in this thesis has been done mainly in the *Riber* and the *STM chamber*. The different environments needed different sample holders. Hence the universal system shown in Fig. 3.2 has been designed.

3.1.1 Riber chamber and Laser

The Riber chamber allows the growth of epitaxial samples with PLD and MBE technologies. Two evaporators allow to deposit two materials with MBE whereas eight different materials can be deposited with PLD. The presence of a mask controlled by a step motor allows to produce thickness steps and wedges during the deposition. A quartz micro balance (QMB) can be placed in the deposition position to calibrate the deposition rate before the sample growth. Before the growth, the sample, fixed on the sample holder, is advanced into the deposition position. The sample holder presents a thermocouple for the temperature control, a Tantalum filament for heating the sample up to 800°C and it allows a complete azimuthal rotation for exploring all the crystallographic directions with the RHEED.

A solid state laser with crystals of Nd-YAG (neodymium-doped yttrium aluminum garnet $NdY_3Al_5O_{12}$) is used for the PLD. It emits a pulsed photon beam with a wavelength of 532 nm. The time of the pulse is below 10 ns and the frequency can be tuned between 10 and 20 Hz. The pulse power is 10 MW. The typical beam spot area is $3 \times 3 \text{ mm}^2$ and the fluence (density of laser energy per pulse and area) on the target surface is 100 MW/cm^2 .

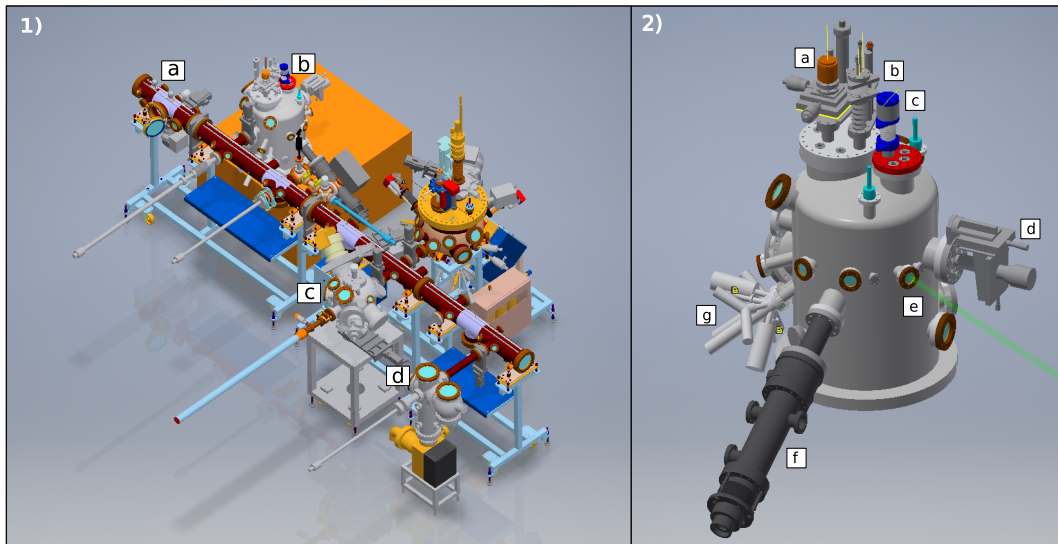


Figure 3.1: (1) Sketch of the complete Ultra High Vacuum system. (a) pre-lock chamber (b) Ribber chamber (c) analysis chamber (d) STM chamber. (2) Ribber chamber: (a) target holder manipulator, step-motors and cooling system (b) mask step-motor and cooling system (c) quartz micro balance manipulator and cooling system (d) sample holder manipulators, oven and thermocouple connections (e) laser window (f) RHEED electron gun (g) MBE evaporators

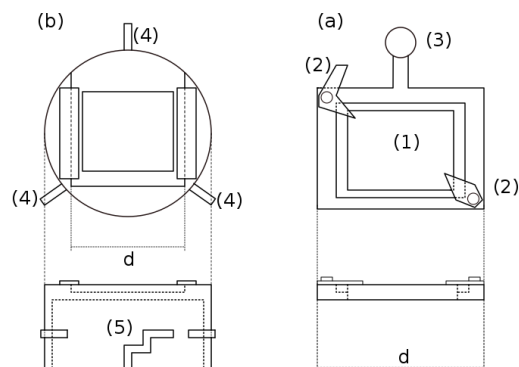


Figure 3.2: Sketch of the two parts that compose the sample-holder. Part (a) presents a slot for the substrates (1). The contact between the substrate and the sample holder is guaranteed by two screwed clamps (2). In the upper part there is a handle (3) for extracting part (a) from (b). Part (b) presents a slot for plugging in part (a). On the side there are three pins (4) and three slots (5) for handling the sample-holder during the transfers.

An optical system allows to focus the laser beam on the target and scan on its surface.

The RHEED electron gun produces an electron beam with an energy up to 30keV. Electric and magnetic lenses inside the RHEED electron gun allow to scan the beam over the sample and change the incidence angle of the electron beam. The diffraction pattern is impressed on a photoluminescent screen and a CCD camera allows to record it.

3.1.2 Pulsed laser deposition

Pulsed Laser Deposition (PLD) is a technique which uses a melted, evaporated and ionized material from a target surface for growing a new layer on a substrate. A highly luminous plasma plume is produced during the ablations event between a nanosecond laser pulse with a high fluence and a target. It allows the evaporation of any kind of material, even the most refractory ones.

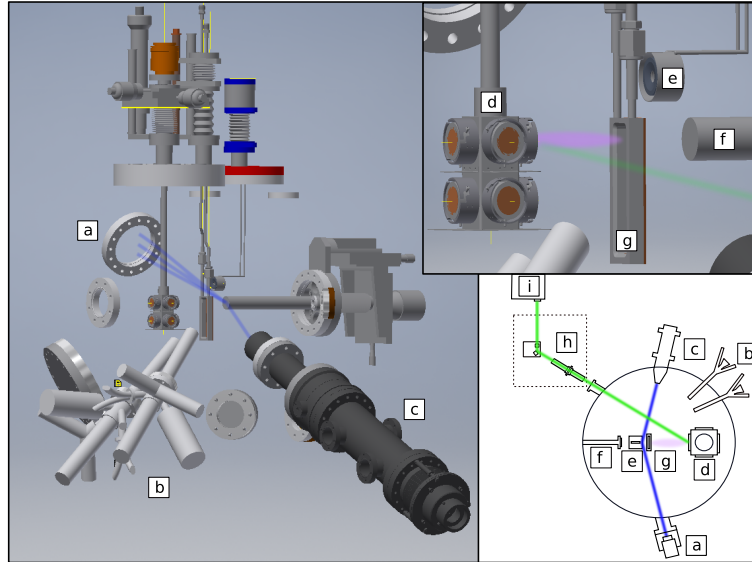


Figure 3.3: Ribber chamber experimental set-up. (blue line) electron beam trajectory for RHEED spectroscopy; (green line) laser trajectory (violet line) plasma plume. (a) RHEED fluorescent screen (b) MBE evaporators (c) RHEED electron gun (d) targets holder (e) quartz micro balance (f) sample holder (g) mask (h) laser optics (i) laser

The phenomenon can be decomposed into three different stages: interaction laser-target, interaction plume-laser and deposition.

Interaction laser-target During the ablation phenomenon on the target surface the laser electromagnetic energy is converted into the excitation of plasmons and unbound electrons. For an electromagnetic wave with a given power density Φ it is possible to evaluate the target electric field amplitude E :

$$E = \sqrt{\frac{2\Phi}{cn\epsilon_0}} \quad (3.1)$$

where ϵ_0 is the permittivity in vacuum, c is the speed of light and n is the refractive index of the evaporated material. The plasma plume is produced when the electric field strength is large enough to reach the material's dielectric breakdown.

The strong electric field produces the ionisation of the material and a high concentration of electrons. Then at the interface of the plasma with the target the pressure can strongly increase ($10^9 Pa$). This causes the plasma propagation into the vacuum [44]. During this process part of the electrostatic energy is dissipated in heat and diffused into the target. Moreover, the heat exchange between the material and the nascent plasma activates a target recoil process. During the laser pulse, droplets of recoil material are formed and ejected from the surface. These droplets can reduce drastically the quality of the deposited layer [45].

The droplet formation can be attributed to different phenomena:

- Subsurface boiling. It occurs when the time for the laser energy conversion into heat is shorter than the evaporation time.
- Recoil ejection. The electrostatic laser pressure on the melted material can eject part of it.
- Exfoliation. This is a hydrodynamic process caused by repeated melt-freeze cycles of the irradiated material. It produces a strong increase of the target roughness and the detachment of part of the material.

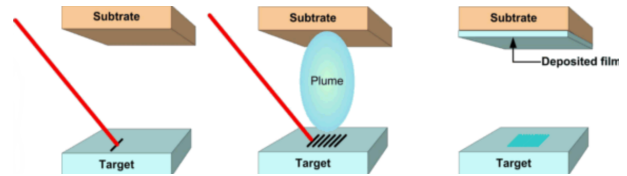
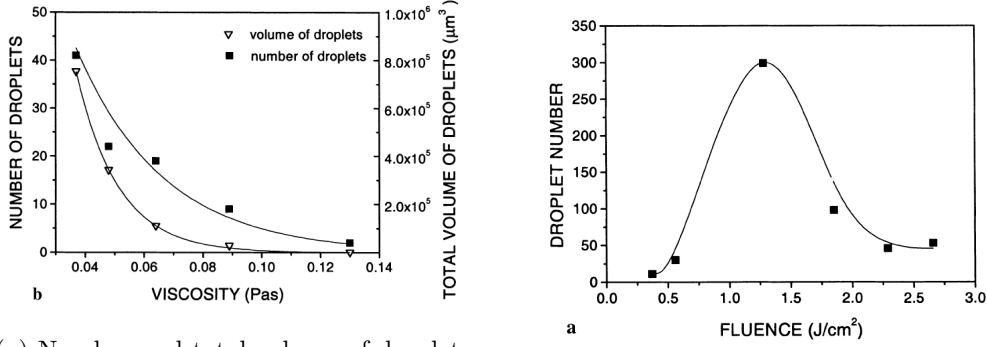


Figure 3.4: Sketch of the three stages of a PLD deposition: interaction laser-target, interaction plume-laser and deposition

Possible solutions to reduce the droplet production are proposed by several studies [45, 46, 47]. The exfoliation can be completely deleted using molten targets near the melting point and with high viscosity. The droplet subsurface boiling and recoil ejection can be reduced decreasing the heat diffusion length $l_D = 2\sqrt{D\tau}$ (where D is the target dielectric function and τ the duration of the pulse), or by tuning the laser fluence. Because metals have a high dielectric function a good solution is to reduce τ . Indeed when the laser pulse length becomes shorter than the characteristic coupling time between the electrons and the lattice, the heat diffusion becomes insignificant. This regime can be reached for τ below some picoseconds.



(a) Number and total volume of droplets and solid particles as a function of target viscosity (b), the applied fluence is 2.3 J/cm² on Polyethylene glycol 1000 [45]

(b) Number of droplets as a function of laser fluence at 708°C on Polyethylene glycol 1000.[45]

Figure 3.5

Interaction laser-plume The interaction between laser and plasma has two main effects:

- The atoms in the plasma plume get ionized by the laser electric field. This interaction can ionize the totality of the plume. It can be explained considering the inverse Bremsstrahlung effect [44] Bremsstrahlung is the effect for which a charged particle emits an electromagnetic radiation when it is deflected by another charged particle.
- The plasma plume screens the target and reduces the heat diffusion.

Optical spectroscopy has been used by Hansen *et al.* [48] to analyze the plasma ionisation in order to study the ionisation degree and the velocity distribution. Despite the plasma formation being a highly non-linear phenomenon, they show that the plume is thermally equilibrated with a Gaussian speed distribution due to the ion-electron recombination.

Deposition PLD allows a high instantaneous deposition rate (10μ m/s) and a slow average deposition rate ($0.5 \text{ \AA}/\text{min}$).

- The high instantaneous deposition rate induces a large nuclei density which favors the homogeneity of the layer-by-layer growth and allows the deposition of solid solutions, i.e. the controlled mixing of two or more materials in the same atomic layer. This allows the formation of a layer with mixed properties between the two materials if the characteristic length of the properties is larger than the characteristic distance between the islands of the different materials [49].
- The slow average deposition rate is fundamental for the epitaxial growth. Indeed between two pulses the deposited material has the time to arrange on the potential minima of the previous layer. The mobility of the deposited material can be increased by heating the substrate.

More details about the epitaxial growth will be presented in Sec. 3.1.4.

3.1.3 Molecular beam epitaxy (MBE)

Molecular beam epitaxy is a method for the growth of epitaxial systems. The materials to deposit are placed into evaporator cells in the UHV system. A resistive filament around the cell heats the material up to the evaporation point. A molecular beam in the direction of the substrate is thus produced. The deposition rate can be controlled tuning the current through the filament. A water cooling system allows to keep the cell temperature stable during the deposition. The kinetic energy of atoms deposited by MBE is lower than the PLD adatoms. It allows to grow layers with less interlayer intermixing. The deposition rate can be controlled in two different ways:

- the micro crystal balance placed in the deposition position allows to calibrate the deposition rate before the growth.
- The RHEED can be used during the deposition. Indeed the RHEED intensity changes as a function of the surface order. It will present, as shown in Fig. 3.6, a maximum when a layer is complete and a minimum when half a layer is deposited.

3.1.4 Thin film epitaxial growth

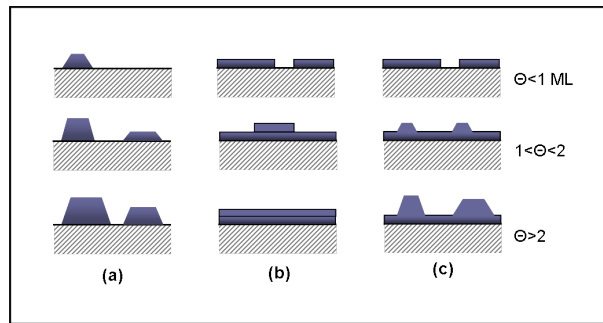


Figure 3.7: Cross-section views of the three modes of thin-film growth. (a) Volmer Weber , (b) Frank van der Merwe and (c) Stranski Krastanov

In this section the main processes for the epitaxial growth of thin mono-crystals are presented. Epitaxial growth is the deposition process that allows to deposit a crystalline overlayer with one well-defined orientation with respect to the substrate crystal structure. The strength of the interaction between adatoms and the substrate determines the growth modes. Three main modes can be defined :

- in **Volmer Weber (VW)** growth the interaction between adatoms is stronger than between the adatoms and the surface. Hence the formation of three-dimensional clusters or islands is favored.
- in **Frank van der Merwe (FM)** growth the interaction with the surface overcomes the adatoms interaction. The adatoms start to form a second layer only when the previous one is completed. This mode is also called layer-by-layer growth and allows to grow complete 2D films.
- the **Stranski Krastanov (SK)** growth is an intermediary process in which the stronger interaction changes during the deposition. In

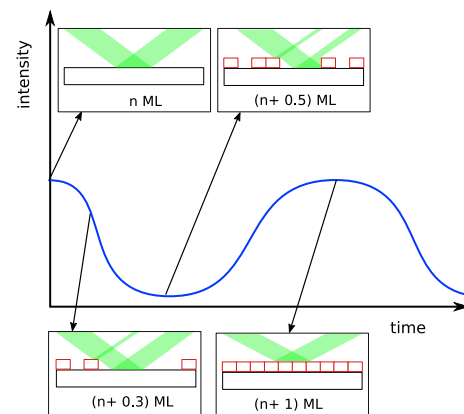


Figure 3.6: RHEED intensity oscillations as a function of the surface order during a layer-by-layer deposition process.

this mode the first layers grow in the layer-by-layer mode whereas subsequent layers form islands. The mode transition occurs at a critical layer thickness h_c , which depends on the chemical and physical properties of the materials.

Two different approaches to determine the critical thickness h_c and hence the growth mode are presented.

Mechanical approach The deposited material and the substrate normally have different lattice parameters and crystal structure. During the epitaxial growth the adatoms arrange in the potential minima of the substrate lattice. Hence the material grows in a deformed configuration to fulfil the epitaxial relations. The transition between a layer-by-layer growth and the islands formation occurs when the system relaxes to minimize the accumulated elastic energy.

In this part a mechanical approach to calculate the critical thickness is presented. Firstly a pseudomorphic epitaxial configuration for the deposited layer is imposed. The elastic energy of the deformed layer is calculated with an elastic approximation. Then the comparison with the dislocation formation energy allows to calculate h_c . Introducing a linear elastic model, the deformation energy can be described as:

$$\epsilon_e = \frac{1}{2} \int_V (\sigma \cdot \epsilon) dV \quad (3.2)$$

where $\sigma \cdot \epsilon = \sum_{ij} \sigma_{ij} \epsilon_{ij}$ is the tensor product between the strain tensor ϵ_{ij} and the stress tensor σ_{ij} . The first describes the crystal deformation and the second describes the force per unit of surface applied to the crystal. Using the Hooke constitutive elastic law the degrees of freedom of the problem can be reduced. It allows to reformulate the tensor product as a function of the strain only:

$$\sigma \cdot \epsilon = \frac{E\nu}{(1+\nu)(1-2\nu)} \epsilon_{ii}^2 + \frac{E}{1+\nu} \epsilon_{ij} \epsilon_{ij} \quad (3.3)$$

where ϵ_{ii} is the track of the tensor which is zero in the incompressible approximation; E is the Young modulus and ν is the Poisson ratio.

The strain can be calculated from the lattice parameters misfit in the given epitaxial relationship:

$$\epsilon_{ii} = \frac{a_i^f - a_i^s}{a_i^s} \quad (3.4)$$

where a^f and a^s are respectively the film lattice parameter and the surface lattice parameter.

The formation of crystal dislocations can reduce the accumulated elastic energy. This effect changes the system topography and favors island formation. The surface energy density γ allows to describe this phenomenon and to calculate the critical thickness h_c . Hence the transition between the two growth modes occurs when the deformed layer energy is equal to the relaxed layer energy.

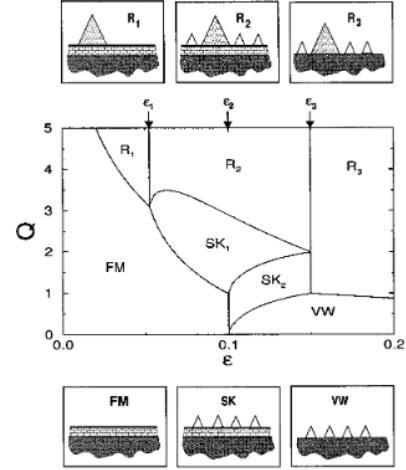


Figure 3.8: Equilibrium phase diagram of a lattice-mismatched heteroepitaxial system as a function of the total amount of deposited material Q and the lattice mismatch ϵ_0 [50]. The small insertions at the top and bottom illustrate the morphology of the surface in the six growth modes described in the text. The small empty triangles indicate the presence of stable islands, while the large shaded ones refer to ripened islands.

For an incompressible material with a surface L^2 and a thickness h one can write:

$$\gamma L^2 + \frac{L^2 h E \epsilon_r^2}{1 - \nu} = \frac{L^2 h E \epsilon_d^2}{1 - \nu} \quad h_c = \frac{(1 - \nu) \gamma}{E(\epsilon_d^2 - \epsilon_r^2)} \quad (3.5)$$

where ϵ_d and ϵ_r are respectively the strain in the deformed layer and in the relaxed one.

Computational models The mechanical model can explain phenomenologically the physics of the transition between the growth modes but hides all the physics of the interlayer interaction in the parameter γ . Moreover it does not take into account the surface instability and the dependence on the temperature.

A thin film grown layer-by-layer can result in a metastable configuration and a perturbation, like an annealing process, can drastically change it. Two computational approaches to consider this phenomenon are here introduced: Asaro-Tiller-Grinfeld [52] developed a model to describe the surface instability and define the apparent critical thickness. This value is defined as the biggest thickness for which the planar film is stable under perturbations.

Baskaran and Smereka [51] used a solid-on-solid atomistic simulation model to study the stability of deposited 2D layers. This model studies the surface energy with a short range bond counting and long range elastic interactions. Moreover it analyzes how these energies change as a function of temperature.

Both models can not be applied to know a-priori the sample growth mode due to the high number of free parameters. They are instead really useful for a phenomenological understanding of the physics of epitaxial growth.

3.1.5 RHEED

Reflection High Energy Electron Diffraction (RHEED) is an experimental technique for studying crystal surfaces. A diffraction pattern is generated by the reflection of a high energy electron beam on a crystalline surface. A phosphorescent screen allows to display in real time the reflected electron pattern.

The diffracted pattern can be studied in order to reconstruct the surface crystal structure. The geometry of the RHEED pattern can be interpreted with two different theories.

- The kinematic theory considers only the diffraction produced by the incident beam and all the interactions between electrons are purely elastic.
- In the dynamical theory the multiple electron scattering effects are taken into account. Indeed scattered electrons can penetrate and interact with the bulk crystal. This phenomenon yields to Kikuchi diffraction patterns.

In this report only the first theory is analyzed. Indeed the elastic constructive interference conditions are sufficient to explain the intensity maxima of the diffraction pattern [53]. In order to simplify the physics

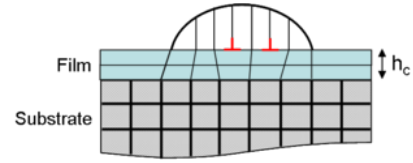


Figure 3.9: SK growth showing island formation above the critical thickness h_c . The lines represent the crystal structure and deformation. Edge dislocations at the film/island interface are highlighted in red.

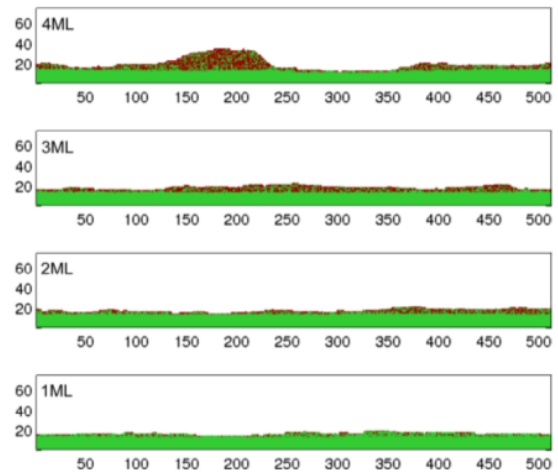


Figure 3.10: Equilibrium configuration obtained upon annealing a flat film of 1ML, 2ML, 3ML, and 4ML of Ge on a flat Si substrate at a temperature of 600 K in Ref. [51]. The simulation was performed on a periodic domain of 512 atoms in the horizontal direction

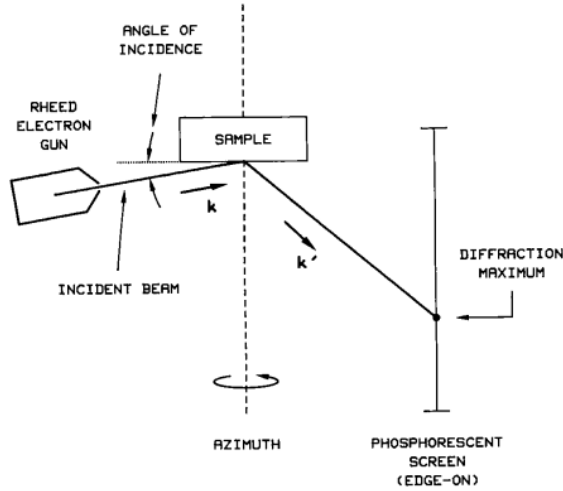


Figure 3.11: [53] Geometry of a RHEED experimental set-up

of the scattering phenomenon and directly understand the diffraction pattern all the discussion will be presented in reciprocal space.

The surface of a perfect crystalline material can be described by the repetition of a unit mesh. It can be described in real space by the vector \mathbf{R} .

$$\mathbf{R} = M_1 \mathbf{a}_1 + M_2 \mathbf{a}_2 \quad (3.6)$$

where \mathbf{a}_1 and \mathbf{a}_2 are the basis vectors whereas M_1 and M_2 are integer numbers. The reciprocal space is defined by the vector \mathbf{r}

$$\mathbf{r} = m_1 \mathbf{a}_1^* + m_2 \mathbf{a}_2^* \quad (3.7)$$

where \mathbf{a}_1^* and \mathbf{a}_2^* are the basis vectors, m_1 and m_2 are integer numbers. Using the relation 3.8 the vectors can be converted from the real to the reciprocal space:

$$\mathbf{a}_1^* = \frac{2\pi \mathbf{a}_2 \times \mathbf{n}}{A} \quad \mathbf{a}_2^* = -\frac{2\pi \mathbf{a}_1 \times \mathbf{n}}{A} \quad (3.8)$$

where \mathbf{n} is the versor perpendicular to the surface and $A = (\mathbf{a}_1 \cdot \mathbf{a}_2) \times \mathbf{n}$.

The incident electron beam can be described by the wave vector \mathbf{k} .

$$\mathbf{k} = \mathbf{p}/\hbar \quad |k| = 2\pi/\lambda \quad (3.9)$$

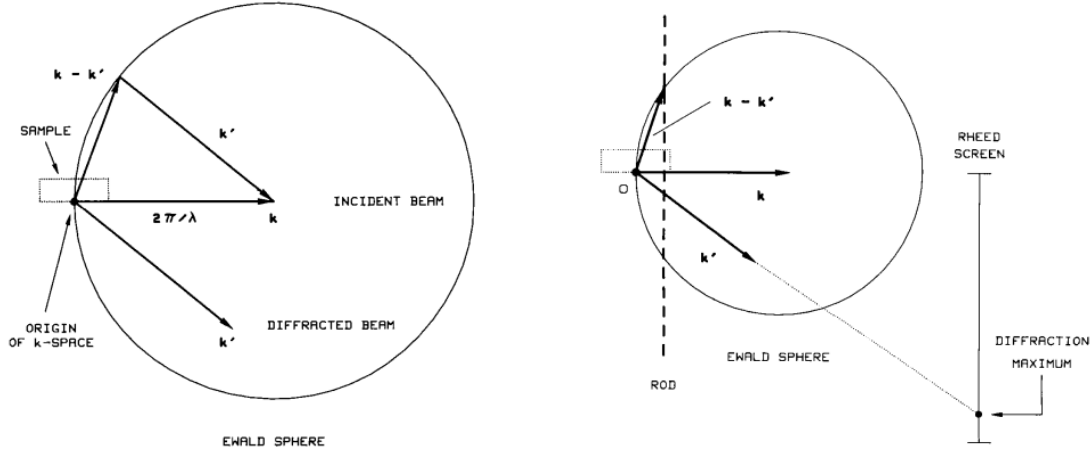
where \mathbf{p} is the electron momentum, \hbar is the Planck constant over 2π and λ is the wavelength. The scattered electron beam emerging from the sample is described by the wavevector \mathbf{k}' .

Using the elastic conservation equations, the Von Laue law sets the conditions for constructive interference:

$$(\mathbf{k} - \mathbf{k}') \cdot \mathbf{R} = m2\pi \quad (3.10)$$

A geometrical figuration, the Ewald sphere, allows to clearly understand the meaning of this condition. Indeed it is possible to draw a sphere in the reciprocal space with a radius $(\mathbf{k} - \mathbf{k}')$. The origin of the reciprocal lattice is set on the sphere surface as shown in Fig. 3.12a(b). The Laue conditions are reproduced by the intersection between the lattice reciprocal rods and the Ewald sphere.

The interception between a sphere and a line is a point. Hence the diffraction should be composed by a distribution of spots. Instead the experiments show constant spaced streak patterns. This phenomenon can



(a) The Ewald sphere construction, shown in cross section in the plane of incidence. The point of incidence of the beam is the origin of k space [53].

(b) A cross section in the plane of incidence that shows how a particular reciprocal lattice rod gives rise to a diffraction spot on the screen [53].

Figure 3.12

be explained taking into account the instrumental broadening, sample broadening and finite temperature effects:

- Instrumental broadening is caused by the kinetic energy distribution of the electron beam. Then the Laue condition is extended for all the \mathbf{k} present in the beam and the Ewald sphere becomes a thin spherical shell. The interceptions become therefore lengthened streaks. This effect is stronger in the first order spots and decreases for the others. Indeed the lengths of the rods' projection on the spherical shell decreases for \mathbf{k}' closer to the sphere center.
- Sample broadening occurs in disordered samples. The surface disorder leads to an imperfect crystal. The reciprocal space rods acquire a finite size. Hence the sphere-rod interception will have a spatial distribution. For instance, a single crystal epitaxially grown can present a step configuration made by atomic terraces. In that case, the reciprocal rods will have a nearly Gaussian cross section whose width is inversely proportional to the width of the terraces.
- The thermal fluctuations of the crystal atoms due to the finite temperature broadens the RHEED pattern. In fact the atoms oscillate and the refracted beam will be sensitive to the statistical distribution of the atoms.

In the following, I will show a method to extrapolate the lattice parameters from the distance between the pattern streaks. The Ewald sphere radius is generally large compared to the distances between the rods. Then it is possible to use the similar triangles principle for obtaining the lattice parameter a^* :

$$W/L = a^* \lambda / 2\pi \quad a^* = \frac{2\pi W}{\lambda L} \quad (3.11)$$

where W is the distance between the streaks, L is the distance between the screen and the sample and λ is the wavelength of the incident beam.

In order to validate Eq. 3.11 it is fundamental to use a high energy electron beam. A high accelerating voltage V is thus required. This makes a relativistic electron approach necessary for the λ formulation:

$$\lambda = \frac{h}{\sqrt{2m_0qV[1 + qV/(m_0c)^2]}} \quad (3.12)$$

where m_0 is the electron rest mass, q is the electronic charge and c is the speed of light.

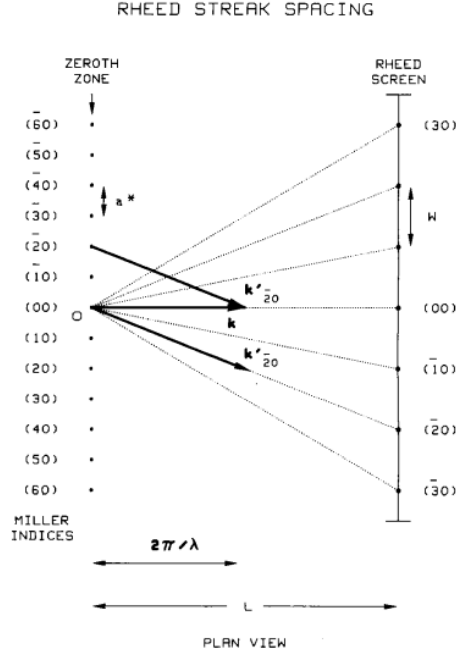


Figure 3.13: A plane view showing the relation between the intra-row spacing of the reciprocal lattice rods of the zeroth zone and the spacing of the observed RHEED streaks

3.1.6 STM chamber

Scanning Tunneling Microscopy (STM) is based on the measurement of the quantum tunneling current between a metallic tip and a sample surface. This current is directly proportional to the surface local density of states. The application of a bias between the tip and the surface allows to change the occupation of the states. A feedback electronic system in combination with piezoelectric motors allows to scan the surface and control the tip height.

STM allows two different kind of measurements:

- In the **spectroscopy mode** the tip is in a given position and the current as a function of the bias voltage is studied. It allows to analyze the surface electronic properties.
- The **microscopy mode** can be performed in two ways. One can fix the distance between the tip and the surface and study the current variation or fix the current and study the tip height. It allows to display a map of the surface density of states down to the atomic resolution. In case of homogeneous electric properties this mode can be used to study the surface topography.

Tunneling current

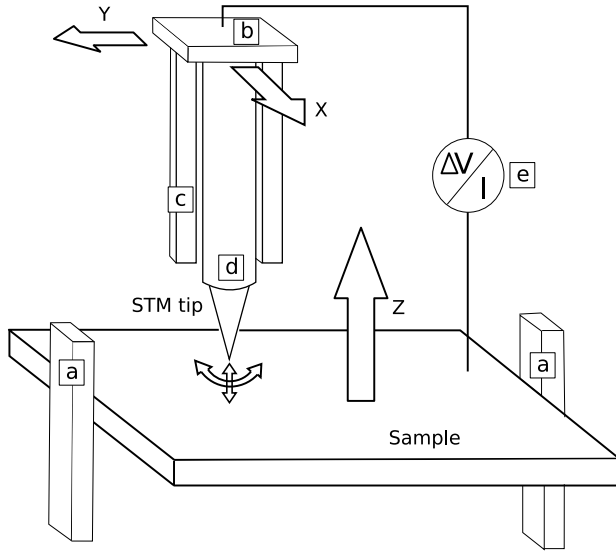
It is possible to write a simple formulation of the tip-sample current solving an easy quantum problem. The wavefunction $\psi_n(z)$ of an electron in a potential $V(z)$ is described by the Schrödinger equation:

$$-\frac{\hbar^2}{2m} \frac{\partial^2 \psi_n(z)}{\partial z^2} + V(z) \psi_n(z) = E \psi_n(z) \quad (3.13)$$

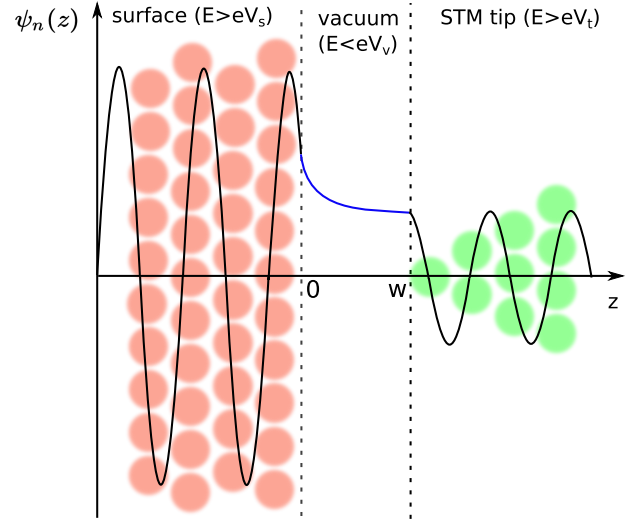
Two cases may exist depending on the difference between the barrier height (eV) and the electron energy E :

$$\psi_n(z) = \psi_n(0) e^{\pm ikz} \quad k = \frac{\sqrt{2m(E - U(z))}}{\hbar} \quad E > eV(z) \quad (3.14)$$

$$\psi_n(z) = \psi_n(0) e^{\pm \kappa z} \quad \kappa = \frac{\sqrt{2m(U - E)}}{\hbar} \quad E < eV(z) \quad (3.15)$$



(a) Sketch of tip and sample degrees of freedom in a STM set-up. (a) Two piezo rails moving the sample along the z direction allow the STM tip to approach the surface. (b) Two piezoelectric motors allow to place the tip in different areas of the sample surface (x, y) in the figure. (c) Finally two precision piezoelectric motors allow the z motion and (d) the oscillation in the (x, z) or (y, z) planes. (d) Tip-sample bias voltage and current measurement.



(b) Plot of the electron wavefunctions in three areas with different potential $V(z)$. An artistic view links the three areas with the STM physics.

Figure 3.14

As shown in Fig. 3.14b when $E > eV(z)$ the wavefunction is a plane wave whereas when $E < eV(z)$ it is an evanescent one. In the STM set-up geometry the space can be divided into three areas (Fig. 3.14b). Here the case of a current from the sample to the tip is shown. In the opposite case all the discussion is inverted. The electron will propagate in the sample ($E > eV(z)$); it will be partially reflected and partially transmitted into the vacuum ($E < V(z)$) and finally will propagate into the tip. The problem of knowing the sample-tip current corresponds to knowing the probability that the electrons close to Fermi level tunnel through the vacuum to the empty tip states. The density of states $\rho(E)$ multiplied with the Fermi distribution $f(E)$ describes the number of states available for the transition at a finite temperature. $\rho(E)$ can be calculated as the number of states in a given energy interval ϵ :

$$\rho(E) = \frac{1}{\epsilon} \sum_{E-\epsilon}^E |\psi_n|^2 \quad (3.16)$$

The probability of transition is described by Fermi's golden rule

$$I = \frac{2\pi}{\hbar} |W|^2 \delta(E_{\psi_s} - E_{\psi_t}) \quad (3.17)$$

where $|W|$ is the matrix element between ψ_s (the sample wavefunction) and ψ_t (the tip wavefunction) and $\delta(E_{\psi_s} - E_{\psi_t})$ shows that only transitions between states with the same energy are allowed. Then the total current I is obtained summing over all the states:

$$I = \frac{4\pi e}{\hbar} \int_{-\infty}^{+\infty} [f(E_f - eV + \epsilon) - f(E_f + \epsilon)] \rho_s(E_f - eV + \epsilon) \rho_t(E_f + \epsilon) |M|^2 d\epsilon \quad (3.18)$$

3.2 AFM

Atomic force microscopy is based on the study of the oscillatory motion of a cantilever when it interacts with the surface of a given material. The AFM allows to display the surface topography with a resolution that can reach a few nanometers. The fundamental components of an AFM set-up are shown in the insert in Fig. 3.15.

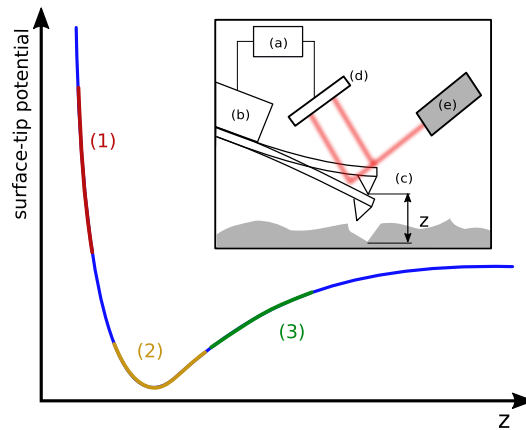


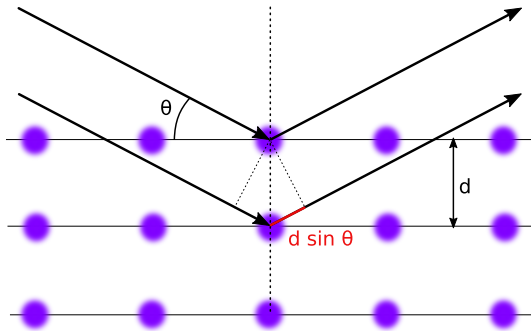
Figure 3.15: Plot of a generic surface potential as a function of the distance from the surface (z). (*insertion*) Sketch of the fundamental components of an AFM set-up. (a) Feedback loop electronics (b) High-precision piezoelectric motors for scanning the surface and set the cantilever height. (c) Cantilever with atomically sharp tip. (d) Photo-diode. (e) Laser generator.

The piezoelectric motors allow to scan the sample surface and approach the cantilever to the surface. The cantilever can be excited to its resonance frequency by a small piezoelectric element. A laser beam is focused on the cantilever tip and reflected on a photo-diode. The change of position of the laser beam on the diode allows to study the oscillation frequency, amplitude and phase of the cantilever. A feedback electronic loop can change the cantilever height as a function of the signal collected by the diode. AFM can be performed in three different modes which are differentiated by the kind of interaction between the tip and the surface.

- In **contact mode**, the tip is approached to the surface up to feel a repulsive interaction, (1) in Fig. 3.15. The cantilever bends and its deflection is measured. The measurements are thus performed in static conditions and the signal could be affected by noise and drift. In order to increase the static signal low stiffness cantilevers are used.
- The **tapping mode** has been developed in order to avoid the friction and the sticking of the tip to the surface. The cantilever is excited to its own resonance frequency and approached to the surface up to have a dynamic contact. When the tip interacts with the sample its oscillation amplitude will reduce due to the tip-surface interaction. During the scan the feedback loop allows to tune the tip height for keeping the cantilever oscillation amplitude constant. In the tapping mode the tip height and the oscillation phase can be recorded. The height gives information about the surface topography and the tip phase is proportional to the energy dissipated by the cantilever in each oscillation cycle. This gives information about sample stiffness variations or adhesion properties.
- In **non-contact mode** the cantilever oscillates in a regime of attraction with the sample surface. The cantilever interacts only with long range interactions like Van der Waals forces or dipole-dipole interactions. They change the cantilever oscillation properties, decreasing the frequency and the amplitude of the oscillations. The feedback loop can be used in order to change the tip height and keep the frequency (frequency modulation) or the amplitude (amplitude modulation) constant. In frequency modulation the tip is excited to its resonance frequency. Normally two different feedback loops are used, one to control the height and the other to tune the tip excitation. This allows to study separately the conservative and non-conservative forces on two different experimental signals. In amplitude modulation the cantilever is excited to a frequency slightly above the resonance one.

When the tip interacts with the surface the tip frequency decreases and thus the oscillation amplitude. Keeping constant the amplitude the tip height can be recorded as a function of the position on the surface. It allows to obtain the surface topography of the sample.

3.3 X-ray diffraction



Diffraction is a phenomenon that occurs when electromagnetic waves scattering with an ordered medium interfere with each other. This occurs when the electromagnetic wavelength is comparable to the distance between the scattering elements in the medium. Since X-ray radiation has wavelengths comparable to the atomic distances in a crystal, X-ray diffraction allows to study the symmetry and the lattice parameters of crystalline materials.

The constructive interference is described in the geometry shown in Fig. 3.16 by Bragg's law:

$$2d \sin \theta = n\lambda \quad (3.19)$$

Figure 3.16: Sketch of the X-ray diffraction geometry

where d is the distance between the atomic planes, θ the X-ray incidence angle with respect to the surface and λ the X-ray wavelength. In this thesis two different X-Ray diffraction techniques have been used for the crystal characterisation.

Laue diffraction

The Laue method studies the X-ray diffraction from a single crystal in a fixed orientation. Since each X-ray wavelength interacts with one atomic plane in the Laue diffraction, white radiation is used in order to accede to multiple scattering and to have information about all the crystalline planes. The diffracted beam is composed by different beams diffracted from the sample with different angles. Each one corresponds to a given crystalline plane.

Laue diffraction can be performed in two different geometries: in the transmission geometry a photosensitive film is aligned with the crystal and the X-ray source, and detects the forward scattered radiation transmitted through the sample. In the back reflection geometry a photosensitive film is placed between the X-ray source and the crystal in order to collect the back reflected X-ray beam. In both geometries the photosensitive film is impressed by a pattern of spots corresponding with the constructive interference from the different crystalline planes. The study of the angular position of these spots allows thus to analyze the crystal orientation and quality. On the other hand a quantitative analysis of the distance between the crystal planes is not possible since the X-ray wavelength that generates each single spot is unknown.

GIXD

Grazing incidence X-ray diffraction (GIXD) is a synchrotron technique that allows the quantitative analysis of crystal structures. It uses small X-ray incident angles in order to be sensitive to the surface crystal structure. This technique is then particularly suited for studying ultrathin films since the X-ray penetration length is comparable with the system thickness and the signal from the substrate is strongly reduced. GIXD is typically performed below the critical angle of the surface material. An evanescent X-Ray wave is exponentially damped in the material and the Bragg reflection arises only from the first atomic layers. Moreover at the critical angle the X-ray electric field is locally amplified and the scattered signal is increased.

During the measurements the combination of the motions of the sample holder and of the X-ray analyzer allows to scan the diffraction peaks in the reciprocal space. Therefore the technique produces spectra of the diffraction intensity as a function of the X-ray moment in the crystal reciprocal space. Synchrotron X-Ray radiation is thus fundamental in order to tune the X-ray moment.

3.4 Experimental techniques to determine the magnetic parameters

In a room temperature ferromagnet, the collinearity of the spin configuration does not allow to directly study the properties of the system and the strength of the interactions. In order to access them it is necessary to study the system's response to an external perturbation, generally the application of an external magnetic field. During this thesis different magnetic techniques have been used in order to give a complete overview of the strength and symmetry of the magnetic interactions. These techniques can be separated into two main categories:

- **spectroscopy techniques** can be used to study how a single parameter changes as a function of the external perturbation. The investigated area is generally related to the dimension of the probe and bigger than the typical length scales of the magnetic phenomena.
- **microscopy techniques** study the spatial distribution of the magnetisation. Methods with different spatial resolution, from micrometers to some tens of nanometers, have been used to study magnetic configurations at different length scales.

Magnetic systems can be characterized by five material dependent parameters (α, K, M_s, A, D). Moreover anisotropic magnetic interactions can occur in crystals with a C_{2v} symmetry like the systems studied in this work. Then the number of parameters for a complete magnetic characterisation increases to nine ($|\alpha|, \alpha_i, M_s, |A|, A_i, |K|, K_i, |D|, D_i$). A list of the techniques used in this work and of the determined magnetic parameters is shown in Tab. 3.1 and in the following text. In Tab. 3.1 the term ($|\dots|$) is used when a technique allows only the determination of an average parameter whereas (\dots_i) indicates that the method allows a direction dependent measurement.

Kerr magnetometry is a magneto-optical spectroscopy technique that studies the change of the polarisation of light due to the interaction with a magnetic medium. It allows to study a qualitative response of \mathbf{M} to the application of an external magnetic field $\mu_0\mathbf{H}_{\text{ext}}$. The application of a magnetic field perpendicular to the easy axis allows the determination of the effective magnetic field $\mu_0 H_{\text{eff}} = 2K_i/\mu_0 M_s^2$ needed to align the magnetisation along the direction of the applied magnetic field.

Vibrating Sample Magnetometry (VSM) is a technique that allows to have a quantitative response of \mathbf{M} to the application of an external magnetic field $\mu_0\mathbf{H}_{\text{ext}}$. It can be used to extrapolate the system magnetisation $M = M_s \mathcal{A} t$, where \mathcal{A} is the sample area and t the sample thickness.

Kerr Microscopy is a magneto-optical microscopy technique using Kerr magnetometry with spatial resolution. In the polar geometry (light incidence perpendicular to the sample surface), it allows to display the map of the out-of-plane magnetisation in the μm -range. It has been used in this thesis to study the dynamics of domain walls (DWs). The DW motion under the application of a perpendicular magnetic field H_z allows to extract the flow speed $v_f = \gamma_0 \Delta / \alpha H_z$ and the Walker speed $v_w = \frac{\pi}{2} \gamma_0 D / M_s$ (see Sec.5.4.1). Studying the dynamics applying at the same time a perpendicular and an in-plane magnetic field H_x allows extracting the DMI field $H_{\text{dmi}} = D / \mu_0 \Delta M_s$.

Brillouin light scattering (BLS) is a magneto-optical spectroscopy technique that studies the scattering phenomenon between light and thermally-activated spin waves. The measurements are performed under the application of a strong in-plane magnetic field $\mu_0 H_{\text{in}}$ that allows to saturate the magnetisation in a given direction. It allows to study properties along different directions. The BLS spectra can be divided into a symmetric and an anti-symmetric part. The symmetric part depends on the crystal symmetry. In the case of systems with a C_{2v} symmetry the frequency of the spin waves depends on the direction of the in-plane anisotropy field $\mu_0 H_{\text{in}}$, which allows to determine the strength of the anisotropy fields. The anti-symmetric part is directly proportional to the strength and sign of the DMI acting on a spin wave perpendicular to the applied magnetic field direction.

		$ \alpha $	α_i	M_s	$ A $	A_i	$ K $	K_i	$ D $	D_i
Kerr Magnetometry	H_{co}									
VSM	M			X						
Kerr Microscopy	v_w			X					X	
	v_f	X			X		X			
	H_{dmi}			X	X		X		X	
BLS	f_{symm}						X	X		
	f_{anti}			X					X	X

Table 3.1: Table of the experimental techniques used for the magnetic characterisation. The term ($|\dots|$) is used when a technique allows only the determination of an average parameter whereas (\dots_i) indicates that the method allows a direction dependent measurement

3.5 Magneto-optical effects

In this section two different phenomena occurring during the interaction between light and magnetism are reported. First a classical theory is described for studying the polarisation change and the attenuation of an electromagnetic wave when it propagates in a medium with an internal magnetic field. The particular cases of Faraday and Kerr effects are discussed. Kerr microscopy and magnetometry are based on these effects. In the second part BLS is described. It studies the scattering phenomena between light and spin waves, related to the thermal excitation of a ferromagnetic magnetisation.

3.5.1 Wave propagation in a magnetic medium

In this part a mathematical formulation for describing the change of polarisation and the attenuation of an electromagnetic wave when interacting with a magnetic medium is discussed. The problem can be solved with the resolution of the Maxwell equations. In their differential form they describe the mutual interaction between four vectorial fields: the magnetic field \mathbf{B} , the electric field \mathbf{E} , the induction field \mathbf{H} and the electric displacement field \mathbf{D} .

$$\nabla \times \mathbf{E} = -\frac{\partial \mathbf{B}}{\partial t} \quad \nabla \times \mathbf{H} - \frac{\partial \mathbf{D}}{\partial t} = \mathbf{j} \quad \nabla \cdot \mathbf{B} = 0 \quad \nabla \cdot \mathbf{D} = \rho \quad (3.20)$$

with \mathbf{j} the current density, and ρ the free charges. The magnetic field \mathbf{B} and the displacement field \mathbf{D} are the responses of the medium to the presence of an induction \mathbf{H} or an electric field \mathbf{E} :

$$\mathbf{B} = \mu_0(\mathbf{H} + \mathbf{M}) = \boldsymbol{\mu}\mathbf{H} \quad \mathbf{D} = \varepsilon_0\mathbf{E} + \mathbf{P} = \boldsymbol{\varepsilon}\mathbf{E} \quad (3.21)$$

where \mathbf{M} and \mathbf{P} are the magnetisation and the polarisation vectorial field. They express the density of permanent or induced dipole moments in a material. Eqs. 3.21 are the constitutive relations between \mathbf{B} and \mathbf{H} , and \mathbf{D} and \mathbf{E} , via the magnetic permeability $\boldsymbol{\mu}$ and the electric permittivity $\boldsymbol{\varepsilon}$.

The magneto-optical problem is equivalent to the study of the electric permittivity $\varepsilon_0\boldsymbol{\varepsilon}_r$ when the polarisation field \mathbf{P} is zero. Since this is the case in metallic magnetic media, we limit the discussion to these media. The solution of the equations system Eqs. (3.20) is complex and not always possible. Therefore a linear response expression is exposed here in order to write a direct relationship between \mathbf{D} and \mathbf{M} . The problem is reduced to write an effective permittivity tensor $\boldsymbol{\varepsilon}$. In general the presence of a magnetic field breaks the time reversal symmetry and the tensor has an anisotropic 3x3 form.

In the interaction between the light and the magnetic material the time reversal is broken when only the light is considered. When also the source of the magnetic field is considered the problem is time-invariant. This allows to reformulate $\boldsymbol{\varepsilon}$ as a hermitian matrix ($\boldsymbol{\varepsilon} = \overline{\boldsymbol{\varepsilon}^T}$). Moreover the systems analyzed with magneto-optical techniques are generally electrically isotropic. Then the electric response can be considered isotropic and $\boldsymbol{\varepsilon} = \varepsilon$.

Introducing the complex gyration vector \mathbf{g} one can formulate:

$$\mathbf{D} = \boldsymbol{\varepsilon}\mathbf{E} = \varepsilon\mathbf{E} + \imath\varepsilon\mathbf{E} \times \mathbf{g} \quad \boldsymbol{\varepsilon} = \begin{pmatrix} \varepsilon & \imath\varepsilon g_z & -\imath\varepsilon g_y \\ -\imath\varepsilon g_z & \varepsilon & \imath\varepsilon g_x \\ \imath\varepsilon g_y & -\imath\varepsilon g_x & \varepsilon \end{pmatrix} \quad (3.22)$$

If also the magnetic response is isotropic the gyration vector is proportional to the magnetisation \mathbf{M} via the Voigt constant Q [54]. Hence in a medium with magnetisation \mathbf{M} one can write $\mathbf{g} = (QM_x, QM_y, QM_z)$ and the permittivity tensor takes the form:

$$\boldsymbol{\varepsilon} = \begin{pmatrix} \varepsilon & \imath\varepsilon QM_z & -\imath\varepsilon QM_y \\ -\imath\varepsilon QM_z & \varepsilon & \imath\varepsilon QM_x \\ \imath\varepsilon QM_y & -\imath\varepsilon QM_x & \varepsilon \end{pmatrix} \quad (3.23)$$

Eq. 3.23 is the fundamental step for understanding the polarisation change of an electromagnetic wave in interaction with a magnetic medium but it does not take into account the geometry of the system. This is done by studying a planar electromagnetic wave propagating along \mathbf{r} in a given medium:

$$\mathbf{E}(\mathbf{r}, t) = \mathbf{E}_0 e^{-\imath(\omega t - \mathbf{k} \cdot \mathbf{r})} \quad \mathbf{H}(\mathbf{r}, t) = \mathbf{H}_0 e^{-\imath(\omega t - \mathbf{k} \cdot \mathbf{r})} \quad (3.24)$$

where \mathbf{k} is the wavevector in the $\hat{u}_k = (x, y, z)$ direction and ω is the wave frequency.

A complex reflective index N can describe the changes of the wave vector in the medium.

$$\mathbf{k} = N\mathbf{k}_0 = (n + \imath\kappa)\mathbf{k}_0 \quad (3.25)$$

where \mathbf{k}_0 is the wavevector in vacuum. The real part n is the refractive index and indicates the phase velocity. The imaginary part κ is the extinction coefficient and wave attenuation in the medium. When this parameter is inserted in a plane wave equation it gives an exponential decay term. It thus describes the penetration length of the wave. The wave vector can be decomposed into its modulus $|k|$ and its direction in the medium described by the versor $\hat{\mathbf{u}}_k = (N_x, N_y, N_z)\hat{\mathbf{u}}_{\mathbf{k}_0}$. The frequency is inversely proportional to the wavelength, according to the equation:

$$\mathbf{k} = \frac{\omega}{c}\hat{\mathbf{u}}_k \quad (3.26)$$

where c is the speed of the light and ω is the frequency.

Now from the Eqs. 3.20 one can derive the wave equation

$$\nabla \times (\nabla \times \mathbf{E}) = \frac{1}{c^2}\boldsymbol{\varepsilon}\frac{\partial^2 \mathbf{E}}{\partial t^2} \quad (3.27)$$

Placing the plane wave solution (3.24) in the wave equation (3.27):

$$[\hat{\mathbf{u}}_k(\hat{\mathbf{u}}_k \cdot \mathbf{E}) - \mathbf{E}]N^2 = \frac{\omega^2}{c^2}\boldsymbol{\varepsilon}\mathbf{E} \quad (3.28)$$

and developing the products:

$$(\boldsymbol{\varepsilon} + \mathbf{N} \cdot \mathbf{N} - N_x^2 - N_y^2 - N_z^2)\mathbf{E} = 0 \quad (3.29)$$

$$\begin{pmatrix} \varepsilon - N_y^2 - N_z^2 & \imath\varepsilon QM_z + N_x N_y & -\imath\varepsilon QM_y + N_x N_z \\ -\imath\varepsilon QM_z + N_y N_x & \varepsilon - N_x^2 - N_z^2 & \imath\varepsilon QM_x + N_y N_z \\ N_z N_x + \imath\varepsilon QM_y & N_z N_y - \imath\varepsilon QM_x & \varepsilon - N_x^2 - N_y^2 \end{pmatrix} \begin{pmatrix} E_x \\ E_y \\ E_z \end{pmatrix} = 0 \quad (3.30)$$

The refraction index components, i.e. the polarisation change and the wave attenuation, are solutions of this system. Moreover they allow to study the wave reflected and attenuated at the interface between several media.

The Faraday effect

The change of polarisation of light transmitted by a magnetic medium is called the Faraday effect. It is observed when an electromagnetic wave with linear polarisation is propagating in a medium along the direction of a magnetic field \mathbf{B} .

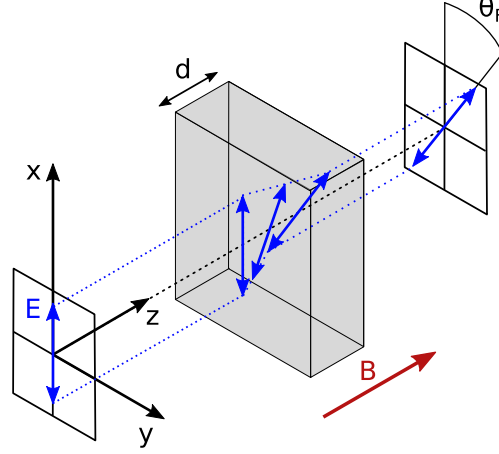


Figure 3.17: Faraday effect geometry. The angle β indicates the polarisation change when a electromagnetic wave propagates in a medium with a magnetic field \mathbf{B} . The medium has a square shape with a thickness d

This effect was discovered in 1845 by Michael Faraday when he observed that the polarisation direction of an electromagnetic wave propagating through a magnetic medium was turned by an angle (θ_F). He found that this angle is directly proportional to the path length d of the wave inside the medium and to the intensity of the magnetic induction field (B).

$$\theta_F = k_V B d \quad (3.31)$$

where k_V is called the Verdet constant.

The Faraday angle can be calculated solving Eq. 3.30 in the geometry shown in Fig. 3.17. The magnetic field $\mathbf{B} = (0, 0, B_z)$ and the wave vector $\hat{\mathbf{u}}_k = (0, 0, 1)$ are set in the z direction. Considering the magnetic susceptibility ($\mathbf{M} = \chi \mathbf{H} = \frac{\chi}{\mu} \mathbf{B}$), Eq. 3.30 takes the form:

$$\begin{pmatrix} \varepsilon - N^2 & i\varepsilon Q \frac{\chi}{\mu} B_z & 0 \\ -i\varepsilon Q \frac{\chi}{\mu} B_z & \varepsilon - N^2 & 0 \\ 0 & 0 & \varepsilon \end{pmatrix} \begin{pmatrix} E_x \\ E_y \\ E_z \end{pmatrix} = 0 \quad (3.32)$$

The eigenfunctions of the matrix are left-handed and right-handed circular waves:

$$E_+ = \begin{pmatrix} \frac{E_0}{2} e^{i\frac{\omega}{c} N_+(B)z} \\ i\frac{E_0}{2} e^{i\frac{\omega}{c} N_+(B)z} \\ 0 \end{pmatrix} \quad E_- = \begin{pmatrix} \frac{E_0}{2} e^{i\frac{\omega}{c} N_-(B)z} \\ -i\frac{E_0}{2} e^{i\frac{\omega}{c} N_-(B)z} \\ 0 \end{pmatrix} \quad (3.33)$$

where $N_+(B)$ and $N_-(B)$ are the two eigenvalues :

$$N_+(B) = n_+ + i\kappa_+ \sqrt{\varepsilon(1 + Q \frac{\chi}{\mu} B_z)} \quad N_-(B) = n_- + i\kappa_- \sqrt{\varepsilon(1 - Q \frac{\chi}{\mu} B_z)} \quad (3.34)$$

The total wave attenuation and polarisation change are found calculating the wave after the propagation in the medium ($z = d$). Taking the sum of the left-handed and right-handed circular waves the Faraday angle reads:

$$E(d) = E_0(d) \begin{pmatrix} \cos(\theta_F) \\ \sin(\theta_F) \\ 0 \end{pmatrix} \quad \theta_F = \frac{\omega d}{c} [N_+(B) - N_-(B)] \quad (3.35)$$

The Kerr effect

The Kerr effect is the phenomenon that occurs at the reflection of an electromagnetic wave from a magnetic medium. Starting with an incoming linearly polarized wave, this effect induces an elliptical polarisation and a change of the polarisation major axis of the reflected wave.

In order to describe this effect a relationship between the wave polarisation before and after the reflection can be written:

$$\begin{pmatrix} E_p^r \\ E_s^r \end{pmatrix} = \begin{pmatrix} r_{pp} & r_{ps} \\ r_{sp} & r_{ss} \end{pmatrix} \begin{pmatrix} E_p^i \\ E_s^i \end{pmatrix} \quad (3.36)$$

where the polarisation is separated into the parallel (E_p) and perpendicular (E_s) electric field components and the indexes r and i indicate the reflected and incidence electric fields and are called Fresnel coefficients. They set the relationship between the components before and after the reflection.

The Kerr effect strongly depends on the geometry of the reflection and the magnetisation direction of the medium. Three geometries are here taken into account (Fig. 3.18):

- in **polar Kerr** the magnetisation is normal to the medium surface and the wave polarisation perpendicular to the magnetisation.
- in **longitudinal Kerr** the magnetisation lies in the surface plane parallel to the wave plane of incidence with an angle θ_0 with respect to the normal to the medium surface.
- in **transversal Kerr** the magnetisation lies in the surface plane perpendicular to the wave plane of incidence with an angle θ_0 .

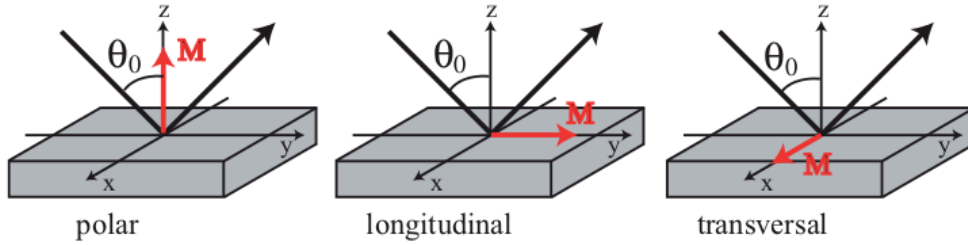


Figure 3.18: Schematic representation of the different Kerr geometries

The magnetic systems studied in this work are composed by a multilayer structure. It is thus important to study the wave reflection and the transmission through the different materials. Here only two media are considered for the sake of simplicity: a non-magnetic medium and another one with magnetisation \mathbf{M} .

The studied system and the wave reflection-transmission are shown in Fig. 3.19. A linearly polarized incident wave is considered and the incident angles in vacuum and in the two materials are $\theta_0, \theta_1, \theta_2$. In order to express the Fresnel coefficients, the dielectric tensors ε for the media are considered:

- In the non-magnetic medium the wave does not change its polarisation and thus ε is diagonal with respect to the electric field components.
- In the magnetic material the linear polarisation is not an eigenfunction because, as in the Faraday effect, the magnetic field turns the wave polarisation. Hence the eigenfunctions of the system are right-handed and left-handed waves. Then Eq. 3.30 becomes :

$$\begin{pmatrix} \varepsilon - N_y^2 - N_z^2 & i\varepsilon Q M_z + N_x N_y & -i\varepsilon Q M_y + N_x N_z \\ -i\varepsilon Q M_z + N_y N_x & \varepsilon - N_x^2 - N_z^2 & i\varepsilon Q M_x + N_y N_z \\ N_z N_x + i\varepsilon Q M_y & N_z N_y - i\varepsilon Q M_x & \varepsilon - N_x^2 - N_y^2 \end{pmatrix} \begin{pmatrix} E_x \\ E_y \\ E_z \end{pmatrix} = 0 \quad (3.37)$$

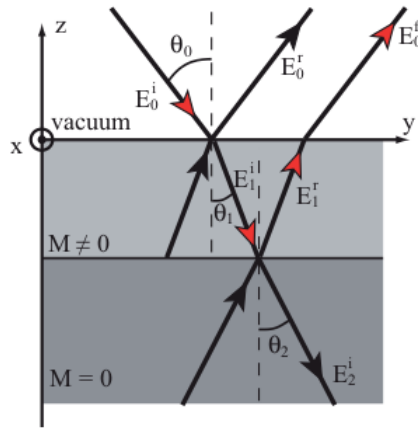


Figure 3.19: Sketch of the system under investigation showing the different incoming and reflected electromagnetic waves

The tangential components of the electric field \mathbf{E} and the magnetic field \mathbf{H} are continuous. Then considering the reflection conditions for the electric field \mathbf{E} and the magnetic field \mathbf{H} at the interfaces the problem can be solved for each Kerr geometry.

In this part the Kerr rotation angle θ_K is shown in the case of the red optical path in Fig. 3.19. Two different incident waves are considered: p-polarized with the electric field along the plane of incidence and s-polarized with the electric field normal to the plane of incidence. For the p-polarisation the Kerr rotation θ_K is defined as the ratio between the Fresnel coefficients r_{ps} and r_{pp} , whereas for the s-polarisation θ_K is $\frac{r_{sp}}{r_{ss}}$:

$$\theta_K^p = \frac{r_{ps}}{r_{pp}} \quad \theta_K^s = \frac{r_{sp}}{r_{ss}} \quad (3.38)$$

The problem has been solved in Ref. [55]. Fig. 3.20 shows the dependence of θ_K^p and θ_K^s on the incident angle for polar and longitudinal Kerr geometries. Analyzing the plot in Fig. 3.20 allows to optimize the geometry of the Kerr set-up in order to optimize the Kerr effect. Note that the maximum Kerr rotation in the polar geometry is obtained when the wave is perpendicular to the surface. In the longitudinal geometry, instead, the Kerr rotation is zero for perpendicular incidence and has a maximum for an angle that depends on the medium and the kind of polarisation.

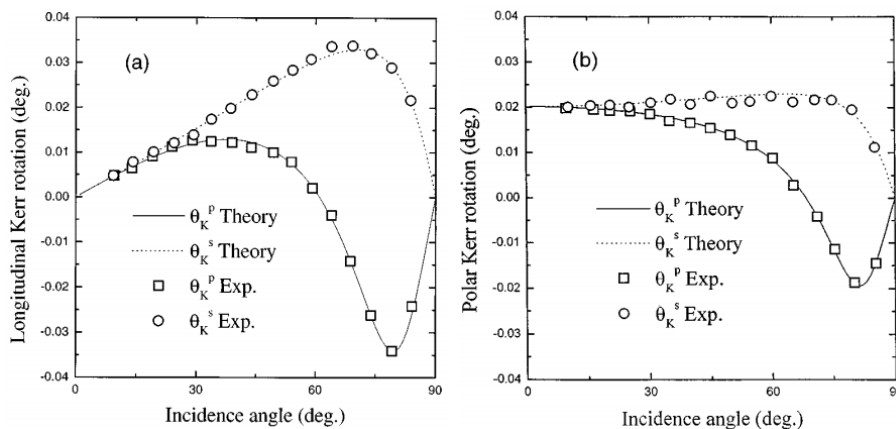


Figure 3.20: Experimental and theoretical p- and s-Kerr rotation curves of (a) a Cu/Co multilayer in the longitudinal configuration and (b) a Co/Pd multilayer in the polar configuration [55]

3.5.2 Focused Kerr magnetometry

Focused Kerr magnetometry is an experimental technique that allows to investigate magnetic hysteresis loops using the Kerr effect. The magnetic field \mathbf{B} can be applied perpendicular or parallel to the sample plane in order to perform measurements in different Kerr geometries. Fig. 3.21 gives a schematic presentation of the experimental set-up used in this thesis.

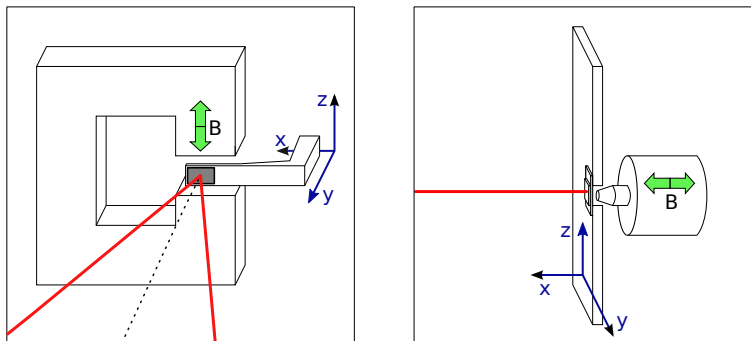


Figure 3.21: Transversal-longitudinal Kerr configuration (left). The magnetic circuit that allows the application of an in-plane magnetic field is shown. Polar Kerr configuration (right) with the electromagnetic coil that allows the application of perpendicular magnetic fields. In both Figures the black arrows show the piezo motor degrees of freedom.

A piezo motor allows to move the sample along three directions (x, y, z) in Fig. 3.21. The sample is placed on different supports for the two configurations as shown in Fig. 3.21:

- Polar Kerr. The sample is placed on a non-magnetic support directly on the motor base while a coil for the application of perpendicular magnetic fields is placed behind the sample.
- Longitudinal and transversal Kerr. The sample is placed on an L-shaped support in order to stay in the gap of a magnetic circuit that therefore applies a magnetic field parallel to the sample plane.

The set up for the measurements is assembled on a non-magnetic optical table. Two optical paths shown in Fig. 3.22 are used :

- The red line shows the laser path. It is generated by a 5.0 mW Red ($\lambda = 632.8nm$) He-Ne laser. The beam is linearly polarized and after two beam splitter crystals reaches a microscope objective that focuses the beam on the sample. This allows to study the magnetic properties locally, with a spot dimension that can reach a few hundreds of nanometers. Indeed in systems with wedge layers the properties change on this scale. Moreover it allows to study the properties of nano-patterned objects. The reflected beam passes through a half-wave plate mounted on a rotating structure. Afterwards a Wollaston prism splits the laser beam into two orthogonal linearly polarized waves that reach a balanced photodiode. This allows to study the Kerr rotation angle.
- The yellow line shows a white light beam. It is used to illuminate the sample for making microscopy images of the sample surface. The white light is produced by a diode and after the reflection on the sample reaches a camera. It allows to display the surface of the sample and to focus the laser on the desired position

The complexity of the wave path does not allow to set a direct relationship between the Kerr intensity and the magnetisation during a hysteresis loop.

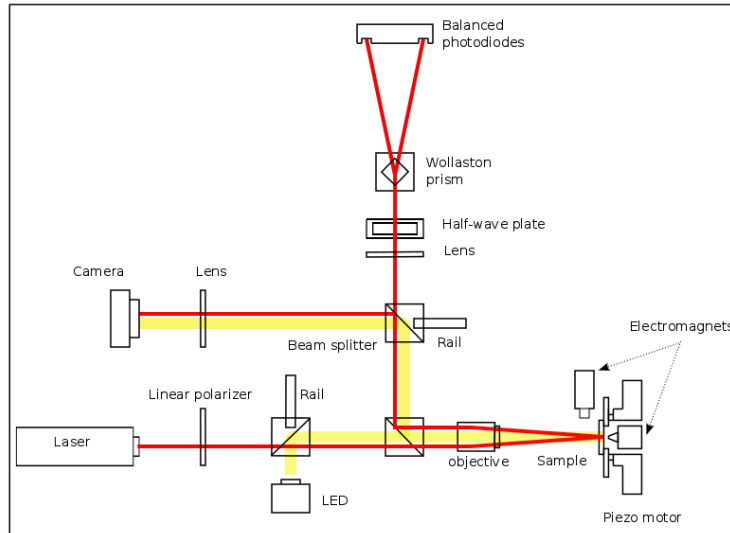


Figure 3.22: Sketch of the focused Kerr magnetometry setup with the main optical components.

3.5.3 Kerr microscopy

Kerr microscopy relies on the Kerr effect in order to image differences in the magnetisation direction at the surface of a magnetic material. In a Kerr microscope, the illuminating light first passes through a polarizer filter, then reflects from the sample surface and passes through an analyzer polarizing filter, before going through a regular optical microscope. Because the different MOKE geometries require different polarized light, the polarizer should have the option to change the polarisation of the incident light (circular, linear, and elliptical). When the polarized light is reflected by the sample material, any combination of the following phenomena may occur: Kerr rotation and Kerr ellipticity. The changes in polarisation are converted by the analyzer into changes in light intensity, which are visible. A camera is used to create an image of the magnetisation direction at the surface from these changes in polarisation.

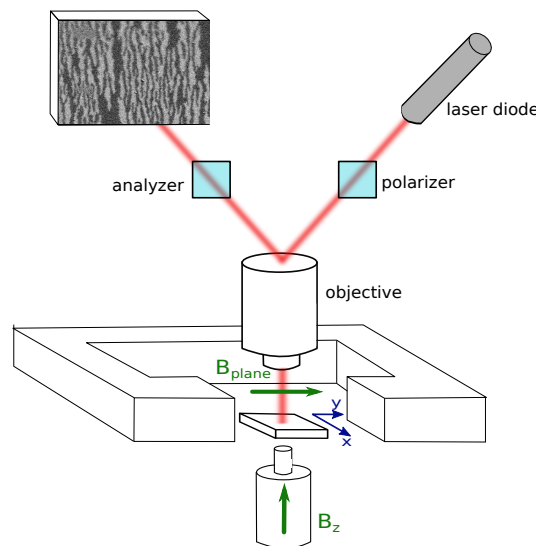


Figure 3.23: Sketch of the set-up assembled on the Kerr microscope stage for the domain wall manipulation

The sample is placed on a stage that allows the scanning in the directions (x, y) . An electro-magnets set-up is implemented in the stage. It allows to apply static and pulsed magnetic fields parallel (y) and orthogonal (z) to the sample surface. As shown in Fig. 3.23, the magnetic field B_{in} is generated in a magnetic circuit gap by electro-magnets, whereas the B_z field is applied directly by an electro-magnet. Different kinds of electro-magnets are used in order to change the duration of the magnetic pulses and/or the magnetic field intensity. Current pulses are generated by a high voltage power supply and controlled by computer

software. This set-up does not allow to apply pulses with a duration of less than a few microseconds. To overcome this problem a microcoil set-up has been developed.

Microcoil The application of magnetic field pulses with a microcoil allows to increase the magnetic field intensity and to reduce the magnetic field pulse time. It is fundamental for studying the DW dynamics because the DW speed has different regimes as a function of the magnetic field strength (Sec. 5.4.1). The microcoils used in our experiment are constituted by a $3.5\mu\text{m}$ -thick copper layer grown by sputter deposition on a surface of silicon. Before the deposition of a continuous film of copper a window is made in the silicon substrate in order to allow the optical observation through the coil. The coils are obtained with a lithography process as shown in Fig. 3.24a

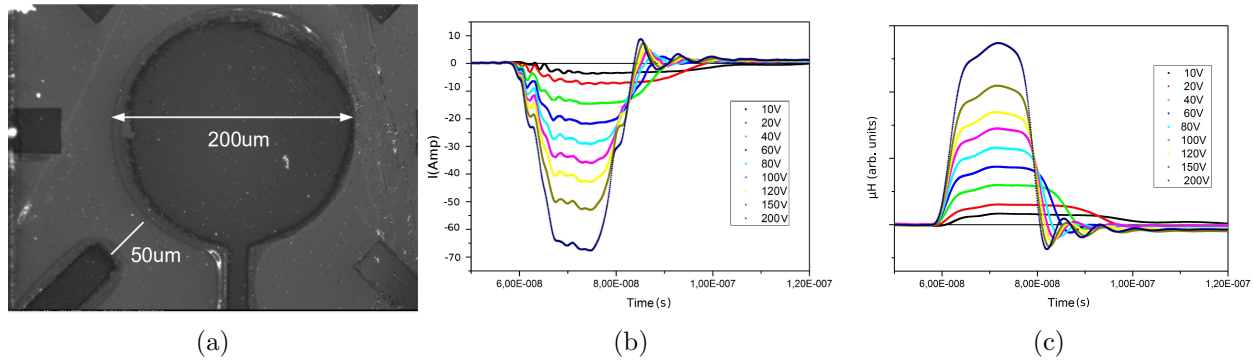


Figure 3.24: (a) Optical image of the micro coil geometry. Lighter contrast : copper layer, darker contrast : Si substrate. (b) Current in the microcoil during the pulse measured with an oscilloscope connected with the electronics. (c) Magnetic field during the pulse measured with a 1mm-diameter coil

The coil's shape is designed in order to increase the mechanical-thermal stability and to enlarge the homogeneity of the magnetic field. The magnetic field is generated by the electric current from the discharge of capacitors. This technique allows to flow high currents (up to 70 Amp) for a very short time ($\approx 10\text{ns}$). Fig. 3.24b shows the current behavior during the pulse measured with an oscilloscope connected with the electronics for different values of tension applied on the capacitor plates. The quality of the pulse shape decreases increasing the voltage and a current oscillation appears during the signal fall for values above 60 V. The magnetic field pulse is measured using a 1 mm diameter coil placed on the sample holder as close as possible to the microcoil. This set-up does not allow a direct measurement of the magnetic field intensity during the pulse due to the strong gradient of the magnetic field intensity and the reduced dimension of the system. However, it is useful to control the shape of the magnetic field pulse and compare it with the shape of the current pulse (Fig. 3.24c). It is possible to perform simulations of the magnetic field distribution in space taking into account the current distribution in this particular geometry. Fig. 3.25 shows the results of the simulations for two different coil diameters and a copper thickness of $3.5\mu\text{m}$.

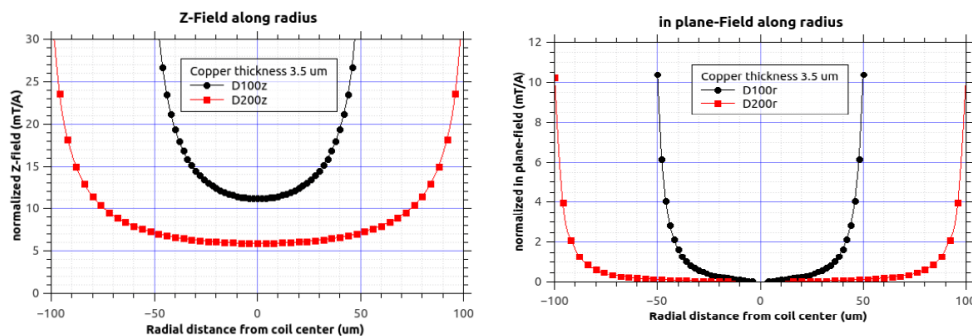


Figure 3.25

For this thesis we decided to use the coils with $200\mu\text{m}$ diameter in order to increase the magnetic field homogeneity and reduce the effect of in-plane fields present close to the coil edge.

Microcoil sampleholder The coil dimensions and the sample holder used in the laboratory for previous works do not allow to study samples with a surface area bigger than $4 \times 4\text{mm}^2$. The samples grown and characterized in this work present mainly a thickness gradient, where the properties change along the sample and a set-up allowing scanning is necessary. Moreover, in order to understand the role of the anisotropic interactions on the DW dynamics a study along different in-plane sample directions is required. In order to reach these technical requirements two different set-ups have been designed and realized during this thesis work.

The first, described in Fig. 3.26 and used for the measurements shown in Sec. 5.4.1, is designed to use the standard coils and permits to study 6 different in-plane directions, and to scan along the sample. The electrical contact of the coil is guaranteed by mechanical pressure imposed by a glass-fibre plate screwed only on one side of the sample-holder. This fixing system appeared to be unstable and if the applied pressure for the electrical contact is not strong enough the microcoil can be tilted. On the other hand, a too strong pressure can cause the breaking of the microcoil silicon support during the assembling. To solve this technical problem and to allow scanning along all the in-plane directions we designed and made a second sample holder. This second sample holder has not been tested and no data were taken. Indeed the conclusions after the measurements performed with the first set-up convinced us to use a different technique for the estimation of the DMI strength.

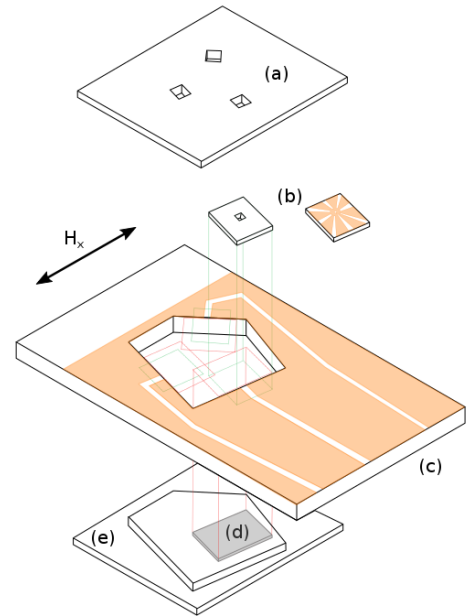


Figure 3.26: Sketch of the set-up designed for mounting the microcoil (b) on the sample surface (d). The green dashed lines show the possible slots for the microcoil and the red lines the relative position of the sample. On the sample-holder base (c) the areas are shown that are covered by copper to guarantee the possible electrical contact for all the microcoil slots. It is done by screwing the element (a) on the base (c) where windows allow the observation of the sample surface. The element (e) is also screwed on the base (c) to guarantee the parallelism of the sample and microcoil surfaces

3.5.4 BLS spectroscopy

Spin waves (SW) are collective excitations of the magnetic ground state. In a quantum mechanical model a quasi-particle called a magnon can be associated to each SW mode. The magnons carry a spin angular momentum ($\hbar\mathbf{k}_{sw}$) with a given energy $h\nu_{sw}$ and its value is determined by the mutual coupling between the spins.

The study of magnons allows probing the magnetic energies that determine the collective excitation. BL scattering is the inelastic interaction between a photon emitted by a laser source with a given energy $h\nu_{in}$ and the thermally activated magnons in magnetic media. The scattering process can be described by the energy and momentum conservation laws:

$$h\nu_{out} = h\nu_{in} \mp h\nu_{sw} \quad (3.39)$$

$$\hbar\mathbf{k}_{out} = \hbar\mathbf{k}_{in} \mp \hbar\mathbf{k}_{sw} \quad (3.40)$$

where $h\nu_{out}$ and $\hbar\mathbf{k}_{out}$ are respectively the photon momentum and energy probed by the technique. During the scattering the photon transmits energy and momentum to the media exciting a magnon (Stokes process (S)) or absorbs energy and momentum annihilating a magnon (Anti-Stokes process (AS)).

In this thesis, SW scattering processes are investigated in the Damon-Eshbach (DE) [56] configuration. An in-plane external magnetic field \mathbf{B}_{ext} is applied perpendicular to the photon beam. \mathbf{B}_{ext} allows to saturate the magnetisation along an in-plane sample direction. In this configuration surface SWs propagate parallel to the photon direction. In perpendicularly magnetized systems saturation is obtained by applying a \mathbf{B}_{ext} stronger than the MCA field $\mu_0\mathbf{H}_{Ki}$. Indeed, in micromagnetic theory the effect of the MCA can be described as an effective magnetic field $\mu_0\mathbf{H}_{Ki} = \frac{2K_i}{\mu_0 M_s^2}$ where K_i is the MCA constant, i is an index indicating a crystallographic direction and μ_0 is the vacuum magnetic permeability.

The DE configuration involves the presence of magnetostatic surface spin waves (MSSW). They have four fundamental properties [57]:

1. The SW propagation occurs with only a *single mode*.
2. Two SWs propagating in opposite directions are located on opposite material interfaces and their intensity *exponentially decays* from the interfaces.
3. They switch interface when the propagation direction is inverted (*field displacement non-reciprocity*).
4. The phase and group velocity point in the same direction (*forward wave*).

These properties allow to understand a BLS spectrum. Property (1) involves the presence of a single couple of symmetric S-AS peaks. The field displacement non-reciprocity plays an important role in the location of the S and AS peaks. Indeed, for Eq. 3.39, the absorbed SW and emitted SW have opposite wave-vectors and thus their properties depend differently on the magnetic interfaces. This phenomenon may break the frequency symmetry between S and AS peaks but it occurs only if the sample thickness (d) is large enough to allow an exponential SW decay ($k_{SW}d \gg 1$).

In magnetic ultrathin films with the presence of interfacial DMI the frequency of the S (f_S) and AS (f_{AS}) peaks can be decomposed into a symmetric and an antisymmetric component.

$$f = \frac{|f_S| + |f_{AS}|}{2} \pm \frac{|f_S| - |f_{AS}|}{2} = f_0(H_{ext}, A, k_{SW}, M_s, d, H_{eff}) \pm f_{anti}(k_{SW}, M_s, d, D) \quad , \quad (3.41)$$

f_0 allows to extrapolate the strength of the effective anisotropy field whereas f_{anti} is directly proportional to the DMI strength. The technique is particularly suited for analyzing anisotropic systems. Indeed, performing BLS spectroscopy with B_{ext} along different directions allows the independent extrapolation of

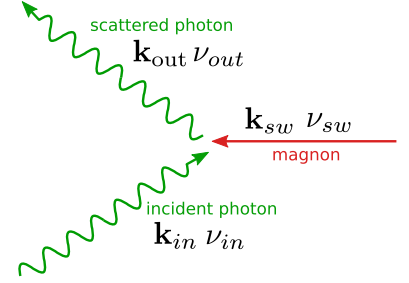


Figure 3.27: Feynman diagram of the Brillouin light scattering phenomenon

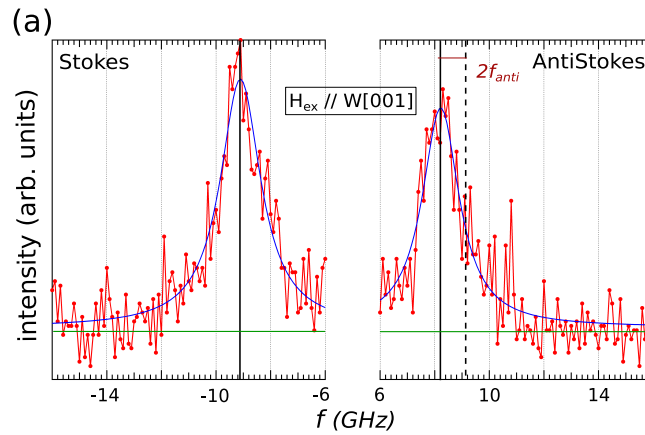


Figure 3.28

Figure 3.29: BLS spectrum of Au/Co(0.65 nm)/W(110) in the DE configuration. Red, experimental data. Blue line, data fit with Lorentzian functions. Green line, background fit. In the S spectra, the distance between the continuous and dashed black line shows the frequency shift between S and AS peaks. (a) BLS spectrum with $B_{ext} = 0.6$ T parallel to the W[001] axis and $k_{SW} = 8.08\mu\text{m}^{-1}$ parallel to the W[1 $\bar{1}$ 0] axis.

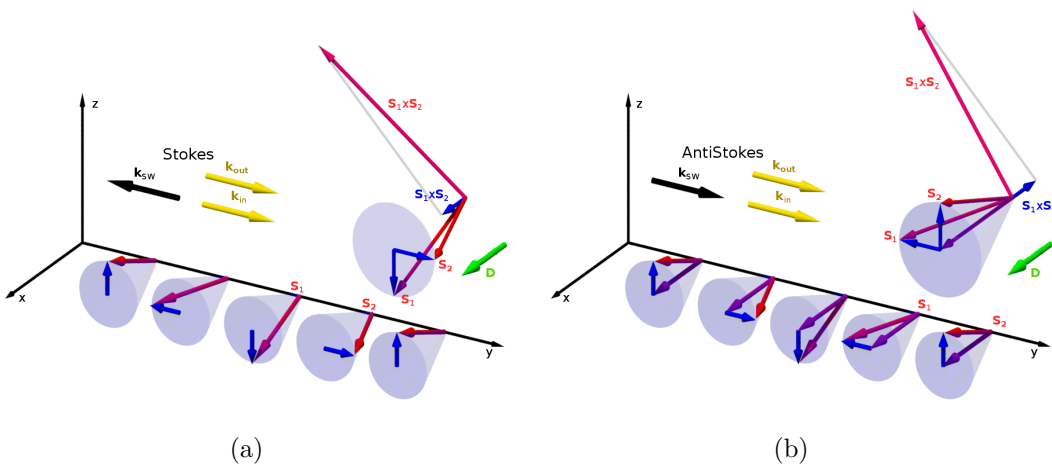


Figure 3.30: Sketch of the BLS phenomenon: (*bottom*) surface SW propagating along the y direction, *red arrow* = spin located at the atom position, *blue arrow* = spin projection on the plane (y,z). (*top-left*) direction of the wavevectors in the S (a) and AS (b) processes, *yellow arrow* incoming and outgoing photon wavevectors, *black arrow* SW wavevector. (*top-right*) representation of the vectorial product between two spins during the SW propagation (*green arrow*) and projection along the DM vector (*green arrow*).

the DMI strength D and the effective fields H_{eff} along different directions. In the ultra-thin film regime the DMI is the only physical phenomenon able to break the S-AS peak symmetry [58][59][60][61].

The sketch in Fig. 3.30 helps to phenomenologically understand this effect. The \mathbf{D} vector of the DMI hamiltonian ($H_{DMI} = \mathbf{D}_{12} \cdot \mathbf{S}_1 \times \mathbf{S}_2$) is positive along the \hat{x} direction. A clockwise perpendicular spin arrangement is thus favored by the DMI. A surface SW with magnetisation along the \hat{x} direction and propagating along the negative \hat{y} direction ($\mathbf{k}_{SW} // \hat{y}$) has an anti-clockwise rotation. The vector product between two spins along the SW direction has a positive component along \mathbf{D} . On the other hand, a SW propagation along the positive \hat{y} direction has a clockwise rotation and a negative component of the vector product along \mathbf{D} . If a photon beam with a positive wavevector along the \hat{y} direction scatters with the magnetic medium a SW with a negative \mathbf{k}_{SW} can be generated (S process) and a SW with a positive \mathbf{k}_{SW} can be absorbed (AS process). This can explain why the S peak in the BLS spectrum has a higher energy than the AS peak.

Set-up

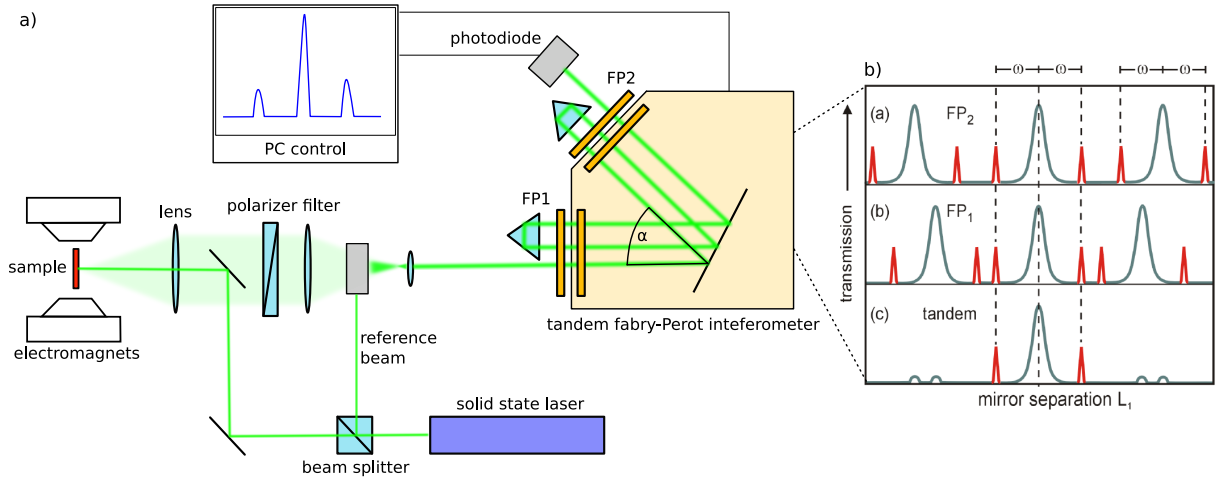


Figure 3.31: (a) Sketch of the main components of a BLS spectroscopy set-up. b) Working principle of a tandem 3x2 Fabry-Perot interferometer

A sketch of the main components of an experimental set-up for BLS studies is schematically shown in Fig. 3.31. Light from a solid state laser is focused onto the sample by an objective lens. The elastically and inelastically scattered light is collected and passed through a polarizer filter. Since in magnetic-optical phenomena a polarisation change occurs this filter allows to eliminate the light inelastically scattered with the phonons. Afterwards the light enters into a tandem 3x2 Fabry-Perot interferometer. The fundamental part of the interferometer consists of two Fabry-Perot etalons. Setting a given value of the angle α [62] allows to eliminate the harmonics of the reflection and eliminate the ambiguities in the analysis of inelastic peaks. Moreover, in order to obtain the high contrast necessary to detect the weak inelastic signals, the light is sent through both etalons three times with a system of mirrors and corner reflectors. Finally the light transmitted by the interferometer is detected by a photodiode and recorded by a personal computer.

3.6 Magnetic microscopy

In this section the main principles of XMCD-PEEM and MFM are described. These are two techniques that allow to display the different components of magnetic configurations at the nanometer scale.

3.6.1 XMCD-PEEM

XMCD-PEEM is a synchrotron technique that combines Photoemission electron microscopy (PEEM) with X-ray magnetic circular dichroism (XMCD).

- XMCD is based on the difference in absorption for a magnetic material between X-rays with opposite circular polarisations.
- PEEM allows to reconstruct a map of the intensity of the secondary electrons extracted via photoemission from the surface of a metal.

XMCD In this part magnetisation-dependent X-ray absorption is presented. The Fermi golden rule allows to estimate the transition probability between the states $|i\rangle$ and $\langle f|$ when the system is exposed to a perturbation, described by the Hamiltonian H' :

$$\Gamma_{i \rightarrow f} = \frac{2\pi}{\hbar} |\langle f|H'|i\rangle|^2 \rho \quad (3.42)$$

where ρ is the density of final empty states. Then magnetisation-dependent X-ray absorption can be obtained if the following conditions are fulfilled:

- The final state $\langle f|$ has different densities of empty states for spin-up and spin-down electrons.
- The electronic excitation between the states has two different circular momenta and spin flips are forbidden.
- The initial state $|i\rangle$ has spin-orbit coupling in order to transform the perturbation angular momentum to the spin momentum.

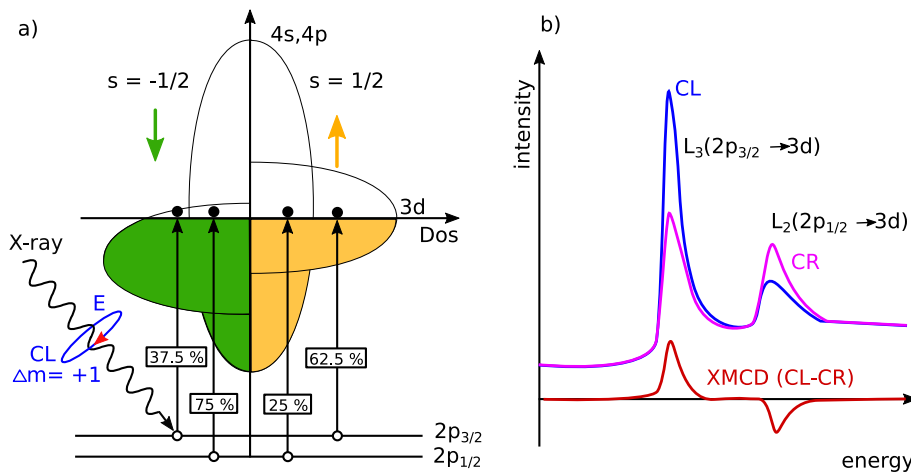


Figure 3.32: a) Sketch of the interaction between a 3d transition metal and circularly polarized light. b) Typical XMCD spectra for a transition metal

The first condition is satisfied in magnetic transition metals like Co, Fe and Ni where the 3d states cross the Fermi level. Indeed the spontaneous magnetisation in these elements arises from the imbalance of spin-up and spin-down electrons in these bands, leading to different densities of empty states.

The second is fulfilled when circularly polarized light excites electrons from the core levels. Left and right circularly polarized light have opposite angular momentum. Moreover the selection rule of electrostatic excitations forbids spin flips. The third condition is satisfied when the initial state is a core level like the 2p-level, which in the final state is split by the spin-orbit coupling in p_{1/2} and p_{3/2} states. These two levels

have opposite spin-orbit coupling and the majority spin of the excited electrons will be opposite for the two transitions. These two transitions are called L_3 ($2p_{3/2} \rightarrow d$) and L_2 ($2p_{1/2} \rightarrow d$).

Fig. 3.32 shows an example of XMCD absorption for the case of left circularly polarized (CL) X-rays. The selection rules determine the allowed transitions ($CL \rightarrow \Delta m = +1; \Delta s = 0$). The spin-orbit coupling in the level can transfer the orbital momentum to the spin momentum and during a transition with $\Delta m = +1$ the excited number of spin-up and spin-down electrons are not the same. In the L_3 (L_2) transition 37.5% (75%) of the excited electrons have spin-down and 62.5% (25%) spin-up. Since the spin-up empty density of states (DOS) is smaller than the spin-down empty DOS the L_3 (L_2) transition with CL (CR) light has a lower intensity. The subtraction between the two spectra (red in Fig. 3.32) is called XMCD spectrum and allows to determine the magnetisation direction of the sample.

PEEM Photoemission Electron Microscopy is a technique that measures the number of electrons emitted from a sample upon irradiation by X-rays. The electrons are accelerated by a strong electric field between the sample and the electrode of the objective lens. During the path between the sample and the detector the image is magnified and corrected by a series of magnetic or electrostatic electron lenses. A micro-channel plate increases the electron signal which is then recorded on a fluorescent screen. The technique collects the secondary electrons generated by an initial Auger process. When X-rays are absorbed by the sample, electrons are excited, leaving empty core states. Electrons from an intermediate state fill the states left empty by the excited electrons, at the same time leading to the excitation of electrons from the same intermediate state to conserve the total energy. These excited electrons create a cascade of low-energy electrons, some of which have enough energy to escape from the sample and to be collected by the PEEM optics.

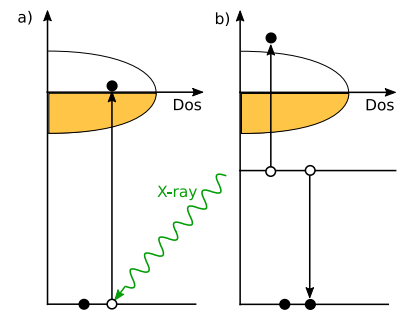


Figure 3.33: a) X-ray absorption and electron transition b) Auger processes

A wide spectrum of electrons is emitted with energies between the energy of the incoming X-rays and the work function of the sample. This distribution of electron energies together with the imperfections of the microscope lenses leads to chromatic aberrations and a reduction of spatial resolution. This problem is partially resolved by the introduction in the electron path of energy-filters to reduce the chromatic aberrations. Moreover back-focal plane apertures can be used to optimize the resolution and the electron transmission.

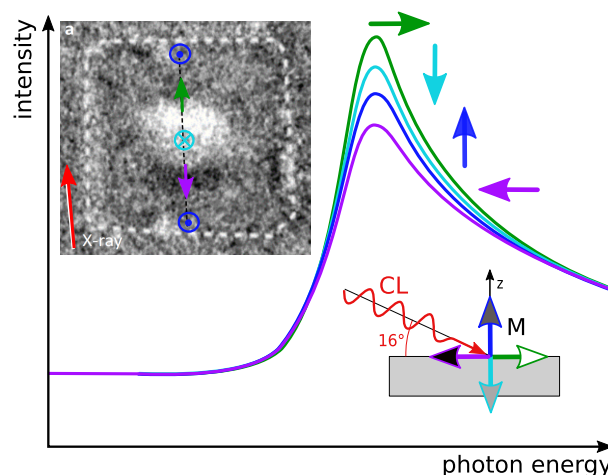


Figure 3.34: Spectra of L_3 edge taken with CL x-rays for different magnetisation directions. *insertion*) XMCD-PEEM image of a skyrmion stabilized in a square dot [6].

XMCD-PEEM Measurements are performed with the incident X-Ray beam with a given angle with respect to the sample surface. Different absorption intensities are obtained for different projections of the magnetisation along the beam direction. Fig. 3.34 shows the different intensities of a L_3 peak obtained with CL polarized light for different magnetisation directions. In the insert the XMCD-PEEM image for a skyrmion stabilized in a square dot is shown.

3.6.2 MFM

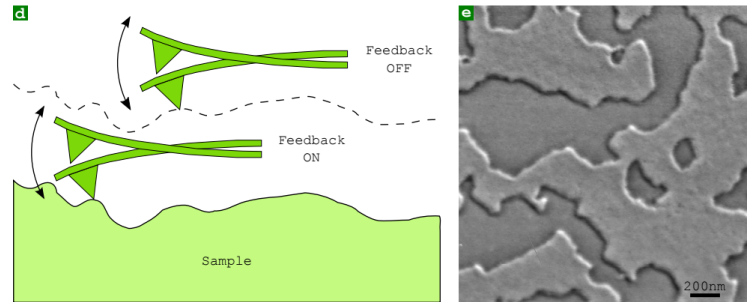


Figure 3.35: (d) Scheme for the two-pass MFM procedure. (e) $2 \times 2 \mu\text{m}^2$ MFM domain pattern of a 4 nm-thick epitaxial FePt(001) film with perpendicular magnetisation (sample and image courtesy: A. Marty and O. Fruchart).

Magnetic force microscopy is a technique based on the Atomic Force Microscope (sec. 3.2). In an MFM microscope a cantilever with a tip covered with a magnetic material is used. Firstly the cantilever scans the surface in the tapping mode. In this mode the electrostatic interactions dominate over the magnetic ones which allows to display the surface topography. Since the electrostatic interactions have short range the cantilever is then raised from the surface up to a height where it feels only the magnetic interactions. A second scan of the surface is performed following the topography map in order to keep a constant distance from the surface (Fig. 3.35(e)). In this regime the cantilever is excited close to its resonance frequency. The phase shift is then detected. It is proportional to the vertical gradient of the force felt by the tip. The second scan allows thus to display a map of the variation of surface magnetic stray field.

In Fig. 3.35(e) an MFM image of a domain pattern in a 4 nm-thick epitaxial FePt(001) film with perpendicular magnetisation is shown. Four different contrasts can be discerned.

- The brighter and darker contrasts indicate the presence of a domain wall. The tip directly interacts with the stray field generated by the strong change of magnetisation between the two domains.
- The intermediate grey contrasts are the sign of magnetic domains. The contrast arises from magnetisation variation due to the interaction with the tip magnetic field. It is thus directly proportional to the sample magnetic susceptibility.

MFM can reach nanometer resolution. In this thesis it is used to image the magnetisation in ultrathin magnetic systems. This kind of systems generates a small stray field due to the small amount of magnetic material. On the other hand the magnetic susceptibility is high and it is possible to observe magnetic domains. At the same time, a high susceptibility implies a strong interaction between the tip and the magnetic configurations meaning that the tip can perturb the magnetic configuration.

Chapter 4

Topological magnetic solitons

In the previous chapter we answered to the question of how the symmetry of the crystal structures influences the symmetry of the magnetic interactions. Here we try to answer to the question of how the magnetic interaction symmetry influences the configuration of magnetic topological solitons. In order to do that we first introduce then main concepts of the topology theory in magnetism and then we describe the model that we construct to describe 1D, domain walls (DWs) and 2D topological magnetic solitons, skyrmions (SKs), in anisotropic systems.

The chapter is divided into five sections:

- In the first section an introduction to the topology in magnetism can is given.
- In the second a continuous micromagnetic model is described in order to study 1D topological magnetic solitons, DWs. The main models used in literature for describing these magnetic configurations are presented under the presence of different magnetic interactions.
- In the third part the results obtained during this thesis work on the effect of anisotropic interactions on DWs in systems with C_{2v} symmetry are presented. In this part we answer to the question of how the symmetry of the magnetic interactions influences the DW configuration.
- Finally we show the micromagnetics models that we developed to describe the stability and the properties of skyrmions in thin films. Then the relationships between the symmetry of the DMI interaction and the skyrmion configurations is described. This allows us to find the conditions for the stabilisation of anti-skyrmions and study their properties and configurations.

4.1 Topology

The last decades part of the research community has focused on the study of topological properties in condensed matter. This research field is interesting due to the fact that simple and basic properties owned by completely different systems involve common complex and fascinating phenomena. In this section I will give a simple introduction to explain the meaning of topology and how to characterize the homotopy classes.

The topology for a magnetic vectorial field will be analysed for one and two-dimensional systems. The presence of a non-trivial topology in magnetism corresponds to the presence of magnetic solitons with topological properties. Then the general concept of Berry phase will be explained in order to elucidate the origin of the emergent fields. Indeed they are the fundamental causes of the topological properties. The topological Hall effect, topological protection and gyrotropic motion are the topological properties that will be analysed in the case of two-dimensional topological magnetic solitons called skyrmions.

4.1.1 Topological number

The discussion described in this section follows the work covered in reference [63].

The term topology has a greek origin and is a composition of two words: *topos*-space and *logos*-study. Topology is the branch of mathematics focusing on the study of the properties of space that are conserved under continuum space transformations. One can define a homotopy class as the set of functions f that can

be continuously deformed into each other.

In this manuscript the discussion is reduced to smooth vector fields $\mathbf{f} : \mathbb{R}^n$ defined in the extended space \mathbb{R}^n , with n the number of space dimensions.

One can understand if two vectorial fields $\mathbf{f} : \mathbb{R}^n$ and $\mathbf{g} : \mathbb{R}^n$ belong to the same homotopy class by performing a projection into a different space. For instance, when the fields are projected on a unit sphere \mathbb{S}^n they will wrap the space in the same way if and only if they belong to the same homotopy class. Therefore the projection, called more generally map, $\mathbf{f} : \mathbb{R}^n \rightarrow \mathbb{S}^n$ can be used to define a quantity owned by all the elements of the same homotopy class, a topological invariant. The mapping degree $deg(\mathbf{f})$ fulfils this property and is defined as the number of times that the vectorial field \mathbf{f} wraps around the unit sphere. It is called the topological number N and is defined as:

$$deg(\mathbf{f}) = N(\mathbf{f}) = \frac{\text{oriented area of } \mathbf{f}(\mathbb{S}^2)}{\text{area of } \mathbb{S}^2} \quad (4.1)$$

The theory of the differential forms can be used in order to calculate the mapping degree over curved spaces, manifolds, independently of the space coordinates. With this formalism the mapping degree reads:

$$N(\mathbf{f}) = \frac{1}{\text{area}(\mathbb{S}^n)} \int_{\mathbb{R}^n} \omega(\mathbf{f}) d\mathbf{x} \quad (4.2)$$

where $\omega(\mathbf{f})$ is the topological charge density. It describes the normal to the n -dimensional surface, i.e. how the vectorial field changes locally on the unit sphere \mathbb{S}^n . It can be formulated as:

$$\omega(\mathbf{f}) = \det(\mathbf{f} | D\mathbf{f}) = \det \left(\mathbf{f} \left| \frac{\partial \mathbf{f}}{\partial x^1} \right| \dots \left| \frac{\partial \mathbf{f}}{\partial x^n} \right| \right) \quad (4.3)$$

4.1.2 Magnetic topological solitons

In this work the studied vectorial fields are the magnetic fields of m -components in an n -dimensional space :

$$\mathbf{m}(\mathbf{x}) = \begin{pmatrix} m_1(x_1 \dots x_n) \\ \dots \\ m_m(x_1 \dots x_n) \end{pmatrix} \quad (4.4)$$

In particular the study is focused on the physics of magnetic solitons with topological properties. A magnetic soliton is a localized magnetic field configuration that in first approximation does not change upon application of an external perturbation. Indeed, magnetic solitons can slightly deform during a perturbation but they come back from different positions to the initial configuration when the perturbation stops. In this thesis two different magnetic topological solitons will be studied:

Domain walls (DW) are the magnetic configuration localized at the transition between two ferromagnetic domains. They can easily be described with a two-dimensional magnetic field ($m=2$) in a mono-dimensional space ($n=1$). In this approximation it has generally a half-integer topological number that depends on the rotation direction, i.e. the DW chirality. The topological number reads:

$$N_{1D} = \int \frac{\sum_{ij}^2 \epsilon_{ij} m_i(x) \partial m_j(x)}{2\pi} dx \quad (4.5)$$

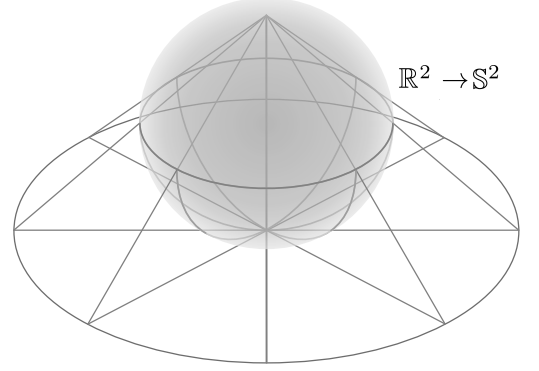


Figure 4.1: Sketch of a stereographic projection from a plane to the surface of a sphere: $\mathbf{f} : \mathbb{R}^2 \rightarrow \mathbb{S}^2$

where ϵ_{ij} is the Levi-Civita symbol and 2π is the length of a unitary circle. Considering the angle θ , that describes the direction of the magnetisation with respect to the space direction \hat{z} (Fig. 4.2), the magnetic field can be described by the function $\theta(x)$ and the topological number takes an easy formulation:

$$N_{1D} = \frac{[\theta(x)]_{x_f}^{x_i}}{2\pi} = W \quad (4.6)$$

where W is the winding number. If the magnetic field comes back to the same initial direction, as shown in Fig. 4.2 for the case of a 360° DW, it assumes only integer values with the sign depending on the DW chirality. Note that magnetisation rotation with $N_{1D} = 1(-1)$ rotates clockwise (anti-clockwise) in the direction of the axis \hat{x} .

Considering a point inside the unit sphere the winding number describes the total number of times that the curve, describing the vectorial field, travels clockwise around this point. In ferromagnetic systems 360° DWs can be found only in particular conditions [64, 65, 66]. In a more general case the magnetisation changes between two magnetic domains with opposite magnetisation directions ($\theta(x_i) = n\pi, \theta(x_f) = \theta(x_i) \pm \pi$). This kind of DWs has a half-integer topological number $N_{1d} = \pm 1/2$.

Skyrmions are localized vortex-like magnetisation configurations with integer topological number. They can be described with a three-dimensional magnetic field ($m=3$) in two-dimensional space ($n=2$). In these dimensions the topological number, known as the skyrmion number N_{SK} , reads:

$$N_{SK} = \iint \mathbf{m} \cdot \left(\frac{\partial \mathbf{m}}{\partial x} \times \frac{\partial \mathbf{m}}{\partial y} \right) dx dy \quad (4.7)$$

Passing to spherical coordinates for the space ($\mathbf{r} = (r \cos \alpha, r \sin \alpha)$) and for the magnetisation ($\mathbf{m} = (m \cos \phi \sin \theta, m \sin \phi \sin \theta, m \cos \theta)$), one can understand the meaning of the skyrmion number. In skyrmion configurations the spatial dependence of the magnetisation can be simplified by setting the perpendicular magnetic variable independent on the in-plane ones ($\theta(r)$) and the in-plane magnetic variable independent on the radius ($\phi(\alpha)$). Then the topological skyrmion number reads:

$$N_{SK} = \frac{1}{4\pi} \iint \frac{d\theta}{dr} \frac{d\phi}{d\alpha} \sin \theta d\alpha dr = \frac{1}{4\pi} [\cos \theta]_{\theta(r=\infty)}^{\theta(r=0)} [\phi]_{\phi_f}^{\phi_i} = p \cdot W \quad (4.8)$$

where p describes the magnetisation direction in the origin ($p=1$ (-1) for $\theta(r=0) = \pi(0)$) and W is the winding number. Considering the same uniform magnetisation, i.e. the same p value, the winding number allows to define the skyrmion (SK) ($\phi(\alpha) \propto \alpha$) with a positive winding number and the anti-skyrmion (ASK) ($\phi(\alpha) \propto -\alpha$) with a negative winding number and thus a topological charge opposite to the one of the SK.

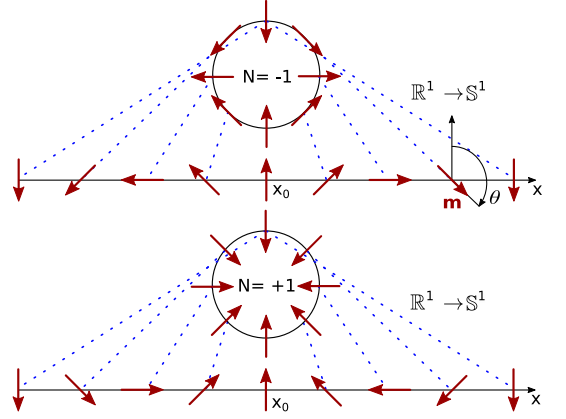


Figure 4.2: Sketch of a stereographic projection from a line to a circle: $\mathbf{m} : \mathbb{R}^1 \rightarrow \mathbb{S}^1$. The red arrows indicate the direction of the magnetisation field. The shown magnetic configurations, known as a 360° domain wall, have an integer topological number.

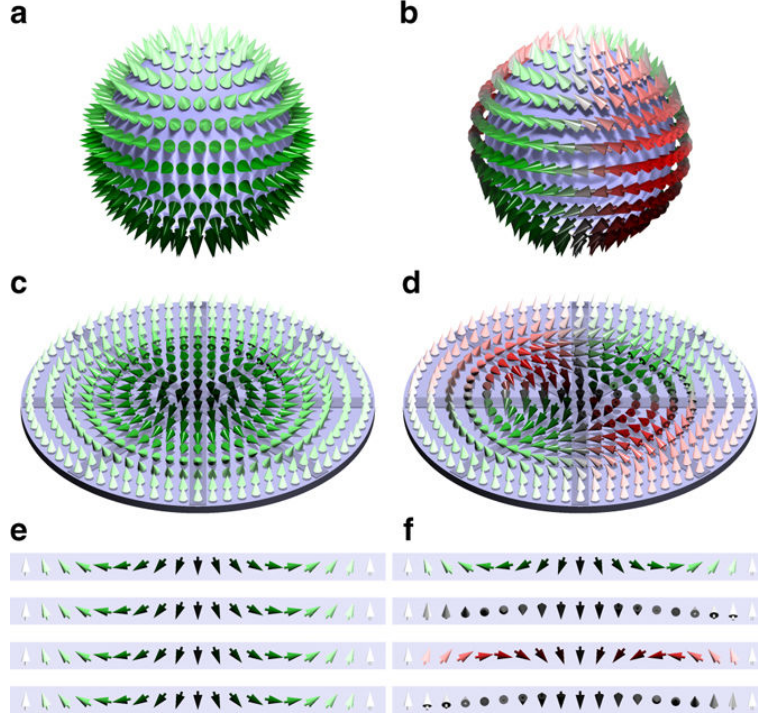


Figure 4.3: Comparison of skyrmion and anti-skyrmion. (a), (b) Néel-like skyrmion and anti-skyrmion schematically shown in (c) and (d) mapped onto a sphere. The color code represents the out-of-plane component of the spins via the brightness, with bright (dark) spins pointing up (down), and their rotational sense in radial direction going from inside out changing from red (clockwise) via gray (vanishing rotational sense) to green (counter-clockwise). (e), (f) Cross sections of the spin textures along the four highlighted directions shown in (c) and (d). Taken from Ref. [18]

4.1.3 Berry phase and breaking of the time reversal symmetry

In this section a quantum-mechanical approach is used in order to define the Berry phase and understand the origin of intrinsic breaking of the time reversal symmetry in systems with a non-trivial topology.

The discussion described in this section follows the work covered in reference [67].

Considering the Hamiltonian $H(\lambda(t))$, defined in the space parameters $\lambda(t)$, one can study the adiabatic evolution of an eigenfunction $|\alpha(t)\rangle$ in a closed curve C . The static Schrödinger equation allows to find the eigenvalues $\epsilon_n(\lambda)$ and the eigenstates $|n(\lambda)\rangle$ at a given time:

$$H(\lambda)|n(\lambda)\rangle = \epsilon_n(\lambda)|n(\lambda)\rangle \quad (4.9)$$

Two different sets $|n(\lambda)\rangle$ and $|n(\lambda)'\rangle$ give the same $\epsilon_n(\lambda)$ if they differ only by a phase:

$$|n(\lambda)'\rangle = e^{i\zeta_n(\lambda)}|n(\lambda)\rangle \quad (4.10)$$

The transformation between the two eigenfunctions is called a Gauge transformation.

The time evolution of a given state $|\alpha(t)\rangle$ can be obtained solving the time-dependent Schrödinger equation:

$$i\hbar\partial_t|\alpha(t)\rangle = H(\lambda(t))|\alpha(t)\rangle \quad (4.11)$$

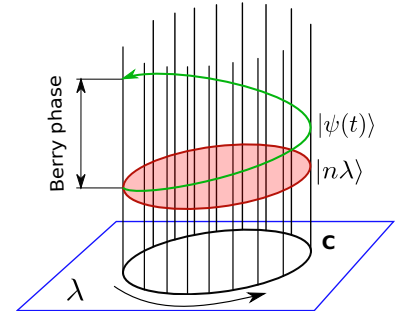


Figure 4.4: Sketch of the evolution of the state $|\alpha(t)\rangle$ (green line) in the space of parameters λ (blue plane) on a closed curve C . The red plane is the set of static solutions to the Hamiltonian $H(\lambda)$

where at $t=0$ the state $|\alpha(0)\rangle = |n(\lambda(0))\rangle$ is considered the eigenstate of the static solution. Since the evolution is adiabatic and it occurs on a closed curve C after a given time T , the system period, the system comes back to the initial state:

$$\lambda(T) = \lambda(0) \quad H(T) = H(0) \quad \epsilon_n(T) = \epsilon_n(0) \quad (4.12)$$

The time evolved state $\alpha(t)$ can generally be written as a linear combination of the static eigenstates of the evolved Hamiltonian:

$$|\alpha(t)\rangle = \sum_n c_n(t) |n(\lambda(t))\rangle \quad (4.13)$$

The problem is then reduced to the study of the coefficients $c_n(t)$. They can be obtained placing the last equation in the time-dependent Schrödinger equation:

$$\hbar \partial_t c_n(t) = -i \epsilon_n(t) c_n(t) - \sum_m c_m(t) \langle n(\lambda(t)) | \partial_t | m(\lambda(t)) \rangle \quad (4.14)$$

For the adiabatic approximation $c_m(t) = c_n(t)$, $|m(\lambda(t))\rangle = |n(\lambda(t))\rangle$ and the equation can be directly solved:

$$c_n(t) = e^{i \int_0^t \langle n(\lambda(t')) | \partial_t | m(\lambda(t')) \rangle dt'} e^{-i \int_0^t \epsilon_n(\lambda(t')) dt'} \quad (4.15)$$

and the evolved state reads:

$$|\alpha(t)\rangle = e^{i \int_0^t \langle n(\lambda(t')) | \partial_t | n(\lambda(t')) \rangle dt'} e^{-i \int_0^t \epsilon_n(\lambda(t')) dt'} |n(\lambda(t'))\rangle \quad (4.16)$$

When $t = T$, i.e. the system is back to the initial state ($\epsilon_n(T) = \epsilon_n(0)$), the second phase becomes equal to unity. The first one is generally called the geometrical phase, or in the case of a closed path the Berry phase $\gamma_n(C)$.

The Berry phase can be reformulated in a purely geometrical representation :

$$\gamma_n(C) = i \int_0^t \langle n(\lambda(t)) | \partial_t | n(\lambda(t)) \rangle dt = i \int_{\lambda(0)}^{\lambda(t)} \langle n(\lambda(t)) | \partial_\lambda | n(\lambda(t)) \rangle d\lambda = \int_{\lambda(0)}^{\lambda(t)} \mathbf{A}^n d\lambda \quad (4.17)$$

where \mathbf{A}^n is the Berry connection that is a pure real quantity. Moreover the Berry phase is a gauge invariant and the connection can be defined up to addition by a differential term :

$$\mathbf{A}^{n'} = \mathbf{A}^n - \nabla \zeta_n \quad (4.18)$$

Note that the Berry connection behaves as a potential vector. Indeed if after a closed path it is non-zero the system presents an intrinsic breaking of time reversal symmetry even if the initial Hamiltonian respected this symmetry. This concept becomes clearer when, using Stoke's theorem, the Berry phase is reformulated as a surface integral :

$$\gamma_n(C) = \int_S \Omega_n(\lambda) d\lambda \quad \Omega_n(\lambda) = \nabla_\lambda \times \mathbf{A}^n \quad (4.19)$$

It can thus be confused with a magnetic field in electrodynamics.

Because of its geometrical nature, the Berry phase is strongly dependent on the chosen path C . However, if two different paths can be transformed one into the other with a smooth continuous transformation the Berry phase does not change. It is indeed a topological invariant. Moreover it is possible to demonstrate that the Berry phase is zero in systems with a trivial topological number ($N = 0$). This means that in systems with non-trivial topology ($N \neq 0$) the Berry phase is non-zero and an intrinsic breaking of the time reversal symmetry occurs. This phenomenon can be described introducing the concept of emergent fields.

4.1.4 Emergent fields and topological Hall effect

The concept of emergent fields allows to understand the effect of the Berry phase on magnetic systems. The discussion described in this section follows the work covered in reference [68].

The dynamics of a free electron in a two-dimensional metallic magnetic material will be studied with this aim. The system's magnetisation is considered to change in space and in time and is described by the vectorial field $\mathbf{M}(\mathbf{r}, t)$.

Then the Hamiltonian of a single electron reads:

$$i\hbar\partial_t|\alpha\rangle = \left[\frac{\hat{\mathbf{p}}^2}{2m} - J\hat{\boldsymbol{\mu}} \cdot \hat{\mathbf{M}}(\mathbf{r}, t) \right] |\alpha\rangle \quad (4.20)$$

where $|\alpha\rangle$ is the electron eigenstate, \mathbf{p} the momentum operator, m the electron mass, $J > 0$ is the strength of the exchange coupling and $\boldsymbol{\mu}$ is the electron magnetic moment.

A framework transformation can be performed in order to reduce the complexity of the exchange interaction between the electron and the magnetisation $\mathbf{M}(\mathbf{r}, t)$.

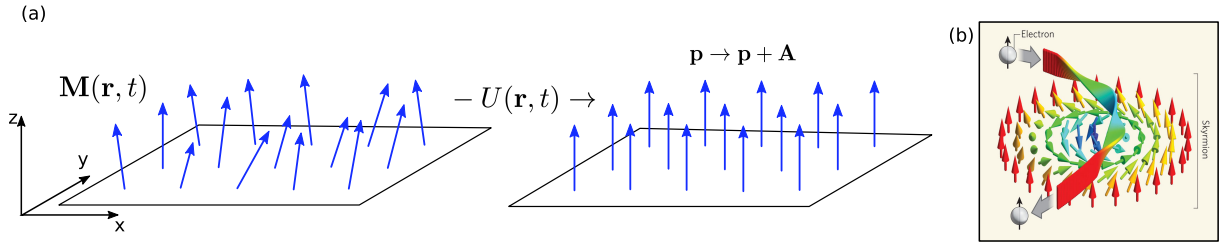


Figure 4.5: (a) Illustration of the effect of the local transformation on the magnetisation felt by a free electron (b) Sketch of the effect of the emergent field from a skyrmionic spin configuration on the motion of a free electron (From ref. [69])

A local transformation $\alpha = U(\mathbf{r}, t)\zeta$ allows thus to define an axis \hat{z} that locally rotates in the magnetisation direction,

$$-J\boldsymbol{\mu} \cdot \mathbf{M}(\mathbf{r}, t) - U(\mathbf{r}, t) \rightarrow \frac{Jg\hbar\mu_B|\mathbf{M}|}{2}\sigma_z = \bar{J}\sigma_z \quad (4.21)$$

where σ_z is the z Pauli matrix and q the electron charge. In this framework the exchange interaction becomes a trivial interaction favoring an electron moment parallel to the new \hat{z} axis. When the unitary local transformation is performed to the complete Hamiltonian, the momentum operator is transformed ($\mathbf{p} \rightarrow \mathbf{p} + e\mathbf{A}$) and the Hamiltonian reads:

$$i\hbar\partial_t\zeta = \left[q^eV + \frac{(\mathbf{p}\mathbb{I} - q^e\mathbf{A})^2}{2m} - \bar{J}\sigma_z \right] \zeta \quad (4.22)$$

with :

$$V = -\frac{i\hbar}{q}U^+\partial_tU \quad \mathbf{A} = -\frac{i\hbar}{q}U^+\nabla U \quad (4.23)$$

where V and \mathbf{A} are 2×2 matrices that describe the effect of the space and time variation of the magnetisation on the electron. With an analogy with the Hamiltonian of a free electron under the influence of electric and magnetic fields, V can be defined as an emergent electric field and \mathbf{A} as an emergent vectorial potential.

In the case of a $\mathbf{M}(\mathbf{r}, t)$ changing smoothly in time and space these potentials can be considered as a perturbation acting on the solutions of the unperturbed Hamiltonian $H_0 = \frac{\mathbf{p}^2}{2m} + \bar{J}\sigma_z$. Then it is possible to define an emergent magnetic field and an emergent electric field:

$$(\mathbf{B}_\sigma^e)_i = \mp \frac{\hbar}{2q^e} \frac{\epsilon_{ijk}}{2} \mathbf{M} \cdot (\partial_j \mathbf{M} \times \partial_k \mathbf{M}) \quad (\mathbf{E}_\sigma^e)_i = \mp \frac{\hbar}{2q^e} \mathbf{M} \cdot (\partial_i \mathbf{M} \times \partial_t \mathbf{M}) \quad (4.24)$$

From these equations one can understand under which conditions the emergent field can be obtained. The emergent electric field $(\mathbf{E}_\sigma^e)_i$ occurs only in systems where the magnetisation changes in time while the emergent magnetic field $(\mathbf{B}_\sigma^e)_i$ can be found when the magnetisation assumes a particular spatial configuration.

Notice that the expression that describes the emergent magnetic field is equivalent to the expression of the topological number in a two-dimensional system (Eq. 4.7). Then if in the system there is a non-trivial topological magnetic configuration, like a skyrmion $N_{SK} = \pm 1$, an electron will feel a Lorentz force arising from the emergent magnetic field and its trajectory will be deviated. This phenomenon is called the topological Hall effect, which was one of the first effects used to detect the presence of skyrmions [[70, 71]].

The other way around, if the skyrmion is free to move it will feel a force in the direction opposite to the electron deviation.

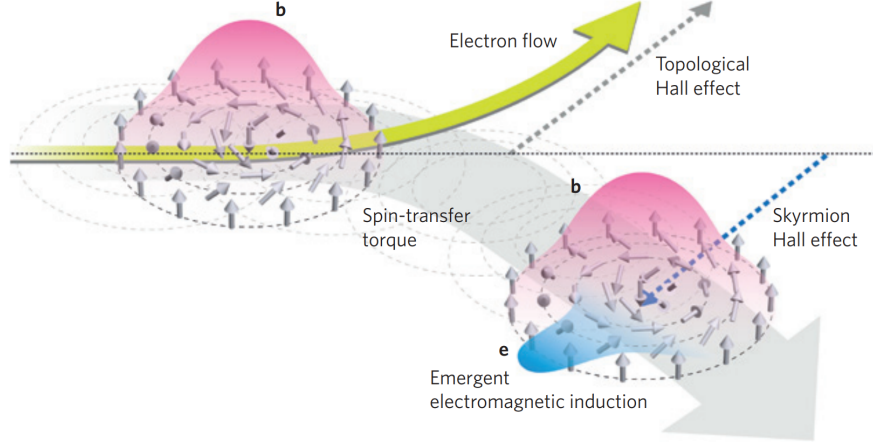


Figure 4.6: "Schematic picture of skyrmion motion and associated physical phenomena under the flow of electrons. Electron current drives the flow of a skyrmion by means of the spin-transfer torque mechanism. Electrons are deflected by the Lorentz force due to the emergent magnetic field \mathbf{b} of the skyrmion. The motion of the skyrmion is accompanied by the time-dependent emergent magnetic field \mathbf{b} (pink), and hence the emergent electric field \mathbf{e} , that is, emergent electromagnetic induction." Taken from [72]

Gyroscopic motion The skyrmion gyroscopic effect has been clearly demonstrated by Thiele [73] who formulated a motion law for a soliton field solution:

$$\overline{\overline{M}} \frac{d\mathbf{v}}{dt} = \overline{\overline{F}} + \mathbf{G} \times \mathbf{v} + \alpha \overline{\overline{D}} \cdot \mathbf{v} \quad (4.25)$$

where $\overline{\overline{M}}$ is a matrix called soliton mass, which depends on the soliton internal degrees of freedom and describes the deformation of the soliton solution. \mathbf{v} is the soliton speed, $\overline{\overline{F}}$ and $\overline{\overline{D}}$ are matrices that describe respectively the forces acting on the soliton and the damping effect. \mathbf{G} is the gyroscopic vector, which causes a lateral deviation of the soliton and in a two-dimensional system reads:

$$G_{ij} = \frac{\mu_0 M_s}{\gamma} \iiint \left[\mathbf{m} \cdot \left(\frac{\partial \mathbf{m}}{\partial x_i} \times \frac{\partial \mathbf{m}}{\partial x_j} \right) \right] dx^3 = \frac{\mu_0 M_s}{\gamma} N_{SK} \quad (4.26)$$

The gyrotensor G_{ij} depends on the skyrmion number and shows directly the effect of the emergent fields in the form of a Magnus force. The direction of this force is then proportional to the topological number [74, 32].

4.1.5 Topological protection

In order to explain the concept of topological protection, let's consider a particular field solution with a non-trivial topology. This solution is not the energy minimum of the analysed system and has the tendency to decay to the system's ground state with a different topology.

Since two objects with different topology can not transform one into the other with a continuous transformation one can expect the non-trivial topological solution to be protected against the decay into the ground state. This does not mean that this non-trivial topological solution can not decay into the ground state, but that this process can occur only through some system singularity.



Figure 4.7: Artistic sketch of the magnetisation configuration of a Bloch skyrmion (upper object) and of a Bloch point (lower object). *(from the 2017 IFF Spring School poster .Copyright: Forschungszentrum Julich)*

An isolated skyrmion is a non-trivial topological solution and has a higher energy than the ferromagnetic ground state. It means that the skyrmion is topologically protected and can not decay into the ferromagnetic background with a continuous transformation. This theoretical assumption made the skyrmion particularly interesting and several studies have been performed in order to evidence the skyrmion topological protection [75, 76, 77, 78]. These works have been useful to the scientific community in the understanding of the skyrmion stability but they did not find any evidence of topological protection. The reason can be simply explained analysing the magnetic configurations in Fig. 4.7 where a skyrmionic magnetic configuration and a Bloch point are shown. The Bloch point is a magnetic three dimensional configuration where the magnetisation locally vanishes in its center. It is a magnetic singularity. The topological protection does not occur for skyrmions because when they are small, a few nanometers, they can not be described with a continuous theory and they can be annihilated by the injection of a Bloch point that crosses the sample thickness.

4.2 Magnetic domain walls in isotropic matter

In ferromagnetic materials of large dimensions one can find areas with different magnetisation directions called magnetic domains. The portion of the space where the magnetisation changes from one direction to the other is a stable localized magnetisation configuration called Domain Wall (DW). The DW is a one-dimensional topological soliton with a half-integer topological number. Indeed the DW propagates with a localized configuration under external perturbations, like magnetic fields or spin currents, and in a continuous magnetisation theory it is topologically protected.

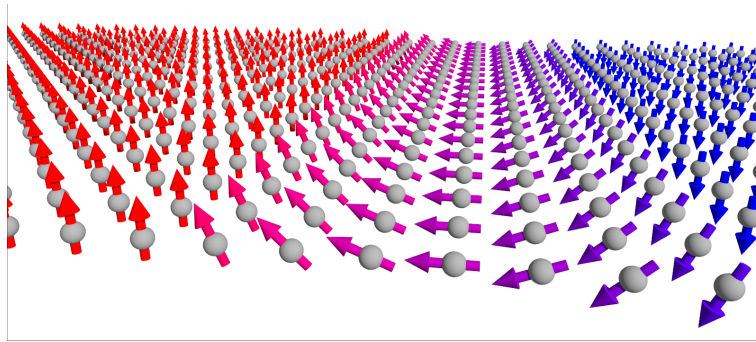


Figure 4.8: Artistic sketch of a domain wall

In this section the DW energy and configuration are studied in two-dimensional ferromagnetic systems that present an out-of-plane magnetisation. The discussion described in this section follows the work covered in reference [38]. The two-dimensional approximation can be used for all the systems where the magnetic layer thickness t is smaller than the magnetic coherence length; i.e. the characteristic length of the magnetisation variation called dipolar exchange length ($l_{ex} = \sqrt{\frac{2A}{\mu_0 M_s^2}}$). These systems are called ultrathin films and they are out-of-plane magnetized when the MCA overcomes the surface dipolar interaction. Indeed, when the magnetisation is parallel to the surface normal the system is subject to a demagnetizing field that promotes an in-plane magnetisation. Considering the dipolar interaction in the local approximation, the perpendicular magnetisation occurs when $K_{MCA} > K_d = \frac{1}{2}\mu_0 M_s^2$.

A one-dimensional micromagnetic derivation of the DW profile and energy will be computed in different energy environments. First only the exchange interaction and an uniaxial anisotropy will be considered and the main method to study the DW profile and energy will be introduced. Then the model will be refined with the addition of the dipolar interaction, of the DMI and finally of an in-plane magnetic field.

DW profile and energy: Linear variation method

A simple one-dimensional micromagnetic model allows studying the DW width and energy. It sets the DW profile with a linear magnetisation behavior. It does not give the exact profile and energy of the DW but allows to understand the role of the different energies and the origin of the localized DW characteristics.

In a 1D model the problem can be approached considering the angle $\theta(x)$ that describes the direction of the magnetisation $\mathbf{m}(x)$ with respect to the \hat{z} direction in the position x , as shown in Fig. 4.9. This method is based on the study of the competition between the uniaxial anisotropy and the exchange interaction:

$$E(x) = K \sin^2(\theta) + A \left(\frac{d\theta}{dx} \right)^2 \tag{4.27}$$

Setting a linear function for $\theta(x)$ varying from $-\pi$ to π the DW energy equation reads:

$$\mathcal{E}(L) = \frac{KL}{2} + \frac{A\pi^2}{L} \tag{4.28}$$

where L is the width of the DW and its value can be found minimizing the expression 4.28:

$$\frac{d\mathcal{E}(L)}{dL} = 0 \quad \implies \quad L = \pi\sqrt{2}\sqrt{\frac{A}{K}} = \pi\sqrt{2}\Delta \tag{4.29}$$

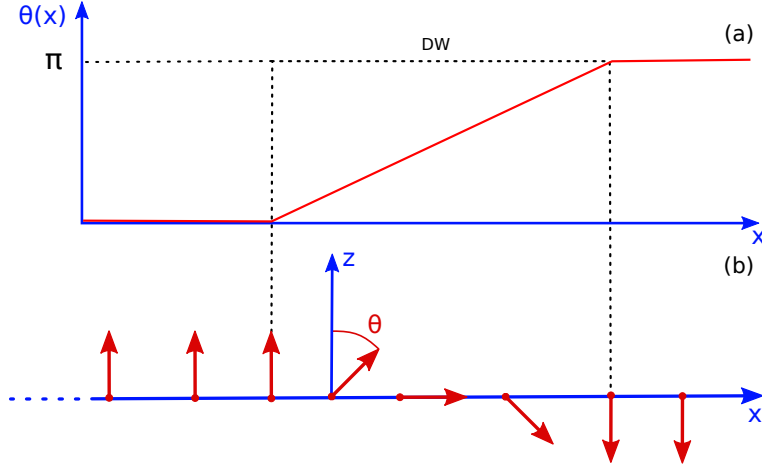


Figure 4.9: (a) Plot of a linear DW profile $\theta(x)$. (b) Vectorial plot of the magnetisation profile $\mathbf{m}(x)$ in a linear DW

where Δ is defined as the anisotropy exchange length or Bloch parameter. Replacing L in Eq. 4.28 the DW energy reads:

$$\mathcal{E} = \pi\sqrt{2}\sqrt{KA} \quad (4.30)$$

Notice that the localized aspect of the DW arises from the competition between the exchange interaction and the magneto-crystalline anisotropy. Indeed the first favors a smooth magnetisation variation while the anisotropy energy is minimized for abrupt rotations.

DW profile and energy: Euler and Brown equations

An exact solution of the DW profile can be obtained using a functional minimisation method. The minimisation of this functional allows to describe the profile of a DW that reduces the energy of the system. In a 1D model the problem can be approached considering two variables; the angle $\theta(x)$ and its gradient $d\theta/dx$ (Fig. 4.9). Indeed the exchange (E_{ex}) and the DMI (E_{DMI}) energies depend on $d\theta/dx$ and the other interactions, like the magnetic anisotropies, have an energy formulation directly dependent on θ .

$$E\left(\theta, \frac{d\theta}{dx}\right) = E\left(\frac{d\theta}{dx}\right) + E(\theta) \quad (4.31)$$

The method describes a finite system $a < x < b$ where the initial conditions are set and the total energy reads:

$$\mathcal{E} = \int_a^b E\left(\theta, \frac{d\theta}{dx}\right) dx + \mathcal{E}|_a + \mathcal{E}|_b \quad (4.32)$$

where $\mathcal{E}|_a$ and $\mathcal{E}|_b$ are the interface energies. The minimisation of the energy functional allows to formulate the Euler relations :

$$\frac{\partial E}{\partial \theta} = \frac{d}{dx} \left[\frac{\partial E}{\partial \frac{d\theta}{dx}} \right] \quad (4.33)$$

$$\frac{\partial E}{\partial \frac{d\theta}{dx}} \Big|_a = \frac{\partial \mathcal{E}_a}{\partial x} \quad (4.34)$$

$$\frac{\partial E}{\partial \frac{d\theta}{dx}} \Big|_b = \frac{\partial \mathcal{E}_b}{\partial x} \quad (4.35)$$

In this section only the exchange energy dependence on $\frac{d\theta}{dx}$ is considered and the DMI will be introduced later. Then the first Euler equation reads:

$$\frac{dE_a}{d\theta} = 2A \frac{d^2\theta}{dx^2} \longrightarrow \frac{dE_a}{dx} = \frac{d}{dx} A \left(\frac{d\theta}{dx} \right)^2 \quad (4.36)$$

The last relation is called the Brown equation and when it is integrated from a to a generic point x reads:

$$E_a(x) - E_a(a) = 2A \left(\frac{d\theta}{dx} \right)^2 - 2A \left(\frac{d\theta}{dx} \right)^2 \Big|_a \quad (4.37)$$

Setting the zero of the energy in the initial point ($E_a(a) = 0$) and for zero divergence ($\frac{d\theta}{dx} = 0$), one can write the local condition:

$$E_a(x) = 2A \frac{d^2\theta}{dx^2} \quad (4.38)$$

This equation shows how the local density of anisotropy and exchange energy are balanced at any location of the system. Moreover the local condition allows to reduce the complexity of the DW energy calculation; i.e. the calculation can be performed in the angle space, and energy does not depend on the DW profile ($\theta(x)$) and the expression of the anisotropy energy:

$$\mathcal{E} = 2 \int_a^b E \left(\theta, \frac{d\theta}{dx} \right) dx = 2 \int_a^b A \sqrt{\frac{E_a}{A}} \frac{d\theta}{dx} dx = 2 \int_0^\pi \sqrt{AE_a(\theta)} d\theta \quad (4.39)$$

The resolution of the DW profile requires the specification of the form of the anisotropy energy. In the next sections the DW profile and energy will be solved in different cases with different energies and symmetries.

4.2.1 Competition between uniaxial anisotropy and exchange interaction

In this section the DW energy and profile will be solved in a 1D system with uniaxial anisotropy and exchange interaction. The anisotropy energy reads:

$$E(\theta) = K_{\text{eff}} \sin^2 \theta \quad (4.40)$$

In K_{eff} all the uniaxial anisotropies can be included, like the surface dipolar interaction in the local approximation ($K_{\text{eff}} = K - K_d$). Using this expression in Eq. 4.39, where θ varies between 0 and π , gives the DW energy:

$$\mathcal{E} = 4\sqrt{AK_{\text{eff}}} \quad (4.41)$$

The DW profile can be obtained solving the Brown differential Eq. 4.36

$$\begin{aligned} K_{\text{eff}} \sin^2(\theta) &= A \left(\frac{d\theta}{dx} \right)^2 \\ \int \frac{1}{\sin(\theta)} d\theta &= \int \sqrt{\frac{A}{K_{\text{eff}}}} dx \end{aligned} \quad (4.42)$$

$$\theta(x) = 2 \arctan(e^{\frac{x}{\Delta}})$$

where $\Delta = \sqrt{A/K_{\text{eff}}}$. This function takes the name of Bloch profile.

Comparing the two models one can notice that the energy for a test function can only be larger than the energy found by functional minimisation. The exact Bloch profile is extended to all the space but at the tails of the function the magnetisation changes slowly and the DW can be considered as a localized configuration and a DW width (L) can be defined. This can be done by calculating the distance between the interceptions of the functions $\theta(x) = \pi$ and $\theta(x) = 0$ with a linear function with the same slope as the Bloch profile in the DW center (Fig. 4.10).

$$\frac{dx}{d\theta} \left(\theta = \frac{\pi}{2} \right) = \sqrt{\frac{A}{K_{\text{eff}}}} = \Delta \quad \rightarrow \quad L = \pi\Delta \quad (4.43)$$

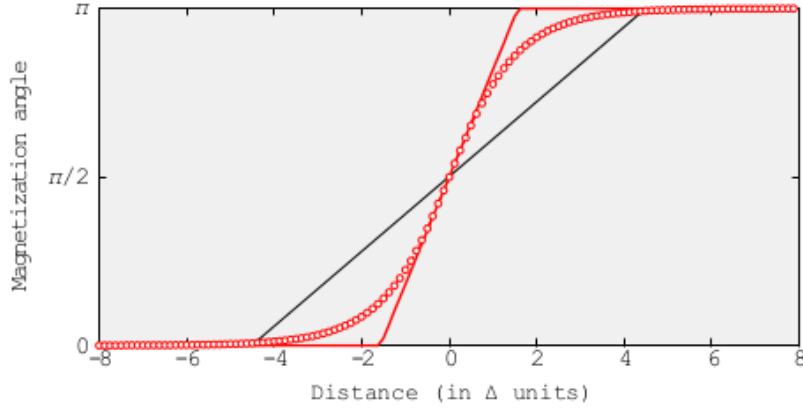


Figure 4.10: Exact solution for the profile of the Bloch domain wall (red dots), linear variational solution (black line), linear profile with the same energy as the exact solution (red line)

4.2.2 Role of the volume dipolar interaction

In the previous sections the magnetisation has been described as a two-dimensional vector field $\mathbf{m} = (m_x, m_z)$. When other interactions with a more complex space dependence are introduced it is fundamental to study the full magnetisation profile $\mathbf{m} = (m_x, m_y, m_z)$. It can be fully described by the two polar angles $(\theta; \phi)$ as shown in Fig. 4.11.

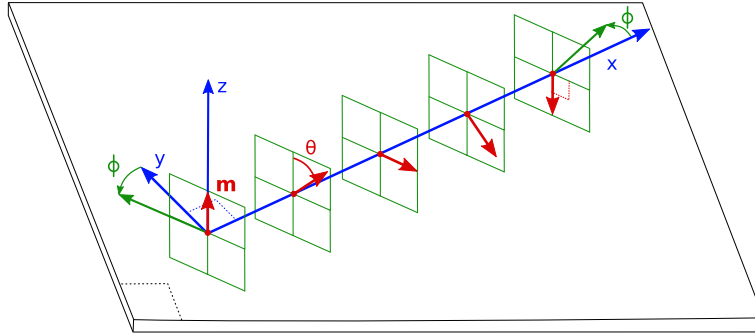


Figure 4.11: Sketch of a generic spin modulation in a thin film system.

The angle ϕ describes the plane in which the magnetisation is rotating and is called the polarisation angle. Two particular DWs with different polarisations are the most general solutions of the micromagnetic problems:

- The Néel wall is a DW where the magnetisation rotates along the direction where the magnetisation varies ($\phi = \frac{\pi}{2} + n\pi$)
- The Bloch wall is a DW where the magnetisation rotates perpendicular to the direction where the magnetisation varies ($\phi = n\pi$)

The presence of volume dipolar interactions breaks the energy degeneration between DWs with different polarisations. Indeed in the case of a Néel DW the magnetisation gradient is non-zero and volume magnetic charges are produced increasing the total dipolar interaction energy. Therefore if there are no other interactions that stabilize a Néel DW the system reduces its energy with a Bloch wall configuration ($\phi = n\pi$).

This effect can be easily studied with the demagnetizing theory. The DW can be approximated by an ellipsoid with the system thickness (t) and the domain wall width ($\pi\Delta$) as main axes (Fig. 4.12). Then the demagnetisation coefficient along the rotation direction reads [79]:

$$N_d = \frac{t}{\Delta\pi} \ln 2 \quad (4.44)$$

and the dipolar interaction energy density as a function of the polarisation angle ϕ reads:

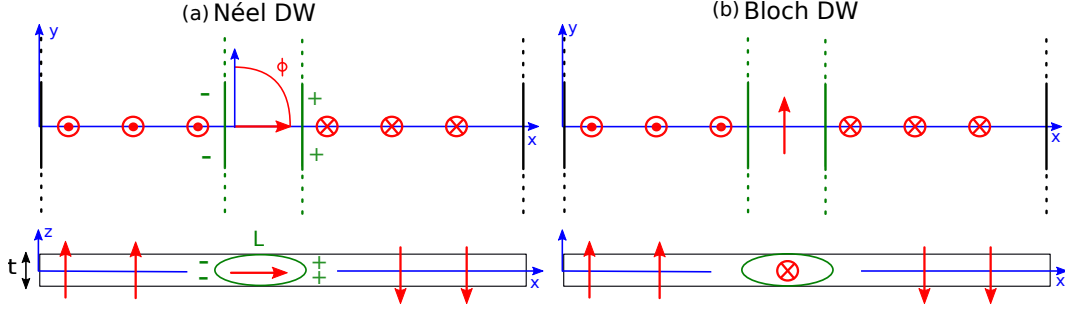


Figure 4.12: (a) Néel DW and (b) Bloch DW in a three dimensional system. (red) magnetisation vectors. (green) demagnetisation ellipsoid and volume magnetic charges.

$$E_d = \frac{1}{2} N \mu_0 M_s^2 \sin^2 \phi = K_d N_d \sin^2 \phi \quad (4.45)$$

the polarisation angle is constant during the magnetisation rotation and the volume dipolar interaction in this approximation does not modify the DW profile. In the limit $N_d K_d \ll K_{\text{eff}}$ the DW energy reads:

$$\mathcal{E} = 4\sqrt{AK_{\text{eff}}} + N_d \Delta K_d \sin^2 \phi \quad (4.46)$$

A simple minimisation with respect to the angle ϕ shows that the dipolar interaction promotes Bloch DWs ($\phi = \pi n$).

4.2.3 Role of the DMI

In this part the effect of the DM interaction on the DW energy, profile and polarisation is discussed [79]. The DMI in an isotropic system promotes a chiral Néel magnetisation rotation ($E_{DMI} < 0 \leftrightarrow \frac{d\mathbf{m}}{dx} \neq 0$). In a one-dimensional model the DMI energy density acquires the form:

$$E_{DMI} = D \left(\frac{d\theta}{dx} \right) \sin \phi \quad (4.47)$$

The term $\sin \phi$ describes the interaction chirality, i.e. the energy has a maximum for a give polarisation and a minimum for the opposite one. Moreover one can notice that a Bloch DW ($\phi = \pi n$) does not gain DMI energy.

Since the DMI energy density depends on $\frac{d\theta}{dx}$ the relations used in Sec. 4.2 read:

$$\frac{d\theta}{dx} = \frac{1}{\sin \theta} \quad a < x < b \quad (4.48)$$

$$\frac{d\theta}{dx} = \frac{D}{2A} \quad x = a; \quad x = b \quad (4.49)$$

- The first relation is identical to the previous case and the DW profile will be the Bloch profile even in presence of DMI. This effect can be understood calculating the DMI energy of a DW:

$$\mathcal{E}_{DMI} = \int_a^b D \left(\frac{d\theta}{dx} \right) \sin \phi \quad dx = \int_0^\pi D \sin \phi \quad d\theta = \pi D \sin \phi \quad (4.50)$$

where the DMI DW energy in polar coordinates does not depend on the angle θ .

- The second relation shows the presence of a magnetisation tilt at the system edges [80]. It depends on the competition between exchange and DMI and relaxes to the collinear domain configuration with the same angular dependence as for the Bloch profile.

The DW energy density as a function of the DW polarisation angle reads:

$$\mathcal{E} = 4\sqrt{AK_{\text{eff}}} + \Delta K_d \sin^2 \phi + \pi D \sin \phi \quad (4.51)$$

The minimisation with respect to ϕ allows to calculate the polarisation angle that minimizes the energy. Two cases can be distinguished :

- if $|D| < D_c$, with $D_c = \frac{4\Delta K_d}{\pi}$, the minimum energy is obtained for an intermediate DW polarisation:

$$\sin \phi = \frac{\pi D}{4\Delta K_d} \quad \mathcal{E} = 2\sqrt{AK_{\text{eff}}} - \frac{\pi D^2}{2D_c} \quad (4.52)$$

- if $|D| > D_c$ the minimum energy is obtained for a Néel DW configuration:

$$\sin \phi = 1 \quad \mathcal{E} = 2\sqrt{AK_{\text{eff}}} - \pi D \quad (4.53)$$

In a real system a Néel and a Bloch DW do not have exactly the same profile (Fig. 4.13). The approximation used for the dipolar field in the model developed in this chapter can not show this difference. In real systems a larger DW can be expected in the case of a Néel DW. It arises from the magnetic volume charges that have the tendency to repulse each other and enlarge the DW; i.e. a larger DW generates weaker dipolar volume charges. A numerical calculation has been performed to confirm this theory by A.Thiaville et al. [79] (Fig. 4.13).

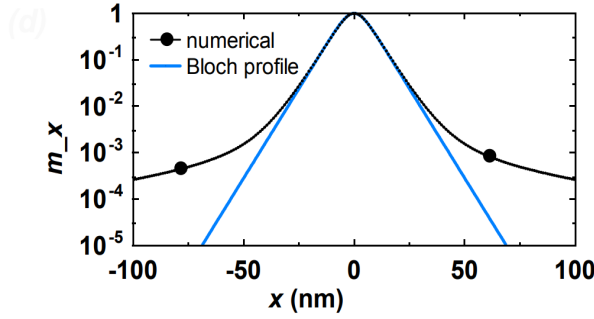


Figure 4.13: (blue) Bloch profile. (black) Numerical resolution of a Néel DW profile with the exact calculation of the dipolar interaction for a given set of magnetic parameters ($D = 2 \text{ mJ/m}^2$, $M_s = 1100 \text{ kA/m}$, $A = 16 \text{ pJ/m}$, $K = 1.27 \text{ MJ/m}^3$) [79]

4.2.4 Effect of an in-plane magnetic field

In this part the effect of an external magnetic field B_{in} applied in the direction of the polarisation of a Néel DW stabilized by DMI is studied. The study is thus limited to the case of strong DMI, i.e. $|D| > \frac{4\Delta K_d}{\pi}$, for which in absence of an in-plane magnetic field the DW polarisation is completely defined by the DMI chirality. Then introducing the Zeeman energy the energy density of the system reads:

$$E(x) = K_{\text{eff}} \sin^2(\theta) + A \left(\frac{d\theta}{dx} \right)^2 \pm M_s B_{\text{in}} \sin \phi \sin \theta - D \left(\frac{d\theta}{dx} \right) \sin \phi \quad (4.54)$$

The in-plane magnetic field term is added to (subtracted from) the energy density when B_{in} is anti-parallel (parallel) to the DW polarisation. Using eq. 4.54 in eq. 4.39, the DW energy reads:

$$\mathcal{E}_{\text{DW}} = 2 \int_0^\pi \sqrt{A(K_{\text{eff}} \sin^2 \theta \pm M_s B_{\text{in}} \sin \phi \sin \theta)} d\theta - \pi D \sin \phi \quad (4.55)$$

The analytical resolution of the integral has a complex formulation, but some physical considerations can be made to simplify the problem. The application of a strong in-plane magnetic field can align the magnetisation of all the system along the direction of the magnetic field and destroy the DW. This happens when $M_s B_{\text{in}} = K_{\text{eff}}$. Therefore if $M_s B_{\text{in}} \ll K_{\text{eff}}$ one can assume that the in-plane magnetic field acts on the DW configuration but that the magnetisation direction in the domains is unperturbed. In that case, eq. 4.55 can be expressed as:

$$\mathcal{E}_{\text{DW}} = 2 \int_0^\pi \sqrt{AK_{\text{eff}} \sin^2 \theta \left(1 \pm \frac{M_s B_{\text{in}} \sin \phi}{K_{\text{eff}} \sin \theta} \right)} d\theta - \pi D \sin \phi \quad (4.56)$$

setting $\frac{M_s B_{\text{in}} \sin \phi}{K_{\text{eff}} \sin \theta} \rightarrow 0$ one can write:

$$\mathcal{E}_{\text{DW}} = 2 \int_0^\pi \sqrt{AK_{\text{eff}} \sin^2 \theta} d\theta \pm 2 \int_0^\pi \sqrt{\frac{A}{K_{\text{eff}}}} \frac{M_s B_{\text{in}} \sin \phi}{2} d\theta - \pi D \sin \phi \quad (4.57)$$

Calculating the integrals one obtains:

$$\mathcal{E}_{\text{DW}} = 4\sqrt{AK_{\text{eff}}} \pm \pi \Delta M_s B_{\text{in}} \sin \phi - \pi D \sin \phi \quad (4.58)$$

The DW polarisation can be easily calculated by the minimisation of the energy with respect to the angle ϕ . When the in-plane magnetic field is parallel to the DW polarisation the DW does not change configuration. When it is anti-parallel different solutions can be found:

- if $\Delta/M_s B_{\text{in}} < D$ the DW has the Néel polarisation promoted by the DMI ($\phi = 0$)
- if $\Delta/M_s B_{\text{in}} > D$ the DW has the Néel polarisation promoted by the magnetic field ($\phi = \pi$)

The presence of an in-plane magnetic field can change the width and profile of the DW. They can be calculated writing the Brown eq. 4.36 with the energy terms from eq. 4.54:

$$K_{\text{eff}} \sin^2(\theta) \pm M_s B_{\text{in}} \sin \theta = A \left(\frac{d\theta}{dx} \right)^2 \quad (4.59)$$

The resolution of this differential equation allows to find the DW profile but the calculations are not trivial. Moreover, in micromagnetism the fundamental parameter for studying the DW properties is the DW width (L). This can be easily calculated by the extrapolation of the magnetisation slope in the center of the DW profile ($\theta = \pi/2$), as shown in sec. 4.2.1.

$$\frac{dx}{d\theta} \left(\theta = \frac{\pi}{2} \right) = \sqrt{\frac{A}{K_{\text{eff}} \pm M_s B_{\text{in}}}} \quad \longrightarrow \quad L = \Delta(B_{\text{in}})\pi \quad (4.60)$$

The presence of a magnetic field parallel (anti-parallel) to the DW polarisation stabilizes (destabilizes) the DW configuration and increases (decreases) its width.

4.3 Magnetic domain walls in C_{2v} symmetry systems

In order to give a theoretical understanding of the DW configurations and energy in the experimental system investigated in this work, I will discuss DWs in systems with a reduced in-plane symmetry in this section. I studied systems with two perpendicular symmetry planes, perpendicular to the system surface. I will use a 1D micromagnetic model in a C_{2v} energy environment in order to study the DW polarisation and width as a function of the crystallographic directions.

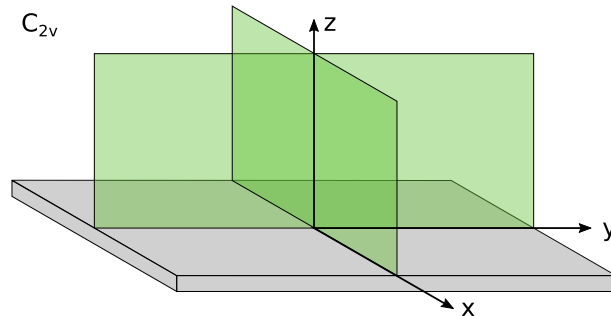


Figure 4.14: Sketch of a system with C_{2v} symmetry, the green planes are mirror symmetry planes.

4.3.1 Role of anisotropic DMI with a C_{2v} symmetry

The model described in this section is developed to study the effect of the anisotropic DMI with a C_{2v} symmetry on the polarisation of a general magnetic rotation. The discussion can then be generalized to DWs. This model was developed together with S. Rohart from LPS (Orsay) [81] [17]. The micromagnetic DMI energy density with a C_{2v} symmetry reads:

$$E_{DM} = - \left((D_{xz}^{(x)})_s L_{xz}^{(x)} + (D_{yz}^{(y)})_s L_{yz}^{(y)} \right) \quad (4.61)$$

This relation is formulated in a frame where the main axes are the high symmetry axes of the system. The importance of the Lifshitz invariant in the determination of the kind of magnetisation rotation has already been discussed in Sec. 4.3.5. Eq. 4.61 shows that the DMI favors, along the main axes, a Néel magnetisation rotation with a chirality that depends on the sign of $(D_{xz}^{(x)})_s$ and $(D_{yz}^{(y)})_s$. It gives no direct information about the magnetisation rotations promoted along the intermediate directions.

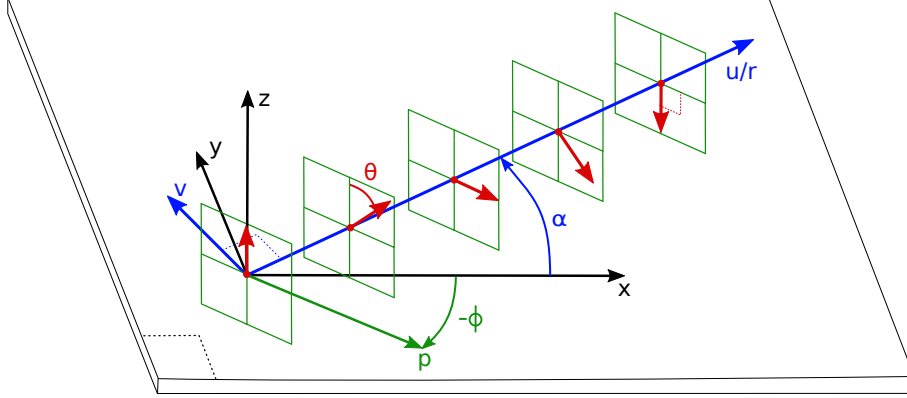


Figure 4.15: Frame used to study the DW profile and polarisation in a system with C_{2v} symmetry

This can be studied considering a new basis $(\hat{u}, \hat{v}, \hat{z})$ (see Fig. 4.15), turned by an angle α with respect to the initial basis (\hat{x}, \hat{y}) . With a change of basis one can obtain the DMI energy of a one-dimensional magnetisation rotation along \hat{u} :

$$E_{DM}(\alpha) = - \int \left[\cos^2(\alpha) D_s^{(x)} + \sin^2(\alpha) D_s^{(y)} \right] L_{uz}^{(u)} d^2r - \int \left(D_s^{(x)} - D_s^{(y)} \right) \cos(\alpha) \sin(\alpha) L_{vz}^{(v)} d^2r. \quad (4.62)$$

This expression presents now both types of Lifshitz invariants. Along a general direction α the DMI promotes an intermediate rotation between the Bloch $L_{uz}^{(v)}$ and Néel $L_{uz}^{(u)}$ configurations. The Bloch rotation is maximized along the $\alpha = \pi/4$ direction when the DMI constants have opposite signs.

In summary, it can be expected that in a general two-fold system the DMI promotes Néel cycloids along the main axes and a mixed configuration between a Néel cycloid and a Bloch spiral along the intermediate directions.

In order to quantifying this effect the DMI energy for a general magnetic modulation is studied. It can be described by $\mathbf{m}(u) = [\sin(k_u u) \hat{u} + \cos(k_u u) \hat{z}]$, lying in the (\hat{u}, \hat{z}) plane. The magnetisation plane is free to rotate changing the polarisation ϕ in order to minimize the energy. Then replacement of the modulation in Eq. 4.62 and the energy minimisation with respect to ϕ allows to write the polarisation angle as a function of the in-plane direction α :

$$\tan \phi = \left(\frac{D_s^{(y)}}{D_s^{(x)}} \right) \tan \alpha \quad (4.63)$$

This result allows to study the modulation polarisation as a function of the angle α and reformulate an expression for the DMI energy density for a 1D modulation along \hat{u} :

$$E_{DMI}(\alpha) = D_s^{\text{eff}}(\alpha) \left(\frac{\partial \theta}{\partial u} \right) \quad (4.64)$$

H

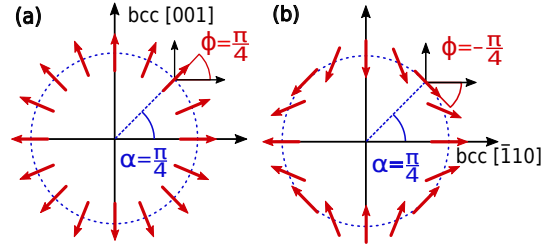


Figure 4.16: Polar plot of the magnetisation direction (ϕ) promoted by DMI as a function of the in-plane direction of variation α (Eq. 4.63) for different $(D_s^{(x)}; D_s^{(y)})$ values: (a) $D_s^{(x)} = D_s^{(y)}$ (b) $D_s^{(x)} = -D_s^{(y)}$

with D_s^{eff} being an effective DMI constant:

$$D_s^{\text{eff}} = D_s^{(x)} \cos \alpha \cos \left[\arctan \left(\frac{D_s^{(y)}}{D_s^{(x)}} \tan \alpha \right) \right] + D_s^{(y)} \sin \alpha \sin \left[\arctan \left(\frac{D_s^{(y)}}{D_s^{(x)}} \tan \alpha \right) \right] \quad (4.65)$$

In order to understand the meaning of this result one can analyze the two different situations illustrated in Fig. 4.16 :

- if $D_s^{(x)} = D_s^{(y)}$ the DMI promotes equi-energetic Néel rotations with the same chirality. The result is the same as the one obtained for isotropic DMI.
- if $D_s^{(x)} = -D_s^{(y)}$ the DMI promotes two Néel rotations with opposite chirality along the main axes and a Bloch rotation with opposite chirality each $\alpha = \pi/4 + n\pi/2$. Even if the magnetisation rotation has a different polarisation along the in-plane directions the DMI gain is isotropic.

Since the DMI gain in a DW does not depend on the DW width the discussion can easily be generalized and the energy of a DW with isotropic exchange, uniaxial anisotropy and anisotropic DMI reads:

$$\mathcal{E}_{DW}(\alpha) = 4\sqrt{AK_{\text{eff}}} - \pi D_s^{\text{eff}}(\alpha) \quad (4.66)$$

D_s^{eff} depends only on the ratio $\frac{D_s^{(y)}}{D_s^{(x)}}$ and in the two analyzed cases, $D_s^{(x)} = D_s^{(y)}$ and $D_s^{(x)} = -D_s^{(y)}$, the DW energy is exactly the same.

4.3.2 Role of the exchange interaction in a system with C_{2v} symmetry

The addition of an anisotropic exchange interaction does not change the polarisation angle ϕ . Even in this case it is possible to write an effective exchange constant that takes into account the change of exchange energy as a function of in-plane angle ϕ . In the main axes frame, the exchange interaction energy density reads:

$$E_{exc} = A_x \left(\frac{\partial \mathbf{m}(\mathbf{r}_i)}{\partial x} \right)^2 + A_y \left(\frac{\partial \mathbf{m}(\mathbf{r}_i)}{\partial y} \right)^2 \quad (4.67)$$

changing from the (\hat{x}, \hat{y}) to the (\hat{u}, \hat{v}) frame and considering the magnetisation rotating along \hat{u} , the previous equation can be written as a function of the angle α :

$$E_{exc}(\alpha) = A_{\text{eff}}(\alpha) \left(\frac{d\theta}{du} \right)^2 \quad A_{\text{eff}}(\alpha) = A_x \cos^2 \alpha + A_y \sin^2 \alpha \quad (4.68)$$

and the energy of a DW in a system with anisotropic exchange and a perpendicular uniaxial anisotropy reads:

$$\mathcal{E}_{DW}(\alpha) = 4\sqrt{A_{\text{eff}}(\alpha)K_{\text{eff}}} \quad (4.69)$$

4.3.3 Role of the biaxial anisotropy

Since the MCA is directly connected to the crystal symmetry, in a C_{2v} symmetry system the magnetic anisotropy is biaxial (Sec. 2.5). This phenomenon can strongly change the DW polarisation as a function of the in-plane direction α . Taking into account the exchange interaction and a biaxial magneto-crystalline anisotropy with a local approximation for the surface magnetic charges, the energy density reads:

$$E(\theta(u), \phi(\alpha)) = A_{\text{eff}}(\alpha) \left(\frac{d\theta}{du} \right)^2 + (K_{\text{out}} - K_{\text{d}}) \sin^2 \theta - K_{\text{in}} \sin^2 \theta \cos^2 \phi \quad (4.70)$$

The solution of the 1D modulation can be obtained placing the biaxial anisotropy in the Euler equation (eq. 4.39). Since the in-plane component of the biaxial anisotropy has the same dependence on θ than the out-of-plane one, the complexity of the calculation can be reduced by integrating the dependence on ϕ in a new effective constant $K_{\text{eff}}^{(\text{in})}(\phi) = (K_{\text{out}} - K_{\text{d}}) - K_{\text{in}} \cos^2 \phi$.

The new energy density reads:

$$E(\theta(u), \phi(\alpha)) = A_{\text{eff}}(\alpha) \left(\frac{d\theta}{du} \right)^2 - K_{\text{eff}}^{(\text{in})}(\phi) \sin^2 \theta \quad (4.71)$$

One can notice that the last equation has exactly the same dependence on θ than the problem solved in Sec. 4.2.1. Then the DW energy can be written as :

$$\mathcal{E}_{DW}(\alpha) = 4\sqrt{A_{\text{eff}}(\alpha)K_{\text{eff}}^{(\text{in})}(\phi)} \quad (4.72)$$

Since the exchange interaction does not depend on the polarisation angle, the angle ϕ as a function of the in-plane direction α can be studied by minimizing the in-plane term of the biaxial anisotropy:

$$\frac{\partial E_{\text{ani}}}{\partial \phi} = 0 \quad \implies \quad \phi = 0 + n\pi \quad (4.73)$$

The biaxial anisotropy promotes a Néel DW along the in-plane easy axis with degenerate chirality, a Bloch DW along the hard axis and a mixed configuration along the intermediate directions (Fig. 4.17).

4.3.4 Competition between in-plane anisotropy and volume dipolar interactions

In this part the study of the DW energy and polarisation will be performed in a system with anisotropic exchange, biaxial anisotropy and volume dipolar interactions. This model was developed together with S. Rohart from LPS (Orsay). The DW energy can be written as (Sec. 4.2.2):

$$\mathcal{E}_{DW}(\alpha, \phi) = 4\sqrt{A_{\text{eff}}(\alpha)K_{\text{eff}}^{\text{in}}(\phi)} + 2\Delta N_{\text{d}}K_{\text{d}} \sin^2 \phi \quad (4.74)$$

The biaxial anisotropy and the volume dipolar interaction favor different polarisation angles. The first promotes a magnetisation along the in-plane easy axis (Sec. 4.3.2) whereas the second favors Bloch magnetisation rotations (Sec. 4.2.2).

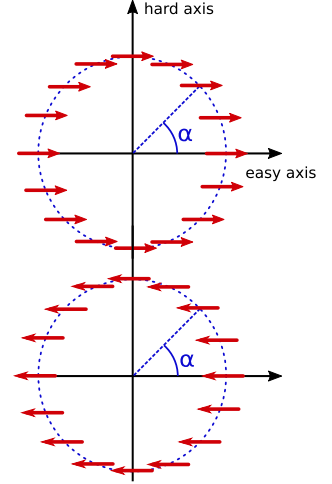


Figure 4.17: Polar plot of the polarisation angles promoted by a biaxial anisotropy

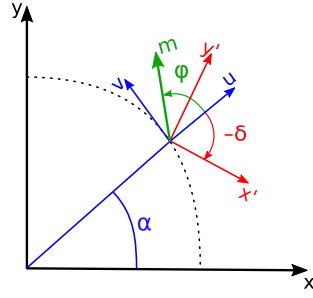


Figure 4.18: Frameworks used for the calculation of the polarisation angle φ . The new framework (x', y') corresponds to the coordinate system where the anisotropy matrix (eq. 4.76) takes a diagonal form

For solving this problem, one can write the modulation energy density in the (u, v) frame fixed on the DW. In order to facilitate the calculation in this section a new frame is considered (Fig. 4.18). The angle φ describes the magnetisation direction with respect to the direction \hat{u} ($\varphi = \phi - \alpha$) and the anisotropic energy density reads:

$$E = -K_{\text{in}} \cos^2(\alpha + \varphi) - NK_{\text{d}} \sin^2(\varphi) \quad (4.75)$$

Eq. 4.75 can be written in matrix form. It takes the name of anisotropy matrix and it reads:

$$\begin{aligned} E &= (\cos \varphi \quad \sin \varphi) \begin{pmatrix} \cos^2 \alpha & -\sin \alpha \cos \alpha \\ -\sin \alpha \cos \alpha & \sin^2 \alpha + k \end{pmatrix} \begin{pmatrix} \cos \varphi \\ \sin \varphi \end{pmatrix} \\ &= (m_x \quad m_y) \begin{pmatrix} \cos^2 \alpha & -\sin \alpha \cos \alpha \\ -\sin \alpha \cos \alpha & \sin^2 \alpha + k \end{pmatrix} \begin{pmatrix} m_x \\ m_y \end{pmatrix} \end{aligned} \quad (4.76)$$

where $(\cos \varphi, \sin \varphi)$ are the magnetisation components in the plane with respect to the direction \hat{u} and $k = \frac{NK_{\text{d}}}{K_{\text{in}}}$ is the dipolar anisotropy constant normalized with the in-plane magneto-crystalline constant. Finding the polarisation angle φ corresponds to finding a new coordinate system (x', y') where the matrix can be written in a diagonal form. The matrix is symmetric and can be diagonalized calculating the eigenvalues:

$$\begin{aligned} \lambda_{1,2} &= \frac{(k+1)}{2} \pm \sqrt{\frac{(k+1)^2}{4} - k \cos^2(\alpha)} \\ &= \frac{1}{2} \left[(k+1) \pm \sqrt{(1-k)^2 + 4k \sin^2(\alpha)} \right] \end{aligned} \quad (4.77)$$

The new frame has the normalized eigenvectors as bases:

$$(x', y') = \left(\frac{v_1}{\|v_1\|}, \frac{v_2}{\|v_2\|} \right) \quad (4.78)$$

$$v_1 = \left\{ \frac{1}{2} \left[\frac{k-1}{\sin \alpha \cos \alpha} + \frac{\sqrt{k^2 + 1 - 2k \cos(2\alpha)}}{\sin \alpha \cos \alpha} + 2 \frac{\sin \alpha}{\cos \alpha} \right]; 1 \right\} \quad (4.79)$$

$$v_2 = \left\{ \frac{1}{2} \left[\frac{k-1}{\sin \alpha \cos \alpha} - \frac{\sqrt{k^2 + 1 - 2k \cos(2\alpha)}}{\sin \alpha \cos \alpha} + 2 \frac{\sin \alpha}{\cos \alpha} \right]; 1 \right\} \quad (4.80)$$

In the base $(x'; y')$ (Fig. 4.18) the anisotropy energy takes an easy expression :

$$E = -K_0 (\mathbf{m} \cdot \mathbf{x}')^2 = -K_0 \sin^2(\varphi - \delta) \quad (4.81)$$

where $K_0 = K_{\text{in}} \sqrt{(1-k)^2 + 4k \sin^2 \alpha}$ and δ is the angle between \hat{u} and \hat{x}' :

$$\tan \delta = \frac{v_1^{y'}}{v_1^{x'}} = \frac{1}{\frac{1}{2} \left[\frac{k-1}{\sin \alpha \cos \alpha} + \frac{\sqrt{k^2+1-2k \cos(2\alpha)}}{\sin \alpha \cos \alpha} + 2 \frac{\sin \alpha}{\cos \alpha} \right]} \quad (4.82)$$

The expression takes an easy form if the nominator and the denominator are multiplied by $\sin(2\alpha)$. Using the trigonometric relation $\sin(2\alpha) = 2 \sin \alpha \cos \alpha$, the angle δ as a function of the in-plane angle α reads:

$$\delta = \arctan \left[\frac{\sin 2\alpha}{2 \sin^2 \alpha - 1 + k - K_0/K_{\text{in}}} \right] \quad (4.83)$$

The DW polarisation minimizes the DW energy when the magnetisation is aligned along the direction \hat{x}' and the calculation of the angle δ allows to understand the DW configuration. In order to compare this result with the one obtained in the other sections, where the polarisation angle ϕ was defined with respect to the \hat{x} direction, it is sufficient to replace the angle δ with $\phi - \alpha$.

Some physical considerations allow to simplify eq. 4.83. Considering general values of the magnetic parameters for thin films ($K_{\text{in}} = 0.3 \cdot 10^6 \text{ J/m}^3$, $M_s = 1.2 \cdot 10^6 \text{ A/m}$, $t = 1 \text{ nm}$, $\Delta = 30 \text{ nm}$), the value of $k = 0.022$. The effect of volume dipolar interactions can be considered as a second order perturbation with respect to the in-plane anisotropy. The model can thus be simplified considering the limit $k \rightarrow 0$. Hence the total effective anisotropy K_0 takes the form:

$$K_0 = K_{\text{in}} \sqrt{(1-k)^2 + 4k \sin^2 \alpha} = K_{\text{in}} \sqrt{1 - 2k + k^2 + 4k \sin^2 \alpha} \quad [k \rightarrow 0] \quad K_0 = K_{\text{in}} - K_{\text{d}}(1 - 2 \sin^2 \alpha) \quad (4.84)$$

where the quadratic term k^2 is neglected and the square root is expanded in a Taylor series until the first order. Placing eq. 4.84 in eq. 4.83, the expression of the angle δ can be simplified :

$$\delta = \arctan \left[\frac{\sin 2\alpha}{2 \sin^2 \alpha - 1 + k - K_0/K_{\text{in}}} \right] = \arctan \left[\frac{\sin 2\alpha}{2 \cos^2 \alpha (k-1)} \right] = \arctan \left(-\frac{\tan \alpha}{1-k} \right) \quad (4.85)$$

where the trigonometric relation $\sin 2\alpha = 2 \sin \alpha \cos \alpha$ has been used. Moreover, one can use the Taylor expansion of the first order of $1/(1-k) \simeq 1+k$ in the limit $k \rightarrow 0$:

$$\arctan(-\tan \alpha - k \tan \alpha) = \arctan(-\tan \alpha) - \frac{\tan \alpha}{1 + \tan^2 \alpha} k = -\alpha - \frac{1}{2} k \sin(2\alpha) \quad (4.86)$$

where the relation $[\arctan(-\tan \alpha - k \tan \alpha)]$ is expanded around $[-\tan \alpha]$ and the trigonometry identities $\left[\frac{\tan \alpha}{1 + \tan^2 \alpha} = 2 \sin \alpha \cos \alpha = 2 \sin(2\alpha) \right]$ are used. In the limit $k \rightarrow 0$, eq 4.86 takes the form $\delta = -\alpha$ and $\phi = 0$, i.e. the magnetisation is parallel to the easy axis for all values of α .

4.3.5 Competition between anisotropic DMI and biaxial anisotropy

In this part the effect of the competition between anisotropic DMI and in-plane anisotropy on the DW energy and polarisation is studied. The DMI promotes a DW magnetisation strongly depended on the ratio between the DMI parameters (D^x/D^y) (Sec. 4.3.1) whereas the in-plane anisotropy favors a magnetisation along the easy axis. The energy density for a DW along the direction α reads:

$$E(\alpha, \phi) = A_{\text{eff}}(\alpha) \left(\frac{d\theta}{du} \right)^2 + K_{\text{eff}}^{\text{in}}(\phi) \sin^2 \theta - D^{\text{eff}}(\phi, \alpha) \frac{d\theta}{du} \quad (4.87)$$

with $D^{\text{eff}}(\alpha, \phi) = (D^x \cos^2 \alpha + D^y \sin^2 \alpha) \cos(\phi - \alpha) + (D^x - D^y) \cos \alpha \sin \alpha \sin(\phi - \alpha)$ and $K_{\text{eff}}^{\text{in}} = (K_{\text{out}} - K_{\text{d}}) - K_{\text{in}} \cos^2 \phi$. Minimizing the energy through the Euler-Lagrange equations, the DW energy can be written as :

$$\mathcal{E}(\alpha, \phi) = E_0 + E_{\text{DMI}} = 4 \sqrt{A_{\text{eff}}(\alpha) K_{\text{eff}}^{\text{in}}(\phi, \alpha)} - \pi D^{\text{eff}}(\phi, \alpha) \quad (4.88)$$

The lowest-energy magnetic configuration can be found minimizing this energy with respect to ϕ :

$$\frac{\partial \mathcal{E}(\alpha, \phi)}{\partial \phi} = \frac{4A_{\text{eff}}(\alpha)K_{\text{in}}(\phi)}{\sqrt{A_{\text{eff}}K_{\text{eff}}^{\text{in}}}} \cos \phi \sin \phi - \pi \left[- (D^x \cos^2 \alpha + D^y \sin^2 \alpha) \sin(\phi - \alpha) + (D^x - D^y) \cos \alpha \sin \alpha \cos(\phi - \alpha) \right] = 0 \implies \phi(\alpha); \quad \mathcal{E}_{DW}(\alpha) \quad (4.89)$$

The solution of this equation allows to study the polarisation angle $\phi(\alpha)$ and the DW energy $\mathcal{E}_{DW}(\alpha)$ as a function of the in-plane direction. However, this equation does not have a general analytical solution and there is no physical hypothesis that allows to simplify the calculation.

Fig. 4.19 shows the numerical solution of eq. 4.89 for four different combinations of magnetic parameters. The anisotropy is kept constant and the anisotropic DMI is changed. The values of the anisotropy constants ($K_{\text{in}} = 0.3 \cdot 10^6 \text{J/m}^3$, $K_{\text{out}} - K_{\text{d}} = 0.5 \cdot 10^6 \text{J/m}^3$) are chosen in order to respect the physics of biaxial anisotropy in ultrathin films and four different combinations of DMI constants are considered:

- (a) $D^y = 1 \text{ mJ/m}^2$ and $D^x = 2 \text{ mJ/m}^2$

- (b) $D^y = 2 \text{ mJ/m}^2$ and $D^x = 1 \text{ mJ/m}^2$

- (c) $D^y = 2 \text{ mJ/m}^2$ and $D^x = -1 \text{ mJ/m}^2$

- (d) $D^y = 1 \text{ mJ/m}^2$ and $D^x = -2 \text{ mJ/m}^2$

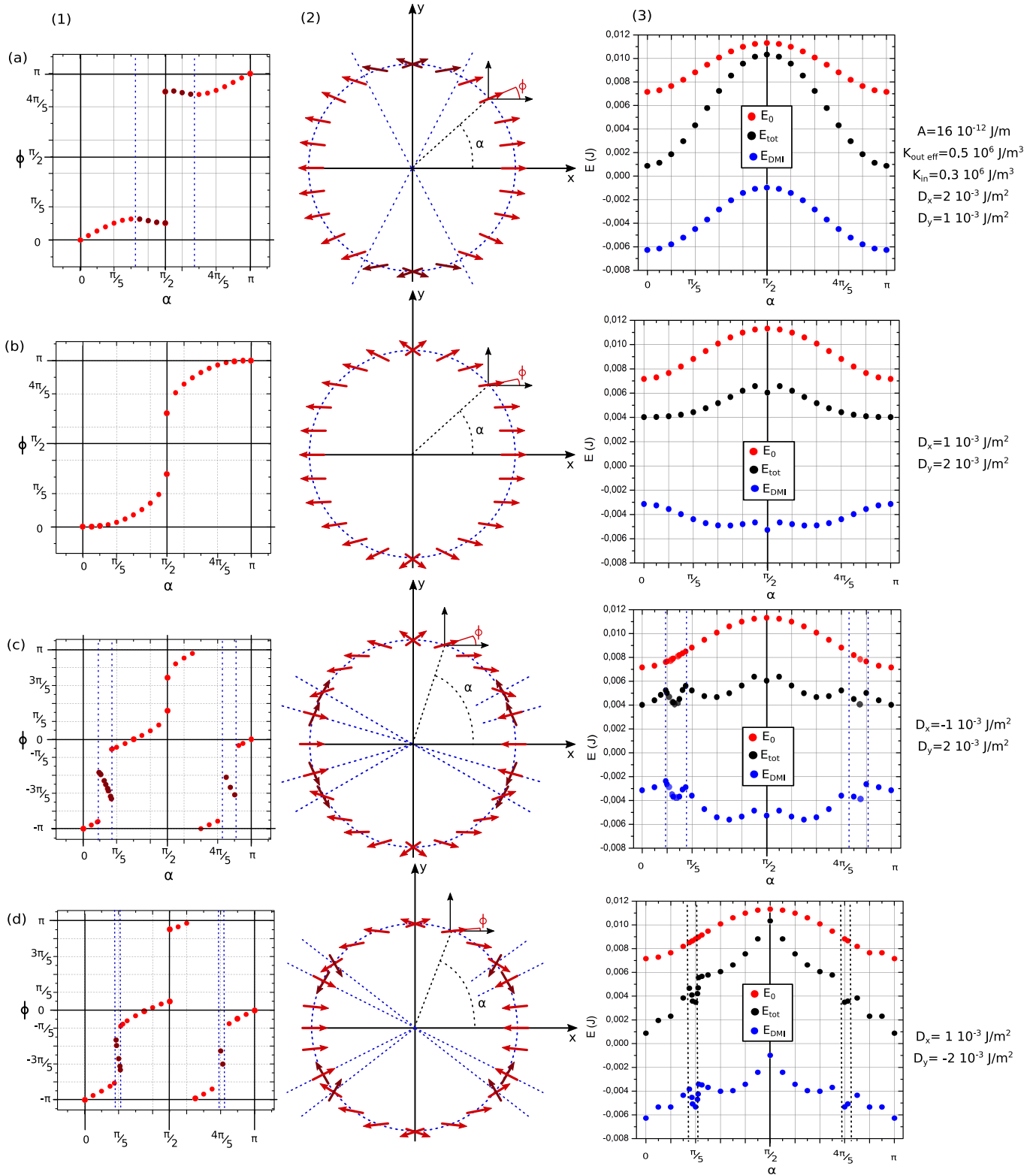


Figure 4.19: (1) Polarisation angle ϕ as a function of the angle α ; (2) Polar plot of graph (1) and (3) DW energy (black) and the components E_0 (red) and E_{DMI} (blue) as a function of the in-plane angle α . The points are the numerical solutions of eq. 4.89. Arrows of different colors are used for positive (light red) and negative (dark red) slopes of the $\phi(\alpha)$ function. The solutions are shown for four different physical combinations of D^y and D^x : $K_{\text{in}} = 0.3 \cdot 10^6 \text{ J/m}^3$, $K_{\text{out}} - K_{\text{d}} = 0.5 \cdot 10^6 \text{ J/m}^3$, (a) $D^y = 1 \text{ mJ/m}^2$ and $D^x = 2 \text{ mJ/m}^2$; (b) $D^y = 2 \text{ mJ/m}^2$ and $D^x = 1 \text{ mJ/m}^2$; (c) $D^y = 2 \text{ mJ/m}^2$ and $D^x = -1 \text{ mJ/m}^2$; (d) $D^y = 1 \text{ mJ/m}^2$ and $D^x = -2 \text{ mJ/m}^2$.

In Fig. 4.19 three different kinds of plots are shown. The first one on the left shows the behavior of the polarisation angle as a function of the in-plane direction. In the cases (c) and (d), points of two different

colors are shown. The lighter indicates a positive slope of the function $\phi(\alpha)$ and the darker a negative one. In the center the same function is shown in a polar plot. The last one shows the behavior of the total DW energy, the DMI component E_{DMI} and E_0 as a function of α . The study is performed for different values and symmetries of the DMI energy in order to extract general informations of the polarisation behavior in systems with a C_{2v} symmetry.

Along the easy axis ($\alpha = 0$), the DMI and the anisotropy stabilize a Néel DW with a chirality depending on the sign of D^x . In the cases (a) and (d), $|D^x| > |D^y|$, and the DW along this direction has the lower energy. Along the hard axis ($\alpha = \pi/2$) the DMI and the in-plane anisotropy are minimized for different magnetic polarisations. The resulting DW is between a Néel and a Bloch DW and has two equi-energetic configurations with complementary polarisation angles ($\phi = \phi_0$; $\phi = \pi - \phi_0$). This angle is $\phi_0 = 57^\circ$ for $D^y = 2 \text{ mJ/m}^2$ and $\phi_0 = 18^\circ$ for $D^y = 1 \text{ mJ/m}^2$.

Along the intermediate directions the polarisation and thus the energy behave in different ways. This behavior can be described considering two different parameters: the angle between the easy axis and the polarisation stabilized by the DMI, $\Delta\phi$, and the energy ratio $E_D/E_K = D_{\text{eff}}(\alpha)/\Delta K_{\text{in}}$, with Δ the DW width. For high values of E_D/E_K the polarisation is closer to the DMI stabilized configuration whereas for lower values it is closer to the easy axis direction.

The DW energy behavior depends on $\Delta\phi$ and $D_{\text{eff}}(\alpha)$, for high values of $\Delta\phi$ the energy competition is stronger, since the polarisation solution is far from the configurations stabilized by the single energies, and the DW energy will increase.

In case (a) the parameter E_D/E_K decreases when α increases, whereas $\Delta\phi$ increases. Then the polarisation as a function of α is a continuous function and, scanning along the α angles, it firstly deviates from the easy axis driven by the increase of $\Delta\phi$, up to the point where the decrease of E_D/E_K dominates and the polarisation behavior changes slope. All the energies increase from the easy to the hard axis since along the easy axis the system has the smallest $\Delta\phi$ and $D_{\text{eff}}(\alpha)$ is the highest.

In case (b) the parameters $\Delta\phi$ and E_D/E_K increase when α increases. The polarisation behavior is monotone, continuous and reaches a higher deviation from the easy axis with respect to case (a). The resulting energy is less anisotropic than in case (a) due to the fact that $\Delta\phi$ is smaller along the easy axis and when it increases it is balanced by the increase of $D_{\text{eff}}(\alpha)$.

The two parameters change in case (c) like in case (b), and in case (d) like in case (a), but in these cases the polarisation presents a discontinuous behavior with an inversion of the $\phi(\alpha)$ slope. In these particular cases eq. 4.89 presents different solutions that can become the energy minimum when α is varying. Then different values of α can be found where two solutions have the same energy and the polarisation switches between the two minima.

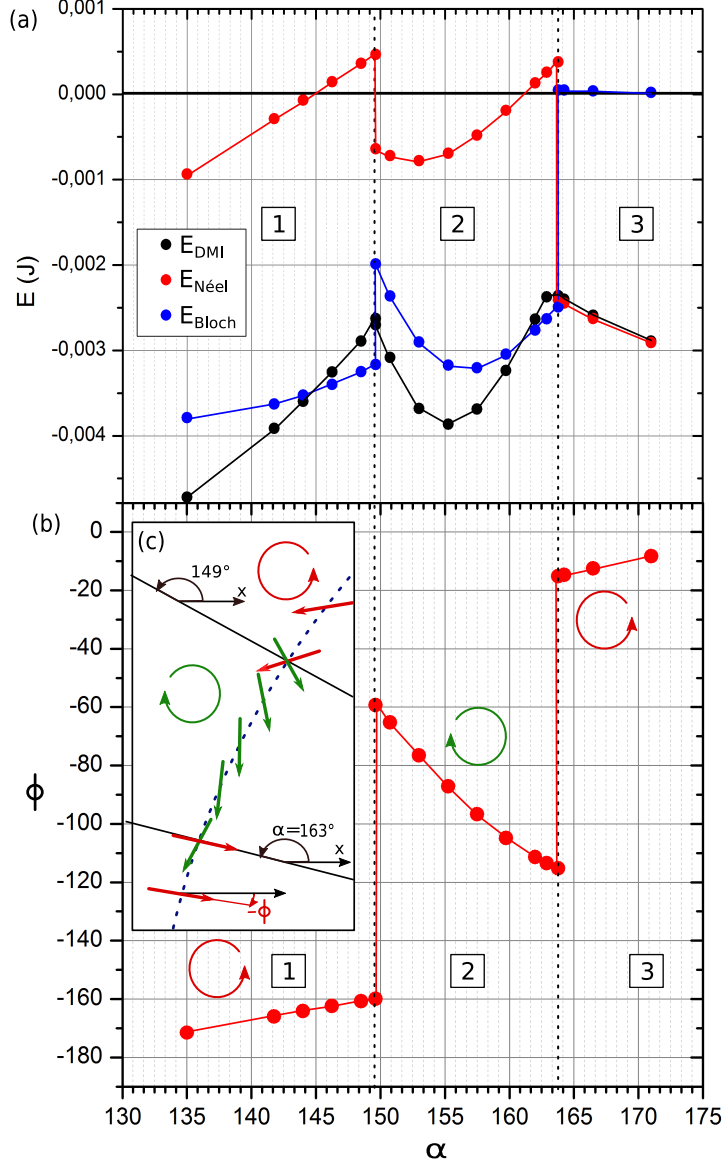


Figure 4.20: Solutions of eq. 4.89 with $K_{\text{in}} = 0.3 \cdot 10^6 \text{J/m}^3$, $K_{\text{out}} - K_{\text{d}} = 0.5 \cdot 10^6 \text{J/m}^3$, $D^y = 1 \text{ mJ/m}^2$ and $D^x = -2 \text{ mJ/m}^2$ (a) Plot of the DMI energy (black) and the two components promoting a Bloch (blue) and a Néel (red) DW. (b) The angle ϕ as a function of α in the area where the slope inversion occurs. (c) Polar plot of the function in (b). The magnetisation vectors are colored green if ϕ rotates clockwise with alpha and red if it rotates anti-clockwise.

In order to understand this phenomenon one should refer to Fig. 4.20 where the DMI energy and the two components $E_{\text{Néel}}$ (red) and E_{Bloch} (blue) are plotted as a function of α , using the magnetic parameters of case (d).

$$E_{\text{Néel}} = -\pi(D^x \cos^2 \alpha + D^y \sin^2 \alpha) \cos(\phi - \alpha) \quad E_{\text{Bloch}} = -\pi(D^x - D^y) \cos \alpha \sin \alpha \sin(\phi - \alpha). \quad (4.90)$$

One can find the plot of the polarisation as a function of α in the region where the polarisation switches occur. Rotating with increasing α one can find three different polarisation domains with different $\phi(\alpha)$ slopes:

- (1) The polarisation is stabilized mainly by the Bloch component of the DMI and the polarisation rotates in a clockwise direction. The first switch of minimum occurs when the DMI Néel component becomes positive; i.e. when the DW acquires a chirality different from the one imposed by the DMI, as shown in Fig. 4.20. Then at $\alpha = 149^\circ$ the magnetisation jumps into a new equi-energetic polarisation $\Delta\phi = 100^\circ$ in order to reduce the DMI Néel component.

- (2) The polarisation in the new configuration has a lower Néel but a higher Bloch energy component and rotates clockwise when α increases again. During this rotation the DMI energy is first reduced and then it increases. The second switch occurs at $\alpha = 163^\circ$ where the Néel component becomes positive again.
- (3) The new configuration is strongly stabilized by the DMI Néel component, the Bloch one is close to zero and the polarisation slope becomes positive (anti-clockwise).

Given the complex behavior of the energies as a function of α it is not possible to give a more accurate phenomenological interpretation of the polarisation behavior in systems with inversion of DMI sign, $D^x/D^y < 0$.

4.3.6 Role of an in-plane magnetic field along the easy axis of a system with C_{2v} symmetry

In this part the effects of the application of an in-plane magnetic field along the easy axis of a system with C_{2v} symmetry is studied. As shown in the previous section, along this direction the in-plane anisotropy and the DMI stabilize a Néel DW. The magnetic field is applied in the direction opposite to the direction of the DW polarisation. Therefore the Zeeman energy, formulated like in eq. 4.55, and the in-plane anisotropy, formulated like in eq. 4.70, are taken into account. The in-plane magnetic field promotes a Néel DW with a polarisation opposite to the one promoted by the DMI. The DW energy in the limit of weak in-plane magnetic field ($M_s B_{in} \ll K_{eff}$) reads:

$$\mathcal{E}_{DW} = 4\sqrt{A(K_{out}^{eff} - K_{in} \cos^2 \phi)} + \pi \left(\sqrt{\frac{A}{K_{out}^{eff} - K_{in} \cos^2 \phi}} B_{in} M_s - D \right) \cos \phi \quad (4.91)$$

The energy minimisation with respect to the angle ϕ allows to study the DW polarisation as a function of the strength of the magnetic field. The problem presents two trivial solutions ($\phi = (0, \pi)$), already obtained in the case without in-plane anisotropy in Sec. 4.2.4. The presence of an in-plane anisotropy introduces other solutions without an analytical expression. The discussion will thus be developed with the support of the numerical plot of eq. 4.91 as a function of B_{in} (Fig. 4.21). The values of the magnetic parameters, used for the numerical calculations, are chosen in order to respect the physics of the experimental ultrathin film with DMI and in-plane anisotropy [17].

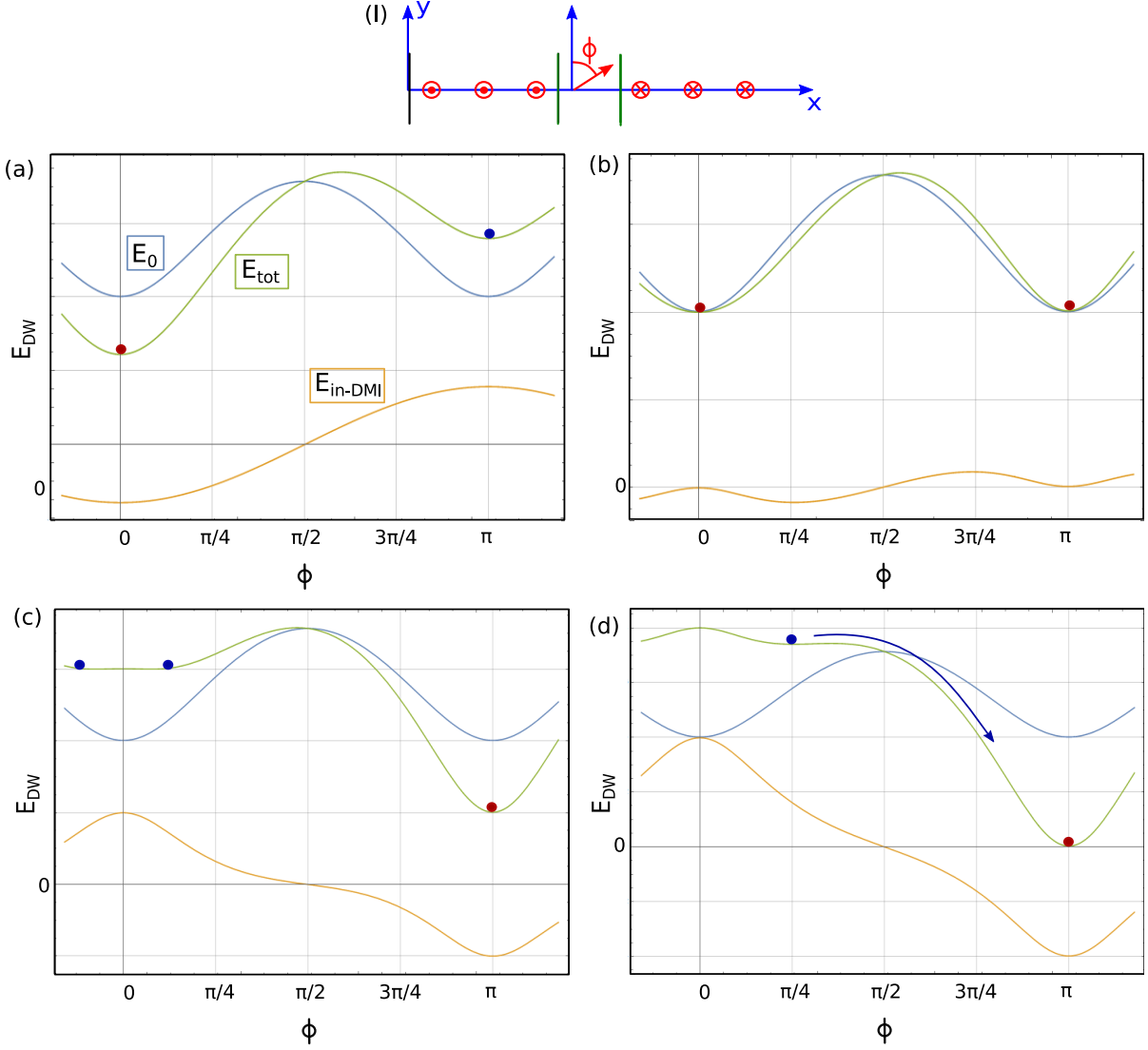


Figure 4.21: (I) frame used to describe the DW energy . (a-b-c-d) Plot of DW energies in eq. 4.91 as a function of the polarisation angle ϕ for three different values of an in-plane magnetic field applied along the direction $\phi = \pi$. (orange) Sum of the DMI and Zeeman DW energy terms, (blue) DW energy without the DMI and Zeeman DW energy terms and (green) total DW energy.

In Fig. 4.21 three energies are plotted as a function of ϕ : (orange) sum of the DMI and Zeeman energy terms (E_{in-DMI}) , (blue) DW energy without Zeeman and DMI terms (E_0) and (green) the total DW energy (E_{DW}). The dots indicate the positions of energy minima: (blue) local minimum and (red) absolute minimum.

Six different situations can be found:

- (a) When $B_{in} = 0$, the term E_{in-DMI} is negative for $\phi < \pi/2$, the solution $\phi = 0$ is the absolute energy minimum and the DW polarisation is determined by the DMI chirality.
- (a)-(b) When B_{in} increases, the solution $\phi = 0$ is the absolute energy minimum up to the values of $B_{in} = \frac{D}{M_s} \sqrt{\frac{K_{out}^{eff} - K_{in}}{A}}$ for which the minima $\phi = 0$ and $\phi = \pi$ have the same energy.
- (b)-(c) Increasing B_{in} , the solution $\phi = \pi$ becomes the absolute minimum, but the magnetisation can not switch due to the presence of an energy barrier generated by the presence of the in-plane anisotropy. The magnetisation, in order for the DW polarisation to switch, has to pass through the hard in-plane axis.
- (c) When $|E_{in-DMI}(\phi = \pi)| = |E_0(\phi = \pi)|$, the energy well of the $\phi = 0$ solution becomes flat as a function of ϕ and the system presents degenerate local minima solutions.

- (c)-(d) When B_{in} increases, $\phi = 0$ becomes a local energy maximum. A new local minimum appears between $\phi = 0$ and $\phi = \pi/2$ and it approaches $\phi = \pi/2$ when $B_{\text{in}}(\phi = 0)$ increases.
- (d) When $E_{\text{in-DMI}}(\phi = 0) = E_0(\phi = 0)$, the energy barrier disappears and the DW polarisation can rotate in the configuration stabilized by the in-plane magnetic field $\phi = \pi$. In this condition the energy of the absolute minimum becomes zero.

4.3.7 Review of magnetic domain walls in a C_{2v} symmetry system

The study of the DW energy and polarisation in systems with C_{2v} symmetry is complex and required the analysis of each magnetic interaction.

The effect of the DMI can be studied by two parameters which describe the strength of the interaction along the main axes, $D_s^{(x)}$ and $D_s^{(y)}$:

- If $D_s^{(x)}/D_s^{(y)} > 0$ the DMI promotes Néel DWs with the same chirality along the main axes and mixed Bloch and Néel DWs along the intermediate directions.
- If $D_s^{(x)}/D_s^{(y)} < 0$ the DMI promotes Néel DWs with opposite chirality along the main axes and mixed Bloch and Néel DWs along the intermediate directions. There is always a direction along which the DMI promotes a pure Bloch DW.

In systems with C_{2v} symmetry the magnetic anisotropy has an in-plane easy axis which promotes a DW polarisation along this direction. The exchange interaction is anisotropic and changes the DW energy and width without changing the DW polarisation. Under the studied conditions the volume dipolar interaction is negligible with respect to the in-plane anisotropy.

The competition between these interactions stabilizes DWs with highly anisotropic energy and polarisation. Along the in-plane easy axis the anisotropy and the DMI stabilize a Néel DW with the polarisation set by the DMI chirality. Along the hard axis the interactions are in competition and two degenerate DW polarisations can be found. Along the intermediate directions, if $D_s^{(x)}/D_s^{(y)} > 0$ the DW polarisation changes smoothly, and if $D_s^{(x)}/D_s^{(y)} < 0$ it changes with abrupt polarisation jumps.

The discussion in this chapter analysed only static configurations. The DWs configurations and energies can become even more complex when the DWs propagate. This will be analysed in the experimental section 5.5.

4.4 2D topological solitons : skyrmions and anti-skyrmions

In this section two micromagnetic models are developed in order to study the stability and the configuration of 2D topological solitons. Given the complexity of the magnetic interactions in systems with C_{2v} symmetry, the discussion is limited to two particular cases:

- A system with isotropic interactions
- A system with isotropic exchange interaction, magnetocrystalline anisotropy and DMI strength with inversion of chirality between perpendicular directions ($D_x = -D_y$).

Skyrmions (SK), are topological solitons which present particle-like properties: they have integer topological charges, interact via attractive and repulsive forces, and can condense into ordered phases. In ferromagnets, skyrmions were originally called two-dimensional (2D) topological solitons and their existence has been predicted in isotropic ferromagnets [82], uniaxial ferromagnets [83, 2, 84] and non-centrosymmetric magnets [33, 2]. Some early indirect experimental evidences of their existence have been obtained in quasi-2D antiferromagnets [85, 86, 87]. More recently indirect [3] and direct observations of skyrmions have been reported in chiral magnets [88] and in ultrathin layers of conventional transition-metal-based ferromagnets in contact with heavy metals [89, 4].

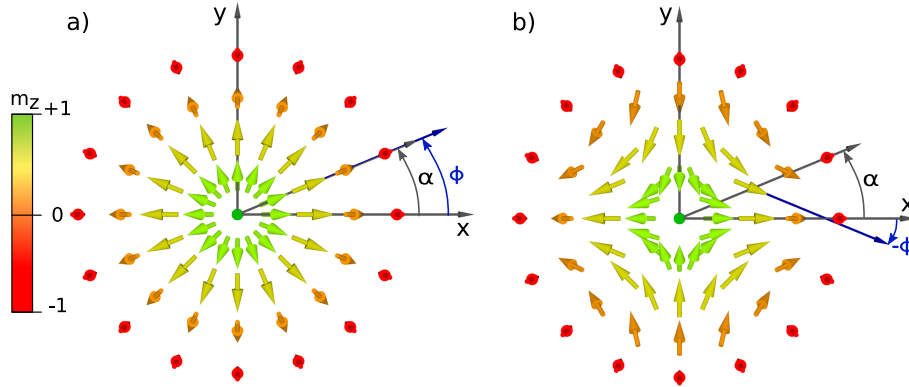


Figure 4.22: Sketch of the skyrmion and anti-skyrmion configurations. The illustration of α , the space angle in the plane, and ϕ , the in-plane magnetisation angle, show the difference between a skyrmion ($\phi(\alpha) = \alpha$) and an anti-skyrmion ($\phi(\alpha) = -\alpha$).

Anti-skyrmions (ASK) are the skyrmion antiquasi-particles. In the same ferromagnetic background they have opposite topological number (Sec. 4.1.2). The ASK have been theorized in bulk magnetic material with a D_{2d} and S_4 symmetry [33]. More recently an ASK lattice has been observed in a crystal with D_{2d} symmetry [16], but not yet in thin film systems. The reason is that most thin film systems showing DMI studied until now were polycrystalline, leading to the same sign and strength of the DMI in any in-plane direction. In order to stabilize ASK in thin films with perpendicular magnetisation, the sign of DMI has to be opposite along two in-plane directions of the film. This may occur in epitaxial thin films with a C_{2v} symmetry [17, 11, 18].

In the next section two different micromagnetic methods that have been developed during this Ph.D work will be presented. The first one has been used to study a SK phase diagram as a function of DMI strength and applied magnetic field in an infinite two-dimensional system. The second one studies the energy difference between a SK and an ASK.

4.4.1 Micromagnetics of skyrmions

In this section a micromagnetic model to study isotropic 2D solitons in thin films is presented. This allows to characterize the size, the configuration and the stability of skyrmions and understand the role of the different magnetic energies in the stabilisation of their local magnetic texture. The presented model is the results

of a collaboration with Anne Bernard-Mantel, Alexis Wartelle, Nicolas Rougemaille, Michael Darques and Laurent Ranno [90].

Since the minimisation of the skyrmion total energy is numerically expensive and without analytical solution, in the present work we set several approximations in order to derive an analytical expression of the skyrmion profile and energy that well respect the physics of the problem. The validity of this method has been confirmed by numerical calculations. This approach allows us to obtain different skyrmionic solutions, study their stability and the conditions of the transformation of one into the other.

The model is developed in order to describe 2D topological spin textures in an infinite ferromagnetic thin film. We consider a ferromagnetic thin film with an easy axis perpendicular to the plane. The system is fully described by the system thickness t , the spontaneous magnetisation M_s , the exchange constant $A_{\text{ex.}}$, the volume magnetocrystalline anisotropy K_u and the DMI constant D . In an isotropic system the soliton has a cylindrical symmetry and the cylindrical coordinates can be used to reduce the complexity of the calculations (Fig. 4.23.a).

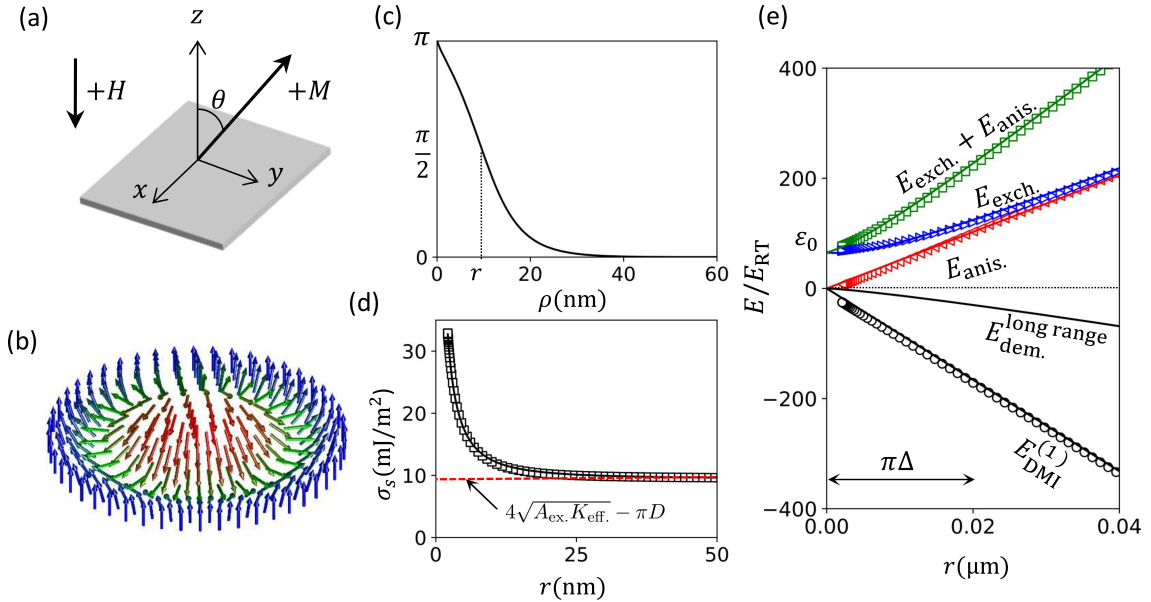


Figure 4.23: **(a)** Schematic view of the ferromagnetic thin film with axis orientations. The magnetisation and magnetic field positive directions (opposite) are indicated. **(b)** Topological soliton $\theta(\rho)$ profile obtained by minimisation of eq. (4.93), as a function of ρ using the parameters $M_s = 1$ MA/m, $K_u = 1.6$ MJ/m, $A_{\text{ex.}} = 10$ pJ/m, $t = 0.5$ nm and $D^{(1)} = 2.8$ mJ/m². **(c)** Topological soliton spin rotation energy density σ_s , defined in section 4.4.1, as function of radius, calculated from eq. (4.93) (black squares) and eq. (4.99) (black line). The DW energy density σ_w is indicated by a dashed line. **(d)** Energies versus soliton radius calculated from eq. (4.93) (symbols) and eq. (4.99) (lines) with the parameters given in (b) and normalized by the RT thermal energy $E_{\text{RT}} = k_B T_{293\text{K}}$. The normalized zero radius energy is indicated as $\varepsilon_0 = E_0/E_{\text{RT}} \sim 31$.

Moreover, we restrict the study to systems where the D values are sufficiently high to stabilize a Néel magnetisation rotation (Sec. 4.2.3). In these conditions, the problem is reduced to the study of the magnetisation angle θ as a function of r .

A magnetic field $\mu_0 H$ may be applied with its positive direction antiparallel to the magnetisation in the soliton center (Fig. 4.23.a).

The soliton energy $E_s[\theta(\rho)]$ is the sum of 5 terms: exchange energy $E_{\text{exch.}}$, anisotropy energy $E_{\text{anis.}}$, DMI energy E_{DMI} , demagnetising energy $E_{\text{dem.}}$ and Zeeman energy $E_{\text{zee.}}$:

$$E_s[\theta(\rho)] = 2\pi t \int_0^\infty \left\{ A_{\text{ex.}} \left[\left(\frac{d\theta}{d\rho} \right)^2 + \frac{\sin^2\theta}{\rho^2} \right] - K_u \cos^2\theta - D \left[\frac{d\theta}{d\rho} + \frac{\cos\theta \sin\theta}{\rho} \right] - \mu_0 M_s H \cos\theta + E_{\text{dem.}} \right\} \rho d\rho \quad (4.92)$$

The demagnetising energy can be decomposed into two terms $E_{\text{dem.}} = E_{\text{dem.}}^{\text{vol.}} + E_{\text{dem.}}^{\text{surf.}}$ corresponding to the contributions from volume and surface magnetic charges. The volume charges appear only when the magnetisation rotates and the surface charges are present inside the soliton but also in the infinite region with uniform magnetisation. Given the long range nature of the demagnetising effects it is difficult to find the function $\theta(\rho)$ which minimizes the E_s functional. It has been done, in absence of DMI, in the case of magnetic bubbles stabilised by the surface demagnetising energy [91, 92] and by Kiselev and co-workers in the presence of DMI [93].

Considering now the energy difference between the topological soliton and the uniform state we obtain the following Euler equation [94]:

$$A_{\text{ex.}} \left[\left(\frac{d\theta}{d\rho} \right)^2 + \frac{1}{\rho} \frac{d\theta}{d\rho} - \frac{\sin 2\theta}{2\rho^2} \right] + D \frac{\sin^2\theta}{\rho} - K_{\text{eff}} \frac{\sin 2\theta}{2} - \mu_0 M_s H \sin\theta = 0 \quad (4.93)$$

Soliton Euler-LaGrange equation: numerical solution

We solved the eq. 4.93 using a shooting method starting from an inverse tangent try function and the two boundaries values : $\theta(0) = \pi$ and $\theta(\infty) = 0$. The following magnetic parameters have been used: $M_s = 1$ MA/m, $K_u = 1.6$ mJ/m², $A_{\text{ex.}} = 10$ pJ/m, $t = 0.5$ nm and $D^{(1)} = 2.8$ mJ/m². The soliton profile $\theta(\rho)$ is shown in Fig. 4.23.b. The soliton radius is defined as the position ρ where $\theta(\rho) = \pi/2$ ($M_z = 0$). In Fig. 4.23.b the exchange (blue triangles), anisotropy (red triangles) and DMI energies (black circles) are plotted versus the soliton radius r .

The DMI and anisotropy energies present a linear variation versus r down to $r \ll \pi\Delta$ (Sec. 4.2.1). On the contrary, in the same radius range, the exchange energy deviates from linearity and tends to a constant value. This is due to the $1/\rho$ exchange term in eq. (4.92) which expresses the rotation of the magnetisation in the (x,y)-plane: when the soliton radius is decreased, the angle between two adjacent spins in this plane increases. This leads to a non-zero exchange energy limit when $r \rightarrow 0$.

Analytical model:

We now build an analytical expression for the 5 different energy terms in order to respect the behaviour of the energies as a function of the soliton radius obtained in the numerical method:

Anisotropy and exchange energies For $r \gg \pi\Delta$ the sum of exchange and anisotropy energies is proportional to $4\sqrt{A_{\text{ex.}}K_{\text{eff}}}$ and both energies contribute equally :

$$E_{\text{exch.}} = E_{\text{anis.}} = 2\sqrt{A_{\text{ex.}}K_{\text{eff}}} \cdot 2\pi r t \quad (4.94)$$

For $r < \pi\Delta$, the exchange energy deviates from linearity and we consider this effect adding a low radius correction:

$$E_{\text{exch.}} = 2\sqrt{A_{\text{ex.}}K_{\text{eff}}} \cdot 2\pi r t + \frac{E_0}{\frac{\pi\Delta r}{2} + 1} \quad (4.95)$$

This gives the $E_0 = 8\pi A_{\text{ex.}} t$ zero-radius limit for the exchange energy, obtained by Belavin and Polyakov [82], and a zero ($r = 0$) $dE_{\text{exch.}}/dr$ derivative. The analytical expressions of $E_{\text{anis.}}$ and $E_{\text{exch.}}$ are plotted by lines in Fig. 4.23.d. This analytical behaviour of the anisotropy and exchange energy is equal to the numerical solution with a maximum error of 3% without fitting parameter.

DMI energy: The DMI energy depends on the total rotation of the magnetisation, it varies linearly with r as observed in Fig. 4.23.d. and its expression reads:

$$E_{\text{DMI}} = -\pi D \cdot 2\pi r t \quad (4.96)$$

The rotation chirality has been chosen in order to reduce the DMI energy. E_{DMI} is negative and decreases the energy cost of the magnetisation rotation, thus it favours the expansion of topological solitons.

Zeeman energy: We use an approximate expression for the Zeeman energy of the topological soliton which represents the Zeeman energy difference between a magnetic cylinder of radius r and uniform $-M_s$ magnetisation and the Zeeman energy of the ferromagnetic state.

$$E_{\text{Zee}} = 2\mu_0 M_s H \cdot \pi r^2 t \quad (4.97)$$

The error associated with this approximation will be discussed in section 4.4.2.

Dipolar energy : The dipolar energy cannot be expressed analytically and approximations have to be used [92]. The local effect of the demagnetising energy in the region where the magnetisation rotates is taken into account using a local approximation and replacing K_u by K_{eff} in eq. (4.92). This local approximation neglects the long range demagnetising effects which become non-negligible as the skyrmion radius grows, as they are proportional to the skyrmion surface. This long range demagnetising energy contribution is at the origin of the formation of classical magnetic bubbles [95] and its role in the stabilisation of skyrmions in thin films has been shown recently [6, 96]. We will use a classical expression for the surface demagnetising energy which represents the demagnetising energy difference between a magnetic cylinder with uniform magnetisation pointing in one direction and the uniform ferromagnetic state with magnetisation pointing in the other direction:

$$E_{\text{dem.}}^{\text{long range}} = -\mu_0 M_s^2 I(d) 2\pi r t^2 \quad (4.98)$$

where $I(d) = -\frac{2}{3\pi} [d^2 + (1-d^2)E(u^2)/u - K(u^2)/u]$, $d = 2r/t$, $u^2 = d^2/(1+d^2)$ and where $K(u)$ and $E(u)$ are the complete elliptic integrals of first and second kind. This formula is a very good approximation to obtain the surface demagnetising energy when the topological soliton radius is much larger than the DW width $r \gg \pi\Delta$. For $r \sim \pi\Delta$ it leads to an overestimation of this energy as it assumes an abrupt variation of the surface charges. However, the impact of this overestimation is limited by the fact that this energy term is at least one order of magnitude smaller in amplitude than $E_{\text{exch.}}$, E_{DMI} and $E_{\text{anis.}}$ for $r \leq \pi\Delta$ (see Fig. 4.23.d) as it was also shown by Büttner et al. [96].

Summing all the energy components the analytical expression of the soliton energy reads:

$$\begin{aligned} E_s &= E_{\text{exch.}} + E_{\text{anis.}} + E_{\text{DMI}} + E_{\text{Zee}} + E_{\text{dem.}}^{\text{long range}} \\ &= \frac{E_0}{\frac{\pi\Delta r}{2} + 1} + 4\sqrt{A_{\text{ex.}}K_{\text{eff}}} \cdot 2\pi r t - \pi D \cdot 2\pi r t + 2\mu_0 M_s H \cdot \pi r^2 t + E_{\text{dem.}}^{\text{long range}} \\ &= \sigma_s \cdot 2\pi r t + 2\mu_0 M_s H \cdot \pi r^2 t + E_{\text{dem.}}^{\text{long range}} \end{aligned} \quad (4.99)$$

where σ_s is the topological soliton magnetisation rotation energy density which is the sum of the exchange, anisotropy and DMI energy densities. For $r \gg \pi\Delta$, it is close to the DW energy density $\sigma_w = 4\sqrt{A_{\text{ex.}}K_{\text{eff}}} - \pi D$. When the radius is decreasing, σ_s is deviating from σ_w , as shown in Fig. 4.23.c .

Topological soliton solutions

Topological soliton solutions are the minima of the soliton energy E_s as a function of the soliton radius r . We call the equilibrium soliton radius r_s . In order to understand the origin of these minima and the role of the different energies in their stabilisation we first fix the parameters $A_{\text{ex.}}$, M_s , K_u and t and plot the total energy for different D values. The fixed parameters do not modify qualitatively the results presented but rather shift the main features to different D values. The different energy terms, except the Zeeman energy, are plotted as function of r in Fig. 4.24.a for three different DMI values ($D^{(1)} = 2.8$ mJ/m², $D^{(2)} = 3.46$ mJ/m² and $D^{(3)} = 3.6$ mJ/m²). The resulting topological soliton energies E_s are shown in Fig. 4.24.b. As the different energy terms are cancelling each other, a small variation of D is enough to modify the slope of $E_s^{(1)}$, $E_s^{(2)}$ and $E_s^{(3)}$.

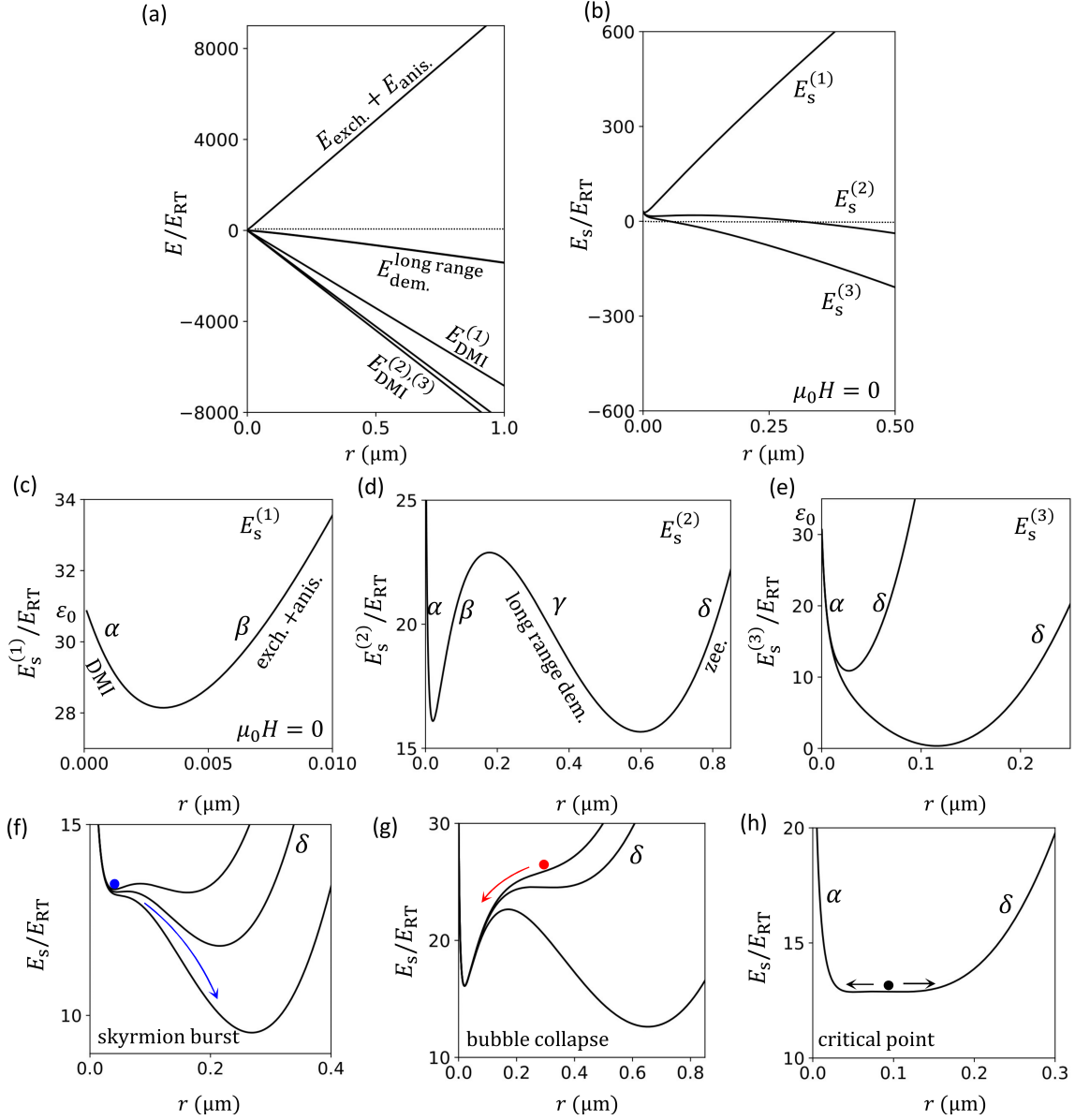


Figure 4.24: (a) Energies versus soliton radius calculated from eq. (4.99) with the same parameters $M_s = 1$ MA/m, $K_u = 1.6$ MJ/m, $A_{ex.} = 10$ pJ/m, $t = 0.5$ nm, for zero applied magnetic field and $D^{(1)} = 2.8$ mJ/m², $D^{(2)} = 3.46$ mJ/m² and $D^{(3)} = 3.6$ mJ/m². (b) Total soliton energies $E_s^{(1)}$, $E_s^{(2)}$ and $E_s^{(3)}$ calculated with the same parameters as in (a). (c), (d) and (e) Soliton energies $E_s^{(1)}$, $E_s^{(2)}$ and $E_s^{(3)}$ for applied magnetic fields of respectively $\mu_0H = 0$ (c), $\mu_0H = 0.28$ mT (d), $\mu_0H = 2$ mT and $\mu_0H = 7$ mT (e). The α , β , γ , and δ letters are indicating the different parts of the $E_s(r)$ curve showing a monotonous dE_s/dr variation.

Skyrmion solutions In Fig. 4.23.d $dE_{exch.}/dr$ is decreasing for $r < \pi\Delta$. This non-linearity may lead to the formation of an energy minimum at r_s in the low radius range as observed in Figure 4.24.c. Indeed, for $r < r_s$ (indicated with an α), the soliton energy variation is dominated by the dE_{DMI}/dr variation while for $r > r_s$ (indicated with a β), the $d(E_{exch.} + E_{anis.})/dr$ variation is taking over. This soliton solution corresponds to what is usually referred to as a skyrmion: its radius is of the order of a few Δ or less and it exists down to $H = 0$. The skyrmion radius increases with D and depends weakly on the applied magnetic field as we will see in Section 4.4.2.

Other solutions can be found when a magnetic field is applied in the direction opposite to the magnetisation in the soliton center.

Bubble solutions and coexistence of skyrmions and bubbles The second situation occurs when the DMI is increased and the positive and negative energy terms become close to compensation over a wide radius range (see $E_s^{(2)}$ in Fig. 4.24.b). In that case, as we can see in Fig. 4.24.c, the positive slope of the exchange and anisotropy is dominating at intermediate radius (β part), but $E_s^{(2)}$ starts to decrease again with r at larger radius (γ part), due to the non-linear decrease in $E_{\text{dem.}}^{\text{long range}}$, before $E_{\text{zee.}}$ with a r^2 variation takes over for larger r (δ part). Consequently, in presence of a magnetic field, two soliton solutions are observed separated by a local maximum of energy. The lower radius solution is the skyrmion solution described in section 4.4.1 and shown in fig. 4.24.c. The second solution presents the characteristics of what is usually described as a magnetic bubble: it will collapse at increasing magnetic field (Fig. 4.24.g) and its size is diverging at $H = 0$. This coexistence of a skyrmion and a bubble solution was evoked in a pioneering work on skyrmions [2] and described in theoretical works from Kiselev et al. [93] and Büttner et al. [96]. The local maximum of energy creates an energy barrier which is at the origin of hysteretic behaviours in the $M(H)$ loops of magnetic bubble materials [95].

Solutions above a critical D_{cs} value The third situation occurs when the DMI reaches the critical D_{cs} value, which we define as the point where the local maximum of energy, as observed in Fig. 4.24.d, is suppressed (see Fig. 4.24.e). Above D_{cs} the total energy $E_s^{(3)}$ presents a negative slope at all r in absence of applied magnetic field (Fig. 4.24.b). In presence of a magnetic field, a minimum of energy is restored in $E_s^{(3)}$ as the positive Zeeman energy variation dominates at sufficiently large radius due to its r^2 variation (δ part in Fig. 4.24.e). For increasing magnetic field this solution is compressing to very small radius without encountering a collapsing field, as it is the case for skyrmions. When the magnetic field is decreased, the topological soliton radius will increase and diverge at $H = 0$ as it is the case for bubbles.

4.4.2 Skyrmion phase diagram

In this section we build a phase diagram of the soliton solutions obtained in the previous section. We have seen that the two fundamental parameters for the existence of the different minima are the DMI constant D and the strength of the applied magnetic field $\mu_0 H$.

In Fig. 4.25 we present the evolution of the topological soliton radius r_s , calculated with the same $A_{\text{ex.}}$, M_s , t , and K_u parameters as in Fig. 4.24, as a function of $\mu_0 H$ and D . The result is shown for a large range of D and $\mu_0 H$ values in Fig. 4.24 and for D close to D_{cs} and low fields in Fig. 4.25.d and e. The main features appearing in Fig. 4.25.a, d and e are represented schematically in Fig. 4.25.b and f. Vertical cross sections of the diagrams in Fig. 4.25.a and d are shown in Fig. 4.25.c and g. Our analytical model allows us to obtain a skyrmion phase diagram similar to the one described by Bogdanov et al. [97] and Kiselev et al. [93] (Fig. 4.25.b) and to complete it with the other soliton solutions at low magnetic fields (Fig. 4.25.f). The asymmetry of the topological soliton phase diagram with respect to the magnetic field comes from the fact that we are describing metastable states of the uniform $-M_z$ reference state.

We have divided the topological soliton phase diagram in different zones:

Single topological solitons zones: zones 1, 2

The skyrmion solutions appear in zone 1. These solutions persist down to $H = 0$ and for negative applied magnetic fields (Fig. 4.25.a). They are suppressed along a blue line visible in Fig. 4.25.b which was defined as the skyrmion busting line in previous works [97, 93]. The skyrmion bursting line ends at the critical point $(D_{\text{cs}}, H_{\text{cs}})$ indicated by a blue dot in Fig. 4.25.b above which no local maximum is observed in $E_s(r)$. This critical point is observed at $H = 0$ and $D_{\text{cw}} = 4\sqrt{A_{\text{ex.}}K_{\text{eff.}}}/\pi$ (4 mJ/m² in our case) in the case where the long range demagnetising effects are neglected [97], where D_{cw} is the critical D value at which the DW energy becomes negative in a thin film [79]. In our case, the critical topological soliton D value D_{cs} is lowered compared to D_{cw} (3.51 pJ/m² compared to 4 pJ/m²), because we take into account the long range contribution in the demagnetising energy, which stabilizes the topological soliton similarly to the DMI energy term. The radii of skyrmions are always smaller than the radius at the critical point $r_{\text{cs}} = r_s(D_{\text{cs}}, H_{\text{cs}})$ (close to 75 nm in our case). In addition the skyrmion radius shows a small susceptibility dr_s/dH , except close to the skyrmion bursting line (see Fig. 4.25c). This is due to the fact that the Zeeman energy term is

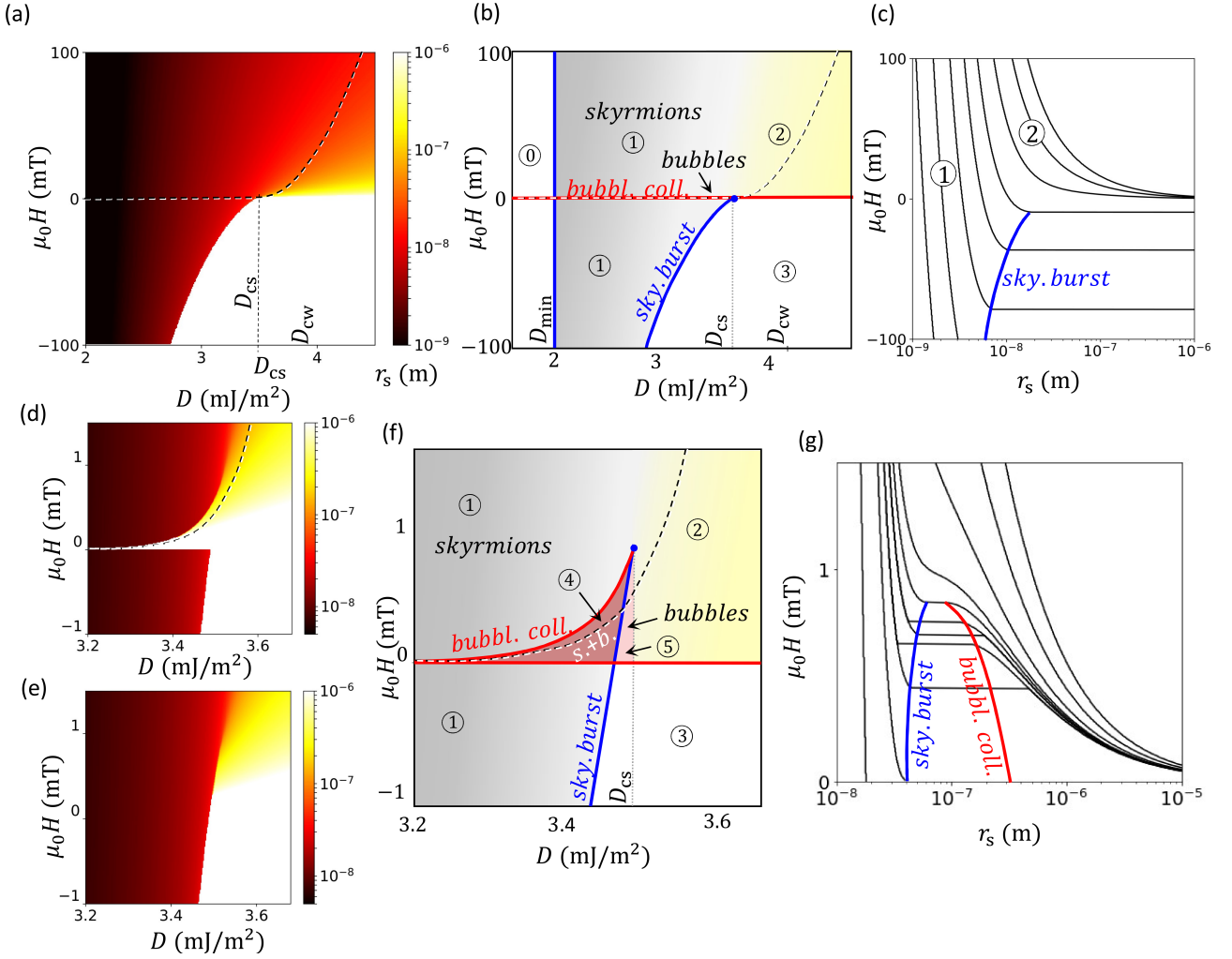


Figure 4.25: (a), (d) and (e) Soliton equilibrium radius as a function of applied magnetic field and parameter D , calculated with the same parameters as in Fig. 4.24. (d) and (e) shows respectively the radius corresponding to the larger/smaller solution, when two solutions coexist. (b) and (f) Schematic representations of characteristic lines appearing in Fig. 4.25a and Fig. 4.25d and defined in Sec. 4.4.2: dashed black line: limit for isolated solitons, green line: bubble collapse line, blue line: skyrmion busting line. (c) and (g) Soliton equilibrium radius as a function of magnetic field for fixed D values. The D values are ranging close to the critical point from $D = 3.476$ mJ/m² to $D = 3.524$ mJ/m² for (c) and from $D = 2.4$ mJ/m² to $D = 4.2$ mJ/m² for (f).

a second order contribution at low radii due to its r^2 variation.

Zone 2 is starting at the critical point (D_{cs}, H_{cs}) and contains the bubble solutions. As observed in Fig. 4.25.c the topological solitons in this zone present a skyrmionic behaviour at high positive magnetic field: low dr_s/dH susceptibility and no collapse field (see Fig. 4.25c). At low magnetic field their susceptibility is large and increases with decreasing field, as it is the case for bubbles. The dashed line in Fig. 4.25.b and f is the line at which the isolated topological soliton energy $s(r_s)$ becomes negative indicating that the ferromagnetic state becomes higher in energy than the non-uniform state. Above this line the low energy cost of topological solitons and domain walls favours the formation of a topological soliton lattice or a stripe/helical phase as described in the works of Bogdanov et al. [97] and Kiselev et al. [93].

We point out that zone 2 is also extending above the critical $D_{cw} = 4$ mJ/m² value. For high magnetic fields, isolated topological solitons with positive energy are restored: when the magnetic field is compressing the topological soliton radius down to $r \sim \pi\Delta$, the non-linearity in the exchange term causes the soliton energy to increase and become positive again: the isolated soliton solution is restored despite the negative domain wall energy at zero magnetic field in this zone. Experimental observations of metastable isolated

topological solitons at high magnetic field can be found in the work from Romming et al. [4] who reported skyrmions in systems with $D > D_{cw}$ under high magnetic fields of a few Tesla.

No isolated soliton: zone 0 and 3

Zone 1 starts along the blue line close to $D = D_{\min.} = 2\sqrt{A_{\text{ex}}K_{\text{eff}}}/\pi$. Below this line, in zone 0, the DMI energy is too low to compensate the anisotropy, the α slope in Fig. 4.24.c becomes positive, and there is no energy minimum in $E_s(r)$. This defines a lower DMI value for the formation of a static topological soliton, however, dynamical solitons [98, 99], not discussed in the present work, can still be created for example using spin polarized currents [100, 101]. In addition, higher order exchange energy terms, not taken into account in the present model, can also lead to the stabilisation of skyrmions in absence of DMI [2, 84, 102, 103]. Zone 3 is delimited by the blue skyrmion bursting line, at which the skyrmion solution disappears, and the $H = 0$ red line. In this zone the negative magnetic field suppresses isolated metastable states. At low magnetic field, for sufficiently large D values, a topological soliton lattice or a stripe/helical phase, not accessible with our isolated soliton model, should be observed in this zone due to a low DW/topological soliton energy cost (see [97, 93, 94]).

Skyrmion and bubble coexistence: zone 4

The region where skyrmion and bubble solutions coexist appears at low magnetic field (zone 4 in Fig. 4.25.f). In Fig. 4.25.d and e we show the radius corresponding to respectively the larger/smaller solution, when two solutions coexist. This zone overlaps with zone 1: a second energy minima corresponding to the bubble solution appears in $\Delta E(r)$ in zone 4 without modifying the skyrmion radius. The coexistence of skyrmion and bubbles is also visible in the diagram vertical cross section in Fig. 4.25.g. Zone 4 is delimited by the bubble collapse red line, the skyrmion bursting blue line and the $H = 0$ line. When D is decreased, the collapse field is decreasing and zone 4 is vanishing because the DW energy becomes too large to be compensated by the surface demagnetising energy.

Critical point (D_{cs}, H_{cs}) In Fig. 4.25.g we show the r_s evolution with magnetic field for a value of D very close to $D_{cs} \sim 3.51$ pJ/m². Below D_{cs} the energy barrier which separates the two solutions, visible in Fig. 4.24.d, is causing hysteretic behaviours in the bubble-skyrmion transformations. Bubbles collapse into skyrmions for increasing magnetic field and skyrmions abruptly expand when the magnetic field is decreased to the bursting field (Fig. 4.24.f and g and Fig. 4.25.g). At $D = D_{cs}$, the hysteretic behaviour is suppressed (blue line in Fig. 4.25.g). This is due to the suppression of the energy barrier separating the two solutions which leads to a remarkably flat $E_s(r)$ energy profile close to r_{cs} as visible in Fig. 4.24.h. This particularity, which is only observed close to the critical point, is due to an almost perfect compensation, when the radius is varying, of the energy cost of the spin rotation by the energy gain of the long range surface demagnetising energy.

The skyrmion-bubble transitions observed here are reminiscent of the critical phenomena observed in the liquid-gas second order phase transition. Firstly, the transitions occurs along lines that terminate at a critical point (D_{cs}, H_{cs}). Secondly, for $D < D_{cs}$ an interval where both solitons coexist is observed similarly to the gas and liquid mixture observed in the temperature versus density plane of the liquid/gas phase diagram. Thirdly, we observe numerically a divergence in the topological soliton compressibility dr_s/dH at the critical point (Figure 4.25.g).

Effect of the approximations on the phase diagram: The presence of the stabilising surface demagnetising energy $E_{\text{dem.}}^{\text{long range}}$ is shifting the critical D value at which the compensation between positive and negative energy terms occurs. This limit corresponds to the frontier at which domain walls will proliferate and isolated solitons or domain walls will not be observed any more at low magnetic fields. However, the expression used to estimate $E_{\text{dem.}}^{\text{long range}}$ leads to an overestimation of this energy. Consequently, while the D_{cs} calculated with the parameters we used is equal to $0.88D_{cw}$, the critical D_{cs} in a real system may be closer to D_{cw} . Concerning the radius of topological solitons, as the expression we use to calculate $E_{\text{dem.}}^{\text{long range}}$ is valid when $r_s \gg \pi\Delta$, we expect that the estimation of r_s is good for solutions in zone 2 as well as bubble solutions in zone 3. Concerning low radius topological solitons, as the non-local demagnetising contributions are weak for $r_s < \pi\Delta$, the approximation used to calculate them has a low impact on the skyrmion radius.

We take as example the experimental results from Romming et al. [4] who have observed skyrmions with $r_s(3T) = 1$ nm and $r_s(1T) = 2$ nm. This radius is reproduced theoretically with an error smaller than 10% using our analytical model and varies by less than 10% if the long range demagnetising term is suppressed. The error associated with the analytical expression of the Zeeman energy that we use comes from a non-compensation of the up and down M_z component in the region where the spins are rotating. When $r \gg \pi\Delta$ this error is negligible ($< 1\%$). For $r = 2\pi\Delta = 20$ nm the error in E_{Zee} is of the order of 5%. For $r = 5$ nm it reaches 30% of E_{Zee} , however, the impact of this underestimation on the topological soliton radius is limited by the fact that E_{Zee} decreases quadratically with r and that the Zeeman energy is always one to several orders of magnitude smaller than the total energy in the $r < \Delta$ range.

4.4.3 The topological soliton quality factor and stability

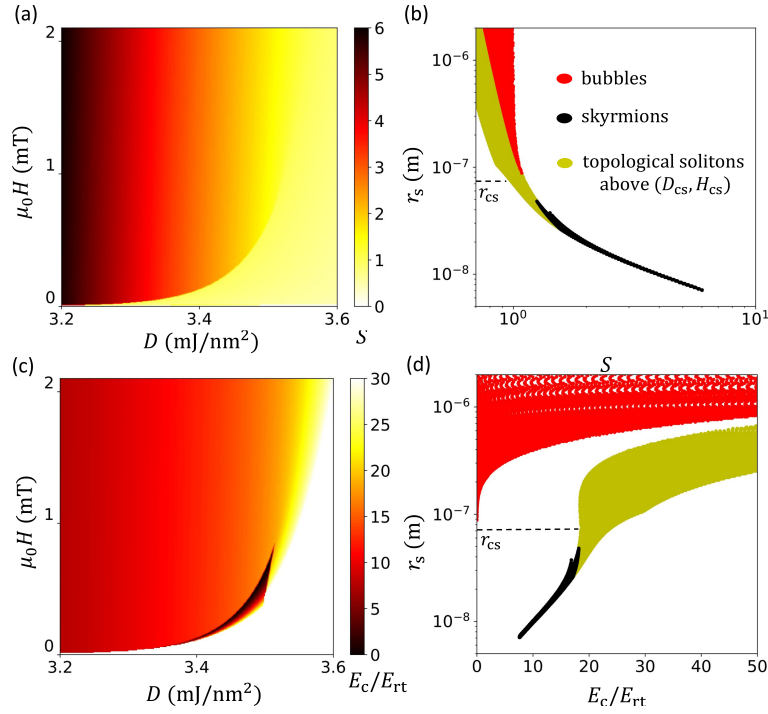


Figure 4.26: (a) Topological soliton S factor corresponding to the solutions in the phase diagram in Fig. 4.25.a. (b) Topological soliton equilibrium radius as a function of the S factor extracted from Fig. 4.25.a and Fig. 4.27.a. (c) Topological soliton equilibrium radius from Fig. 4.25.a as a function of their collapse energy barrier E_c defined in section 4.4.3 and normalized by the RT thermal energy $E_{RT} = k_B T_{293K}$. (d) Topological soliton equilibrium radius as a function of E_c/E_{RT} extracted from Fig. 4.25.a and Fig. 4.27.c.

In order to estimate the role of the long range surface demagnetising energy in the stabilisation of a given topological soliton with radius r_s , we introduce the skyrmionic quality factor S which represents the ratio between the energy cost of the spin rotation and the gain from the long range surface demagnetising energy for a given topological soliton at r_s :

$$S(r_s) = - \frac{E_{\text{exch.}} + E_{\text{anis.}} + E_{\text{DMI}}}{E_{\text{dem.}}^{\text{long range}}} \quad (4.100)$$

The S values corresponding to solutions from Fig. 4.27.a are shown in Fig. 4.27.b. For $r_s \ll \pi\Delta$ the skyrmionic quality factor is large: $S \gg 1$ as $E_{\text{anis.}}$, $E_{\text{dem.}}^{\text{long range}}$ and E_{DMI} tend to zero while $E_{\text{exch.}}$ tends to E_0 (Fig. 4.23.d). On the contrary, large skyrmions with $r_s \gg \pi\Delta$ are only formed when the energy cost of the spin rotation is lower than the energy gain due to the long range demagnetising effect which implies $S < 1$. To check this correlation between the size and the S factor of a given topological soliton, we plot the soliton radius as a function of S in Fig. 4.27.c. Bubbles and skyrmion solutions from zone 4 and 1 are shown respectively in red and black while topological solitons above the critical point (zone 2) appear in yellow. Coexisting skyrmion and bubble solutions from zone 4 show two distinct characteristic radius

ranges, above $r_{cs} = 75$ nm for bubbles with S close to 1 and below r_{cs} for skyrmions with $S > 1$. However, above the critical point, the radius of topological solitons as well as their S factor can be tuned continuously across r_{cs} . The correlation between the size and the S factor is very different depending on the value of S . Topological solitons with S close to 1 show a large radius distribution while the radius of skyrmions and compact topological solitons at high magnetic field are strongly correlated with S (Fig. 4.27.b).

Topological soliton stability

The analytical soliton model allows us to calculate the energy barrier protecting the solitons from collapse. This collapse energy represents the energy necessary for the soliton to annihilate via compression. This gives an estimation of the stability of a topological soliton, keeping in mind that our continuous model may become irrelevant at the atomic scale and that other annihilation mechanism with lower energy paths may exist, in particular in the presence of defects or edges [78]. We define the topological soliton collapse energy barrier as $E_c = E_0 - E_s^{\min}$, where E_s^{\min} is the local minimum in $E_s(r)$. The bubble collapse energy is defined as $E_c = E_s^{\max} - E_s^{\min}$ where E_s^{\max} is the local maximum.

In Fig. 4.27.c we plot the collapse energies corresponding to solutions from Fig. 4.25.a divided by $E_{RT} = k_B T_{293K}$. In Fig. 4.27.d we show the topological soliton radius as a function of the collapse barrier E_c/E_{RT} , where the topological solitons from zone 2 are represented in red while skyrmion and bubble solutions from zone 1 and 3 appear respectively in black and yellow. In zone 3 the segregation of skyrmion and bubbles in two different radius ranges, due to the presence of the energy barrier separating them in $\Delta E(r)$, appears again clearly. The most compact (smaller) topological solitons show a low E_c and an exponential dependence of E_c versus r_s . On the contrary magnetic bubbles from zone 3 (in yellow in Fig. 4.27.d) show a strong dispersion in their collapse energies due the sensibility of r_s to the applied magnetic field, as visible in Fig. 4.27.c. Above the critical point, the topological soliton in zone 2 (red dots in Fig. 4.27.d) shows a tunable collapse energy for a given r_s . For topological solitons of intermediate size (100 nm) and above, RT stability is easily obtained, due to the large value of $E_0/k_B T_{293K} = 31$. The size of the RT stable topological solitons can be decreased by increasing the exchange constant and the thickness. For example, changing the magnetic parameters from $A_{ex} = 10$ pJ/m and $t = 0.5$ nm to $A_{ex} = 15$ pJ/m and $t = 0.7$ nm, E_0 is increased by a factor of 2 and we obtain metastable ($E_c/E_{RT} > 20$) topological solitons at RT with $r_s \sim 10$ nm.

that have been drawn in preceding papers neglecting long range dipolar coupling remain valid (boundary conditions, out-of-plane profiles and energies) [58, 80]. The only difference between the two configurations is the $\phi(\alpha)$ relationship; $\phi = \alpha$ for a Sk ($W = 1$) and $\phi = -\alpha$ for an ASk ($W = -1$).

In order to verify the validity of our analytical results we have performed micromagnetic simulations without dipolar interactions. We used an adaptation of the object-oriented micromagnetic framework code (OOMMF) [104, 80] including anisotropic DMI (see Fig. 4.28). The calculation is performed in a 400-nm diameter, 0.6-nm thick circular dot with typical magnetic parameters for systems where isolated skyrmions have been experimentally observed ($A = 16$ pJ/m, $K_{\text{eff}} = 0.2$ MJ/m³ and $D = 2$ mJ/m²) [6]. Comparing Sk and ASk obtained respectively with $D_x/D_y = 1$ and -1 , identical energies and out-of-plane profiles are found. The $\phi(\alpha)$ relation is confirmed validating the different assumptions in our model (in particular the hypothesis that ϕ is independent on r).

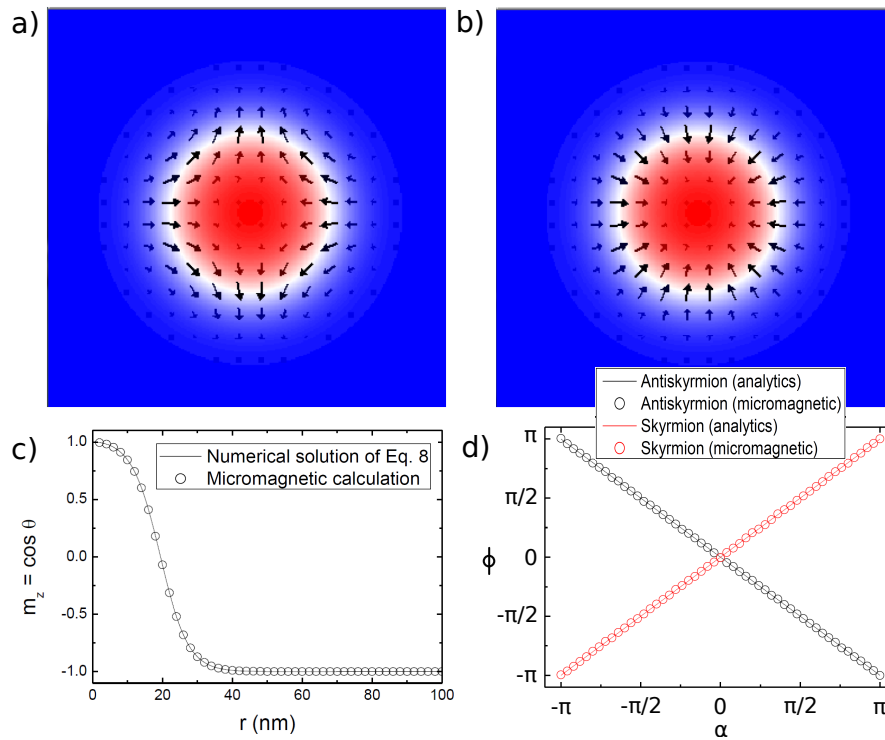


Figure 4.28: Micromagnetic simulations of the magnetisation maps for a skyrmion (a) and an anti-skyrmion (b) (scalebar : 10 nm). The arrows represent the in-plane magnetisation and the color code the out-of-plane magnetisation (red = up, white = in-plane and blue = down). (c) and (d) Comparison between analytic modelling and simulations of the m_z profile and the $\phi(\alpha)$ relationship, for Sk and ASk. In (c) the Sk and ASk profiles are indiscernable.

Role of dipolar couplings

Determining the role of dipolar interactions in the stabilisation of Sk with micromagnetic analytical calculations is particularly difficult. This interaction has often been neglected [58, 105, 94, 80] or analytically expressed under approximations [92, 106, 107]. The two-fold symmetry of the ASk magnetic configuration does not allow using a circular symmetry, increasing the difficulty of this approach. Therefore, we performed a study of the dipolar interaction effects on the Sk and ASk configurations with the support of micromagnetic simulations using OOMMF [104] with an anisotropic DMI. For stabilizing Sk and ASk in the absence of an external magnetic field, we confine them into 0.6 nm thick circular dots with a diameter of 400 nm, using a mesh size of 1 nm.

Phenomenology of dipolar interactions: The effect of the dipolar interaction on the size and stability of Sk and ASk in a dot can be phenomenologically understood considering the contributions from the surface and volume charges.

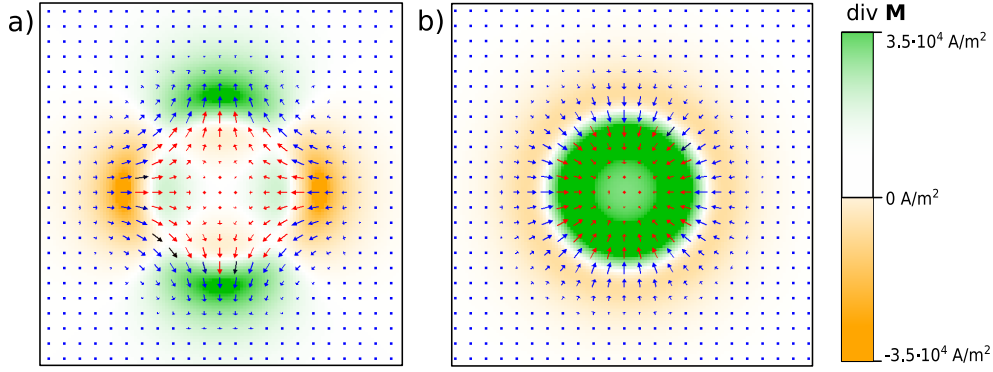


Figure 4.29: Plane view of a magnetic skyrmion **(a)** and an anti-skyrmion **(b)** in a dot with a lateral size of 115 nm. The colors represent the magnetic volume charges ($\nabla \mathbf{m}$) with the color code shown at the right. The arrows represent the magnetic configurations with their colors representing the out-of-plane component (red = up, blue = down). The radius of the magnetic configurations does not depend on the dot size for dots larger than about 100nm and are stable without the application of an external magnetic field, with $M_s = 5 \cdot 10^5$ A/m, $A_{\text{ex}} = 16$ pJ/m, $K_{\text{eff}} = 200$ kJ/m³, $D = 2.0$ mJ/m². Isotropic DMI ($D_x = D_y$) allows the stabilisation of a skyrmion whereas anisotropic DMI ($D_x = -D_y$) stabilizes an anti-skyrmion.

Magnetic surface charges σ arise when the magnetisation vector has a component along the surface normal \mathbf{n} , i.e. $\sigma = M_s \mathbf{m} \cdot \mathbf{n}$. In a perpendicular thin film, they arise from the two surfaces of the film. Therefore, the texture core and the surroundings display opposite charge signs and the energy due to the dipolar interaction is reduced when the magnetic flux closes between the core and the surroundings [6, 106]. Therefore a Sk or an ASk configuration confined in a dot tends to increase its radius in order to demagnetize the system [6, 106]. The surface charges do not depend on the in-plane magnetisation and the associated dipolar interaction is identical for a Sk and an ASk with the same shape and area.

Magnetic volume charges are generated from the volume magnetisation divergence and are therefore present in the vicinity of magnetic textures, and strongly depend on their details. The maps of the volume charges for a Sk and an ASk configuration are shown in Fig. 4.29. The Sk maps present a circular symmetry and the volume charges arise from the Néel-like magnetisation rotation. The ASk maps shows a 2-fold symmetry and the presence of Bloch-like rotations along intermediate directions ($\phi = \pi/4 + n\pi/2$). For the ASk, the charges are maximum along the main axes \mathbf{x} and \mathbf{y} , due to the Néel type rotations. However, the signs along \mathbf{x} and \mathbf{y} are opposite due to the opposite chirality.

The impact of the volume charges can be decomposed in two effects. First, the charges locally increase the energy of the transition region, in the same manner as for a flat domain wall. The dipolar energy cost of a domain wall oriented at an angle α with respect to the \mathbf{x} axis is $\delta_N \cos^2(\phi - \alpha)$, where δ_N corresponds to the dipolar cost of a Néel wall [79]. For a large Sk or ASk, such arguments based on the energy of a flat domain wall remain qualitatively valid [80] and lead to a significant difference between the two textures. For a skyrmion, where $\phi = \alpha$, the dipolar energy is isotropic, equal to δ_N , while for an anti-skyrmion, where $\phi = -\alpha$, the energy strongly varies as a function of α and becomes zero in the regions where the spin rotations are Bloch-like. Considering a circular texture of radius R , the additional cost to the dipolar-free micromagnetic energy described earlier is $2\pi t R \delta_N$ and $\pi t R \delta_N$ for skyrmions and antiskyrmions, respectively. This means that anti-skyrmions are expected to display a lower energy and a larger equilibrium diameter than skyrmions. A second effect couples the flux arising from the volume charges over the entire texture. Inside a skyrmion, the charges have the same sign everywhere, opposite to the sign outside the texture. On the contrary, both inside and outside an anti-skyrmion the charges have signs that are opposite along the main axes. The total volume charges both inside and outside the texture thus cancel leading to a further decrease of the dipolar energy with respect to the skyrmion.

The total energy of the ASk is thus reduced with respect to the Sk due to the difference in the distribution

of volume magnetic charges. Moreover, the presence of anisotropic volume charges may deform the ASk shape, as we will discuss later.

Stability and shape of anti-skyrmions

To investigate in more detail the effect of the dipolar interaction on the stability and shape of Sk and ASk, we studied their energy and radius as a function of the spontaneous magnetisation M_s (Fig. 4.30). In order to consider only the effects of the volume charges and the flux closure of the surface charges we keep K_{eff} constant during the variation of M_s and use the same parameters as in the simulations with simplified dipolar interactions in Fig. 4.28. M_s was varied between $0.1 \cdot 10^6$ A/m and $1.8 \cdot 10^6$ A/m. In Fig. 4.30(a) the Sk and ASk energies are considered as the energy difference between a dot with a Sk or an ASk and its relative single domain state. Taking this difference allows eliminating the effect of the DMI on the edge magnetisation [80, 108]. Since the ASk can present a shape which is not circular, we consider an effective radius ($r = \sqrt{\mathcal{A}/\pi}$) calculated from the area \mathcal{A} . We consider \mathcal{A} as the space region of the Sk and ASk where $m_z > 0$. For small values of M_s the Sk and the ASk are mainly stabilized by the competition between the exchange, anisotropy and DMI [90] energies that were shown to be equal for Sk and ASk. The dipolar interaction is negligible and the Sk and the ASk have comparable energy and radius. When M_s increases the dipolar interaction plays a larger role. The Sk and ASk radii increase (Fig. 4.30(b)) to allow a more efficient flux closure between the surface magnetic charges. Both configurations lower the energy but the difference in volume charges favors the ASk. When for larger M_s the dipolar energy becomes larger than the DMI energy, the total energy of the Sk and the ASk decreases and their radius increases until they feel the repulsive effect from the dot edge [80]. In this regime, the Sk and ASk shape and dimensions strongly depend on the symmetry and size of the microstructures in which they are confined and the volume charges become the driving force for defining the magnetic configuration.

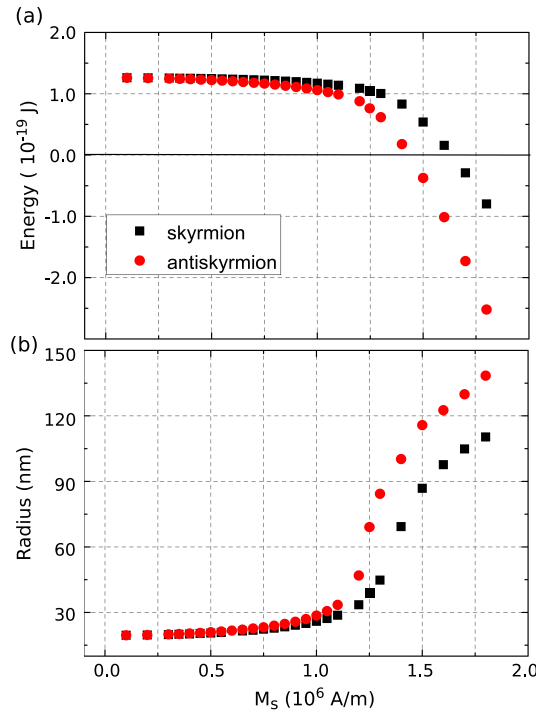


Figure 4.30: Energy (a) and radius (b) of a skyrmion (black) and an anti-skyrmion (red) as a function of the spontaneous magnetisation M_s . The simulations are performed in circular dots of 400 nm diameter and 1 nm thickness with a fixed out-of-plane effective anisotropy K_{eff} . $A_{\text{ex}} = 16$ pJ/m $K_{\text{eff}} = 2 \cdot 10^5$ J/m³ $D = 2.0$ mJ/m²)

Upon increasing M_s , the ASk changes its shape in order to promote Bloch-like rotations, which do not generate volume charges and thus cost less dipolar energy. Because DMI promotes Bloch-like rotations along intermediate crystallographic directions ($\phi = \pi/4 + n\pi/2$), the ASk has the tendency to acquire a square shape (Fig. 4.31). This configuration allows to increase the ratio between Bloch and Néel rotations. Even

if the total domain wall length increases going from a circular to a square shape, this can still lead to a minimisation of the total DMI and dipolar energy.

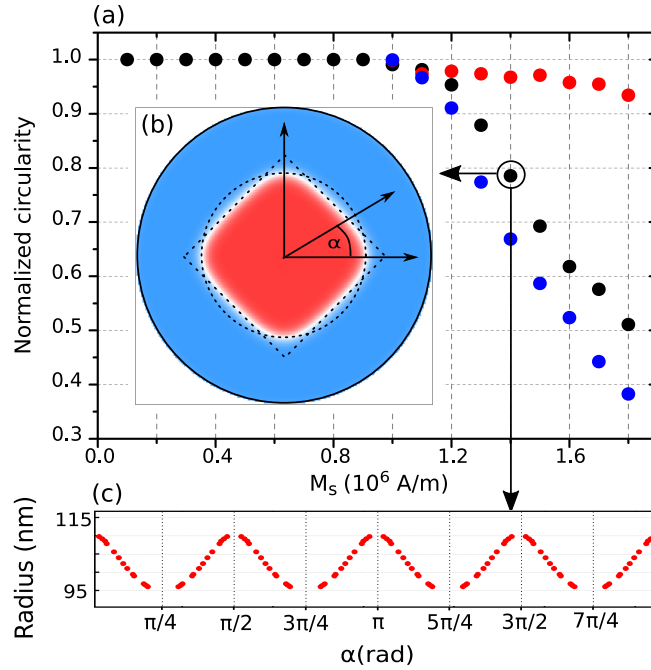


Figure 4.31: **(a)** Normalized circularity factor C_n as a function of M_s for an anti-skyrmion stabilized in dots with a diameter of 500 nm (blue), 400 nm (black) and 200 (red). **(b)** Magnetic configuration of an anti-skyrmion ($M_s = 1.4 \cdot 10^6$ A/m, $A_{\text{ex}} = 16$ pJ/m, $K_{\text{eff}} = 2 \cdot 10^5$ J/m³, $D = 2.0$ mJ/m²) with a sketch that shows the square-circular shape. **(c)** Radius of an anti-skyrmion as a function of the in-plane angle α

In order to quantify this tendency, we calculate the normalized circularity factor $C_n = \frac{4\pi\mathcal{A}/\mathcal{P}^2 - \pi/4}{1 - \pi/4}$, where \mathcal{A} and \mathcal{P} are, respectively, the area and the perimeter of the texture (set of points where $m_z = 0$). This normalized circularity factor may vary from $C = 1$ (circle) to $C = 0$ (square). The Sk has a circular symmetry and this factor is thus equal to 1. Fig. 4.31 shows the plot of the normalized circularity for an ASk as a function of M_s , stabilized in dots of different diameters (200, 400 and 500 nm). We can distinguish two different regimes. For small values of M_s , the volume charges do not influence the ASk shape, the circularity is equal to $C = 1$ and does not depend on the dot size. For larger M_s values, the moment rotation with an angle ($\phi = \pi/4 + n\pi/2$) is favored and the ASk circularity decreases upon increasing M_s . In small dots, the confinement does not allow the ASk to expand, and constrains the texture shape to the dot shape. In larger dots, the ASk shape adapts to the internal energies, which results in a shape closer to the square configuration. Increasing the dot size even further, the ASk configuration becomes unstable for these large values of M_s and a labyrinth-like domain structure is formed.

Finally, in order to have a numerical confirmation of the Sk and ASk stabilisation mechanisms, we studied the energies as a function of the Sk and ASk radius for a given value of M_s . We choose $M_s = 1.25 \cdot 10^6$ A/m in order to study the regime where the dipolar interactions are important. These simulations were performed starting from two different initial states, respectively with a radius larger and smaller than the equilibrium one. The conjugate gradient minimisation algorithm has been used for minimizing the energy, starting from these initial states. During the relaxation towards equilibrium, all the components of the Sk and ASk energies have been tracked as a function of the radius, i.e. for each minimisation step we recorded the energies and calculated the radius of the Sk or the ASk [Fig. 4.32(a,b)]. Implicitly we suppose here that the configurations follow a physical minimum energy path, which is not necessarily always the case as shown using more complex methods [109, 76, 110, 111]. In order to confirm our results, we compared the obtained energy with the analytical results, as a function of the texture diameter. In both approaches the anisotropy and the DMI energies are proportional to the radius as expected.

Upon diameter increase, anisotropy and exchange energies increase and DMI and dipolar energies decrease, all almost linearly. The balance between these terms is rather subtle as all these energies almost

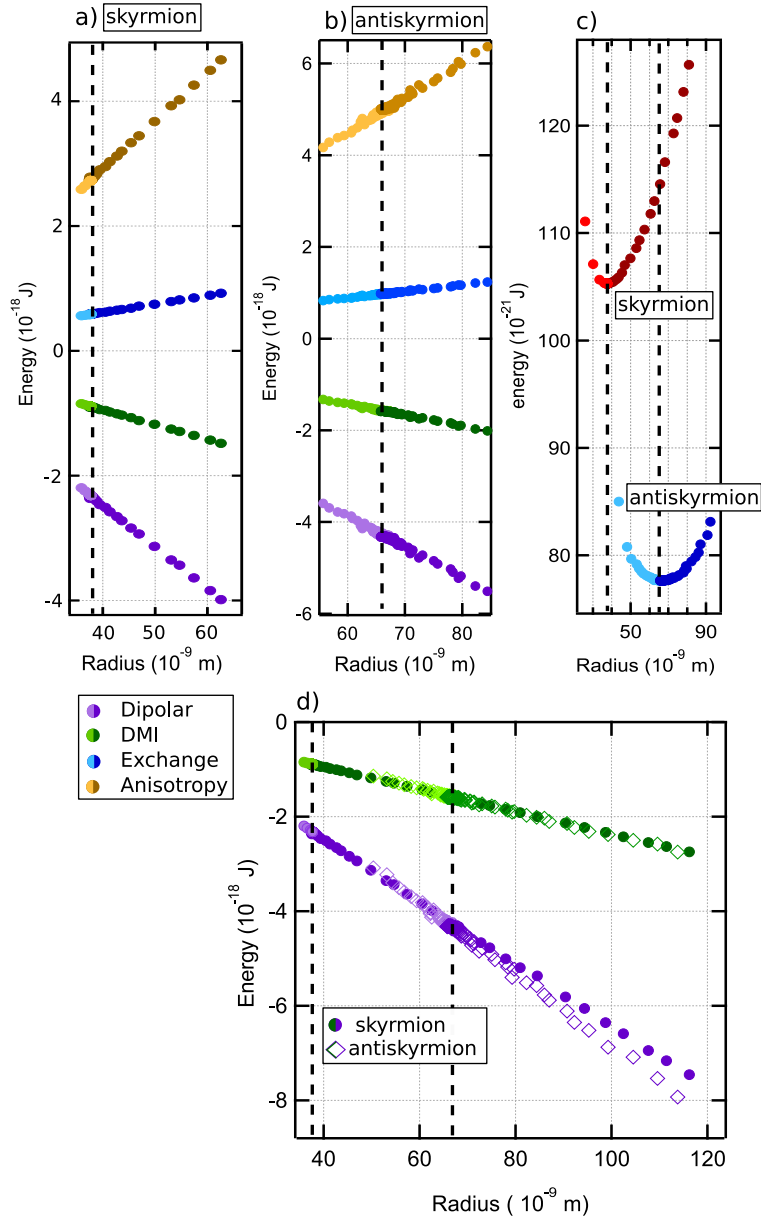


Figure 4.32: Magnetic energies of a skyrmion (a) and an anti-skyrmion (b) as a function of the radius for a given set of magnetic parameters ($M_s = 1.25 \cdot 10^6$ A/m, $A_{ex} = 16$ pJ/m, $K_{eff} = 2 \cdot 10^5$ J/m³, $D = 2.0$ mJ/m²). (c) Total energy for a skyrmion (red) and an anti-skyrmion (blue) as a function of the radius. (d) Comparison between the DMI (green) and the dipolar interaction (violet) for a skyrmion (dots) and an anti-skyrmion (squares) as a function of the radius. The vertical dotted lines in all panels correspond to the equilibrium radius of Sk and/or ASk

compensate (the absolute value of the total energy is more than one order of magnitude smaller than the absolute value of any of the separate energies). In Fig. 4.32(c) we show that for a given set of magnetic parameters the ASk is more stable than the Sk and it has a bigger radius. It can be understood considering Fig. 4.32(d) where the behavior of the DMI and of the dipolar interaction energies are compared as a function of the radius. One can notice that the DMI has the same behavior for the Sk and ASk, unlike the dipolar energy, which upon increasing radius decreases faster for the ASk than for the Sk. This difference is the fundamental reason for the energy difference between the Sk and the ASk. Even if this difference at equilibrium is not visible in the energy range shown in Fig. 4.32(d) it becomes fundamental in the anti-skyrmion/skyrmion energy range Fig. 4.32(c). Indeed, the Sk and ASk configurations are determined by the competition between all the magnetic energies and any small variation of one of the energies can imply a strong change of the Sk and ASk energy and radius.

4.4.5 Review on 2D topological solitons

Micromagnetic models have been developed in order to study 2D topological solitons.

In the first part we have developed an analytical topological soliton model containing expressions of the long range demagnetising and exchange curvature energies, two key ingredients to stabilise bubbles and skyrmions in ferromagnetic thin films. This allowed us to study systematically topological soliton solutions over a wide range of parameters and explore quantitatively the possible transitions between small and large topological solitons. In the skyrmion-bubble transition a critical point is present above which the transformation between both spin textures becomes continuous. While the distinct characteristics of skyrmion and bubbles remain, their common nature as topological solitons is emphasized. Above the critical (D_{cs}, H_{cs}) point, the topological soliton can not be strictly named a skyrmion or a bubble, as it possesses some characteristics of both objects, and it may be addressed as supercritical skyrmion.

In the second part we have shown that when the dipolar interactions are neglected one can write the ASk energy in a circular symmetric form. The Sk and the ASk in systems with different symmetry but the same strength of magnetic interactions have the same size and stability energy. The presence of dipolar interactions breaks the circular symmetry of the ASk energy. With the support of micromagnetic simulations we have studied the energy and the shape of Sk and ASk as a function of M_s and explained the role of the dipolar interaction. We can distinguish three different effects. The interaction due to the surface charges does not break the circular symmetry and stabilizes in the same way Sk and ASk. The volume charges depend on the in-plane moment configuration. While the Sk configuration shows homochiral Néel moment rotation, anti-skyrmions show partly Néel and partly Bloch rotations. The latter do not produce magnetic charges. The ASk configuration is therefore more stable and the tendency to favor Bloch rotations induces a square shape. Moreover the presence of Néel rotations with different chirality induces a partial flux closure effect and further increases the ASk stability. Since both Sk and ASk are stable when all the magnetic energies cancel each other, a small variation of a single parameter like the dipolar energy can have a large influence on the shape and energy of the textures.

Chapter 5

Experimental results: magnetism in C_{2v} epitaxial systems

In the previous chapters we used micromagnetic approaches in order to describe the relationship between the crystal symmetry, the magnetic interaction symmetry and the topological solitons in epitaxial magnetic thin films. The theoretical results are used here to analyse the experimental data described in this chapter.

The experimental work shown in this thesis started at the end of 2014. At the time isolated skyrmions had been evidenced experimentally only under the application of a strong magnetic field (a few Tesla) and at low temperature ($T=4K$) [4]. Moreover, the origin of DMI in ultrathin materials with broken inversion symmetry was not completely understood.

The work of this thesis started with the aim of studying the origin of DMI in order to design a strategy for nucleating isolated skyrmions at room temperature in ultrathin films. With a similar aim the scientific community focused on the study of ultrathin multilayer materials grown with sputtering techniques. The experimental samples obtained in this way may present rough interfaces with material interdiffusion. Since the DMI is an interface effect it should be strongly affected and its interaction reduced by the interdiffusion. We therefore decided to study DMI in good quality epitaxial films with sharp interfaces, which could be used as model systems to compare with theoretical calculations of interface DMI.

This chapter is divided into three main parts, presenting the different magnetic systems that were grown and analysed. For each system I first describe the growth parameters and crystal symmetry, followed by the results of the magnetic characterisation and finally the results from the magnetic microscopy measurements. This explanation path allows to understand how the symmetry and quality of the crystals determine the symmetry of the magnetic properties and how the magnetic configurations depend on them.

The reported experimental work has been done with fundamental support of Philippe David and Valerie Guisset of the "Pôle Epitaxie".

5.1 Materials for stabilizing isolated skyrmion

In order to find the right combination of materials for stabilizing isolated skyrmions in ultrathin films several properties have to be fulfilled:

- **Strong DMI:** The strength of the DMI in ultrathin films strongly depends on the quality of the interface between a heavy metal (HM) and a ferromagnetic material (FM). Theoretical studies show that the DMI strength increases in systems with **sharp interfaces** [31]. A way to avoid interlayer mixing is to use materials that do not form alloys.

In addition to the material choice, we decided to grow trilayer systems with two different magnetic HM\FM metal interfaces (HM1 \ FM \ HM2). This allows obtaining samples that can be studied with different experimental techniques since the upper heavy metal layer protects the magnetic layer from oxidation. Moreover, using materials with opposite DMI sign ($\mathbf{d}_{\text{HM1/FM}} \cdot \mathbf{d}_{\text{HM2/FM}} < 0$) at the two interfaces allows to increase the DMI on the magnetic layer ($\mathbf{d}_{\text{HM1\FM\HM2}} = \mathbf{d}_{\text{HM2/FM}} + \mathbf{d}_{\text{HM1\FM}}$)

(Fig. 5.1). Indeed, a mirroring symmetry operation does not conserve the chirality; i.e. a clockwise spin rotation becomes anti-clockwise if the system is upside-down.

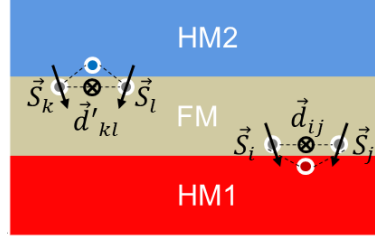


Figure 5.1: Sketch of a trilayer system. (blue and red) Heavy metals and (brown) ferromagnetic material. The $\mathbf{d}_{\text{HM1/FM}} \cdot \mathbf{d}_{\text{HM2/FM}} < 0$ have an opposite sign with respect to the interface but the geometrical positions sums their effects on the ferromagnetic layer.

- **Out-of-plane magnetisation:** According to the Moriya rules (Sec. 2.3.2) the DMI vector lies in the plane perpendicular to the direction of the breaking of the inversion symmetry. In an ultrathin system with interfacial DMI the \mathbf{d} vectors therefore lie in the system plane. Then the DMI effects manifest themselves only in out-of-plane magnetized systems. An out-of-plane magnetisation can be obtained in ultrathin films tailoring the interface magnetic anisotropy (Sec. 2.5).

5.2 W\Co\Au and W\Co\Pt

Tungsten (W) is a refractory metal with high surface energy and high spin-orbit coupling. At the start of this PhD work there was no information on the DMI strength and sign that it could induce in a magnetic material. High quality W single crystal films can be obtained by the growth on a Al_2O_3 surface. These properties convinced us to start our trilayer system with a W layer.

Cobalt (Co) was chosen as the magnetic layer because it is a room-temperature ferromagnetic transition metal and because there is a rich literature on its magnetic properties when deposited on a heavy metal. Moreover it can grow epitaxially on W layers. The drawback of the W\Co interface comes from the fact that the W interface anisotropy promotes a strong in-plane magnetic anisotropy [112]. The upper layer was chosen in order to overcome this problem. Two different materials, gold (Au) and platinum (Pt), have been deposited in order to obtain an out-of-plane magnetisation. Both materials induce a strong out-of-plane interface anisotropy when they are at the interface with a Co layer [112, 113]. Moreover, a high value of the DMI at the Co\Pt interface had already been demonstrated [114] [115][116].

5.2.1 Crystal relationships in epitaxial systems

In this part a short review of the literature on the epitaxial relationships and the obtained crystal structures between the materials composing the W\Co\Pt and W\Co\Au trilayers is shown.

$\text{Al}_2\text{O}_3 \setminus \text{W}$

The bulk W (tungsten) crystal is body-centred cubic (bcc) with lattice parameter $a = 3.1652 \text{ \AA}$.

Al_2O_3 takes the name of aluminium oxide or sapphire and it has a hexagonal close-packed (hcp) lattice with the main parameters $a = 4.785 \text{ \AA}$, $c = 12.991 \text{ \AA}$. The absence of porosity and of grain boundaries makes this crystal an excellent substrate for deposition techniques. There are three different Al_2O_3 orientations, (0001), ($1\bar{1}00$) and ($11\bar{2}0$), that allow the epitaxial growth of a W crystal:

$$\text{W}(111) \parallel \text{Al}_2\text{O}_3(0001) \quad \text{W}(112) \parallel \text{Al}_2\text{O}_3(1\bar{1}00) \quad \text{W}(110) \parallel \text{Al}_2\text{O}_3(11\bar{2}0) \quad (5.1)$$

RHEED [117] analysis showed that the W grows with a better crystal quality in the relationship $\text{W}(110) \parallel \text{Al}_2\text{O}_3(11\bar{2}0)$. This is because the W(110) planes are the most dense in the bcc structure maximizing the W interatomic interactions and thus the surface energy.

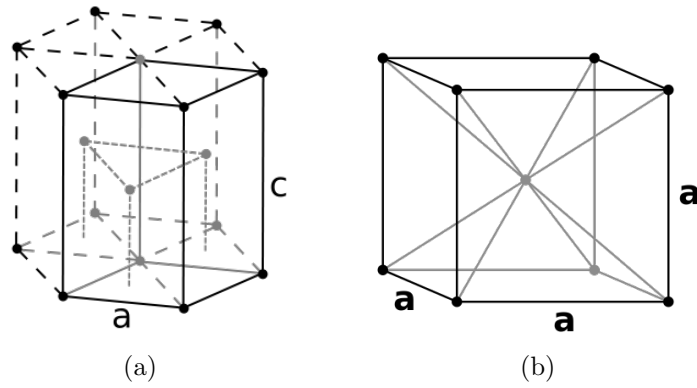


Figure 5.2: Crystal structures: (a) hexagonal close-packed (b) body-centred cubic

The W atoms, during the deposition, minimize their energy by sitting into the vacant octahedral sites of the Al terminal plane. During the W(110) surface growth on Al_2O_3 ($11\bar{2}0$) the W [111] is the most dense row of atoms and has the tendency to align along the Al_2O_3 [0001] direction. Then two symmetric epitaxial relationships are near degeneracy as shown in Fig. 5.3:

- In the relation called A the $[1\bar{1}1]$ direction of the W surface is parallel to the [0001] direction of the sapphire surface.
- In the relation called B the $[1\bar{1}\bar{1}]$ direction of the W surface is parallel to the [0001] direction of the sapphire surface.

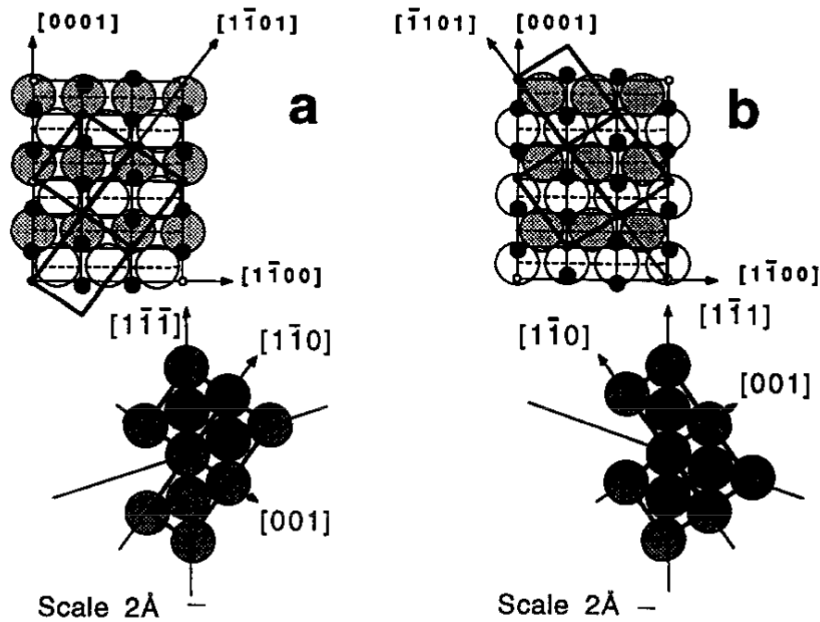


Figure 5.3: Schematic representation of the two faces of an Al termination ($11\bar{2}0$) plane showing the epitaxial arrangement of W thereon. The Al atoms are shown as filled circles. The underlying two rows of oxygen atoms are shown as large open circles and large shaded circles, respectively. The vacant octahedral sites are shown as small open circles. (a) Corresponds to the epitaxial relation described as case A in the text and (b) corresponds to the epitaxial relation described as case B in the text.

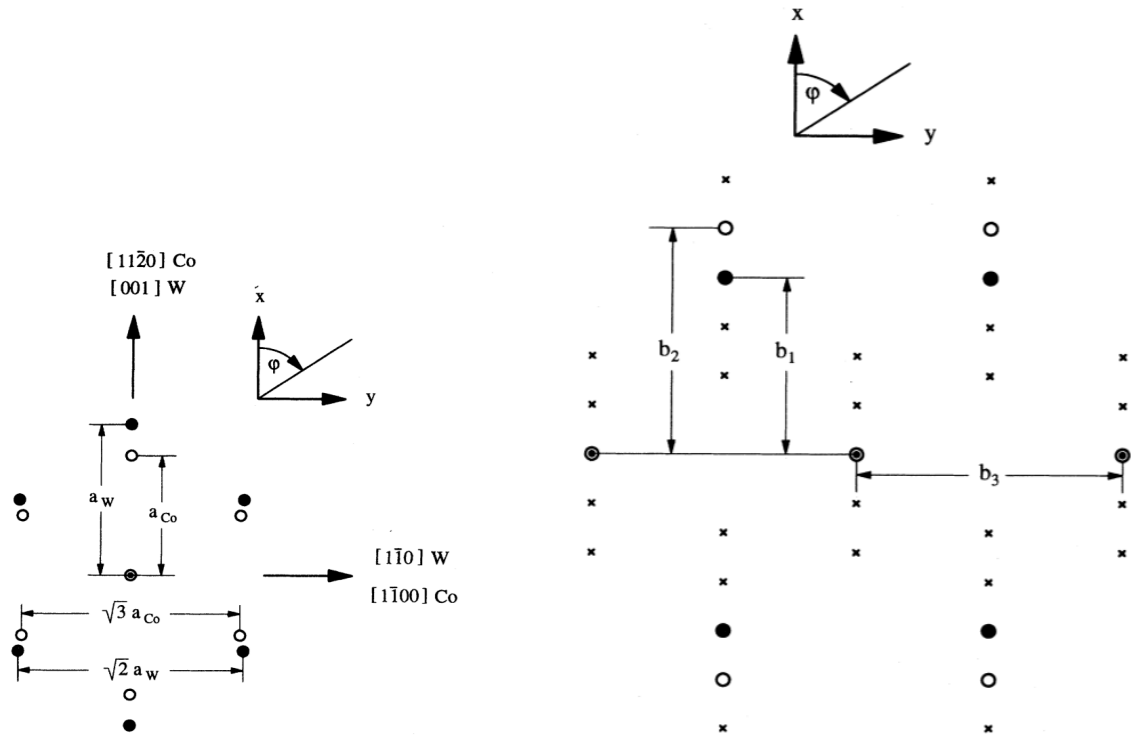
X-ray diffraction measurements [117] show a good layer-by-layer epitaxial deposition with a small tilt between the W and Al_2O_3 planes (0.04°). Moreover in both cases twin crystals with different populations can be found. For case A the epitaxial relation for the higher density population was found to be $W[\bar{1}12] \parallel \text{Al}_2\text{O}_3(1\bar{1}00)$ and the lower density population was found to be $W[1\bar{1}2] \parallel \text{Al}_2\text{O}_3(1\bar{1}00)$.

Since in this work we are interested in the study of the simplest possible crystal, we need to avoid the presence of different epitaxial configurations that could deteriorate the quality of the next layers. In the case of W(110) on Al_2O_3 the problem has been solved by the introduction of a thin layer of Molybdenum (Mo) between the two materials [118]. Mo has a lattice parameter slightly smaller than the one of W and grows on Al_2O_3 with the same epitaxial relationships as W. When the W grows on top of the Al_2O_3 \ Mo stack it assumes the same configurations than without the Mo interlayer, but when an annealing process is performed only one relationship ($W[\bar{1}12] \parallel \text{Al}_2\text{O}_3(1\bar{1}00)$) is energetically favorable [118]. The obtained monocrystal has a rectangular primitive cell with C_{2v} symmetry.

W\Co

Cobalt (Co) is a room-temperature ferromagnetic transition metal. Its crystal in bulk structure is hexagonal close-packed (hcp) with lattice parameters $a : 2.5071\text{\AA}$ and $c : 4.0695\text{\AA}$ at room temperature. The hexagonal (0001) surface has C_{3v} geometry and can grow epitaxially on the bcc W(110) surface.

One possible epitaxial relationship between a hcp (0001) surface and a bcc (110) surface takes the name of Nishiyama-Wassermann (NW) orientation [119]. In this orientation the bcc [001] direction is parallel to the hcp [11 $\bar{2}$ 0] direction, like it is shown in Fig. 5.4a.



(a) The sketch of the Nishiyama-Wassermann orientation between the rectangular bcc(110) (solid circles ●) and hcp (0001) (open circles ○)

(b) Diffraction pattern of Co (0001) (open circles ○) on W (110) (solid circles ●) in the regime between 1 and 4 monolayers Co

Figure 5.4

Since the Co hcp (0001) and the bcc (110) surfaces have different symmetry and atomic distances, the Co layer will grow strained and elastic energies will be accumulated. Then the Co grows in different configurations as a function of the layer thickness because the increase of the elastic energies. In Sec. 3.1.4 the role of the crystal strain in this phenomenon has been shown. One can define a monolayer (ML) of Co as the number of absorbed atoms needed to fill an atomic layer $\text{ML} = 2\text{\AA}$.

Three different regimes have been found from the analysis of [120] :

- Up to 1ML the interaction between the Co atoms is weak, the Co atoms feel mostly the substrate potential and the crystal grows pseudomorphically.
- When the thickness increases the interaction between the Co atoms becomes stronger, strain increases and the Co crystal starts to relax. The lattice misfits along the main in-plane crystallographic directions

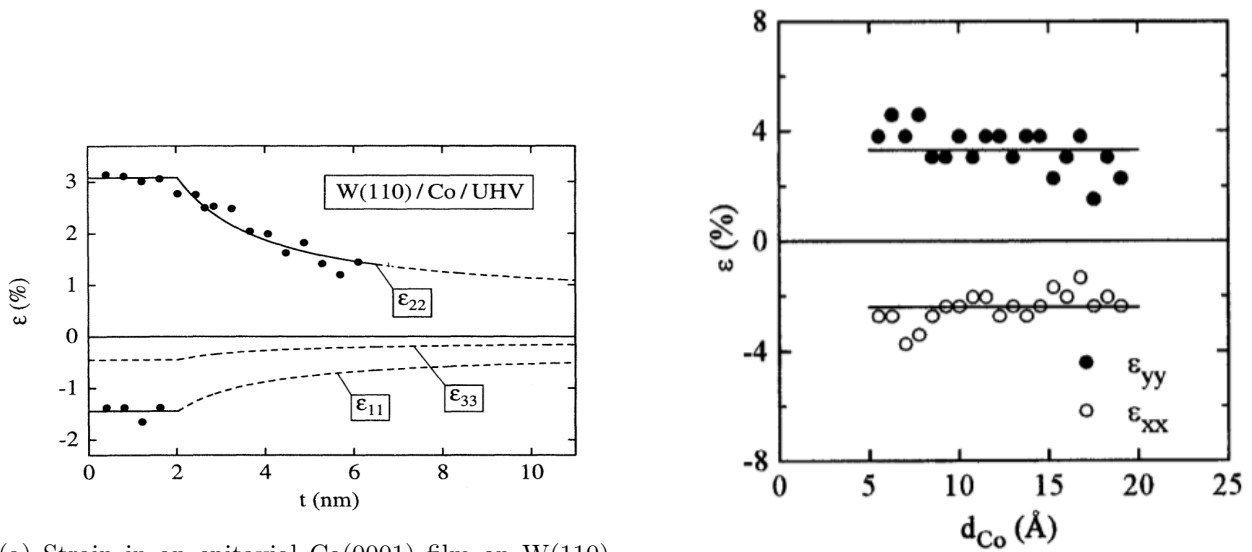
are:

$$\Delta a_{\text{bcc}[\bar{1}10]} = \frac{\sqrt{2}a_W - \sqrt{3}a_{\text{Co}}}{\sqrt{2}a_W} = 2.98\% \quad \Delta a_{\text{bcc}[001]} = \frac{a_W - a_{\text{Co}}}{a_W} = 20.79\% \quad (5.2)$$

where a_W and a_{Co} are respectively the bulk bcc and hcp lattice parameters. Along the $\text{bcc}[\bar{1}10]$ direction the Co is expected to grow pseudomorphically ($a_x = \sqrt{2}/2a_W$), up to 10 Co monolayers (1ML $\simeq 0.2$ nm) [120]. Along the $\text{bcc}[001]$ direction, the misfit instead is large implying that the Co structure relaxes for a thickness between 2 and 4 ML ($a_y = 3.56/4.56 \frac{a_W}{2}$ [120]), with a_x and a_y defined in Fig. 5.16. Along the $\text{bcc}[001]$ direction, the Co-W crystal forms a superstructure with a period of $9a_y$ (1.1 nm).

- During the growth, for thickness beyond 4 ML, the Cobalt layer relaxes and the strain decreases as shown in the analysis of the LEED pattern (Fig. 5.4b).

In Fig. 5.5b the experimental values of ϵ are plotted as a function of the Co layer thickness up to 4 ML .



(a) Strain in an epitaxial Co(0001) film on W(110) versus thickness t . Experimental data taken by LEED spectroscopy in [120] are fitted by the full lines using the strain model explained in the chapter.

(b) Strain in an epitaxial Co(0001) film on W(110) versus thickness t . Experimental data taken by LEED spectroscopy in [112]

Figure 5.5

The experimental data have been interpreted by the elastic energy minimisation theory in a linear continuum elasticity theory. Two regimes are considered for the dependence of the strain on the thickness.

- In the first regime the pseudomorphic constraint along y imposes a x and z Poisson-type contraction.
- In the second regime beyond the critical thickness $t_c = 2.0$ nm the strain relaxation is described by the equation:

$$\epsilon_{ii} = \epsilon_{ii}^0 [\alpha + (1 - \alpha)(t_c/t)] \quad (5.3)$$

where ϵ_{ii}^0 is the strain in the first regime. The constant residual strain $\epsilon_{ii}^0 \alpha$ is the strain for an infinite thickness layer.

The magnetic anisotropy depends directly on the crystal surface symmetry (Sec. 2.5). In a second order approximation the total anisotropy energy density for a biaxial system reads:

$$E_{mc} = K_{\text{out}} \sin^2(\theta) + K_{\text{in}} \sin^2(\varphi) \cos^2(\theta) \quad (5.4)$$

The volume and surface anisotropy constants are the sum of the magneto-crystalline and the magneto-elastic constants ($K_i = K_i^{\text{mc}} + K_i^{\text{me}}$). The magneto-elastic constants can be calculated from the crystal strain. Considering the magneto-elastic constants B_i calculated in [121], one can write the relation between magneto-elastic anisotropy constants and the strain:

$$K_{\text{out}}^{\text{me}} = -B_1 \epsilon_{22} - B_2 \epsilon_{33} - B_3 (\epsilon_{22} + \epsilon_{11}) \quad K_{\text{in}}^{\text{me}} = B_1 (\epsilon_{11} - \epsilon_{22}) \quad (5.5)$$

Experimentally the magneto-elastic and the magneto-crystalline anisotropy constants can not be separated but a dependence on the growth regimes has been found [120]:

	regime $t < t_c$	regime $t > t_c$
K_{out}^v	$-3.3 \times 10^5 \text{J/m}^3$	$-0.7 \times 10^5 \text{J/m}^3$
K_{out}^s	$0.0 \times 10^{-3} \text{J/m}^2$	$-0.5 \times 10^{-3} \text{J/m}^2$
K_{in}^v	$-7.6 \times 10^5 \text{J/m}^3$	$-4.7 \times 10^5 \text{J/m}^3$
K_{in}^s	$0.1 \times 10^{-3} \text{J/m}^2$	$-0.7 \times 10^{-3} \text{J/m}^2$

Au (111) and Pt(111) on Co(0001)

Platinum (Pt) and Gold (Au) are noble metals and they have a fcc crystal lattice with the lattice parameter respectively $a_{\text{Pt}} = 3.9242\text{\AA}$ and $a_{\text{Au}} = 4.078\text{\AA}$.

In Fig. 5.6(a) a sketch of the fcc structure is given. The hcp (0001) and the fcc (111) surfaces have the same crystal symmetry C_{3v} . For a single or double monolayer it is impossible to define a difference between the two crystal stacks. The difference occurs when three layers are deposited. The fcc has a ABC structure whereas the hcp has ABA.

Pt and the Au grow on top of the Co with the fcc $[\bar{1}\bar{1}1]$ direction parallel to the hcp $[\bar{1}100]$ direction. In order to understand if a pseudomorphic growth of Pt or Au on the Co is energetically favorable one can analyze the bulk lattice mismatch along one of the main symmetry directions:

$$\Delta a_{\text{hcp}[11\bar{2}0]} = \frac{\sqrt{2}/2a_{\text{Pt}} - a_{\text{Co}}}{a_{\text{Co}}} = 10.6\% \quad \Delta a_{\text{hcp}[11\bar{2}0]} = \frac{\sqrt{2}/2a_{\text{Au}} - a_{\text{Co}}}{a_{\text{Co}}} = 15.3\% \quad (5.6)$$

The lattice mismatch does not allow a pseudomorphic growth of the two materials on the Co surface [112].

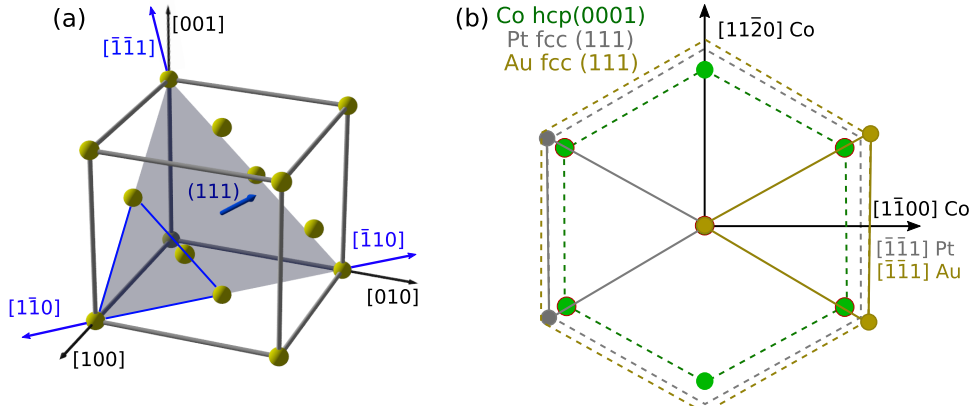


Figure 5.6: (a) Crystal structure of a fcc lattice. The plane (111) is lighted in blue. (b) Epitaxial relationship between the Co hcp (0001) and the Pt fcc (111) surface.

5.2.2 Substrate preparation and characterisation

The quality of the substrate strongly influences the quality of the sample and the quality of the sample can change the magnetic properties. In order to study the crystal magnetic properties, to perform BLS spectroscopy or to study the DW motion it is fundamental to have a homogeneous system. Indeed impurities in the samples can strongly influence the results. In the DW motion a high density of defects involves a high density of pinning centers that increases the magnetic field needed to exit from the creep regime. In BLS spectroscopy the defects can act as scattering points for the Spin Waves and enlarge the resonance peaks. On the other hand, there are situations where a high density of defects can help to achieve the researched physics. For instance, we have seen that skyrmions are stable without applied field in a small range of magnetic parameters (Sec. 4.4.2) or in nano-patterned structures. In a continuous film the presence of small defects may lead to confinement and allow the stabilisation of skyrmionic bubbles.

The substrates used during this work are 50.8mm (2 inch) commercial C plane (0001) sapphire wafers. The wafer presents two sides, one polished to the atomic step roughness and one unpolished. In order to use these substrates for the deposition several steps have to be carried out:

- **Back deposition:** During the epitaxial deposition it is fundamental to heat the sample to perform annealing processes. Since the oven in the deposition chamber works via the emission of photons and the sapphire is transparent to visible radiation, it is necessary to cover the unpolished wafer side with a layer of some heavy metal that helps the photon absorption. This deposition is performed in a sputtering deposition chamber on the full wafer. Initially a W 15 nm layer was deposited, but it was subsequently replaced with Tantalum (Ta). Ta has a stronger adhesion with the sapphire, i.e. the bond between the two surfaces is stronger.
- **Orienting:** Before cutting, the substrate is oriented with Laue diffraction in order to find the direction where the grown Co will have the main axes.
- **Cutting:** The substrate slot in the deposition chamber has a $86 \times 68 \text{ mm}^2$ dimension and the wafer has to be cut. The substrates are cut along specific directions in order to obtain the Co main axes along the long and short sample directions.
- **Cleaning:** before entering in the UHV chamber the substrates have to be cleaned in order to avoid the degradation of the vacuum and to allow a homogeneous crystal growth.

The wafer surface quality can strongly change from one piece to the other, and the cutting, orientation and back deposition can degrade the substrate quality. Therefore during this work several protocols have been developed in order to obtain the highest substrate surface quality.

Crystal orientation and cutting

In Sec. 5.2.1 we have seen that epitaxial W(110) on Al_2O_3 grows with the main axes oriented with a given angle with respect to the Al_2O_3 main axes. In particular, as shown in Fig. 5.7, the W [110] direction after the annealing will be parallel to the sapphire $[\bar{1}104]$ direction. Laue diffraction on (11 $\bar{2}$ 0) Al_2O_3 has been performed in order to find this crystallographic direction with respect to the Al_2O_3 [0001] direction that is perpendicular to the flat border of the wafer.

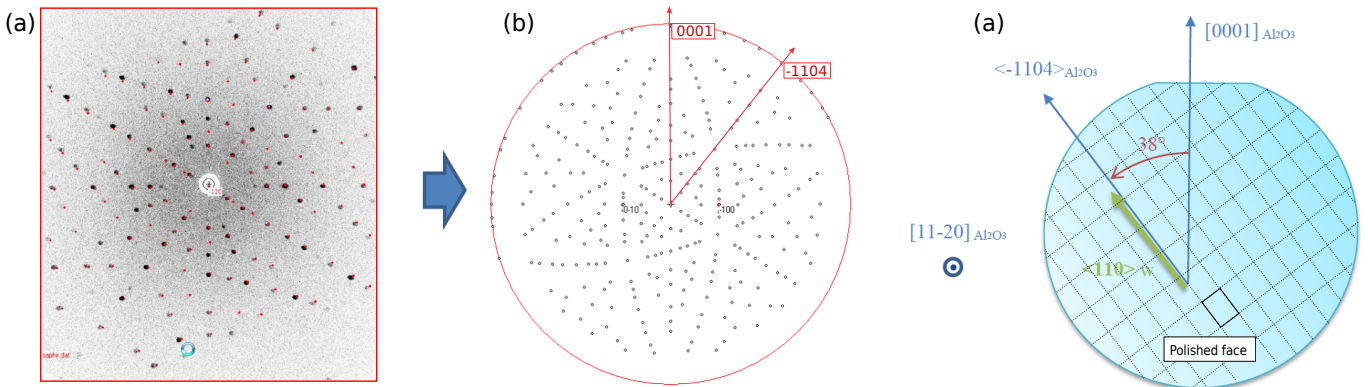


Figure 5.7: (a) Laue diffraction pattern from the sapphire wafer (b) Expected diffraction pattern for a (11 $\bar{2}$ 0) Al_2O_3 surface and fit of the experimental data (c) Sketch of the crystallographic directions necessary for the wafer cutting.

The measurements and the analysis have been performed by Jérôme Debray from the pôle 'Cristaux Massifs' of the Institut Néel. This study allows to cut the substrates with the longer side parallel to the W[110] direction. The cutting has been performed with a diamond saw. A sketch of the lines along which the sample is cut are shown in Fig. 5.7(c).

Surface quality

In this part several methods for cleaning the substrate surface will be discussed. The substrate surface can have different kinds of contaminant materials and defects of different dimensions. In order to avoid a

high density of defects and obtain the most homogeneously grown crystal it is necessary to characterize and remove the impurities and the defects. Since the impurities and the defects are different on each wafer, all the wafers used for the crystal growth have been analysed.

Optical microscopy and AFM have been performed to study the presence of contaminant materials and defects on the surface at the nanoscopic scales. Fig. 5.8(a) shows a crystal with a high density of scratches whereas Fig. 5.8(b) shows a substrate surface with holes. They are a few nanometres deep, they may be caused by errors in the polishing and make the substrates unusable for a layer-by-layer epitaxial growth.

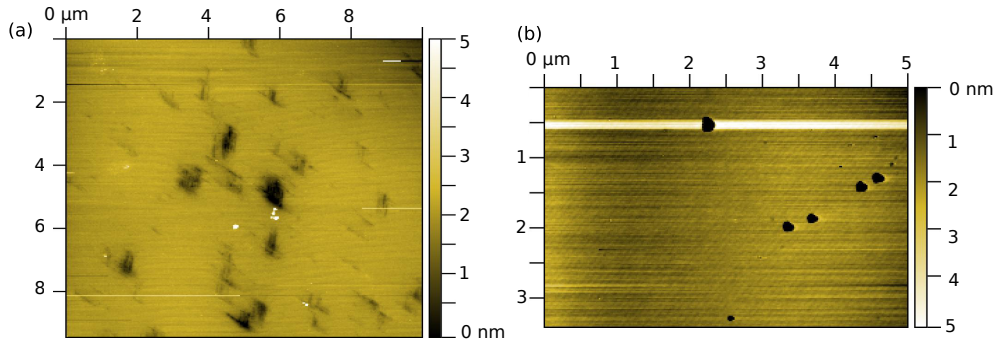


Figure 5.8: AFM microscopy in tapping mode of the surface of commercial Al_2O_3 wafers (a) atomically flat surface with the presence of 2-5 nm deep scratches (b) atomically flat surface with the presence of holes deeper than 3 nm.

Only the substrates with an atomically flat surface and without defects have been chosen for continuing the substrate preparation. Fig. 5.3 shows a substrate surface with the presence of large atomic terraces. They are 2\AA high and $1\ \mu\text{m}$ wide.

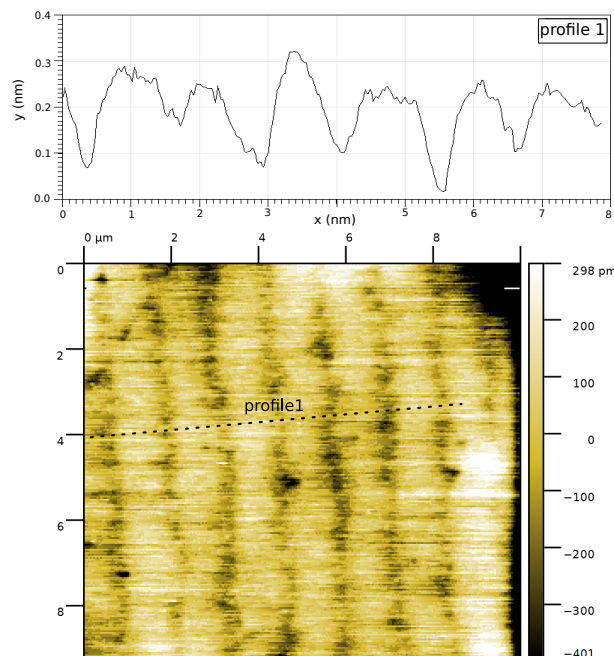


Figure 5.9: AFM microscopy in tapping mode of the surface of a commercial Al_2O_3 wafer shows the presence of atomic terraces. The plot shows the surface height along the black line (profile 1)

The substrate surface was often found with larger dimensions contaminants, that have been studied with optical microscopy. Fig. 5.10 shows a substrate surface with a presence of contaminants on the microscopic scale. The origin of these contaminants is not understood, a chemical study with Energy-dispersive X-ray spectroscopy (EDS-X) shows a high concentration of carbon indicating an organic nature.

In order to avoid extra defects and contaminants on the surface during the process of back deposition, orientation and cutting, the cleaning of the surface has been performed on cut substrates and after a

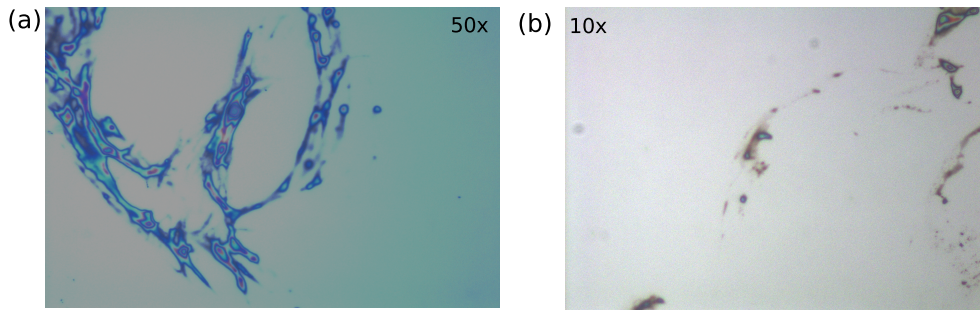


Figure 5.10: Optical images of contaminants on a surface of a commercial Al_2O_3 wafer : (a) 50x magnification image; (b) 10x magnification image.

W deposition on the unpolished face. A critical point during the cleaning process was to eliminate the contaminants without removing the W or Ta layer. A continuous W or Ta layer is fundamental in order not to generate gradients of temperature on the sample during the annealing processes. Three different approaches have been tested for cleaning the surfaces:

- **Chemical approach:** the substrates have been exposed to the modified RCA protocol [122]. The protocol has been repeated several times changing the time of exposure to $\text{H}_2\text{SO}_4 + \text{H}_2\text{O}_2$ 3:1 (18 min, 18 min + 2 min, 18 min + 4 min). Optical images have been taken of the surface after each step. Up to 18+2 min. the surface still presents contaminants. At 18+4 min. the contaminants start to reduce their volume but the W or Ta layer is locally removed. Moreover AFM microscopy (Fig. 5.11) has been performed on the substrates exposed for 18+4 min to $\text{H}_2\text{SO}_4 + \text{H}_2\text{O}_2$. The surface quality is strongly reduced and a high density of small holes is found.

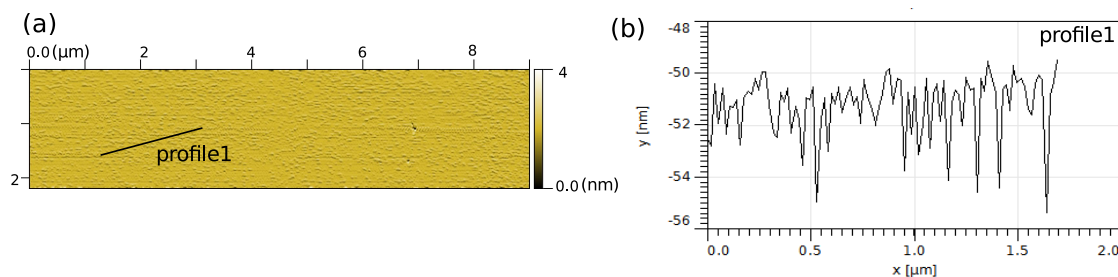


Figure 5.11: (a) AFM microscopy in tapping mode of the surface of a commercial Al_2O_3 wafer after the modified RCA protocol with $\text{H}_2\text{SO}_4 + \text{H}_2\text{O}_2$ 18+4 min exposure time. The surface presents a high density of small holes. (b) The size and the depth of the holes is shown in the height plot along the black line (profile 1)

The obtained results with the modified RCA protocol do not satisfy the quality pre-requisites necessary for the layer-by-layer epitaxial deposition.

- **Thermal approach:** the substrates have been exposed to a heating process under controlled atmosphere. This process has been implemented in an oven under O_2 atmosphere. After a treatment at relative low temperature (1000°C) for 1 hour the contaminants do not disappear and the W layer starts to show signs of degradation. For higher temperature (1200°C) for 1 hour the substrate surface starts to change morphology. The AFM image in Fig. 5.12 shows the topography of a cluster formed on the surface after the thermal process.

The surface quality obtained with the chemical and heating processes again did not satisfy the pre-requisites for the epitaxial growth. It is important to affirm that a deeper study and a more precise analysis could be performed in order to obtain better results. On the other hand I preferred to change strategy and find a process that allows to clean only the polished face without modifying the W back layer. A possibility was to use Plasma cleaning, which allows to act only on one surface.

- **Plasma cleaning:** the polished face of the substrate is exposed to a plasma of O_2 . Several combinations of power and time have been used. The exposure for 15 min. with 10W power gives the best

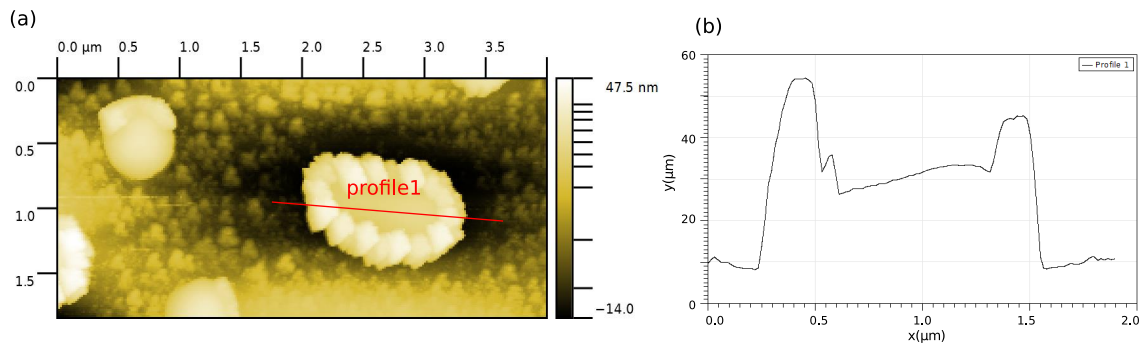


Figure 5.12: (a) AFM microscopy in tapping mode on the surface of a commercial Al_2O_3 wafer after a thermal process (1200°C for 1 hour) in an oven under controlled O_2 atmosphere. The surface shows the presence of clusters. (b) The height and lateral dimension of the cluster are shown in the height plot along the black line (profile 1)

results and allows to strongly reduce the surface covered by the contaminants without deteriorating the W layer that in this process is hidden from the plasma. The substrate surface after the process shows an atomic roughness. In Fig. 5.13 the plot of the height shows a surface modulation of ± 0.2 nm that corresponds to the thickness of one atomic layer. The absence of atomic steps makes this surface a perfect base for growing layer-by-layer epitaxial systems.

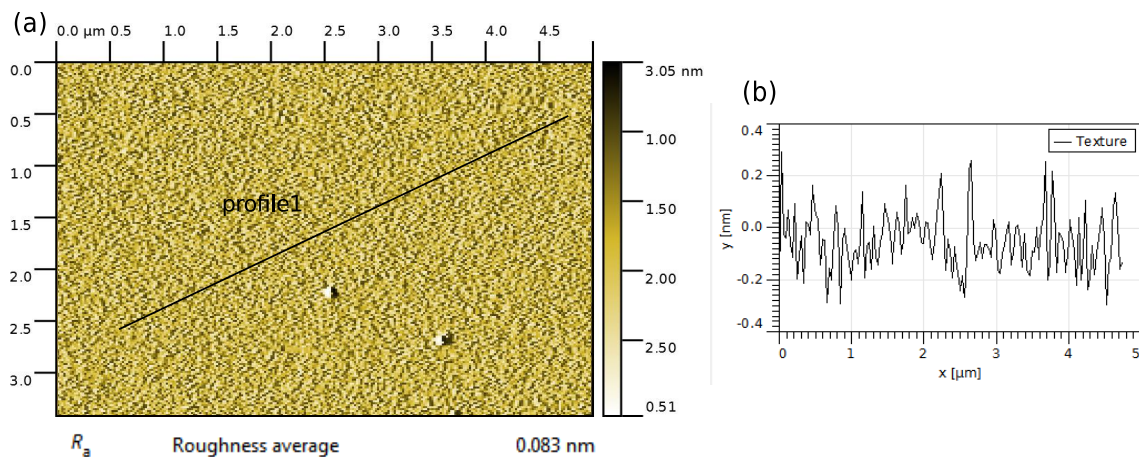


Figure 5.13: AFM microscopy in tapping mode on the surface of a commercial Al_2O_3 wafer after the exposure to 15 min. with 10W of O_2 plasma. (a) The surface is atomically flat and without atomic terraces for a wide area $5 \times 3.5 \mu\text{m}^2$. (b) The height plot along the black line (profile 1) shows surface modulations of ± 0.2 nm

Even in this case longer exposition time or stronger power change the surface topography. In Fig. 5.14 the AFM image for 15 min. with 20W power are shown. The surface presents a high density of small holes of 1-2 nanometers deep and 10 nm wide.

Before entering the substrate into the UHV system it is important to perform an extra cleaning. This process is performed with the application of:

- 5 min in RBS detergent under ultrasound application.
- 5 min in acetone under ultrasound application.
- 5 min in ethanol .
- drying with N_2 .

The drying process is extremely delicate and can strongly influence the substrate surface quality.

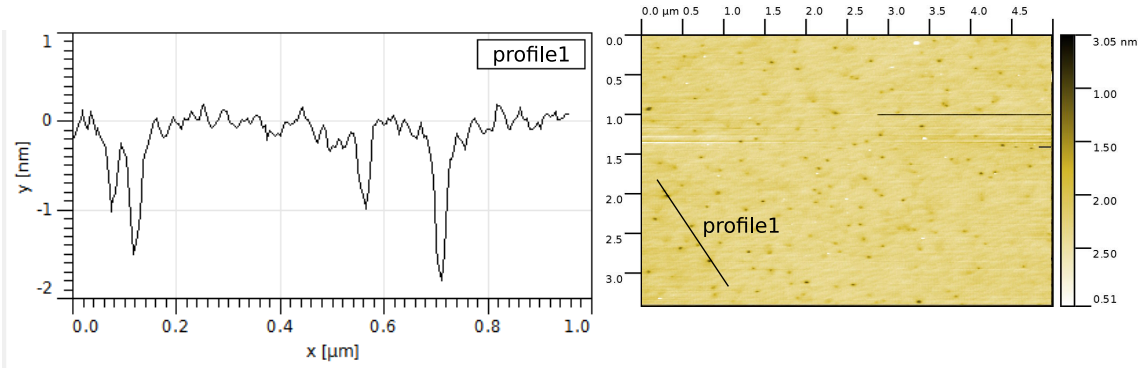


Figure 5.14: AFM microscopy in tapping mode on the surface of a commercial Al_2O_3 wafer after the exposure to 15 min. with 20W of O_2 plasma. (a) The depth and dimensions of the holes are shown in the height plot along the black line (profile 1) (b) It shows the presence of a high density of holes of small size.

5.2.3 Growth parameters and crystal orientation

In this part the processes and technical parameters that have been used during this thesis work for the deposition of W\Co\Pt and W\Co\ Au trilayers in the UHV chamber are described.

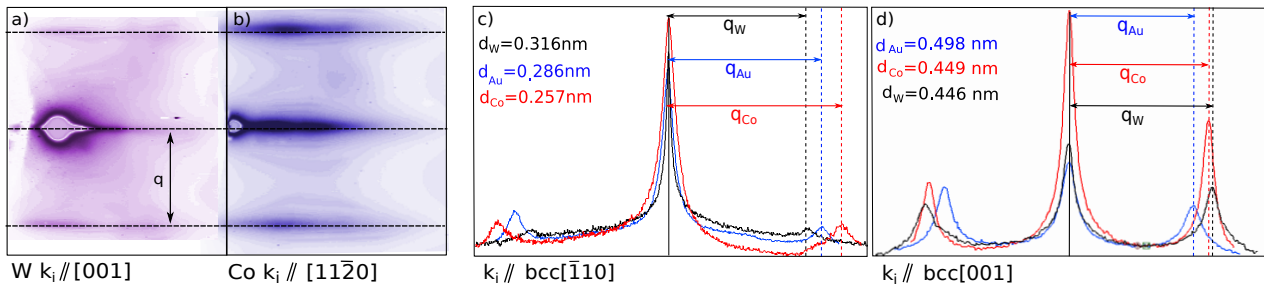


Figure 5.15: a) RHEED pattern of the W(110) surface with the electron beam parallel to the [001] direction. b) RHEED pattern of the Co surface with the electron beam parallel to the $[11\bar{2}0]$ direction (parallel to the bcc [001] direction). c) d) Plots of the RHEED intensity from the Gold (blue), Cobalt (red) and Tungsten (black) surfaces with the electron beam along the bcc[001] in c) and along the bcc $[\bar{1}10]$ in d)

The substrates are exposed to two thermal treatments. The first one is performed in the oven in the "Analysis" chamber (Sec. 3.1). The current is increased in a filament up to 5.5 Amp and kept constant until the pressure goes back in the 10^{-10} mPa range. The substrate is then moved into the Riber chamber where the oven current is increased up to 12 Amp (800 °C) and kept constant for 1 hour. This double stage thermal treatment allows to degas the substrate without deteriorating the vacuum of the Riber chamber. During the deposition or between two stages RHEED measurements are performed in order to control the epitaxial relationships and the quality of the crystals.

The $(11\bar{2}0)$ surface of the Al_2O_3 single crystal is first used as the substrate for growing a thin film of Mo (0.8 nm) followed by the deposition of a 8 nm thick W film. A high laser power ($p \simeq 1.2\text{W}$) and a focused spot are necessary for the target evaporation and to obtain a deposition rate of 0.1 nm/min. The obtained stack is annealed at 1200 K for 1 hour. During this annealing the Mo underlayer promotes the selection of a unique epitaxial relationship, avoiding twins and yielding a single-crystalline film [118]. Reflection High-Energy Electron Diffraction (RHEED) (Fig. 5.15) confirms the disappearance of the W twins and the correct epitaxial relationship (Fig. 5.16). Since the W and the Mo lattice parameters are really close ($a_W - a_{Mo} = 2pm$) it is impossible to discriminate the two materials in the RHEED pattern.

A Co film is deposited with different profile shapes as a function of the experiment to be carried out. Co wedge layers are grown in order to study the magnetic properties as a function of the sample thickness

whereas samples with constant thickness steps are realized for the study of DW motion or for performing BLS spectroscopy (Fig. 5.17). The thickness modulation can be realized by covering part of the sample during the deposition with the mask.

The best condition for layer-by-layer growth was obtained by progressively warming the sample from room temperature to 448 K while the Co thickness increases from 0 to 1.5 nm. In order to reduce the droplet formation, for the Co deposition the laser power was decreased to $P \simeq 0.8W$ and the spot size increased obtaining a slow deposition rate ($0.5\text{\AA}/\text{min}$) from a larger target surface.

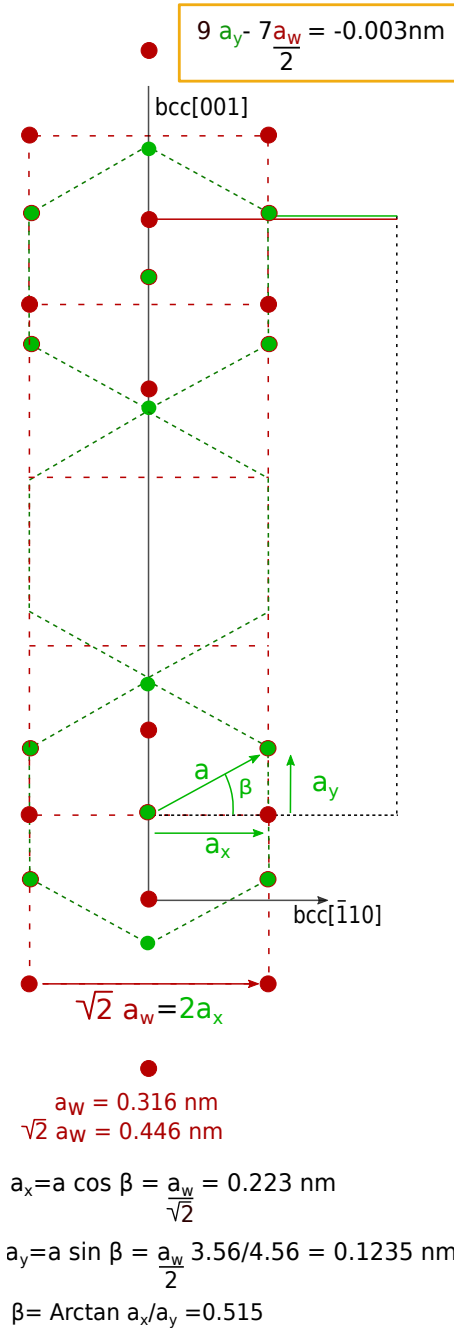


Figure 5.16: Sketch of the complete Co/W superstructure.

The immiscibility between Co and W guarantees a flat and sharp interface. RHEED patterns [123] demonstrate the retained single crystal feature through the Nishiyama-Wassermann epitaxial relationship. The lattice misfits along the main in-plane crystallographic directions are $\Delta a_{bcc[\bar{1}10]} = \frac{\sqrt{2}a_w - \sqrt{3}a_{Co}}{\sqrt{2}a_w} = 2.98\%$ and $\Delta a_{bcc[001]} = \frac{a_w - a_{Co}}{a_w} = 20.79\%$ where a_w and a_{Co} are respectively the bulk *bcc* and *hcp* lattice parameters. Along the *bcc* $[\bar{1}10]$ direction the Co is expected to grow pseudomorphically ($a_x = \sqrt{2}/2a_w$), up to 10 Co monolayers (1ML $\simeq 0.2 \text{ nm}$) [120]. Along the *bcc*[001] direction, the misfit instead is large implying

that the Co structure relaxes for a thickness between 2 and 4 ML ($a_y = 3.56/4.56 \frac{a_W}{2}$ [120]), with a_x and a_y defined in Fig. 5.16. Along the $bcc[001]$ direction, the Co-W crystal forms a superstructure with a period of $9a_y$ (1.1 nm), reasonably smaller than the characteristic magnetic length scales even in ultrathin Co films.

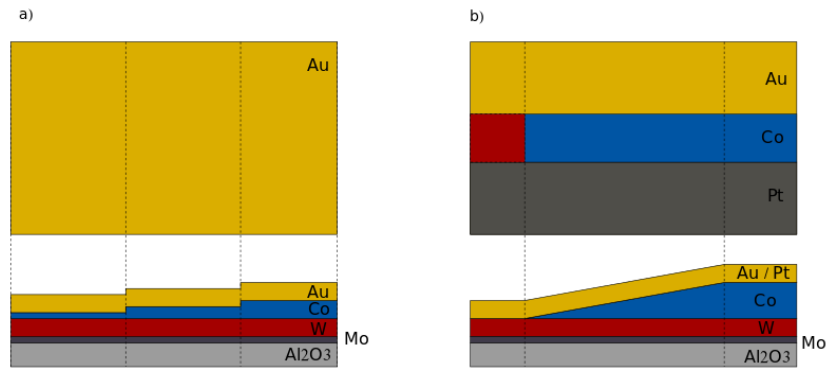


Figure 5.17: Sketch of two different kinds of samples that can be realized using the mask during the deposition.

Finally, a 1.5 nm-thick *fcc* Au(111) or/and Pt(111) cap layer are deposited at room temperature in order to promote out-of-plane anisotropy and protect the stack from oxidation. The mask allows to deposit the two materials separately in the same sample (Fig. 5.17). A part of the sample can be left without capping layer in order to perform in-situ STM directly on the Co layer and study along the wedge the layer-by-layer growth. Au and Pt present a high heat conductivity, meaning that the deposition conditions have to be optimized in order to reduce the presence of recoil droplets. Fig. 5.18 shows the presence of recoil droplets of Au on a continuous film of Au. In order to reduce this phenomenon the laser spot is strongly defocused in order to reduce the laser fluence for decreasing the local heat.

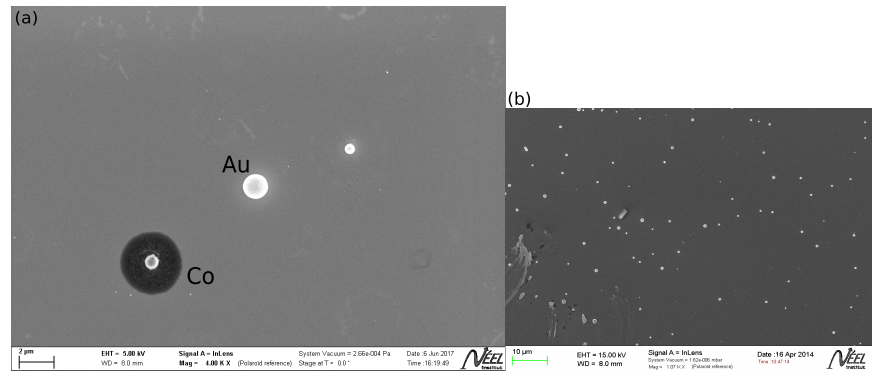


Figure 5.18: EDSX image of a continuous Au film with the presence of Au droplets.

The RHEED patterns in Fig. 5.15 confirm the relaxed growth of the Au layer. The Au and Pt *fcc* (111) surfaces have a C_{3v} symmetry that summed to the rest of the stack does not change the total system symmetry (C_{2v}).

5.2.4 Crystal symmetry characterisation by GIXRD

Grazing incidence X-ray diffraction measurements were performed in collaboration with Maurizio de Santis (Institut Néel) at the BM32 beamline of the European Synchrotron Radiation Facility, on the capped Au/Co/W(110) multilayer with a homogeneous Co layer of 3 ML thickness. These measurements have been performed to confirm the RHEED measurements and to study the complete 3D stack symmetry. GIXRD allows to scan the reciprocal lattice of the stack.

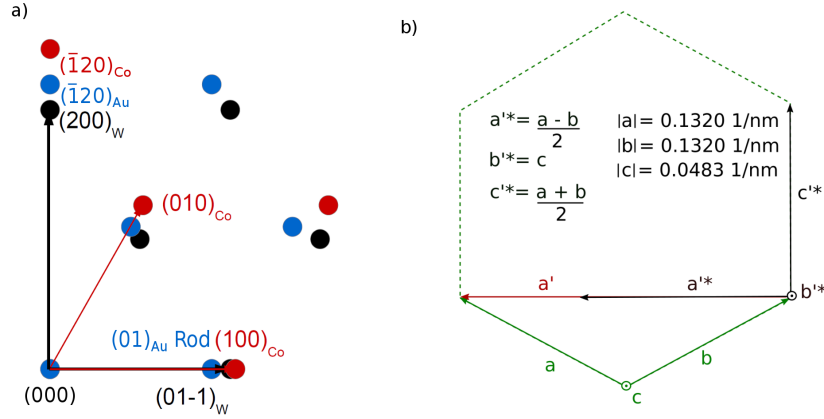


Figure 5.19: a) Bragg peaks for *fcc* Au(111)/Co(0001)/*bcc* W(110) crystals in their epitaxial relationship. b) Sketch of the reciprocal frameworks fixed on the Al_2O_3 crystal used to describe the Bragg peaks and values of the lattice parameter for a Al_2O_3 crystal.

The Bragg peaks can be described in a reciprocal framework fixed on the Al_2O_3 crystal. The Al_2O_3 crystal has a C_{3v} symmetry whereas Au/Co/W(110) has a C_{2v} symmetry. Then, in order to better describe the W, Co and Au peaks we define a new framework with perpendicular axes as shown in Fig. 5.19. Hence we can formulate an expression for the lattice configuration in the reciprocal space:

$$\mathbf{Q} = (Ha^*, Kb^*, Lc^*) \quad |\mathbf{Q}| = \sqrt{(H\sqrt{3}|a|)^2 + (K|c|)^2 + (L|a|)^2} \quad (5.7)$$

with the reciprocal lattice parameter defined in Fig. 5.19. The momentum transfer modulus was scanned in the surface plane ($Q_z = 0.08 \text{ \AA}^{-1}$) along both the *bcc*(001) and *bcc*($\bar{1}10$) directions. In the first case, shown in Fig. 5.20, three Bragg peaks are observed corresponding to W(002), Au($\bar{1}20$) and Co($\bar{1}20$) reflections, respectively. The registry position of the cobalt layer along the *bcc*($\bar{1}10$) direction is confirmed by the scan of Fig. 5.21. In this case only one additional peak is observed, attributed to the relaxed Au layer. The Co(100) peak merges with the W($\bar{1}10$) one. Angular scans show that the main crystallographic axes of the Co film are aligned with the tungsten ones. Defining β as the angle between the Co bonds 01 and 01' (Fig. 5.16), the distortion of the Co crystal can be determined. This angle can be calculated from the position of the Co peaks (100) and (010) ($\beta = 0.51$). This value is comparable with the one obtained by RHEED measurements and one can conclude that the Co/W interface is hardly modified by the capping layer growth.

The scan along Q_z with fixed values of (Q_x, Q_y) on the Co($\bar{1}20$) peak allows to determine the complete crystal symmetry of the Co layer. The presence of two peaks in Fig. 5.22 demonstrates the hcp nature of the Co crystal. Indeed the spacing between the two peaks corresponds to the distance between the two Co layers ($d=0.419$ nm)

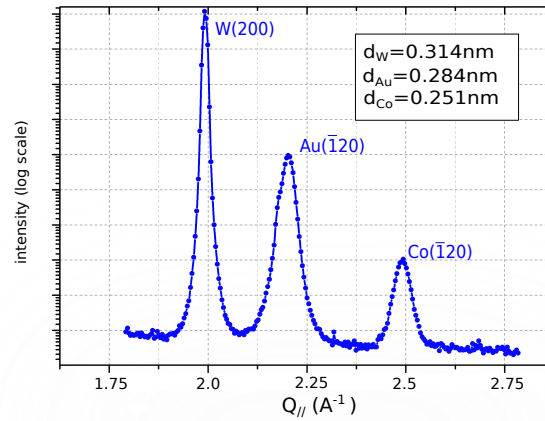


Figure 5.20: GIXRD measurements performed scanning the momentum transfer parallel to the surface plane, along the $bcc(001)$ direction

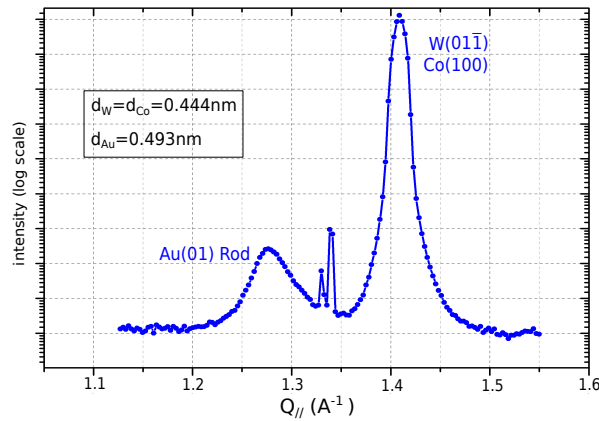


Figure 5.21: Scan parallel to the $bcc(\bar{1}10)$ direction

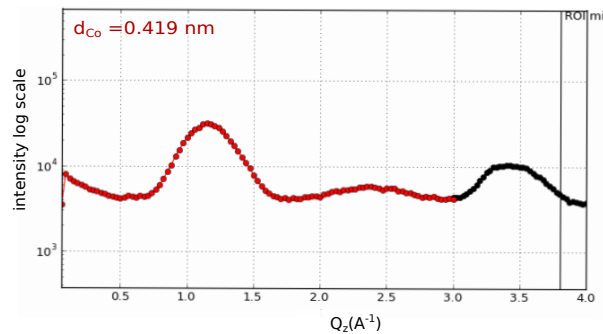


Figure 5.22: Scan along the Q_z direction with fixed values of (Q_x, Q_y) on the $Co(\bar{1}20)$ peak

5.2.5 Crystal surface characterisation by STM

STM has been performed on the uncapped part of a Au-Pt/Co/W(110) sample deposited with a Co thickness gradient. These measurements had the aim to verify the layer-by-layer growth of the Co layer and calibrate the Co thickness. Fig. 5.23 shows the STM pictures taken along a Co wedge. The Co islands, as shown in Fig. 5.23(f), have the height of the Co interplane distance (2\AA), and their lateral size increases for increasing values of the Co thickness. The growth is not perfectly layer-by-layer, since in Fig. 5.23(b) three atomic levels can be detected. However, the sample can be considered to have a homogeneous thickness from the magnetic point of view because the characteristic exchange length (l_{ex}) is comparable with the average distance between the islands [124]. These images allow us to have an extra confirmation of the sample

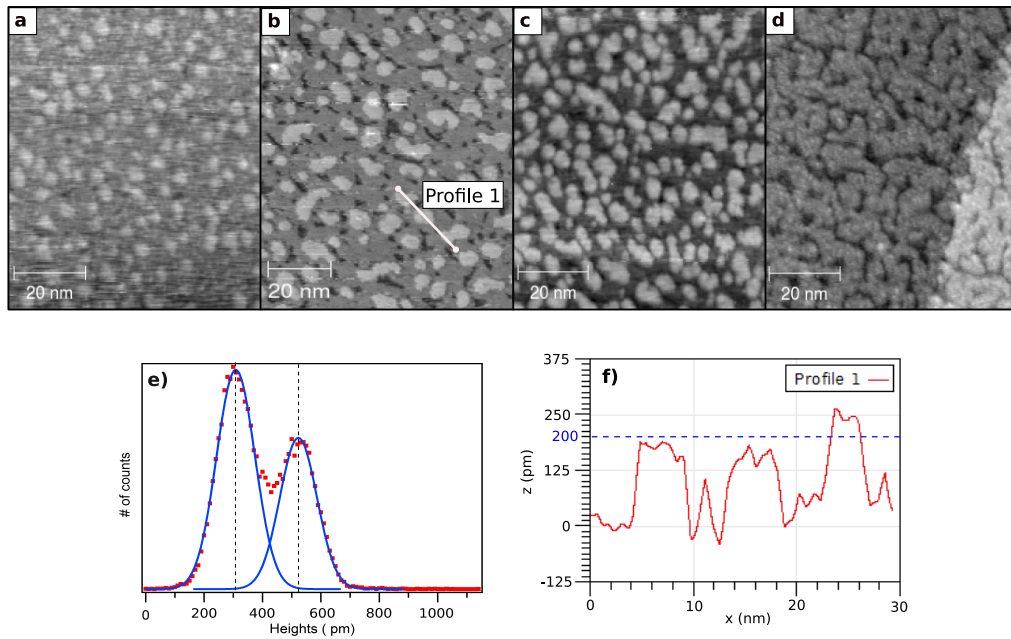


Figure 5.23: STM pictures of Co islands during a quasi-layer-by-layer deposition in different positions along a Co wedge. a) 1.15 ML b) 1.45 ML c) 1.62 ML d) 1.93 ML are the thickness of the Co layer that can be calculated studying the coverage ratio of Co islands. e) Plot of the heights of the islands as a function of the STM picture (b). f) plot of the island heights along profile 1 in the STM picture (b)

thickness. Indeed it is possible to calculate the ratio of surface covered by islands as a function of the position in the wedge. The data are fitted with a Gaussian function for each atomic step, as in Fig. 5.23(e). The thickness in ML ($t = n + CR$) is calculated via the islands coverage ratio $CR = \frac{I(n+1)}{I(n+1)+I(n)}$, where $I(n)$ is the Gaussian integral for a given layer n . The higher step linewidth function is constrained using the value of the lower step function. This allows to avoid the broadening of island sizes due to the STM tip shadow effect.

5.3 Magnetic characterisation

In this section the magnetic characterisation of the W\Co\Pt and W\Co\Au systems is presented. These epitaxial systems have a C_{2v} symmetry. It arises from the bcc W(110) surface that at the interface with the hcp Co(0001) can induce anisotropy in the interface interactions like the DMI and the magneto-crystalline anisotropy. The fcc Pt (111) and the fcc Au (111) layers do not change the system symmetry.

Kerr magnetometry allows the acquisition of hysteresis loops along the sample wedges and thus to study the changes of magnetic properties as a function of the thickness. Since the spin-orbit interaction connects the space and the magnetic degrees of freedom one can expect magnetic interactions with the same symmetry as the crystal structure.

DW dynamics is theoretically described with a micromagnetics model. This allows to understand the studies performed on the DW expansions and how calculate the DMI strength and sign along different in-plane directions. Finally, BLS measurements allowed us to determine the quantitative values of the magnetic interactions along the different crystallographic directions.

5.3.1 Kerr magnetometry

Focused Kerr magnetometry has been used to study the magnetic hysteresis loops as a function of the Co thickness. These measurements were performed on samples with wedged Co layers. The Co wedges are designed in order to study two transitions in the magnetic order.

- The **paramagnetic-ferromagnetic** transition occurs at low thickness, generally between 1 and 2 ML for Co, and it depends on the thickness dependence of the Curie temperature (2.8).
- The **out-of-plane to in-plane** transition occurs when the surface dipolar interaction starts dominating the interface anisotropy.

Following the works in literature on similar systems [120], the Co wedge is designed and deposited with a thickness varying from 0 to 8 ML. The transitions can thus be studied analysing different positions of the same sample.

W\Co\Pt

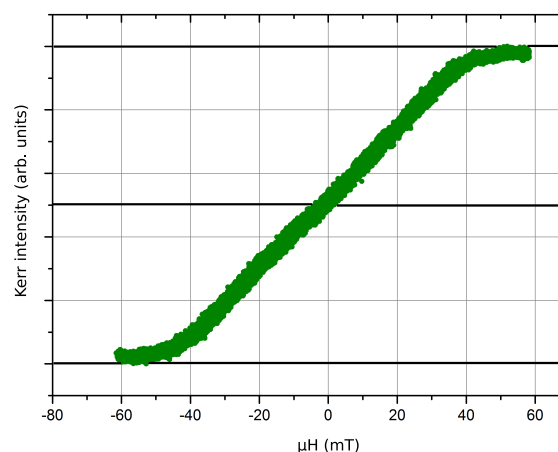


Figure 5.24: Hysteresis loop obtained by focused polar Kerr on a Pt/Co/W(110) system with 3 Co ML.

Fig. 5.24 shows the polar magneto-optic response of the W\Co\Pt system when an external magnetic field is applied perpendicular to the surface. The magnetic field and the beam are aligned and the method is sensitive to the perpendicular component of the magnetisation. The hysteresis loop shows no coercivity and zero magnetic remanence. This indicates that the normal to the sample is a hard magnetic axis of the system and that the easy axis is in the sample plane. This means that the in-plane Co/W interface anisotropy

dominates over the Co/Pt out-of-plane anisotropy for all the thicknesses studied. Indeed hysteresis loops with a shape similar to the one shown in Fig. 5.24 were found for all the points studied along the Co wedge.

The measurements have been performed on a sample as shown in Fig. 5.17(b). In this sample one can find a small region between the Pt capped part and the uncapped part where the Pt layer decreases with a steep wedge generated by a shadow effect of the mask during the Pt deposition (Fig. 5.25(a)). Interesting results have been found in this region. Indeed the shapes of the hysteresis loops in Fig. 5.25(b) show the presence of an out-of-plane magnetisation. For small Co thickness a hysteresis loop with zero coercivity is found, typical of the paramagnetic order. For larger thickness the system becomes ferromagnetic with an out-of-plane magnetisation up to 8 ML and a large coercive field of 20 mT.

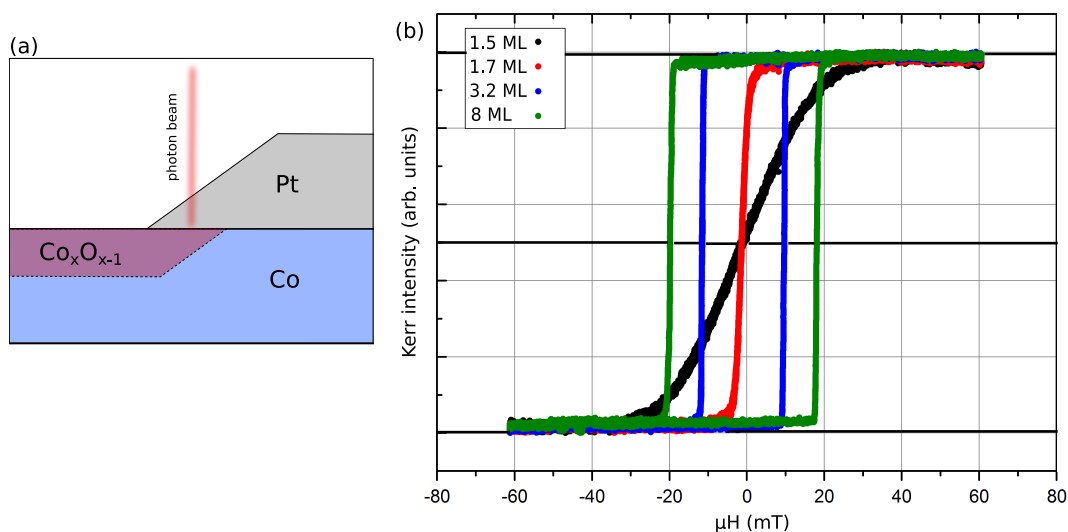


Figure 5.25: (a) Sketch of the sample section where the Kerr measurements are performed. (b) Hysteresis loops obtained by focused polar Kerr on different points of the Co wedge in a Pt/Co_xO_{1-x}/Co/W(110) system.

This result can be explained considering a partial oxidation of the Co layer. It reduces the real thickness of the Co layer and induces a new interface Co_xO_{1-x}/Co that may induce an out-of-plane anisotropy. In literature, systems with a Co_xO_{1-x}/Co interface [106] can be found that show an out-of-plane magnetisation, but usually with the other interface also favoring an out-of-plane magnetisation. In our case, the other interface (Co/W) favors in-plane magnetisation, suggesting a strong perpendicular anisotropy at the Co_xO_{1-x}/Co interface.

W\Co\Au

The hysteresis loops obtained for different Co thicknesses in the W\Co\Au wedge are plotted in Fig. 5.26. The polar Kerr cycles are measured as a function of the out-of-plane magnetic field strength. For small thickness the Curie temperature is below room temperature, i.e. the magnetic correlation between the Co moments is weaker than the thermal fluctuations. In this regime the Co is paramagnetic and there is no Kerr signal [39]. The black loop in Fig. 5.26 (1.7 ML) shows the presence of a finite magnetisation, a saturation field of $\mu_0 H_{\text{sat}} = 10$ mT and the absence of coercivity. This indicates a superparamagnetic state where the Co islands are ferromagnetic with a weak mutual interaction. The out-of-plane interfacial MCA is the prevalent effect for the thickness range between 1.7 ML and 4.5 ML. Indeed the square hysteresis loop (red line in Fig. 5.26) for out-of-plane magnetic field shows the presence of an out-of-plane easy axis. The change of shape and the increase of the saturation field for the largest thickness (blue line in Fig. 5.26) show that for that thickness the easy axis is not parallel to the applied field anymore. When the thickness increases [4.5 – 5.1 ML], the volume MCA is comparable to the interface one and the easy axis progressively tilts in

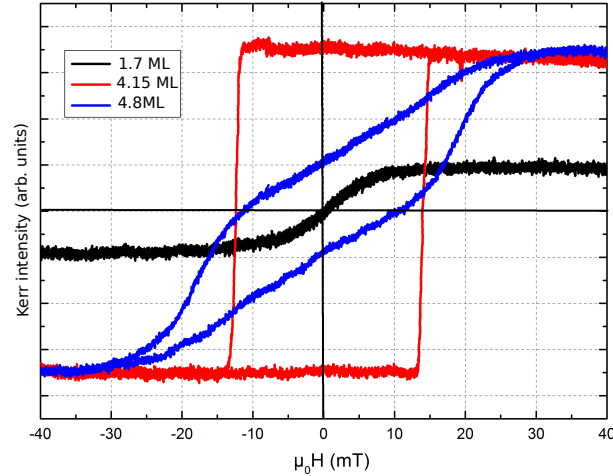


Figure 5.26: Hysteresis loops obtained by focused polar Kerr on different positions along a Co wedge in Au/Co/W(110).

the sample plane. The spin reorientation range depends on the strength of the in-plane MCA imposed by the epitaxial growth on W(110) and hence on the surface quality. The spin reorientation transition range in our sample is comparable with the thickness values found by [112] for the same system.

5.4 DW motion

In this section the main models used in this work for the description of the DW dynamics in the presence of magnetic fields are described. The DW dynamics strongly depends on the DW profile and energy and thus on the magnetic interactions that determine them. Since real systems are inhomogeneous the DW dynamics can be strongly influenced by the distribution in space of the magnetic energies. The magnetic configurations can pin in points (pinning centers) where the magnetic properties change abruptly.

The DW dynamics will first be studied in homogeneous systems with the Landau-Lifshitz-Gilbert equation in the macro-spin approximation. This approach will be used for describing the speed of a DW in an out-of-plane magnetised system under the presence of DMI. After that, the presence of pinning centers will be considered and the creep theory will be introduced.

5.4.1 DW motion in systems with DMI

In this section the DW motion is described in a macrospin approximation where the DW magnetisation distribution is replaced by a single spin \mathbf{m} parallel to the direction of the magnetisation in the center of the DW.

The dynamics of the DW is then reduced to the study of the effect of the different torques generated by the external magnetic field \mathbf{H} parallel to the magnetisation of one of the domains. Moreover the effect of the different magnetic interactions on the macrospin can be introduced using the concept of effective magnetic field $\mu_0 \mathbf{H}_{\text{eff}} = -\delta E_{\text{tot}}/\delta \mathbf{m}$.

The dynamics of a macrospin is described by the Landau-Lifshitz-Gilbert equation:

$$\frac{d\mathbf{m}}{dt} = -\gamma \mathbf{m} \times \mathbf{H}_{\text{eff}} - \alpha \mathbf{m} \times \frac{d\mathbf{m}}{dt} \quad (5.8)$$

where γ is the electron gyromagnetic ratio and α is the damping parameter. The equation can be simplified considering the damping term as a second order effect ($\alpha \ll 1$) and replacing the $d\mathbf{m}/dt$ term of the damping part by the effect of the torques without damping:

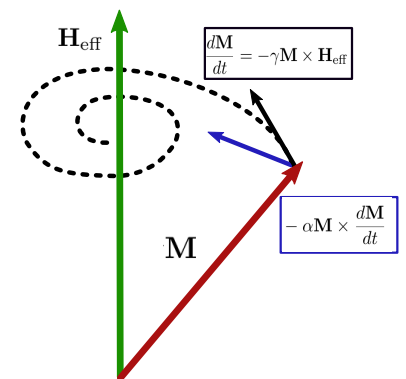


Figure 5.27: sketch of the vectorial component of eq:5.8

$$\frac{d\mathbf{m}}{dt} = -\gamma\mathbf{m} \times \mathbf{H}_{\text{eff}} - \alpha\mathbf{m} \times (\gamma\mathbf{m} \times \mathbf{H}_{\text{eff}}) \quad (5.9)$$

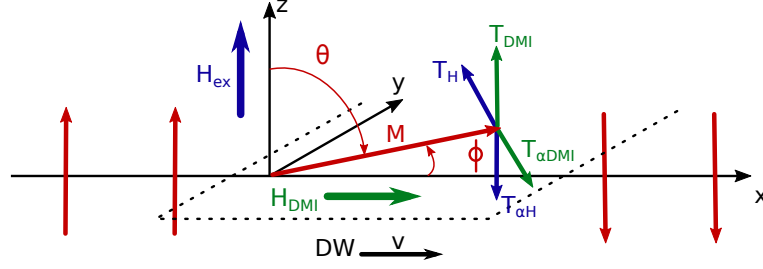


Figure 5.28: Sketch of a Néel DW and of the torques that act on the DW macrospin when an external magnetic field is applied.

The discussion is limited to the dynamics of a Néel DW stabilized by DMI in a system magnetised along \hat{z} as shown in Fig. 5.28. The external magnetic field is applied in the positive \hat{z} direction and produces a torque T_H on the DW macrospin in the positive ϕ direction. When the magnetisation deviates from the equilibrium direction favored by the DMI, the DW energy is increased. This can be described using the effective magnetic field $H_{\text{DMI}} = \frac{D}{\Delta\mu_0 M_s} \sin \phi$ parallel to the \hat{x} direction that produces a torque $T_{\text{DMI}} = \gamma H_{\text{DMI}}$ in the $-\theta$ direction. The damping resulting from this torque generates another torque $T_{\alpha\text{-DMI}} = \alpha\gamma H_{\text{DMI}}$ that acts in the $-\phi$ direction against T_H . The total torque in the ϕ direction reads:

$$T_\phi = \gamma H - \gamma\alpha \frac{D}{\Delta\mu_0 M_s} \sin \phi \quad (5.10)$$

two different situations can occur as a function of the strength of the external magnetic field.

Steady motion: if $H < \alpha \frac{D}{\Delta\mu_0 M_s}$ the external field does not overcome the pull-back DMI torque. Since T_{DMI} increases with the increase of ϕ a stable configuration ϕ_0 can be found.

$$\phi_0 = \arcsin \left(\frac{1}{\alpha} \frac{\Delta\mu_0 M_s H}{D} \right) \quad (5.11)$$

In these conditions the system is in the steady regime and the DW motion is characterized by a fixed tilt angle ϕ_0 . The DW propagates when a torque rotates the macrospin in the direction of one of the magnetic domains. The DW speed can be thus calculated studying the torque along θ . Since $\alpha \ll 1$ one can neglect the effect of the external field damping torque $T_{\alpha\text{-DMI}} \simeq T_H \rightarrow T_{\alpha\text{-H}} \simeq \alpha^2 T_{\text{DMI}}$. The variation of θ under the action of the torque reads:

$$\frac{\partial\theta}{\partial t} = T_{\text{DMI}} = \gamma \frac{D}{\Delta\mu_0 M_s} \sin \phi_0 = \frac{\gamma H}{\alpha} \quad (5.12)$$

In a framework fixed on the DW the total time derivative is zero and one can write:

$$\frac{D\theta}{Dt} = \frac{\partial\theta}{\partial t} + \frac{\partial\theta}{\partial x} \frac{\partial x}{\partial t} = \frac{\partial\theta}{\partial t} + v \frac{\partial\theta}{\partial x} = 0 \quad (5.13)$$

where v is the DW speed. Then considering a linear variation of θ as a function of x (Sec. 4.2) the DW speed reads:

$$v = \frac{\partial x}{\partial\theta} \frac{\partial\theta}{\partial t} = \frac{\pi\Delta}{\pi} T_{\text{DMI}} = \frac{\gamma\Delta H}{\alpha} \quad (5.14)$$

notice that the DW speed is phenomenologically induced by the presence of DMI but it does not depend on this interaction. It is directly proportional to the applied field and the DW width and inversely proportional to the damping parameter. One can demonstrate that this relationship holds whatever the torque keeping the DW structure is (démag, DMI, in-plane field, ...).

Precessional regime: if $H > \alpha \frac{D}{\Delta \mu_0 M_s}$ the external field overcomes the pull-back DMI torque and the macrospin starts to precess around the external magnetic field. For high values of H one can consider $T_{\text{DMI}} \ll T_{\alpha-H}$ and the DW motion is only caused by the external field damping torque. The DW speed reads:

$$v = \frac{\pi \Delta}{\pi} T_{\alpha-H} = \gamma \alpha \Delta H \quad (5.15)$$

One can notice that contrary to the previous case now the DW speed is directly proportional to the damping term.

One can define the transition between the steady and the precessional motion considering the maximum external field that the DMI can compensate. This field takes the name of the Walker breakdown field $H_{\text{walker}} = \alpha H_{\text{DMI}} = \alpha \frac{D}{\Delta \mu_0 M_s}$ and corresponds to the value of the field for which the DW has the maximum speed (Fig. 5.33).

Domain wall motion in systems with DMI and in-plane anisotropy

In system with C_{2v} symmetry the in-plane anisotropy and the DMI stabilise a Néel DW along the crystal easy axis. The DW dynamics can be calculated along this direction considering the DMI torque and the torque generated by the anisotropy effective field $H_K = \frac{2K_{\text{in}}}{\mu_0 M_s} \sin \phi \cos \phi$. Then the total torque for a DW with a ϕ polarization reads:

$$T_\phi = \gamma H - \gamma \alpha \sin \phi \left(\frac{D}{\Delta \mu_0 M_s} + \frac{2K_{\text{in}}}{\mu_0 M_s} \cos \phi \right) \quad (5.16)$$

As for the previous case 5.4.1 the dynamics can be separated into two regimes. The transition between the steady and the precessional motion can be obtained calculating the angle ϕ_0 for which the torque is maximum. It can be calculated solving the equation.

$$\frac{\partial T}{\partial \phi} = 0 \quad (5.17)$$

replacing ϕ_0 in the previous equation one can obtain the walker break down field. This problem does not present an analytical solution and must be solved numerical case by case. On the other hand one can notice that the DW motion in the steady regime arises from the DMI and in-plane anisotropy pull-back torques but the speed does not depend on their strength ($v = \frac{\gamma \Delta H}{\alpha}$).

Domain wall motion in the presence of an in-plane magnetic field

In this section, the dynamics is studied of a DW stabilised by DMI, when an in-plane magnetic field $B_{\text{in}} = \mu_0 H_{\text{in}}$ is applied in the direction of the polarisation of the DW (Sec. 4.2.4). Fig. 5.29 shows the direction of the torques acting on the DW magnetisation in a macrospin approximation.

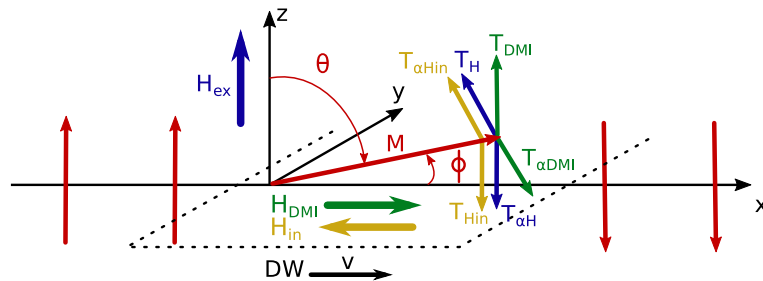


Figure 5.29: Sketch of a Néel DW and of the torques that act on the DW macrospin when two external magnetic fields are applied along the \hat{z} and the $-\hat{x}$ directions.

One can notice that the torques generated by B_{in} are parallel (anti-parallel) to the DMI ones when the field is applied parallel (anti-parallel) to the DW polarisation. Then all the calculations developed in Sec. 5.4.1 can be generalized replacing T_{DMI} with $T_{\text{DMI}} \pm T_{\text{Hin}}$. The DW speed in the two regimes reads :

$$v_{\text{steady}} = \frac{\gamma \Delta (B_{\text{in}}) H}{\alpha} \quad v_{\text{precessional}} = \gamma \alpha \Delta (B_{\text{in}}) H \quad (5.18)$$

with $\Delta(B_{\text{in}}) = \sqrt{\frac{A}{K_{\text{eff}} \pm B_{\text{in}} M_s}}$ that changes as a function of B_{in} as shown in Sec. 4.2.4. Notice that the in-plane magnetic field changes the DW width and therefore the DW speed.

The Walker field changes as a function of B_{in} and reads:

$$H_{\text{Walker}} = \alpha(H_{\text{DMI}} \mp H_{\text{in}}) = \alpha \left(\frac{D}{\Delta \mu_0 M_s} \mp H_{\text{in}} \right) \quad (5.19)$$

The in-plane magnetic field applied parallel (anti-parallel) to the DW polarisation destabilises (stabilises) the DW configuration and promotes (delays) the precession of the DW magnetisation.

The problem can be generalize in the case of systems where the DW polarization is stabilize by DMI and in-plane anisotropy. In this particular situation the torques have to be compared with DW polarization angle ϕ_0 for which the torques are maxima. This problem has not a numerical solutions and have to be solved numerical for each particular situation. One can notices that the angle ϕ_0 depends on the strength of the in-plane magnetic field and the Walker field decreases increasing H_{in} .

Soliton motion regime

When the DW speed reaches the Walker break-down the DW enters in the precessional motion. In presence of DMI the DW speed does not decrease but stays constant and a plateau in the $v(H_z)$ behaviour is found. A physical explanation of this phenomenon is given in the work of Yoshimura et al. [125] and Pham et al. [113]. The precessional regime is described by the formation of a couple of Bloch lines (BL) that propagate along the DW until they are expelled at the DW edge or annihilated with other BLs nucleated in other DW sections (Fig. 5.31(d)). In presence of DMI the subsequently formed BLs have different energies since their rotation sense are opposite, either parallel or anti-parallel to the rotation sense favored by the DMI.

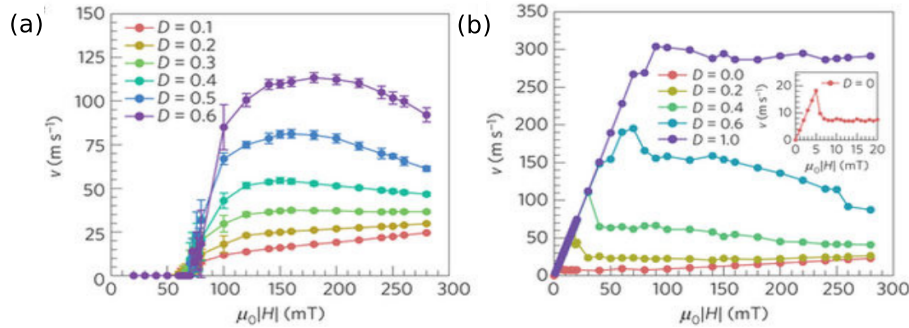


Figure 5.30: Simulated $v(H_z)$ curves in asymmetric Co/Ni wires for different values of the DMI. (a) In the presence of defects. (b) In perfect wires. Taken from Ref. [125]

The DMI causes a different width for BLs with opposite rotation sense. Like for a DW, the speed of the BLs depends on the magnetisation rotation width. One can thus expect that the BLs with different rotation sense have different speeds.

The generation of BLs can be described considering the topological number of the BL. Indeed, considering the DW direction as the axis of a 1D system one can apply the topological theory described in Sec. 4.1.1 and associate to each BL a topological charge. The BL with an anti-clockwise (clockwise) rotation carry a negative (positive) topological charge $N_{1D} = -1/2$ ($N_{1D} = +1/2$). Moreover one can associate a magnetic volume charge $Q = 1$ ($Q = -1$) when the magnetisation around the BL is head to head (tail to tail).

Four different BLs are distinguished in Fig. 5.31 as a function of the topological number and magnetic charge. During the nucleation of a couple of BLs the magnetic and topological charges are conserved and BLs with opposite charges are nucleated together. Since each couple presents different energy, width and speed, two consecutive couples will collide and annihilate with the emission of spin waves. This phenomenon acts as a channel for the dissipation of the DW energy and when the external field increases it avoids the entrance of the DW in the precessional motion. The DW speed stays thus constant at the same speed as at the Walker field (Fig. 5.30)

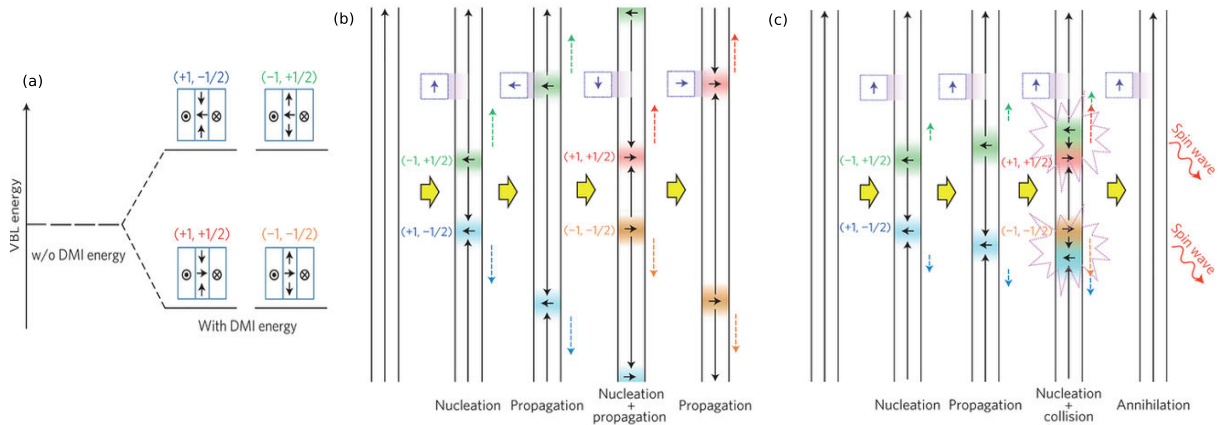


Figure 5.31: [125] (a) Energy splitting of the four BLs when a DMI that promotes clockwise DWs is introduced. The BLs are characterized by a magnetic charge $Q = \pm 1$ and a topological charge $N_{1D} = \pm 1/2$. (b) Propagation of BLs in absence of DMI. (c) propagation of BLs in the presence of DMI.

5.4.2 Creep regime

In an inhomogeneous system the DW energy depends on its position and if its energy is not high enough the DW motion will be strongly influenced by the spatial variation of the energy due to the inhomogeneities. Indeed, when the DW energy is lower than the energy variations in the system the DW stops in positions called pinning centers. An external force can deform the segment of the DW between two pinning sites and increase the DW length. This phenomenon can be described with an elastic-like energy term. When this energy is higher than the depinning energy, i.e. the energy necessary to extract the DW from the pinning potential well, the DW propagates. This phenomenon can be described with a statistical model that takes into account the competition between deformation-elastic, pinning and applied f forces in order to describe the speed of DWs [126]. When the temperature is taken into account, the speed can be described with an Arrhenius law:

$$v \propto e^{-\beta U_c \left(\frac{f_c}{f}\right)^\mu} \quad (5.20)$$

where U_c is a scaling energy constant, μ is a dynamics exponent, f_c and f are respectively the critical force to move a DW at zero temperature and the applied external force.

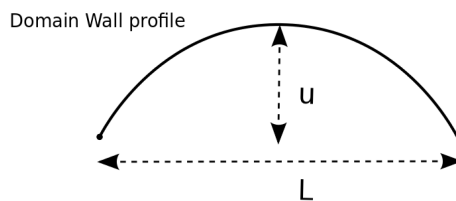


Figure 5.32: Sketch of the geometrical parameters used to describe the deformation of a DW (u) between two pinning points with a distance (L)

In an ultrathin magnetic film the DW can be described as a 1D object decomposed into segments between the different pinning centers. The parameters in eq. 5.20 can thus be determined studying a single DW segment between two pinning centers placed at a characteristics distance L . The DW deformation is described by the distance u as sketched in Fig. 5.32.

The total free energy of the DW segment reads:

$$F(u, L) = \mathcal{E}_{DW} t \frac{u^2}{L} - (\Delta \xi^2 L)^{\frac{1}{2}} - M_s H t L u \quad (5.21)$$

where t is the layer thickness, \mathcal{E}_{DW} the 1D DW energy, H the applied magnetic field, ξ the characteristic length of the disorder potential and $\Delta = f_{pin}^2 n_i \xi$, with f_{pin} the local pinning force and n_i the density of surface pinning centers.

Eq. 5.21 contains three terms:

- The first term is an elastic energy that favors the reduction of the DW lengths.
- The second term is the pinning energy strength.
- The last term is the Zeeman energy from the application of the external field.

One can define the constant L_c in order to understand the role of the DW length on the DW dynamics. L_c is called characteristic collective pinning length and its value is found setting the energy balance between the elastic and the pinning components.

$$E_{el}(L_c, u = \xi) = E_{pinn}(L_c) \quad L_c = \sqrt[3]{\frac{\mathcal{E}_{DW}^2 t^2 \xi}{\Delta}} \quad (5.22)$$

When $L < L_c$, the elastic energy dominates and the DW adjust its configuration to reach the optimal configuration. As an example, for a Pt/Co/Pt [126] system a value of $L_c = 25nm$ was found analysing the defects induced by the Co terraces.

Another interesting constant is the H_c critical magnetic field. This is the value of the external field needed to overcome the pinning effect under the condition $L = L_c$

$$E_{Zeeman}(L_c) = E_{pinn}(L_c) \quad H_c = \frac{\mathcal{E}_{DW} t \xi}{M_s t} \frac{1}{L_c^2} \quad (5.23)$$

In a system at $T = 0$ K, H_c is the field value for which the DW starts to move. At finite temperature the thermal activation allows the DW to move for H values smaller than H_c .

From the elastic strings [127] theory one can write the correlation function $\langle (u(x+L) - u(x))^2 \rangle$ that allows writing a scaling law for the displacement u and for the energy E :

$$u(L) \propto u_c \left(\frac{L}{L_c} \right)^\zeta \quad E(L) \propto U_c \left(\frac{L}{L_c} \right)^{2\zeta-1} \quad (5.24)$$

where, from the scaling theory [128], ζ is a constant that depends on the system dimension. For a one-dimensional system $\zeta = 2/3$. U_c and u_c are scaling constants respectively for the energy and the length of the DW:

$$U_c = \left[\frac{\mu u_c (\mu + 1) \xi}{2} \right]^\mu \frac{\mathbf{E}_{DW} t u_c^2}{(1 + \mu)} L_c \quad (5.25)$$

where $\mu = (2\zeta - 1)/(2 - \zeta)$ and the free energy reads:

$$F(u, L) = U_c \left(\frac{L}{L_c} \right)^{2\zeta-1} - 2M_s H t L_c u_c \left(\frac{L}{L_c} \right)^{\zeta+1} \quad (5.26)$$

The free energy depends only on two terms, the first one favours the reduction of the DW length whereas the second promotes the lengthening of the DW.

Studying the minimum of eq. 5.26 one can find the value of L that reduces the pinning energy barrier. This energy barrier can be used in an Arrhenius law to characterize the DW speed:

$$v \propto \exp \left[-\beta U_c \left(\frac{H_c}{H} \right)^\mu \right] \quad (5.27)$$

where $\mu = (2\zeta - 1)/(2 - \zeta)$ and in a 1D system becomes $\mu = 1/4$.

The DW speed in the creep regime depends strongly on the DW energy and in anisotropic systems one can expect an anisotropic DW expansion. When the external field increases the DW acquires energy and becomes less sensitive to inhomogeneities of the system. Then for high magnetic fields the DW changes behaviour and can enter in the flow regime.

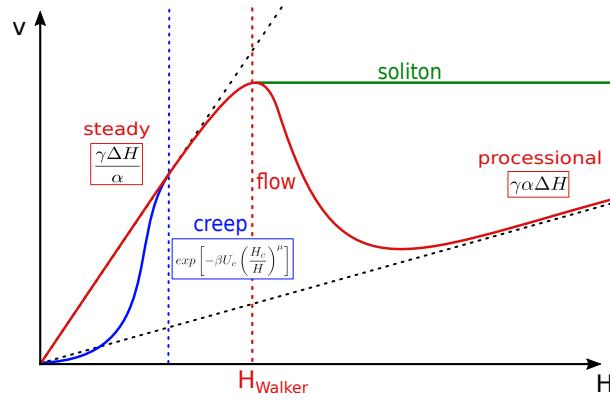


Figure 5.33: Review of the DW regimes described in this section

5.5 Kerr microscopy and DW motion

In this section the results obtained from the study of the DW dynamics in a W\Co\Au sample are shown. In the first part the DW motion is studied in the creep regime under the application of in-plane and out-of-plane magnetic fields. In the second part the same measurements are performed in the flow regime.

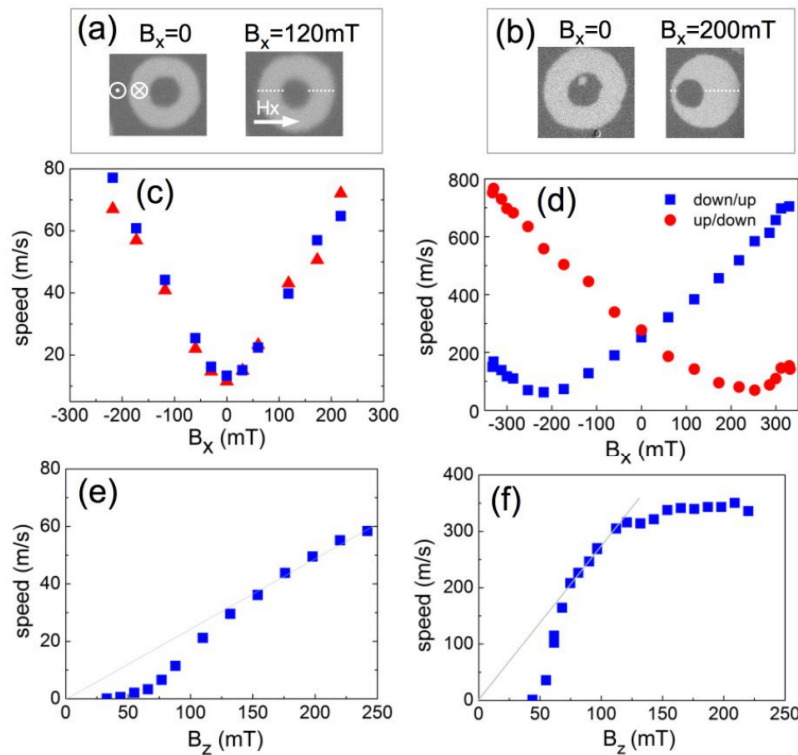


Figure 5.34: . (a)-(b): differential Kerr images showing the expansion of a domain during the application of an out-of-plane field B_z , without and with the simultaneous application of an in-plane field, in Pt/Co/Pt (a) and Pt/Co/AlOx (b); (c)-(d): DW velocity vs. in-plane field B_x for Pt/Co/Pt ($B_z = 88$ mT) (c) and Pt/Co/AlOx ($B_z = 132$ mT) (d). (e)-(f): DW velocity vs B_z for Pt/Co/Pt (e) and Pt/Co/AlOx (f). The thin lines in (e,f) emphasize the slope of the linear regime. Taken from Ref. [113]

The experiments are performed studying the expansion of a magnetic domain in order to analyse the DW speed along all the directions in the plane. Two different measurements have been performed:

DW speed as a function of an out-of-plane magnetic field B_{out} First the system is saturated with the application of a strong magnetic field along the out-of-plane easy axis. Then a magnetic field pulse is

applied in the opposite direction in order to nucleate a magnetic domain. Another magnetic field pulse B_{out} allows to expand the domain by domain wall propagation. The study of the DW speed as a function of B_{out} allows to determine the depinning field, the transition between the creep and the flow regimes, and the Walker field (Sec. 5.4.1). From the depinning field and the transition between the creep and the flow regimes the homogeneity of the system can be evaluated whereas from the value of the Walker speed the strength of the DMI can be determined [113].

$$v_{walker} = \frac{\gamma_0 \Delta H_{walker}}{\alpha} = \frac{\gamma_0 D}{M_s} \quad (5.28)$$

DW speed under pulses of B_{out} as a function of a continuous in-plane magnetic field B_{in} An out-of-plane field is applied in order to nucleate a domain after the sample saturation as for the previous method. In isotropic systems the application of a magnetic field pulse B_{out} expands the domain with a circular symmetry (Fig. 5.34(b)). A continuous in-plane magnetic field B_{in} can be applied for breaking the symmetry of the DW propagation. If the DWs have a Néel chiral configuration, generally stabilized by DMI, the DWs on opposite sides of the same magnetic domain have opposite polarisations, one parallel and one antiparallel to the magnetic field direction. Therefore the in-plane magnetic field stabilises one DW and destabilises the other. In the creep regime the DW speed depends mainly on the DW energy and in the flow regime on the DW width. Both the DW energy and width are modified by the application of the in-plane magnetic field and the DW speed is thus different for the two DWs. When the strength of the in-plane field B_{in} increases there is a value of $B_{in} = B_{min}$ for which the DW configuration of the destabilised DW switches polarisation. This corresponds to a minimum in the DW speed as a function of B_{in} , both in the flow and in the creep regimes. This problem has been studied with a 1D micromagnetic model in the case of a Néel DW stabilised by DMI in Sec. 4.2.4. Therefore the value of B_{in} allows to probe the strength of the micromagnetic DMI constant:

$$D = \frac{\Delta M_s}{B_{min}} \quad (5.29)$$

This method has been used in systems with isotropic DMI [116, 113, 129, 115, 130, 131]. In this section we use this method on the systems studied in this thesis, which have a C_{2v} symmetry and for which anisotropic DW configurations are expected. The effects of the anisotropic interactions on the DW propagation are discussed.

5.5.1 Creep regime

The measurements are performed on a W\Co\Au sample with a 0.65 nm thick and flat Co layer. The sample is first saturated with a strong magnetic field pulse of $B_z = 50$ mT for 100 ms and then a shorter pulse of $B_z = 4.6$ mT is applied for 4 ms in the opposite direction in order to nucleate a single magnetic domain. After that, two 4 ms pulses of $B_z = 4.6$ mT are applied to expand the domain. The Kerr images in Fig. 5.35b show a differential image between the final state with the expanded domain and the state after domain nucleation.

The shape of the magnetic domain obtained with only an out-of-plane field evidences the anisotropic nature of the system. Indeed, as shown in Fig. 5.35b, the domain is elongated along the in-plane easy axis, the $W[\bar{1}10]$ direction. Since in the creep regime the DW speed is proportional to the DW energy we can thus deduce that the energy of the DW is lower along the easy axis.

During the domain expansion the DW speed is studied as a function of the strength of a constant B_{in} field between -35 mT and $+35$ mT, along the direction of its application. In these measurements it is important to minimise the sample tilt with respect to the in-plane field axis. When the sample is tilted, the in-plane field has an out-of-plane component that switches direction when the in-plane field is switched. This will lead to different B_z fields for opposite in-plane fields and thus influence the DW propagation speed needed to calculate the DMI strength. To minimize the out-of-plane component, a study of the propagation of the two opposite DWs is performed under a strong B_{in} field and the sample tilt is adjusted until the same DW speed is obtained for opposite DWs when B_{in} is switched.

In order to investigate the effect of the anisotropic interactions, the measurements are performed with a B_{in} magnetic field along three different crystallographic directions.

B_{in} parallel to the in-plane easy axis direction ($W[\bar{1}10]$).

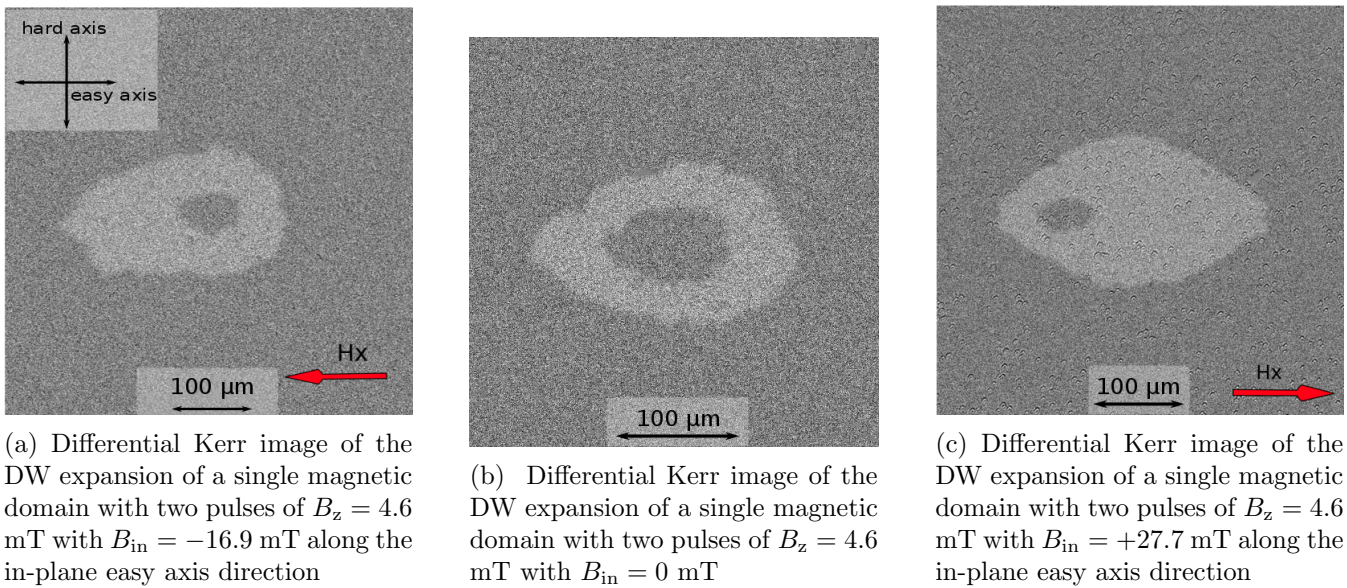


Figure 5.35

The DW speed as a function of B_{in} (Fig. 5.35) shows the speed behavior expected by the theory (Sec. 4.3.6; [116, 113, 129, 115, 130, 131]). The determination of the B_{min} field is not possible in this case since the speed behavior does not show a minimum as a function of B_{in} . On the other hand, the symmetry of the DW speed as a function of B_{min} curves indicates the presence of a DMI giving clockwise domain wall helicity. A minimum may exist for larger B_{in} fields, but we could not apply a B_{in} field stronger than $+35$ mT, since at this value the energy barrier between the two out-of-plane magnetisation ground states is strongly reduced facilitating the domain nucleation. The nucleation density for a small B_z pulse therefore increases and different domains merge, making it impossible to measure a single domain expansion. This problem could in principle be solved by reducing the B_z pulse duration. However, this is not possible using the standard Kerr microscopy set-up since 4 ms is the time needed for our electromagnets for reaching $B_z = 4.6$ mT.

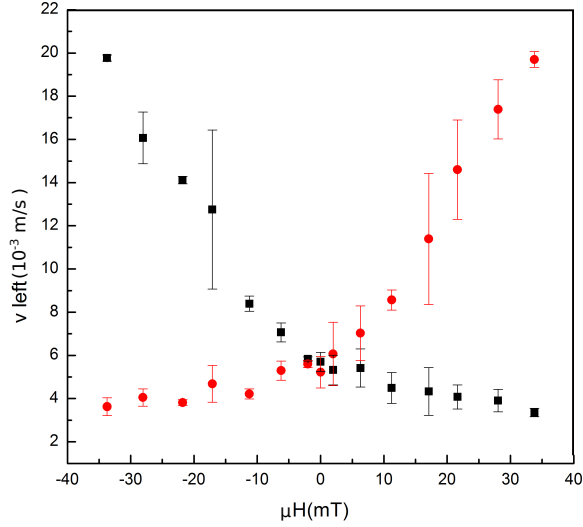


Figure 5.36: Plot of the DW speed versus B_{in} . The red spots are for the right DW whereas the black spots are for the left DW in Fig. 5.35. The experimental error is estimated from the standard deviation calculated from the DW speeds extrapolated from 5 differential Kerr images with the same B_{in} .

The DW speed is calculated from the ratio between the distance covered by the DW during the B_z pulse and the pulse duration. From the DW speed behavior as a function of B_{in} one can thus deduce that $B_{min} > 35$ mT. The $D_s^{(x)}$ parameter has been studied using static approaches in systems without in-plane anisotropy [116, 113, 129, 115, 130, 131]. In systems with in-plane anisotropy the B_{in} necessary for switching the DW has been discussed in Sec. 4.3.6. The DW along the in-plane easy axis has a Néel polarisation stabilized by DMI and the in-plane anisotropy. The value of B_{in} for switching the DW polarisation B_{min} depends thus also on the K_{in} parameter. Eq. 4.91 allows to extrapolate $D_s^{(x)}$ that reads:

$$D_s^{(x)} = t \left(\sqrt{\frac{A}{K_{out}^{eff} - K_{in}}} B_{min} M_s - \frac{4}{\pi} \sqrt{A(K_{out}^{eff} - K_{in})} \right) \quad (5.30)$$

An estimation of $D_s^{(x)}$ is possible considering the other magnetic parameters obtained from other experimental methods. $K_{out}^{eff} = 199$ kJ/m³ and $K_{in} = 136$ kJ/m³ are obtained by BLS measurements (Sec. 5.6) and $M_s = 1.1510^6$ A/m by vibrating sample magnetometry (VSM). The exchange constant is set to the typical value for Co thin films ($A=16$ pJ/m) [80, 79]. When $B_{min} = 35$ mT is used in Eq. 5.30, it gives a negative value for $D_s^{(x)}$. This occurs because the term $\frac{4}{\pi} \sqrt{A(K_{out}^{eff} - K_{in})}$ is larger than $\sqrt{\frac{A}{K_{out}^{eff} - K_{in}}} B_{min} M_s$. This means that the effect of DMI on the DW is weaker than the stabilisation effect by the in-plane anisotropy. We can conclude that B_{min} needed to switch the DW polarisation has to be strongly outside the range of in-plane fields we can attain.

B_{in} parallel to the hard axis $W[001]$ direction.

Fig. 5.37 and Fig. 5.38 show respectively differential Kerr images and the extrapolated DW speed when B_{in} is applied along the hard axis ($W[001]$). The DW speed has a particular and complex behavior. The simple one-dimensional model developed in Sec. 4.3.6 does not allow to explain these results. The micromagnetic calculations developed in Sec. 4.3.5 show that along the hard axis the DW has a mixed polarisation between a Néel and a Bloch DW with two degenerate solutions with complementary angles. The polarisation angle of these solutions can be obtained by knowing the DMI and the in-plane anisotropy parameters.

This model does not take into account a 2D exchange interaction that guarantees a smooth magnetisation variation between the DW polarisations obtained in Sec. 4.3.5. Indeed, in a real 2D system one can expect that along the hard axis the DW magnetisation presents a fast and continuous variation between the degenerate DW polarisations, a so-called Bloch Line (BL). The energy and the configuration of the BL under an in-plane magnetic field is not easy to calculate with analytical methods. This makes it impossible to give a quantitative determination of the magnetic parameters along the system hard axis.

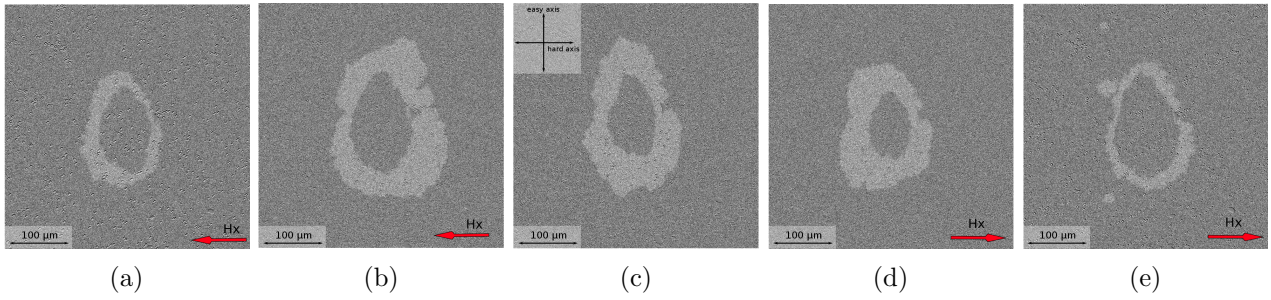


Figure 5.37: Differential Kerr images of DW expansion of a single magnetic domain with B_{in} along the hard axis direction with two pulses of $B_z = 4.6$ mT. The pictures are taken with different values of B_{in} [a) = -22.5 mT ; b) = -11.4 mT ; c) = 0 mT ; d) = $+11.5$ mT ; e) = $+22.5$ mT]

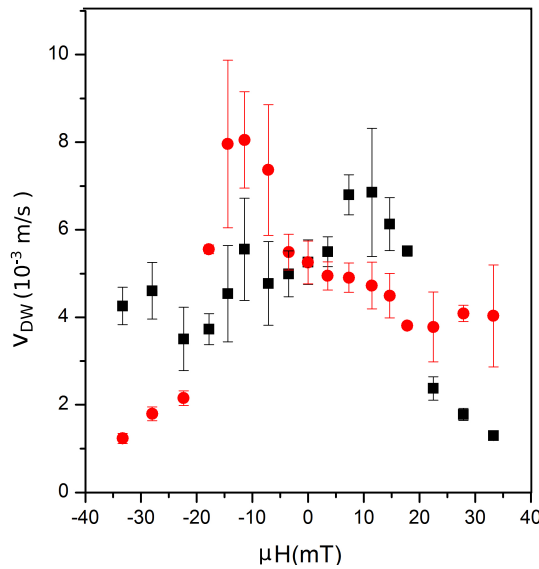


Figure 5.38: Plot of the speed DW versus B_{in} . The red spots are for the right DW whereas the black spots are for the left DW.

B_{in} along an intermediate angle.

In Fig. 5.39 the differential Kerr images show the DW expansion under the application of a magnetic in-plane field B_{in} along a direction that makes an angle of 37° with respect to the in-plane easy axis.

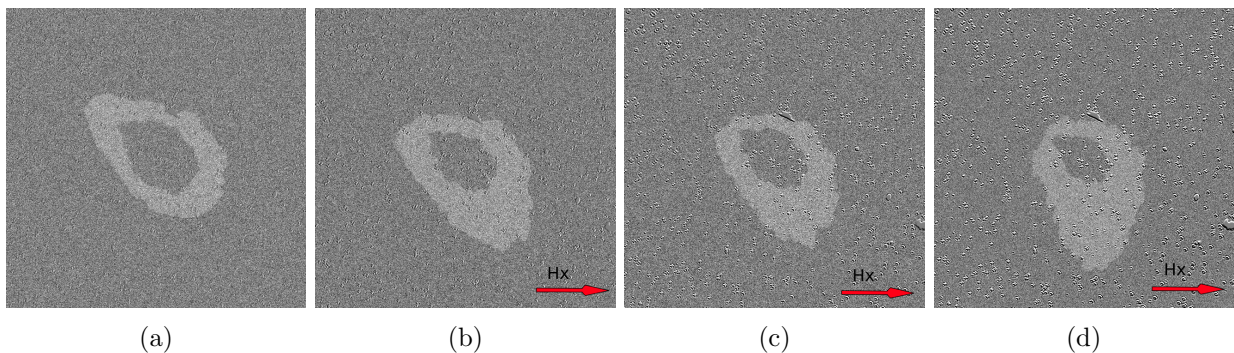


Figure 5.39: Differential Kerr images of the DW expansion of a single magnetic domain with B_{in} along a direction that makes an angle of 37° with respect to the easy axis under two pulses of $B_z = 4.6$ mT. The pictures are taken with different values of B_{in} [a) = 0 ; b) = 13.9 mT ; c) = 19.2 mT ; d) = 30.1 mT)

The Kerr images and the plot in Fig. 5.40 show that the direction of the maximum DW speed, defined with the angle θ with respect to the easy axis, changes as a function of the intensity of the applied in-plane

magnetic field. This effect can be explained considering that the DW polarisation changes as a function of B_{in} . This phenomenon can be interpreted considering the complex DW configuration in a system with C_{2v} symmetry. In the creep regime the faster DW is the one with the lower energy and in absence of B_{in} the lowest energy DW is along the easy axis. The Zeeman interaction reduces the energy of the DW parallel to the direction of the magnetic field. At the same time, it changes the DW polarisation. Then the faster motion will be for DWs between the easy axis and the direction where the DW polarisation is parallel to B_{in} .

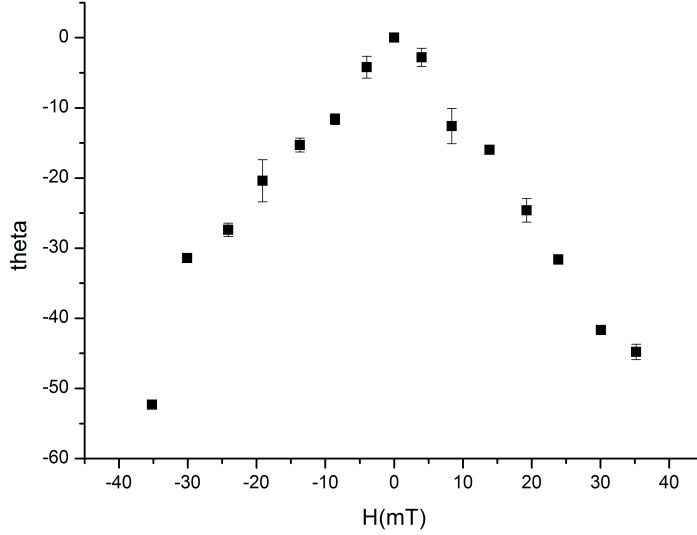


Figure 5.40: Plot of the angle of maximum DW speed θ as a function of B_{in} applied along 37° . The zero of θ is set along the easy axis

5.5.2 Regimes of the DW dynamics

During this work the Kerr microscopy set-up has been upgraded in order to apply higher out-of-plane magnetic fields and to reduce the pulse time. This was done using the microcoils described in Sec. 3.5.3. The different DW dynamics regimes could thus be reached and studied in the same system as the one analysed in the creep regime (Sec. 5.5.1). Fig. 5.41 shows the DW speed along the easy axis as a function of an out-of-plane magnetic field up to $B_z = 163$ mT.

The lack of experimental data in Fig.5.41 does not allow a unique interpretation of the DWs dynamics. In the following part of this section we consider the presence of three different regimes. We justify this decision because the analysis in this condition could lead to the evaluation of different magnetic parameters. On the other hand it is fundamental to compare these values with the ones obtained with others experimental techniques in order to validate the taken hypothesis.

- *Creep regime.* In the range of magnetic fields from $0 < B_z < 55$ mT the shape of the domain is rough and the speed behavior is exponential as a function of B_z (Sec. 5.4.2)
- *Flow regime.* In the range of magnetic fields from $55\text{mT} < B_z < 70$ mT the shape of the magnetic domains becomes smooth, the speed behavior is linear and the fit of this slope intercepts the zero in agreement with the theory:

$$v = \frac{\gamma_0 \Delta}{\alpha} B_z \quad (5.31)$$

where γ_0 is the gyromagnetic ratio, Δ the Bloch parameter and α is the damping constant. Considering the anisotropic parameters extrapolated by the BLS measurements ($K_{out}^{eff} = 199$ kJ/m³ and $K_{in} = 136$ kJ/m³) and the exchange constant set to the typical value for Co thin films ($A=16$ pJ/m), the Bloch parameter can be calculated as $\Delta = 15.9$ nm. Replacing Δ in eq. 5.31, the experimental data can be used to extract the damping parameter $\alpha = 0.65$. The Co layer grows strained on the W(110) surface,

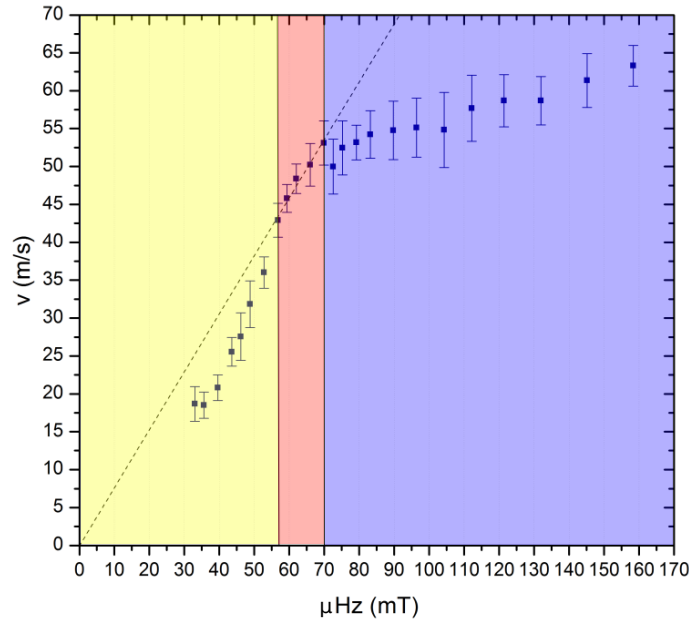


Figure 5.41: Plot of the DW speed as a function of the out-of-plane magnetic field B_z . Three dynamics regimes can be found: (yellow) creep regime, (red) steady flow regime and (blue) soliton motion regime

which induces the presence of crystal dislocations. These crystal defects could be the reason of the obtained high damping parameter [132, 133].

- *Soliton motion regime.* In the range of magnetic fields from $70 \text{ mT} < B_z < 163 \text{ mT}$ the speed behavior should be flat through the Bloch lines annihilation process as discussed in sec. 5.4.1. In our case, the speed slightly increases as a function of B_z . A similar effect was found in Ref. [125] in simulations of systems with weak DMI in the presence of defects.

We have seen that the in-plane anisotropy does not play a role in the determination of the Walker field (Sec. 5.4.1). Indeed, the effective in-plane magnetic field goes to zero when the equilibrium DW polarisation angle during the steady motion tends to $\pi/2$. Then the extrapolation of the Walker speed $v_{\text{Walker}} = 53 \text{ m/s}$ allows to directly estimate the DMI coefficient along the easy axis.

$$D_s^x = \frac{v_{\text{Walker}} M_s t}{\gamma_0} = 1.1 \text{ pJ/m} \quad (5.32)$$

5.5.3 Steady flow regime

The plot in Fig. 5.41 allows to chose the magnetic field value for the study of the DW expansion in the steady flow regime. In Fig. 5.42 the DW speed under a pulse of $B_z = 60 \text{ mT}$ for 20 ns is plotted as a function of the in-plane magnetic field B_{in} along the easy and along the hard axis. Along both directions the speed behavior has a minimum for negative values of the magnetic field, which can be explained with the theory exposed in Sec. 5.5 and shows the presence of a clockwise DW chirality. The DW speed behavior differs between the two directions. Along the easy axis (blue and violet dots) the slope of the speed as a function of B_{in} is steeper then along the hard axis (orange and red dots). Moreover along the hard axis the minima are smoother and flatter than along the easy axis. These differences can be explained considering the different DW configurations along the two directions; i.e. a Néel DW stabilised by in-plane anisotropy and DMI along the easy axis and a Bloch line due to the competition between in-plane anisotropy and DMI along the hard axis.

The change of the Bloch line configuration as a function of B_{in} is complex and the simple 1D model in Sec. 5.5 can not describe this behavior, while it can be applied with some modifications along the easy axis. Considering $B_{\text{min}} = 55 \text{ mT}$, one can calculate the DMI constant along the easy axis (Eq. 5.33):

$$D_s^{(x)} = t \left(\sqrt{\frac{A}{K_{\text{out}}^{\text{eff}} - K_{\text{in}}}} B_{\text{min}} M_s - \frac{4}{\pi} \sqrt{A(K_{\text{out}}^{\text{eff}} - K_{\text{in}})} \right) \quad (5.33)$$

Using the same magnetic parameters used for Eq. 5.30, one can notice that the B_{min} value is not large enough and the term $\sqrt{\frac{A}{K_{\text{out}}^{\text{eff}} - K_{\text{in}}}} B_{\text{min}} M_s$ is smaller than $\frac{4}{\pi} \sqrt{A(K_{\text{out}}^{\text{eff}} - K_{\text{in}})}$. This result shows a strong disagreement between the experimental value of B_{min} and the static model for describing the DW switching in presence of in-plane anisotropy (Sec. 5.5).

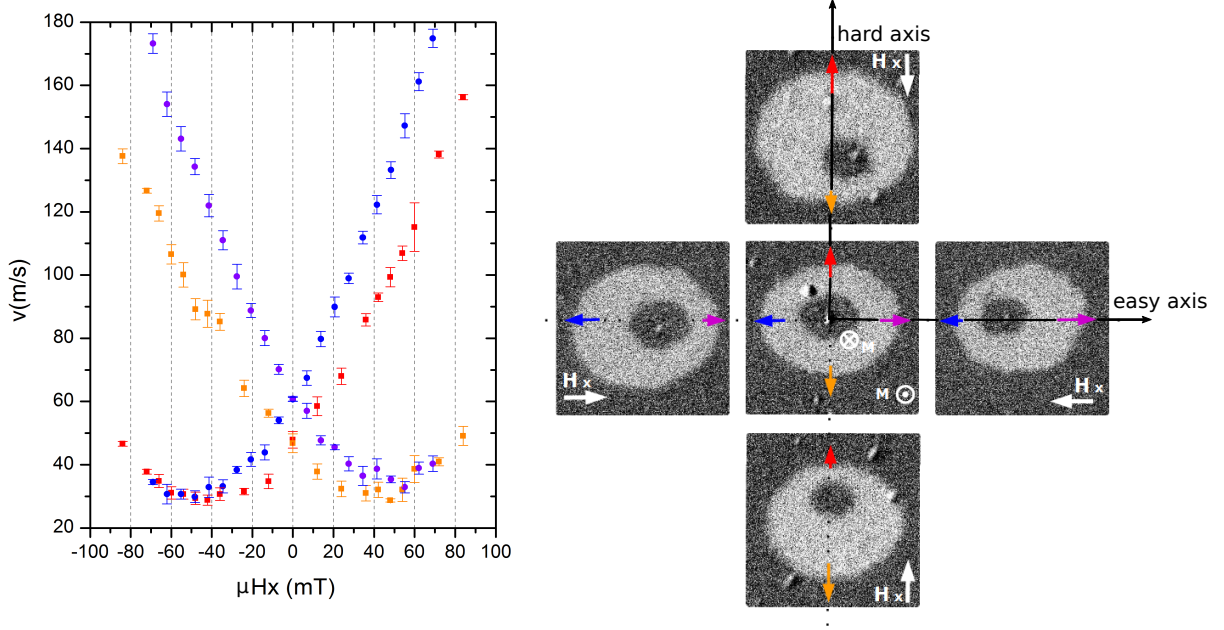


Figure 5.42: Plot of the DW speed as a function of the in-plane field B_{in} along the easy (blue, violet) and hard (orange, red) axes under the application of a B_z of 60 mT for 20 ns. The differential Kerr images show the DW expansion and the direction of the applied field (white arrows)

The origin of this disagreement is probably that we used a static model for describing the DW dynamics. The static model is working well for studying the DW speed in absence of in-plane anisotropy because the DW energy as a function of the polarisation angle shows a simple behavior: one minimum and one maximum that switch as a function of the in-plane magnetic field strength (Sec. 4.2.4). For small B_{in} the DW polarisation is imposed by the DMI and for larger values by the in-plane magnetic field.

The DWs propagate under the effect of a B_z pulse. Two different DW dynamics regimes have been shown in Sec. 5.4.1. For small B_z the DWs propagate with a fixed polarisation angle (steady motion) and for larger B_z the DW polarisation continuously changes during the propagation (precessional motion). In absence of in-plane anisotropy the dynamics of the DWs does not influence the final DWs polarisation and when the out-of-plane magnetic field is switched off the DWs go back to the initial configuration.

The same discussion can not be used for the study of the DW dynamics in systems with in-plane anisotropy. In this case the DW energy as a function of the polarisation angle shows two minima separated by an energy barrier. The minima correspond to two Néel DW configurations, one promoted by DMI and the other by the in-plane magnetic field. The energy barrier arises from the in-plane magnetic anisotropy. If the DWs propagate in the steady motion regime the DWs switch polarisation only for high values of B_{in} and the Eq. 5.33 is valid. If the DWs propagate in the precessional motion regime the DW polarisation changes during the motion. It allows to the DW to overcome the energy barrier and relax to its absolute minimum polarisation configuration after the out-of-plane magnetic pulse.

The DW speed measurements in Fig. 5.42 are performed in the steady motion regime since $B_z < B_{\text{Walker}}$ in absence of in-plane magnetic field. When the in-plane magnetic field is applied B_{Walker} decreases. Therefore the DW polarisation switching occurs when the Walker field becomes smaller than the applied field B_z and the DWs enter in the precessional regime (Sec. 5.4.1). The DMI parameter can be calculated setting

$B_{\text{in}} = B_{\text{min}}$ and $B_{\text{Walker}} = B_z$ for the calculation of the angle ϕ_0 . The numerical solution of this problem allows to evaluate the DMI parameter along the easy axis ($D_s^{(x)} = 0.32 \text{ pJ/m}$).

where $\alpha = 0.65$ from the study of the Walker speed and $\Delta(B_{\text{min}}) = \sqrt{\frac{A}{K_{\text{eff}} \pm B_{\text{min}} M_s}}$ with the anisotropy parameters calculated from the BLS measurements ($K_{\text{out}}^{\text{eff}} = 199 \text{ kJ/m}^3$ and $K_{\text{in}} = 136 \text{ kJ/m}^3$) and the exchange constant set to the typical value for Co thin films ($A = 16 \text{ pJ/m}$).

In Fig. 5.43 the DW speeds along all the in-plane directions are plotted as a function of the intensity of a continuous in-plane magnetic field applied along a direction that makes an angle of 40° with respect to the easy axis. The study is performed in the flow regime and a pulse of $B_z = 60 \text{ mT}$ for 20 ns is applied for expanding the domains. The data analysis was performed with the help of Benjamin Canals (Institut Néel). As in the creep regime case, the direction of the maximum speed changes as a function of B_{in} . Without B_{in} the speed has a twofold in-plane symmetry with two maxima along the easy axis. The application of the in-plane magnetic field breaks this symmetry. The maximum speed direction rotates in a direction opposite to the magnetic field direction. The minimum speed saturates at 30 mT and it shows a characteristic double minima energy well. The maximum slope shape is not monotonous and shows a shoulder for ϕ angles opposite to the B_{in} direction with respect the maximum speed direction.

These particular shapes of the DW speed behavior as a function of the in-plane angle could be characteristic of the presence of Bloch lines that move inside the DW under the effect of the in-plane magnetic field. This assumption needs high-resolution microscopic analysis and theoretical studies in order to be confirmed.

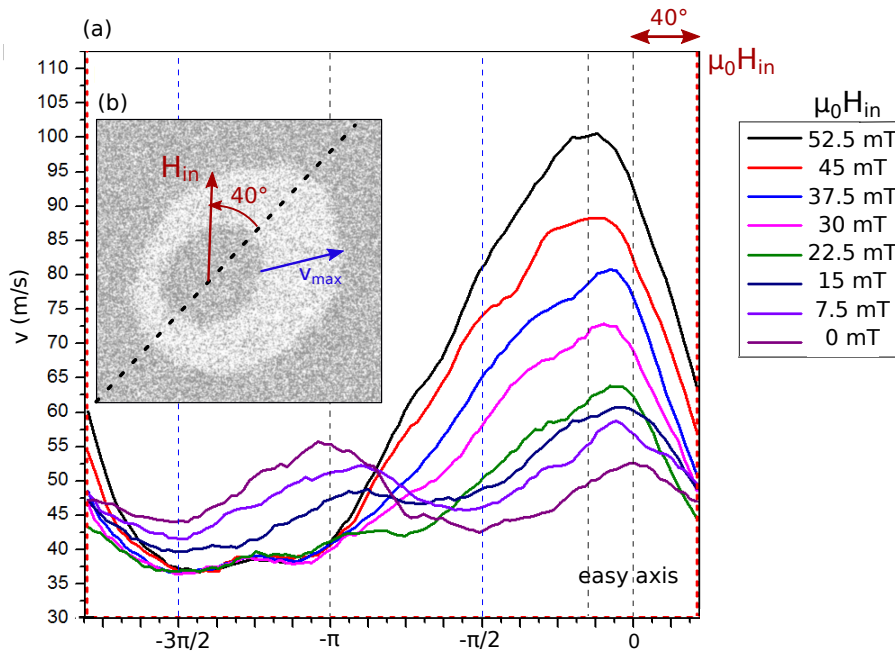


Figure 5.43: (a) Plot of the DW speed along all the in plane directions under a pulse of $B_z = 60 \text{ mT}$ for 20 ns and as a function of a magnetic field applied along a direction that makes an angle of 40° with respect to the easy axis. (b) Differential Kerr image of the DW expansion under a B_z pulse of 60 mT for 20 ns and a constant $B_{\text{in}} = 45 \text{ mT}$ applied along the direction of the red arrow. The direction of the maximum speed is indicated by the blue arrow.

5.5.4 DW dynamics review

The main aim of the study just presented was to use the dynamics of DWs to determine the DMI parameters in W\Co\Au sample with a 0.65 nm thick Co layer and a C_{2v} symmetry. The DW propagation along the hard axis did not allow the determination of the DMI, due to the complexity of the DW configuration and its dynamics.

Along the easy axis, the in-plane anisotropy and the DMI stabilise a Néel DW and the standard methods have been modified to determine the DMI (D_s^x). The study of the Walker breakdown speed suggests a $D_s^x = 1.1$ pJ/m, whereas the study of the DW motion under the application of an in-plane magnetic field gives a $D_s^x = 0.32$ pJ/m. The two values are in disagreement. It can be explained by a possible error in the evaluation of the Walker breakdown field. Indeed in sec.?? the hypothesis of the presence of three DW dynamics regime could be fault.

The study of the DW speed as a function of an in-plane field along an intermediate angle between the easy and the hard axis shows a particular behaviour due to the complexity of the DW dynamics in systems with C_{2v} symmetry. This complexity makes it impossible to describe the DW dynamics in C_{2v} symmetry systems with one-dimensional models along a general in-plane direction.

5.6 Brillouin light scattering spectroscopy

We have performed Brillouin Light Scattering spectroscopy measurements in the Damon-Eshbach (DE) configuration [56] on a W\Co\Au sample with a Co thickness of 3 ML [17]. These measurements were performed together with Mohamed Belmeguenai, Yves Roussigné and Andreï Stashkevich from LSPM-CNRS in Villetaneuse (France).

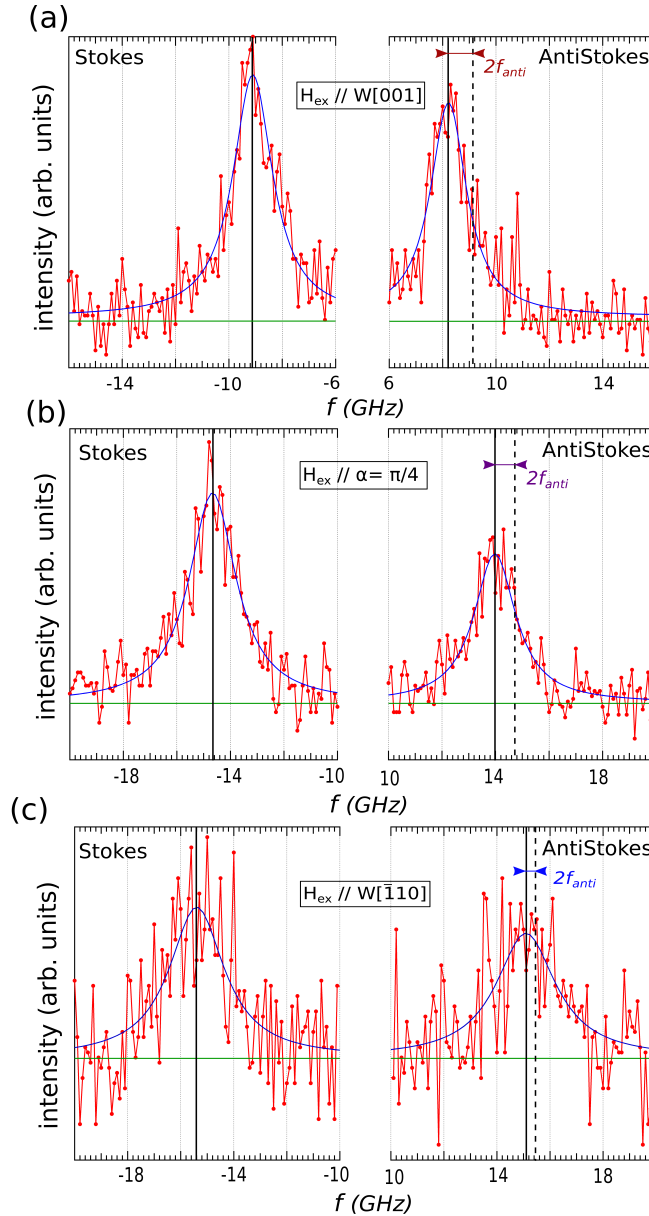


Figure 5.44: BLS spectra on Au/Co(0.65 nm)/W(110) with \mathbf{k}_{SW} along three in-plane directions. Red: experimental data. Blue line: data fit with Lorentzian functions. Green line: background fit. In the AS spectra, the distance between the continuous and dashed black lines shows the frequency shift between S and AS peaks. (a) BLS spectrum with $\mu_0 H_{\text{ext}} = 0.6$ T parallel to the $\text{bcc}[001]$ axis and $k_{\text{SW}} = 8.08$ / μm parallel to the $\text{bcc}[\bar{1}10]$ axis (b) BLS spectrum with $\mu_0 H_{\text{ext}} = 0.5$ T along an in-plane direction that makes an angle of $\pi/4$ with respect to the $\text{bcc}[\bar{1}10]$ axis and $k_{\text{SW}} = 18.09$ / μm . (c) BLS spectrum with $\mu_0 H_{\text{ext}} = 0.5$ T parallel to the $\text{bcc}[\bar{1}10]$ axis and $k_{\text{SW}} = 18.09$ / μm parallel to the $\text{bcc}[001]$ axis.

This technique is particularly suited for the study of anisotropic systems because it allows to extract the magnetic properties independently along any direction. The application of an external magnetic field H_{ext} is used to saturate the magnetisation along an in-plane direction and the thermally activated SW will depend on the magnetic interactions in the direction perpendicular to the applied field. The direction in the sample plane along which the properties are studied can be described by the angle α . This is the

angle between \mathbf{k}_{SW} (the direction along which the magnetisation varies) and the *bcc* $[\bar{1}10]$ crystallographic direction (Fig. 5.16). In this set of measurements three different directions have been studied, the two main crystal axes ($\alpha = 0; \alpha = \pi/2$) and the intermediate one $\alpha = \pi/4$.

The BLS spectrum in systems with DMI can be separated in a symmetric $f_0 = (|f_{\text{S}}| + |f_{\text{AS}}|)/2$ and an antisymmetric component $f_{\text{anti}} = (|f_{\text{S}}| - |f_{\text{AS}}|)/2$. The study of f_0 with H_{ext} along the main crystallographic directions allows to estimate the magneto-crystalline anisotropy (MCA) constants K_i , in the direction of the applied field, while f_{anti} allows to extract the sign and strength of the DMI acting on a Néel spin cycloid along the SW wavevector.

The symmetric frequencies $f_0^{[\bar{1}10]}$ and $f_0^{[001]}$, when H_{ext} is respectively applied along $[\bar{1}10]$ and $[001]$, can be calculated [134] as,

$$f_0^{[001]} = \frac{\gamma\mu_0}{2\pi} \sqrt{[H_{\text{ext}}^{[001]} - H_{\text{in}} + Jk_{\text{SW}}^2 + P(k_{\text{SW}}t)M_{\text{s}}][H_{\text{ext}}^{[001]} - H_{\text{out}} + Jk_{\text{SW}}^2 - P(k_{\text{SW}}t)M_{\text{s}}]} \quad (5.34)$$

$$f_0^{[\bar{1}10]} = \frac{\gamma\mu_0}{2\pi} \sqrt{[H_{\text{ext}}^{[\bar{1}10]} + H_{\text{in}} + Jk_{\text{SW}}^2 + P(k_{\text{SW}}t)M_{\text{s}}][H_{\text{ext}}^{[\bar{1}10]} - H_{\text{out}} + H_{\text{in}} + Jk_{\text{SW}}^2 - P(k_{\text{SW}}t)M_{\text{s}}]} \quad (5.35)$$

where γ is the gyromagnetic ratio, $J = \frac{2A}{\mu_0 M_{\text{s}}}$ is the SW stiffness with A the exchange stiffness and M_{s} the spontaneous magnetisation, $P(k_{\text{SW}}t) = 1 - \frac{1 - \exp(-|k_{\text{SW}}|t)}{|k_{\text{SW}}|t}$ is a geometric factor associated to the SW dynamics with t the sample thickness. H_{out} and H_{in} can be defined as the anisotropy fields, i.e. the magnetic field needed to saturate the magnetisation respectively from the out-of-plane easy axis ($\theta = 0; \phi = 0$) and from the in-plane easy axis ($\theta = \pi/2; \phi = 0$) to the in-plane hard axis ($\theta = \pi/2; \phi = \pi/2$). Analysing the spectra in Fig. 5.44 can give a numerical estimation of the MCA constants. In this work, the S-AS peaks occur for small values of k_{SW} , i.e. $Jk_{\text{SW}}^2 \ll H_{\text{ext}}$, so that the exchange contributions to the resonance BLS peaks can be neglected.

The spontaneous magnetisation ($M_{\text{s}} = 1.15 \cdot 10^6$ A/m) is inferred from the out-of-plane hysteresis loop obtained with a vibrating sample magnetometer (VSM). Evaluating $f_0^{[001]} = 8.53$ GHz and $f_0^{[\bar{1}10]} = 15.24$ GHz with respectively $\mu_0 H_{\text{ext}}^{[\bar{1}10]} = 0.5$ T and $\mu_0 H_{\text{ext}}^{[001]} = 0.6$ T, we obtain $K_{\text{in}} = \frac{1}{2}\mu_0 M_{\text{s}} H_{\text{in}} = 136$ kJ/m³ and $K_{\text{out}} - K_{\text{d}} = \frac{1}{2}\mu_0 M_{\text{s}} H_{\text{out}} = 199$ kJ/m³. Note that published results on the same system [112] showed a comparable out-of-plane anisotropy, but a larger in-plane anisotropy.

The difference in frequency between the Stokes and anti-Stokes peaks, $2f_{\text{anti}}$, arises from the different effect of DMI on SW modes with opposite \mathbf{k}_{SW} [60, 135]. In ultra-thin films, DMI is the only physical phenomenon liable to break the S-AS peak symmetry [135]. BLS is thus particularly suited for the investigation of anisotropic DMI, especially because the extracted data are independent from any other anisotropy present in the system such as MCA, and from the strength of H_{ext} . The SW frequency shift in a system with interfacial DMI [$D(t) = D_{\text{s}}/t$] in the DE geometry can be formulated as [60, 136]:

$$2f_{\text{anti}} = \frac{2\gamma}{\pi} \frac{D(t)}{M_{\text{s}}} k_{\text{SW}} = \frac{2\gamma}{\pi} \frac{D_{\text{s}}}{M} k_{\text{SW}}. \quad (5.36)$$

M , the magnetic moment per unit surface ($M = M_{\text{s}} t$), is obtained directly from VSM measurements, allowing a thickness-independent determination of the DMI strength, D_{s} . In Fig. 5.45 $2f_{\text{anti}}$ is plotted as a function of k_{SW} along the main axes (*bcc*[001] ; *bcc*[\bar{1}10]) and along an intermediate direction ($\alpha = \pi/4$). The points in the plot are extracted from the center of the Lorentzian distribution used to fit the S and AS peaks (Fig. 5.44). The error bars (δf) are obtained by a Levenberg-Marquardt error algorithm. The difference in the magnitude of errors (Fig. 5.45) between the in-plane directions is related to an instrumental issue that leads to a decrease of the signal-to-noise ratio in the BLS spectra when the magnon frequency increases (Fig. 5.44).

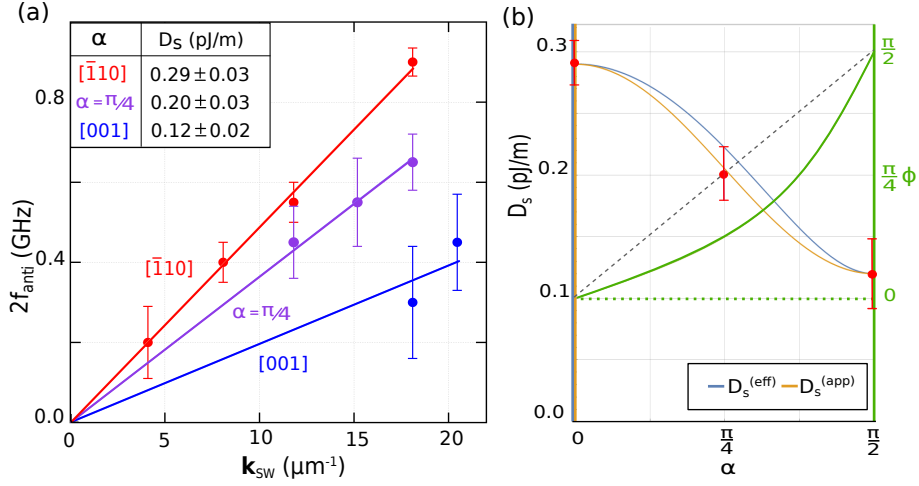


Figure 5.45: **(a)** S-AS frequency shift ($2f_{\text{anti}}$) as a function of SW wave-vector (k_{SW}) for different in-plane directions α . The dots are the experimental data and the lines are linear fits yielding the DMI strength (D_s). **(b)** Blue and orange lines : micromagnetic calculated $D_s^{(\text{eff})}$ (Eq.5.38) and $D_s^{(\text{app})}$ (Eq.5.37) as a function of the in-plane directions (α); red dots: D strength evaluated from the experimental data; green line: micromagnetic calculated magnetisation direction promoted by DMI (Eq.4.63) as a function of the crystallography directions; dashed line: Néel-like cycloid

The plot in Fig. 5.45 demonstrates that along all directions $2f_{\text{anti}}$ has a positive value, showing that the DMI promotes a clockwise spin spirality. Such a clockwise chirality (positive value of D) is in agreement with results found for sputtered MgO/CoFeB/W samples [137] and is opposite to the chirality in AlOx/Co/Pt films [61, 108]. Moreover, the DMI is strongly anisotropic. In the table in Fig. 5.45(a) the values of D_s parallel to the H_{ext} direction are shown. The DMI strength is a factor 2 to 3 higher along $bcc[\bar{1}10]$ than along $bcc[001]$, even taking into account the large error bar especially along the $[001]$ direction. This difference is also confirmed by the intermediate value found for the DMI strength for SWs propagating along the intermediate angle $\alpha = \pi/4$.

5.6.1 Derivation of the effective DMI ($D_s^{(\text{eff})}(\alpha)$)

Experimentally we have found a 2-3 times larger DMI along the $[\bar{1}10]$ than along the $[001]$ in-plane directions. In order to understand the relation between the crystal symmetry, the micromagnetic DMI anisotropy and the symmetry of the spin modulation $\phi(\alpha)$ we can use the micromagnetic model developed for a one-dimensional magnetisation modulation in a system with C_{2v} symmetry (Sec. 4.3.1).

The apparent DMI constant $D_s^{(\text{app})}$ can be defined as the DMI component acting on the DE spin wave as a function of the in-plane direction (α). In Sec. 4.3.1 the optimum configuration $\phi(\alpha)$ has been obtained minimising the energy with respect to ϕ . Here the $\phi(\alpha)$ relationship is set by the BLS geometry. Indeed in the DE geometry the SWs can be described as $\mathbf{m}(u) = \mathbf{M} + \delta\mathbf{m}(u)$, with $\mathbf{M} \propto \hat{v}$ is imposed by \mathbf{H}_{ext} . The component $\delta\mathbf{m}(u)$ is a Néel cycloid lying in the (\hat{u}, \hat{z}) plane. Then $D_s^{(\text{app})}$ calculated from the DMI energy density of the SW reads:

$$D_s^{(\text{app})} = D_s^{(x)} \cos^2 \alpha + D_s^{(y)} \sin^2 \alpha \quad (5.37)$$

This correspond to the Néel component of the total DMI. Eq. 5.37, plotted in Fig. 5.45(b), perfectly matches the experimental data. The DE geometry does not necessarily measure the SWs having the lowest energy, in particular it does not allow evaluating the component of DMI that favors Bloch spirals, which can be evaluated changing the BLS geometry. In order to estimate this component, one can replace in Eq. in Sec. the values of $D_x = D_s^{(x)}/t = 0.43$ mJ/m² and $D_y = D_s^{(y)}/t = 0.2$ mJ/m² obtained experimentally. The resulting modulation function is plotted with green lines in Fig. 5.45 and the relative effective DMI (orange

in Fig. 5.45) reads:

$$D_s^{eff} = D_s^{(x)} \cos \alpha \cos \left[\arctan \left(\frac{D_s^{(y)}}{D_s^{(x)}} \tan \alpha \right) \right] + D_s^{(y)} \sin \alpha \sin \left[\arctan \left(\frac{D_s^{(y)}}{D_s^{(x)}} \tan \alpha \right) \right] \quad (5.38)$$

As predicted from Eq. 4.62, along the main axes $D_s^{(eff)} = D_s^{(app)}$ and the biggest mismatch occurs along $\alpha = \pi/4$. In principle, the Bloch component (the difference between $D_s^{(eff)}$ and $D_s^{(app)}$) can be obtained by measuring the SW spectra along the magnetic field direction when this field is applied along $\alpha = \pi/4$. However, in our sample this component should be small and difficult to measure.

5.6.2 Review on BLS spectroscopy measurements

We have used BLS spectroscopy in the Damon-Eshbach configuration to investigate the DMI in an out-of-plane magnetized epitaxial Au/Co(0.65 nm)/W(110) trilayer. The asymmetry of the BLS spectra allows to estimate the presence of a DMI that promotes a clockwise chirality with a DMI strength 2 to 3 times larger along bcc[110] than along bcc[001]. BLS in the Damon-Eshbach configuration allows only the calculation of the DMI parameter for Néel magnetic rotations. In systems with a C_{2v} symmetry the DMI promotes Néel magnetic rotations only along the main crystal axes. A micromagnetic model has been used to estimate the strength of the DMI along all the in-plane directions and calculate the DW polarisation promoted by DMI in Au/Co(0.65 nm)/W(110) systems.

The DMI values obtained by the study of the DW motion and by BLS are in agreement:

$$D_s^x(\text{DWmotion}) = 0.31 \text{ pJ/m} \quad D_s^x(\text{BLS}) = 0.29 \text{ pJ/m} \quad (5.39)$$

It allows to confirm both the experimental method for evaluating the DMI values in system with a C_{2v} symmetry.

5.7 Internal DW configuration and elliptical skyrmions

The magnetic characterisation of the W\Co\Au system allows to predict the DW configurations with the support of micromagnetic calculations. The anisotropic DMI and the presence of in-plane anisotropy make the DW energy and polarisation strongly anisotropic. The model developed in Sec. 4.3.5 analyses the DW polarisation angle as a function of the in-plane directions in a system with C_{2v} symmetry. The introduction of the magnetic parameters obtained with the magnetic characterisation can thus give information about the DW configurations. The characterisation of the W\Co\Au crystal shows that the anisotropic DMI and the in-plane anisotropy arise from the symmetry of the W\Co interface. The Co crystal is a slightly deformed hcp crystal with the (0001) face in the system plane. Since this crystal is only weakly deformed ($\beta = 0.515$ rad) in the growth on the W bcc (110) face, the exchange interaction can be considered in first approximation isotropic. The typical value for Co of the exchange stiffness ($A = 16$ pJ/m) will be taken for the following discussion. The other parameters are taken from the BLS measurements on W\Co\Au :

$$K_{\text{out}} - K_{\text{d}} = 199\text{kJ/m}^3 \quad K_{\text{in}} = 136\text{kJ/m}^3 \quad D_{\text{s}}^x = 0.29\text{pJ/m} \quad D_{\text{s}}^y = 0.12\text{pJ/m} \quad (5.40)$$

Placing these values in Eq. 4.89 in Sec. 4.3.5, the polarisation variation as function of the in plane angle (α) can be obtained, as shown in Fig. 5.46.

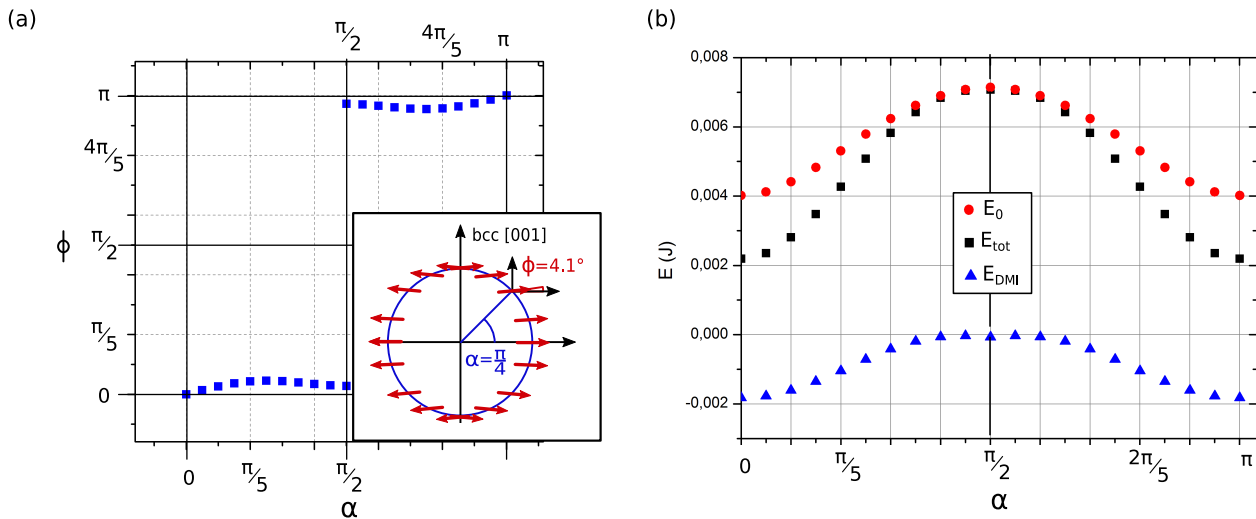


Figure 5.46: (a) Plot and polar plot of the numerical solution of Eq. 4.89 in Sec. 4.3.5 with the magnetic parameters obtained from the BLS measurements (b) Plot of the total energy (black), of the DMI component (blue) and of the subtraction of the two terms (red) for a 1D modulation propagating in the α in-plane direction

The DMI is 2.5 times stronger along the in-plane easy axis and stabilizes, together with the in-plane anisotropy, a Néel DW with a clockwise chirality. Along the hard axis the two interactions are in competition and two degenerate solutions can be found ($\phi_{\text{hard}} = 3.8^\circ$ and $\phi_{\text{hard}} = 180^\circ - 3.8^\circ$). The one-dimensional model does not take into account the exchange along the α direction, that promotes smooth polarisation variations and allows to predict the presence of a Bloch Lines.

The W\Co\Au sample characterized by BLS does not allow the nucleation of skyrmions because the out-of-plane anisotropy dominates the DMI and the surface dipolar interaction (Sec. 4.4.2). In order to decrease the out-of-plane anisotropy and the DMI and to increase the dipolar interaction, the Co thickness can be increased. It should thus be possible to design a W\Co\Au stack with the right Co thickness for nucleating skyrmionic bubbles. These topological solitons can only be stabilized in the presence of a confinement (Sec. 4.4.2). This can be obtained by the application of an external field in the direction opposite to the skyrmion core magnetisation [5, 106, 74] or by using the dipolar field in patterned structures [6] or on defects in a continuous film. In an anisotropic system with C_{2v} symmetry like W\Co\Au it is theoretically

possible to stabilize skyrmion bubbles with an elliptical shape [18]. It relies on the presence of an anisotropic DW energy. In $W/Co/Au$ the Néel DW stabilized by DMI and in-plane anisotropy along the easy axis has an energy lower than the DW along the hard axis (Fig. 5.46). Then one can expect that a skyrmion bubble in this system breaks its circular symmetry and elongates along the hard axis in order to increase the DW surface perpendicular to the easy axis.

In this section the methods and the approaches for the stabilisation of elliptical skyrmion bubbles in $W/Co/Au$ are shown. After the optimisation of the conditions for the skyrmion stabilisation the sample magnetisation is imaged by MFM and XMCD-PEEM.

5.7.1 Conditions for skyrmion nucleation

The $W/Co/Au$ systems have been grown with a thickness wedge in order to find the right thickness for the skyrmion stabilisation.

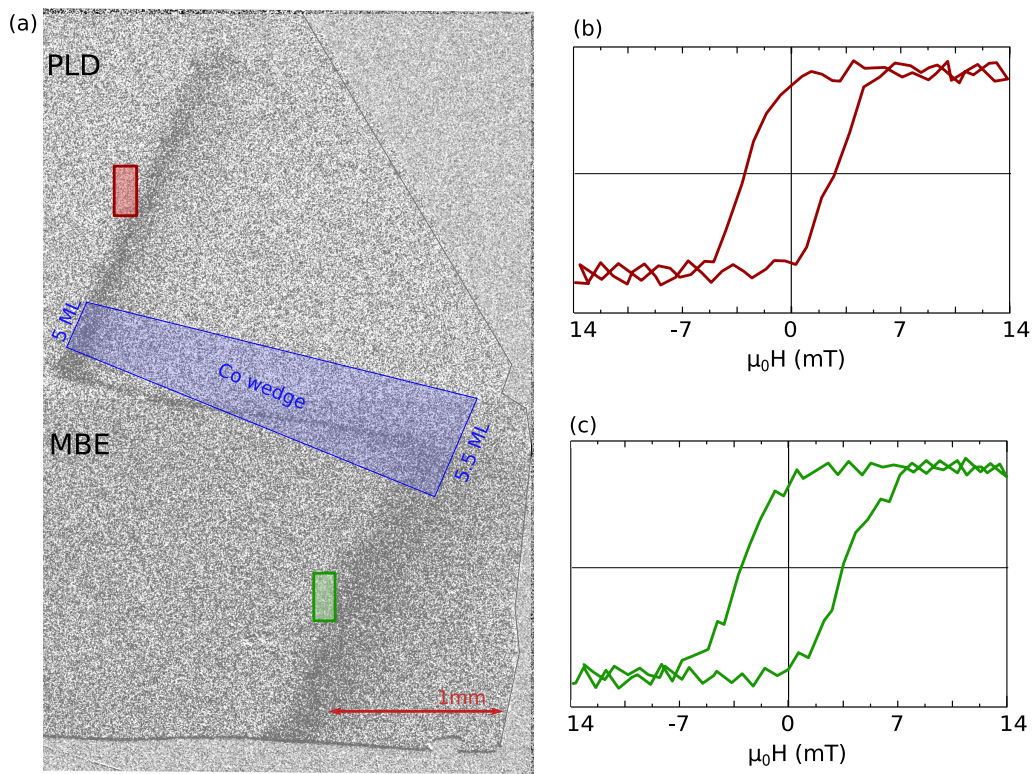


Figure 5.47: (a) Differential Kerr image after the sample saturation with an out-of-plane field. The green and the red rectangles indicate the areas where the polar Kerr hysteresis loops are acquired: (b) (red) in the Au PLD capped area (c) (green) in the Au MBE capped area. The blue trapezium shows the Co thickness along the wedge.

Fig. 5.47 shows the polar Kerr hysteresis loops with a magnetic field applied perpendicular to the surface of the $W/Co/Au$ system. Improvements of the UHV system allow to deposit Au capping layers with two different techniques on different zones; i.e. PLD and MBE. Kerr microscopy measurements show that the out-of-plane anisotropy in the MBE capped part is higher than in the PLD capped part. Indeed, the transition between out-of-plane and in-plane magnetisation occurs between 4.4 and 5 ML for the PLD capped part and between 4.8 and 5.5 ML for the MBE capped part. This phenomenon can be explained considering the dynamics of the crystal growth with the two techniques. The adatoms deposited by PLD have a higher kinetic energy than the adatoms deposited by MBE. Since the Co surface has a low surface energy Au-Co intermixing occurs during the growth and in the PLD deposition the effect is stronger. This intermixing can strongly reduce the strength of the interface anisotropy. The DMI from the Co/Au interface should

decreases as well by the interface mixing. Here we consider that the full stack interface DMI (D_s^x, D_s^y) remains unchanged since the Co\Au DMI is found to be weak [138] and in our BLS measurements it is impossible to know how much DMI arises from this interface.

The presence of two capping layers allows to study skyrmionic bubbles in two different energy environments. For a given perpendicular anisotropy value K_{eff} , in the MBE-capped part the DMI is lower and the surface dipolar interaction is larger than in the PLD-capped part due to the larger thickness. In Fig. 5.47 a differential Kerr image shows the presence of demagnetized areas. The images are taken after saturating the sample and the dark gray contrast indicates the sample areas naturally demagnetized. It occurs when the DW energy is small and the surface dipolar interaction promotes a demagnetized state. In this area the right energy conditions for the stabilisation of skyrmion bubbles are fulfilled.

Dots of different diameters have been lithographed on a continuous film. These structures have been designed in order to confine skyrmions. The lithography process is described in Fig. 5.48

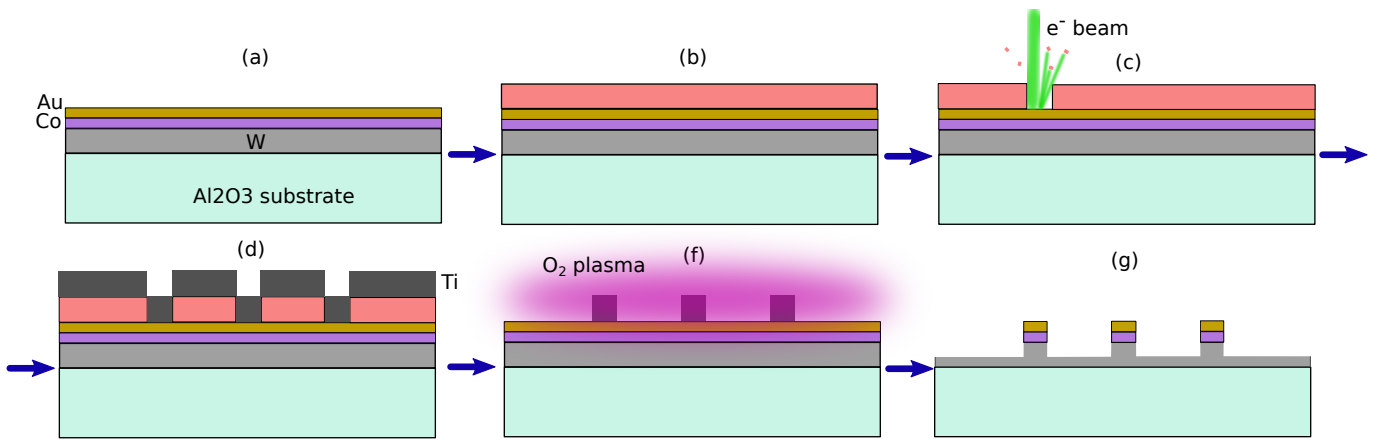


Figure 5.48: (a) Sample section as deposited. (b) An electron sensitive resin is put on the sample. (c) The resin is exposed to an electron beam in the areas where the material will stay after the procedure. (d) A layer of Ti is deposited on the exposed sample. (e) Chemical products are used to lift-off the resin and an oxygen plasma is used for edging the Ti and the sample unprotected by the Ti. (f) Final structure.

The lithography process allows to pattern dots with diameters from 150 nm up to 500 nm with a step of 25 nm (Fig. c5.49). Moreover big $130 \times 130 \mu\text{m}^2$ squares of continuous film are patterned in order to study the eventual changes in the magnetisation properties with Kerr microscopy between the lithography steps. Letters and numbers were also lithographed to help navigating on the sample surface when microscopy techniques with a reduced field of view are used.

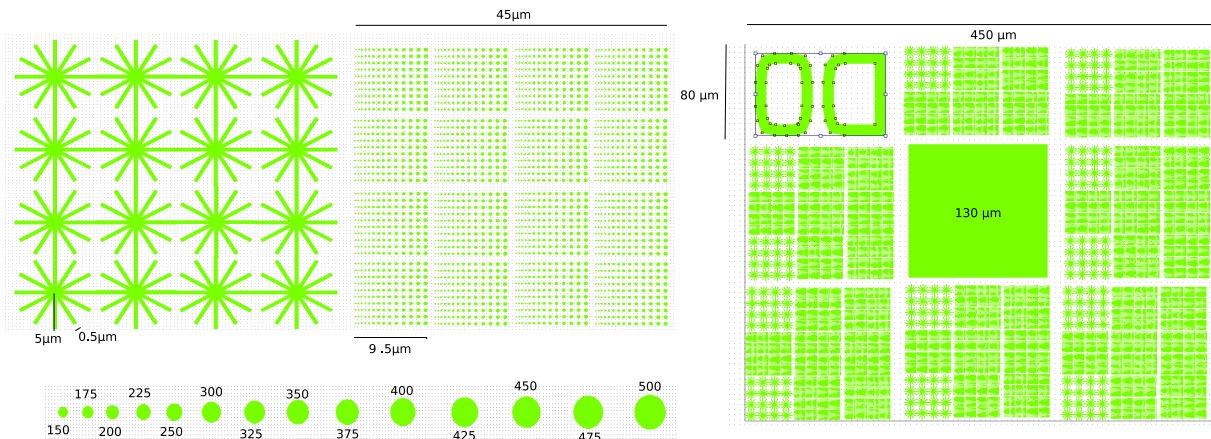


Figure 5.49: Design of the nanostructures patterned on the W\Co\Au continuous film

The patterning is performed in the transition area between out-of-plane and in-plane magnetisation. In order to help the nucleation of skyrmionic bubbles the system is demagnetized with an oscillatory out-of-plane field with an amplitude decreasing from a value larger than the anisotropy field down to zero.

5.7.2 MFM on nanopatterned W\Co\Au

MFM measurements have been performed on a nanopatterned W\Co\Au system. The measurements were performed with the help of Simon Le-Denmat from the pôle "Optique et Microscopie" of the Institut Néel. The sample presents a Co wedge with a thickness between 3 and 6 ML, covered by a Au layer deposited with MBE. Since the MFM measurements are difficult to perform on ultra-thin films due to the low stray field emitted by the sample, a high magnetic moment tip with 20 nm of Cr-Co has been used to increase the magnetic sensibility. On the other hand a tip with a high magnetic moment can have some drawbacks; i.e. the skyrmions are stable when all the magnetic energies compensate each other and the tip stray field may deform the skyrmion configuration.

Fig. 5.50 shows a topographic image of the nanopatterned dots and a magnetic microscopy image performed with MFM. The observed dot magnetisation depends mainly on three factors: The relation between the diameter of the dot and the characteristic demagnetisation length, the presence of local defects and the deformation of the magnetisation configuration by the MFM tip. The skyrmion bubbles are well confined when the dot diameter is comparable with two times the characteristic dipolar length of the demagnetized labyrinth-like domain structure [139]. In the analyzed sample this physics is strongly hidden by the presence of defects and by the deformation during the interaction with the MFM tip. Despite the disorder the magnetic configurations may be divided into three categories as a function of the dot diameter:

- **150-300 nm** The dots present mostly a uniform magnetisation. Theoretically the number of dark (magnetisation up) and bright (magnetisation down) dots should be equal after the demagnetisation procedure. In the image we observe a larger number of dark dots. This could arise from the interaction with the tip stray field or from an error in the calibration of the magnetic field during the demagnetisation process.
- **300-450 nm** Most dots present skyrmionic bubbles. The surface dipolar interaction should favor the presence of a circular domain in the center of the dot. In fact, all the skyrmionic bubbles are on the edge of the dots. One can suppose that they are pinned on some local defect.
- **450-500 nm** The dot diameter is too large, the skyrmionic bubbles are not confined and they deform in order to better demagnetize the dot.

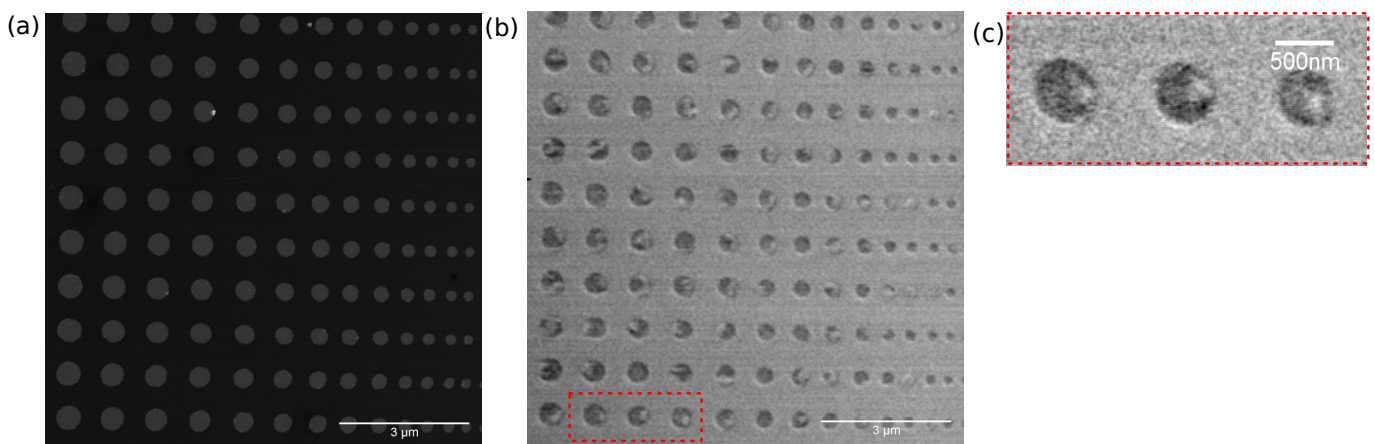


Figure 5.50: (a) AFM Topography image of nanopatterned dots of W\Co\Au. (b) Second pass phase shift MFM image with a 20 nm Cr-Co tip lifted 10 nm ($10 \mu\text{m} \times 10 \mu\text{m}$) (c) Second pass phase shift MFM image with a 20 nm Cr-Co tip lifted 8 nm ($3 \mu\text{m} \times 1.2 \mu\text{m}$) on the red zone in (b)

Fig. 5.50(c) shows a high resolution scan on the red delimited zone in Fig. 5.50(b). The second pass height of the MFM is modified in order to optimize the sensibility and the resolution of the MFM image. Indeed, when the second pass is reduced the spatial resolution increases, but the sensibility decreases due to the reduction of the cantilever oscillation. These images were taken with the aim of studying the effect of the anisotropic energies on the skyrmionic configuration but no clear physics could be obtained. We assume that the stray field of the tip is strong enough to deform the skyrmionic configurations making it impossible to evidence any anisotropy in these magnetic configurations.

5.7.3 XMCD-PEEM on W\Co\Au

XMCD-PEEM measurements on W\Co\Au samples have been performed on the HERMES beamline in the SOLEIL synchrotron with the aim of displaying the internal structure of the DWs and of skyrmionic bubbles. XMCD-PEEM is a delicate and complex technique that can allow to display the projection of magnetisation from three dimensions onto a plane with nanoscopic resolution (tens of nanometres). Several beam time shifts have been necessary to optimize the samples and the set-up looking for the required resolution for displaying the internal configuration of DWs. The capping layer thickness is a critical parameter for obtaining a good magnetic signal. Indeed when the layer is too thick the PEEM does not collect electrons from the Co layer whereas when the thickness is too thin the Co layer is exposed to oxidation that changes the sample properties. In the PEEM set-up the sample can be sputtered with an Ar plasma, but the calibration of this process is critical and a small error can destroy all the sample layers. A 1.5 nm Au-capping layer has been found as optimum thickness for performing PEEM measurements.

In addition, a flat and clean surface is necessary to avoid electric discharges between the sample and the microscope objective. Since 20 kV are applied, discharges can be destructive for the system. We have observed that such discharges strongly change the magnetic order of the affected area (Fig. 5.51). The areas struck by the beam display a lower out-of-plane anisotropy.

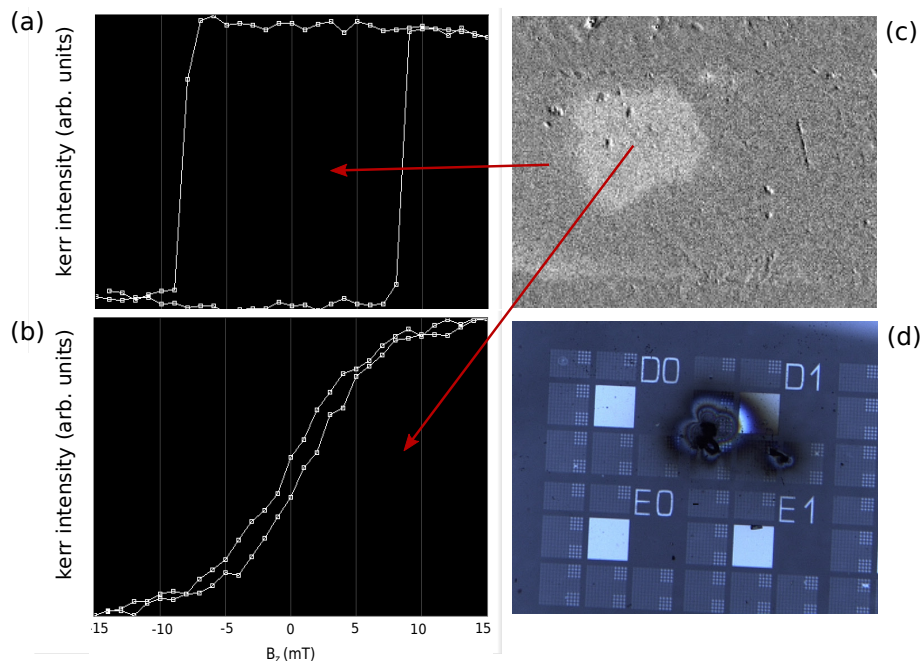


Figure 5.51: (d) Optical image of the consequence of discharges in the PEEM set-up (c) Differential Kerr image of a continuous out-of-plane magnetized system after the application of an out-of-plane field pulse of 10 mT for 10 μ s. The lighter part is the region modified by the discharges. (b) and (a) Polar Kerr hysteresis loops from the region struck by a discharge and as deposited under the application of an out-of-plane magnetic field. The square loop indicates the presence of an out-of-plane magnetisation whereas the loop in (b) shows that the normal of the sample is no longer the system easy axis. It means that the anisotropy is decreased in the area struck by the discharge.

During our three XMCD-PEEM beamtimes, several technical problems were encountered concerning the instrument, which did not allow to obtain a resolution better than 100 nm. Since the DWs in the reorientation zone have an expected width around 50 nm it was not possible to display the internal DW structure.

XMCD-PEEM measurements were performed on a nanopatterned sample and on a sample with a continuous film to observe the magnetic domain structure.

Nanopatterned sample Before imaging the sample magnetisation, X-ray absorption spectroscopy (XAS) and XMCD spectra were taken in order to verify the presence of X-ray magnetic circular dichroism at the Co $L_{2,3}$ -edges.

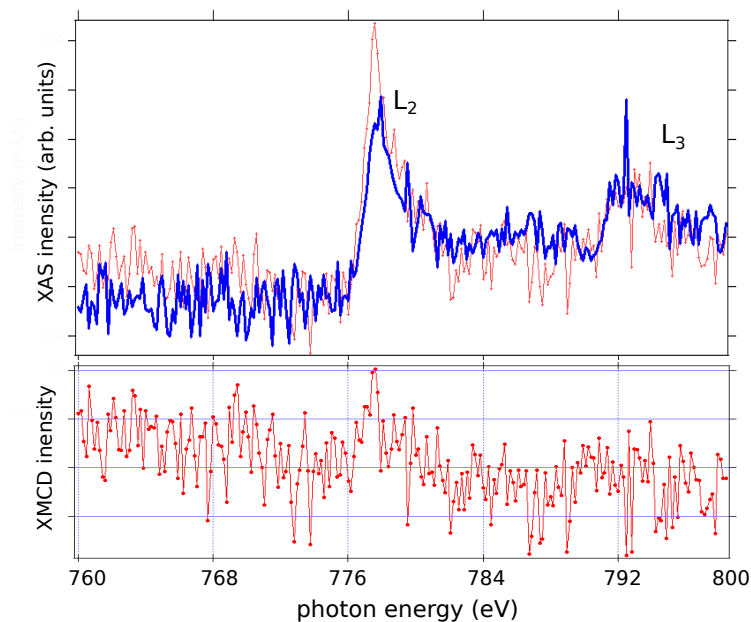


Figure 5.52: XAS spectra with two photon polarisations, (red) circular left (blue) circular right. The XMCD spectrum is obtained by the subtraction of the two XAS spectra.

The spectra in Fig. 5.52 show that the signal-to-noise ratio at the Co edges is very low. The observed dichroism is therefore very small. This weak signal may arise from a layer of Ti or Ti-oxide left on the structures after the lithography process. In principle, the Ti thickness and the edging process were calibrated in order to remove all the Ti on top of the dots and leave a continuous film of W for guaranteeing the electrical conduction between the nanopatterned structures. A mistake in the calibration process may thus be responsible for a remaining Ti layer on the structures which is too thick to obtain a good contrast at the Co edges. This interpretation is confirmed by the spectra on the part of the sample protected during the lithography processes, where the Co edges are more intense and a clear dichroism is present. Unfortunately, it was therefore impossible to perform the XMCD-PEEM measurements on the nanopatterned sample.

Continuous film The XAS from the continuous film of a W\Co\Au sample is shown in Fig. 5.53.

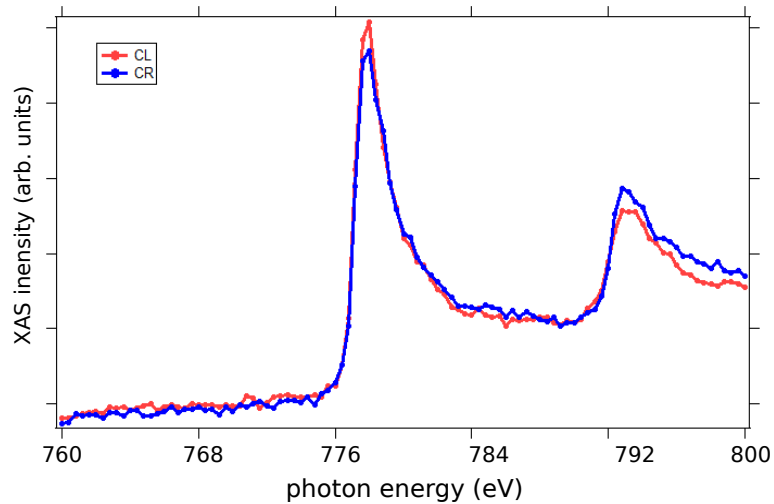


Figure 5.53: XAS spectra at the Co L_2 and L_3 edges with two photon polarisation, (red) circular left (blue) circular right.

The Co $L_{2,3}$ spectra were again acquired with left and right circularly polarized light and the difference in the peak intensities shows the presence of magnetic dichroism.

The X-Ray beam in the PEEM makes an angle of 16° with the sample plane, while the magnetisation is out-of-plane. The projection of the magnetisation direction on the incoming beam direction measured by XMCD is thus small, but strong enough to guarantee good conditions for the XMCD-PEEM measurements.

The sample was demagnetized by the application of an out-of-plane oscillatory field before the entrance in the XMCD-PEEM set-up. Inside the set-up a small magnetic field can be present due to the magneto-electric lenses of the PEEM, which can slightly change the magnetisation configuration. This can explain the presence of a larger region with white contrast in Fig. 5.54. Notice the presence of skyrmionic bubbles randomly distributed on the surface. One possibility is that they are stabilized on the crystal defects, where the out-of-plane anisotropy may be higher. Fig. 5.54(a) and Fig. 5.54(b) have been taken on two different positions in the area naturally demagnetized by the surface dipolar interaction. The skyrmionic bubbles have an irregular shape and a size around 300-600 nm. The PEEM resolution did not allow to analyze the internal magnetisation and there is no clear evidence of an anisotropy in the shape.

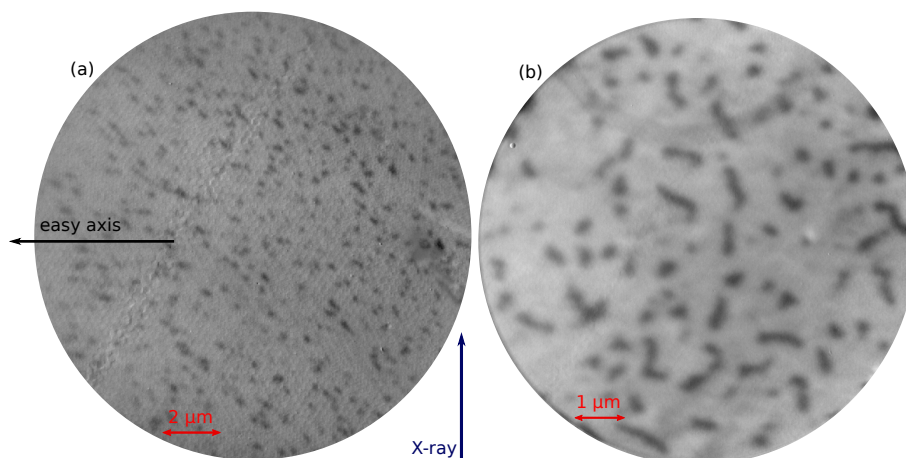


Figure 5.54: XMCD images with the X-Rays perpendicular to the in-plane easy axis with $20 \mu\text{m}$ (a) and $10 \mu\text{m}$ (b) fields of view.

5.7.4 Comments on the research of elliptical skyrmions in the W\Co\Au system

The W\Co\Au system presents the anisotropic energy environment necessary for the stabilisation of elliptical skyrmions. Skyrmionic bubbles have been stabilized in nanopatterned structures. MFM images show the presence of skyrmionic bubbles on the nanopatterned structures. The interaction with the tip and local defects deform the skyrmion bubbles shape, which hides the anisotropic properties. Technical problems during the lithography did not allow to study this system with XMCD-PEEM. However, this technique allowed to show the presence of skyrmionic bubbles in a continuous film. They are probably stabilized on the structural defects. Unfortunately, problems with the XMCD-PEEM set-up did not allow to study the internal configuration of these skyrmionic bubbles.

5.8 W\Co\Au-Pt solid solution

The W\Co\Au system presents interesting anisotropic properties, but it was impossible to reveal elliptical skyrmions due to the deformations induced by the defects and by perturbations induced by the experimental techniques. One possible strategy in order to increase the chance of stabilizing such skyrmions is to increase the DMI interaction and the anisotropic properties. In this way the energy fluctuations induced by the defects should have less impact on the magnetic configuration.

From the study of the magnetic properties of the W\Co\Au and W\Co\Pt systems and from literature we know that Co\Au has a strong out-of-plane anisotropy and a low DMI whereas the Co\Pt interface induces a strong DMI but its out-of-plane anisotropy is weaker than the in-plane anisotropy of W\Co. Therefore a system with mixed properties between Co\Au and Co\Pt interfaces might have the right energy environment to display elliptical skyrmions.

In the deposition chamber it is possible to deposit a Au-Pt solid solution. A layer with a solid solution is composed by small islands of two or more materials, which are only partially mixed and where the distance between the island is smaller than the magnetic exchange lengths. Then the layer can be considered homogeneous from the magnetic point of view with properties averaged between the materials.

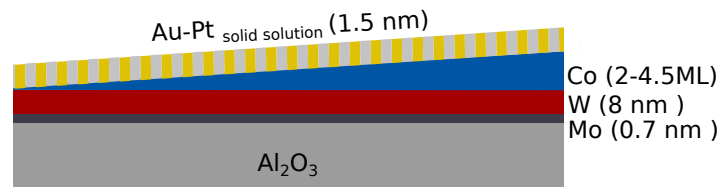


Figure 5.55: Sketch of the W\Co\Au-Pt_{solid solution} structure

The Co\Au-Pt_{solid solution} interface could show really interesting magnetic properties. The system should have a strong DMI because of the presence of Pt at the top Co interface and at the same time it should be magnetized out-of-plane, with a transition to in-plane magnetisation taking place for a lower Co thickness than in the W\Co\Au system because of the smaller perpendicular anisotropy. Since the transition happens at a lower Co thickness, the anisotropic properties induced by the W\Co interface should be larger in the transition region. A sketch of the complete deposited stack is shown in Fig. 5.55.

5.8.1 Growth of the Au-Pt_{solid solution}

The Mo, W, and Co layers are grown in the deposition chamber in the UHV system as shown in Sec. 5.2. The Co wedge layer is grown with a thickness from 1 to 4.5 ML in order to study for small thickness the paramagnetic-ferromagnetic transition and for thicker Co the reorientation of the magnetic easy axis from out-of-plane to in-plane.

In order to deposit a solid solution it is essential to increase the density of grown nuclei as much as possible. This was possible using the PLD technique and alternating Au and Pt depositions. In each deposition step, 0.2 ML of material is deposited. Fortunately Au and Pt have similar evaporation conditions, which allows to fix the laser intensity to 0.65 W. The laser beam is defocused for the Au deposition in order to reduce the production of recoil droplets.

5.8.2 Magnetic characterisation

The magnetic properties of the W\Co\Au-Pt_{solid solution} system as a function of the Co thickness have been studied with Kerr magnetometry. The Au-Pt_{solid solution} layer is composed of 33 % of Pt and 66% of Au. In this section the hysteresis loops obtained by the analysis of the polar Kerr effect as a function of an out-of-plane magnetic field for different Co thickness are shown.

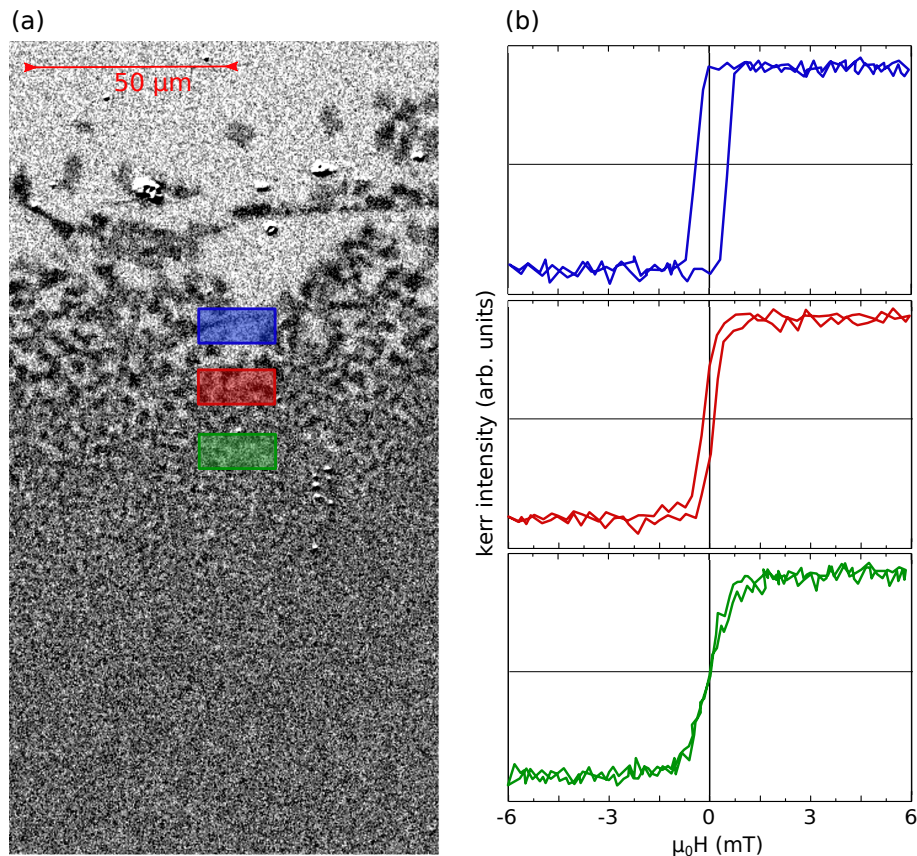


Figure 5.56: (a) Differential polar Kerr image taken after saturation of the system by the application of a strong out-of-plane field (b) Polar Kerr hysteresis loops as a function of an out-of-plane field, the plot colors indicate the areas in (a) where the Kerr signal is collected.

The paramagnetic-ferromagnetic transition due to the increase of the Curie temperature occurs at 1.6 ML. The differential Kerr microscopy image in Fig. 5.56(a) shows the presence of unstable demagnetized magnetic domains. The image is taken after the sample saturation with a strong out-of-plane field. The gray contrast in the bottom of the image shows the presence of a paramagnetic state whereas the light-grey one indicates ferromagnetic order. The presence of different dark contrasts in the transition shows the presence of thermally unstable magnetic domains. The hysteresis loop in Fig. 5.56(b) confirms the presence of a transition from a paramagnetic state to weak ferromagnetic order with a small coercivity. The multidomain configuration is caused by the thermal fluctuations that allow to switch the magnetisation between the two out-of-plane directions.

In the ferromagnetic part between 1.6 and 3.5 ML, the presence of an interesting magnetisation reversal dynamics has been investigated with polar Kerr microscopy. Fig. 5.57 shows the plot of the Kerr intensity as a function of an out-of-plane field and the corresponding differential Kerr images.

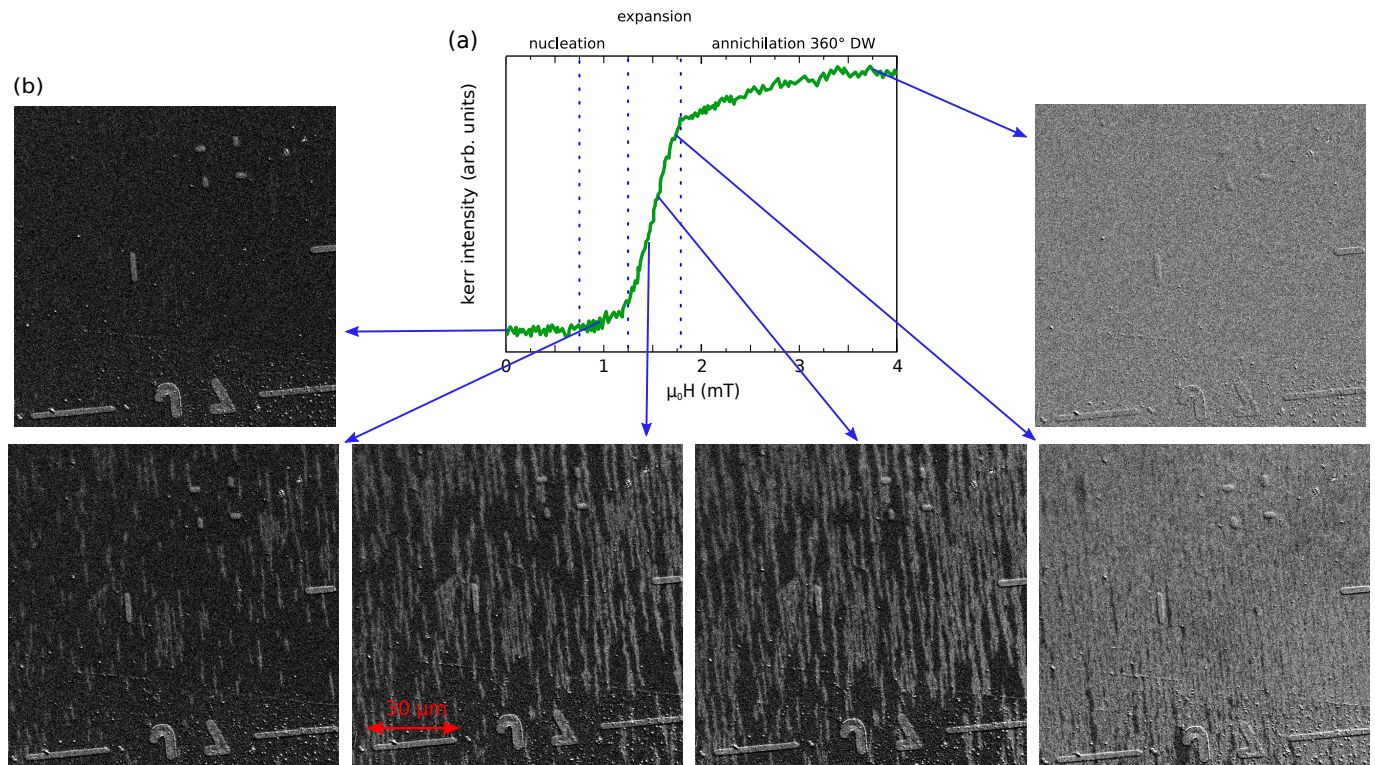


Figure 5.57: (a) Polar Kerr intensity as a function of an out-of-plane magnetic field. (b) Differential Polar Kerr images. The pictures are obtained as the difference between the image of a saturated state and the magnetic configuration after the application of the field shown with the arrows on plot (a)

The magnetisation reversal can be divided into three regimes:

- **Nucleation** After a flat part the Kerr signal starts to increase: small domains appear and their density increases as a function of the applied field.
- **Anisotropic expansion** Around 1.25 mT the domains expand mainly along the in-plane easy axis direction. This is the confirmation of the presence of strong anisotropic interactions in the W\Co\Au-Pt_{solid solution} system. Since the DW speed directly depends on the DW energy one can expect a high DW energy anisotropy in this system.
- **360° DW annihilation** At 1.76 mT the white domains cover all the surface. Even if the microscopy resolution does not allow to distinguish black domains the Kerr signal shows a moderate slope up to the complete saturation that occurs around 4 mT. This slope can be explained considering the magnetic domain dynamics. When the white domains expand they meet each other but they do not merge reducing the black domains to a 360° DW configuration. These magnetic configurations are particularly stable and are annihilated for magnetic fields higher than the DW propagation field.

The periodicity of these stripe domains decreases when the sample thickness increases. This can be explained by the competition between the DW energy and the surface dipolar interaction between the domains. When the Co thickness increases the DW energy decreases due to the reduction of the out-of-plane anisotropy and the dipolar interaction increases due to the larger magnetic volume.

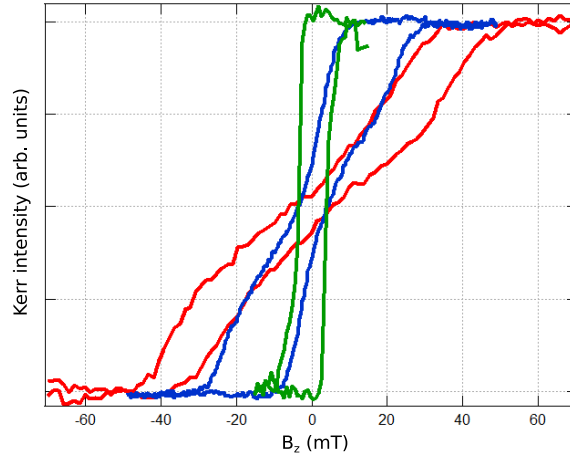


Figure 5.58: Polar Kerr hysteresis loops as a function of an out-of-plane magnetic field for different positions along the Co wedge.(green 3 ML, blue 3.8 ML and red 4 ML)

Fig. 5.58 shows the hysteresis loops in the transition area where the magnetic easy axis transits towards the sample plane. This phenomenon occurs for a Co thickness between 3.5 and 4.1 ML. Notice that the saturation field in this region strongly increases, the remanent magnetisation is small and before the saturation the Kerr signal has a change of slope. This is an indication of the role of the dipolar interaction. Indeed the slope changes, because when the size of the domains increases in one direction due to the applied magnetic field, the dipolar field in the direction opposite to the applied field increases as well. So the smaller the domains opposite to the applied field become, the more the magnetic field has to increase in order to compensate the dipolar field.

The high saturation field and the small remanent magnetisation indicate the presence of a strong surface dipolar interaction. It promotes the demagnetisation of the system and protects the domains from switching. This region shows the perfect magnetic conditions for the stabilisation of skyrmionic bubbles.

5.8.3 MFM on W\Co\Au-Pt solid solution

Magnetic Force Microscopy has been performed on the W\Co\Au-Pt_{solid solution} sample in order to study the stripe domain size and shape in the area where the easy axis transits into the sample plane ($\simeq 4$ Co ML). The measurements were performed together with Olivier Fruchart. In the MFM set-up it is possible to apply out-of-plane magnetic fields. Starting from a demagnetized magnetic configuration an out-of-plane magnetic field can be applied to change the stripe shape and size and try to confine elliptical skyrmionic bubbles. The demagnetisation in this area occurs naturally due to the presence of a strong surface dipolar interaction and a small DW energy. Fig. 5.59 shows the phase shift of the MFM cantilever during the second pass in a $2.5 \times 2.5 \mu\text{m}^2$ zone as a function of an out-of-plane magnetic field. The magnetic contrast in the images is small due to the low magnetic sensitivity, i.e. hundreds of 10^{-3} degrees. Even though a high magnetic moment tip (20 nm CoCr) has been used, the low stray field from the thin Co layer does not allow to obtain a higher sensitivity.

In the image there are four different contrasts. The intermediate contrasts arise from the interaction of the tip with the out-of-plane magnetized domains. The brighter and darker contrasts may be a measurement artefact that could arise from the tilt of the tip and its oscillation direction. Indeed when the tip is tilted and oscillates with an angle with respect to the sample normal, it induces a difference in the face shift between when the tip passes from a positive to a negative stray field and from a negative to a positive one.

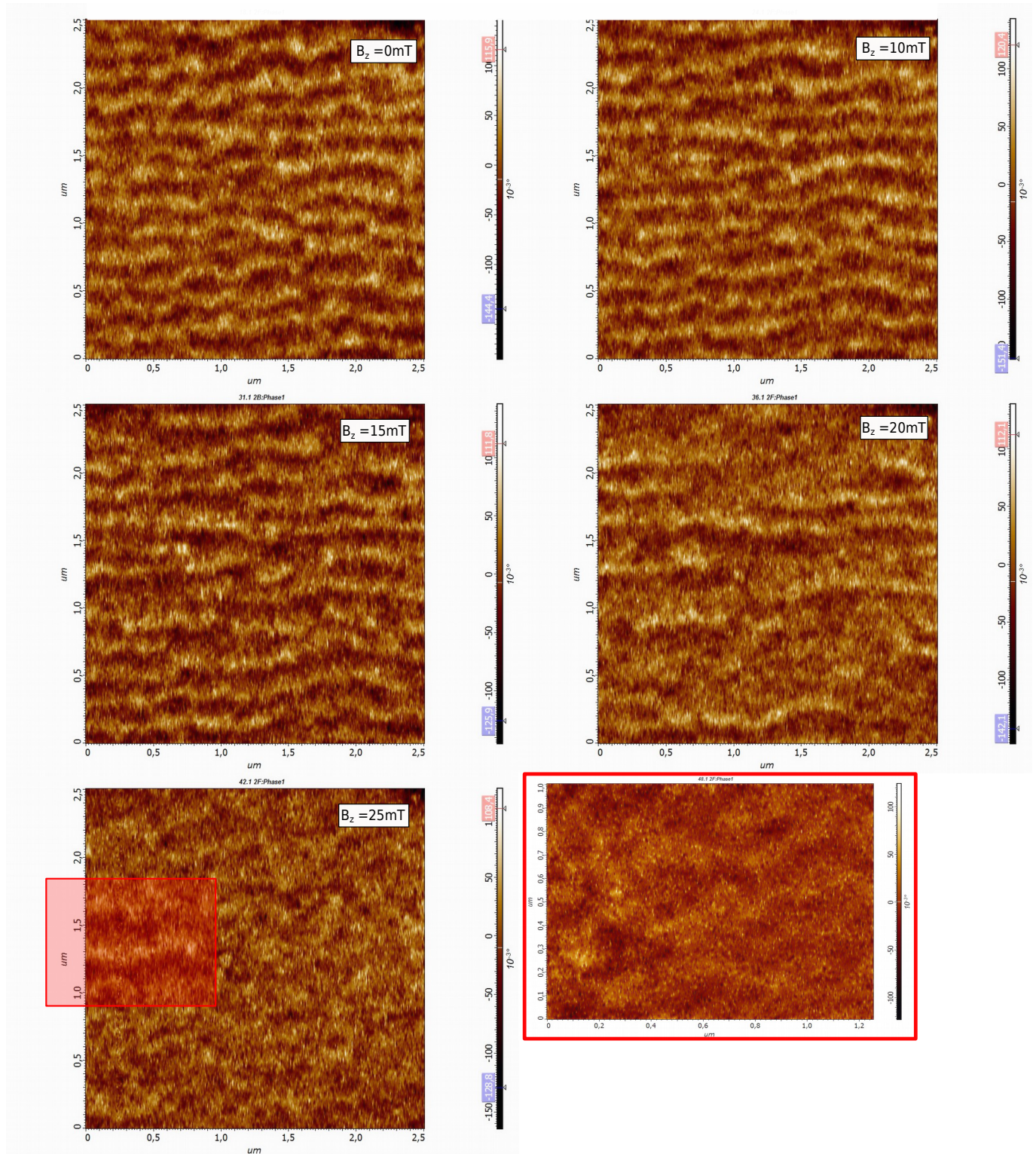


Figure 5.59: The phase shift of the MFM cantilever during the second pass in a $2.5 \times 2.5 \mu\text{m}^2$ zone as a function of an out-of-plane magnetic field. The red profile in the bottom left image indicates the area where the bottom right image is taken.

The images show the presence of a stripe domains configuration. The stripes are parallel to the easy axis with a zigzag shape. Even if the displayed magnetisation is a static configuration, magnetic domains are elongated along the easy axis because of the domain wall dynamics (Sec. 5.8.2). This configuration is not energetically favorable because the magnetisation modulation occurs mainly along the hard axis. Along this direction the DW energy density is larger than along the easy axis because of the competition between the DMI and the in-plane anisotropy. The DWs have indeed the tendency to orientate along the easy axis to

reduce their energy density. On the other hand, when the DWs rotate it increases its length. The compromise between the decrease of the DW energy density and the increase of the DW length stabilizes a tilted DW configuration that may explain the DW zigzag shape.

A magnetic field is applied along the magnetisation of the domains with the dark contrast in order to confine skyrmionic bubbles. The Zeeman energy promotes the increase of the area of these domains. Different effects occur as a function of the magnetic field strength :

- ($0 < B_z < 10$ mT) The domains do not change much their area. Some domains in the $B_z = 0$ image have an extended area with collinear magnetisation and when the magnetic field is applied they reduce their area.

The domain periodicity is around 100 nm and does not change under the field application (Fig. 5.60). The lack of a complete magnetic characterisation does not allow to calculate the DW width. However, the invariance of the dark domain width indicates that the magnetic domains do not have a collinear magnetisation and the imaged magnetic configuration corresponds to a continuous magnetisation variation. Therefore the periodicity (λ) corresponds to a 360° DW width. It allows to give an approximate value of the effective anisotropy constant:

$$\lambda = 2\pi \sqrt{\frac{A}{K_{\text{in}}^{\text{eff}}}} \quad \rightarrow \quad K_{\text{out}}^{\text{eff}} + K_{\text{in}} = 4\pi^2 \frac{A}{\lambda^2} = 47.3 \cdot 10^{-3} \text{ J/m}^3 \quad (5.41)$$

The main clear effect of the magnetic field is the reduction of the zigzag shape. Indeed, the area of the black contrast domains becomes larger, the domain are straight without increasing too much the dipolar energy.

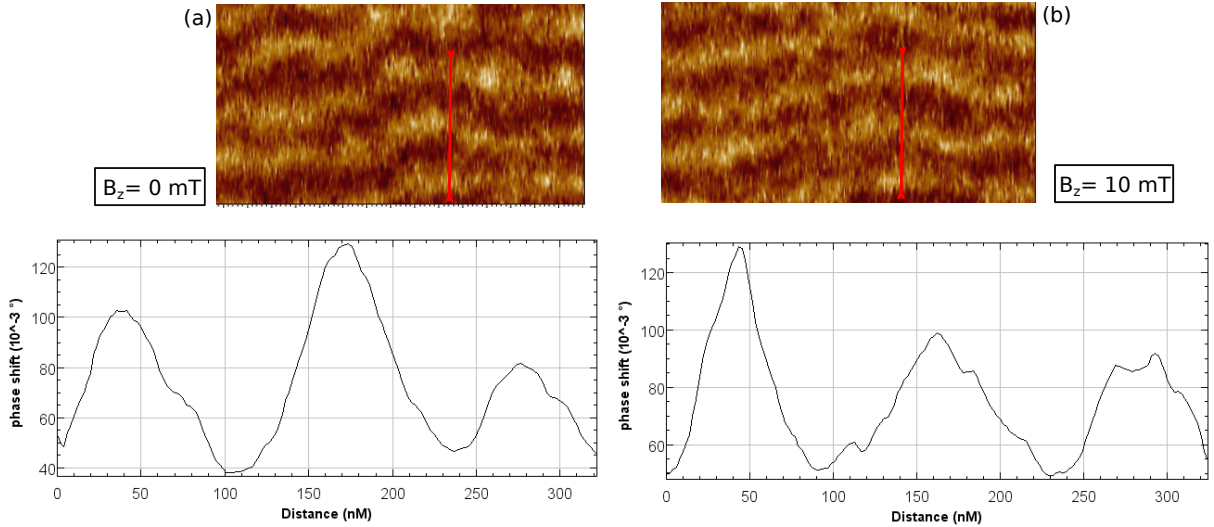


Figure 5.60: MFM images under the application of (a) $B_z = 0$ and (b) $B_z = 10$ mT. The plot shows the phase shift variation along the red line in the MFM images.

- ($15 < B_z < 20$ mT) The Zeeman effect starts dominating over the surface dipolar interaction and the dark domains extend their area.
- ($B_z = 25$ mT) The magnetic field is strong enough to reduce and annihilate the bright domains. Only one bright domain is still visible, on the left of the $B_z=25$ mT image (Fig. 5.60). A new scan was thus performed in a reduced area in order to increase the resolution and the information about the domain shape. In the new image the domain had disappeared. This could be an effect of the tip magnetic field. Indeed the tip was saturated in the direction of the application of the magnetic field in order to avoid flipping of the tip magnetisation during the measurements.

The analysis of the MFM images of the W\Co\Au-Pt_{solid solution} is difficult due to the low magnetic sensitivity. We did not manage to observe any elliptical skyrmionic bubble. Theoretically when a magnetic

domain becomes a skyrmionic bubble its shape should be determined by the DW energy and assume an elongated shape along the hard axis. All the nanometric domains observed in the MFM image are elongated along the easy axis. Moreover, one can expect that when the magnetic domains become small enough to reveal the skyrmionic properties, the MFM magnetic signal becomes smaller than the noise level.

5.8.4 XMCD-PEEM on W\Co\Au-Pt solid solution

XMCD-PEEM measurements on W\Co\Au-Pt_{solid solution} have been performed at the Nanospectroscopy beamline in the ELETTRA synchrotron. The measurements have been performed at several points along the Co wedge. The sample has been demagnetized with an oscillatory out-of-plane field and Kerr microscopy measurements show the presence of the stripe domains along all the Co wedge. The XMCD-PEEM measurements were performed with the aim of studying the stripe; configuration as a function of the Co thickness and analyse the DW internal magnetisation. The sample was first mounted with the easy axis parallel to the beam direction. Since the XMCD-PEEM contrast depends on the magnetisation projection along the beam direction this geometry allows to study the presence of Bloch DWs along the hard axis and Néel DWs along the easy axis.

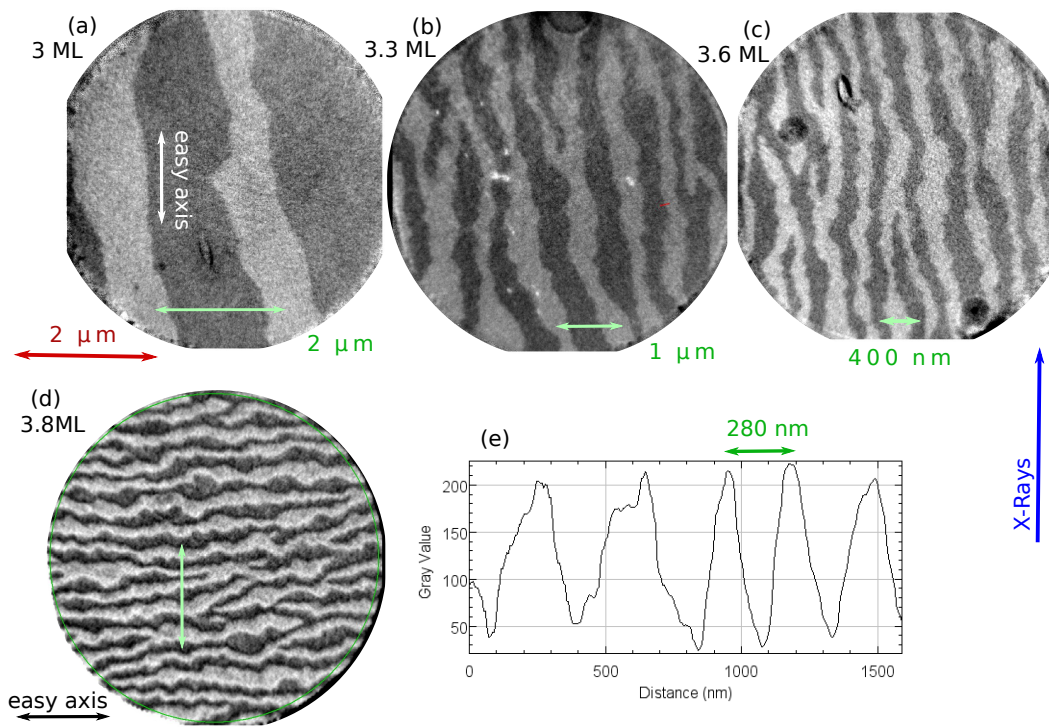


Figure 5.61: XMCD-PEEM images with the x-rays parallel to the easy axis for (a), (b) and (c) and parallel to the hard axis for (d), with a 5 μm field of view. (e) Contrast profile along the green line in Fig. (d).

The images in Fig. 5.61 show the presence of only two magnetic contrast levels from domains magnetized parallel to the sample surface normal. For small Co thickness the DW width may be smaller than the XMCD-PEEM resolution ($\simeq 50$ nm) (Fig. 5.61(a)(b)(c)). The stripe configuration is inhomogeneous but it is possible to evidence the change of the periodicity from $\simeq 2$ μm to 180 nm when the Co thickness increases from 3 ML to 3.9 ML. The MFM measurements showed that the DW width should be larger than the resolution of the PEEM (30-40nm for the PEEM at Nanospectroscopy) for 3.8 ML of Co. For this thickness the resolution should thus be high enough to display the internal DW magnetisation, but the image with the beam parallel to the easy axis shows only the two magnetic contrast levels corresponding to the perpendicular domains. In a second measurement, the sample was turned to align the x-ray beam along the hard axis. Fig. 5.61(d) shows a stripe domain configuration with a minimum periodicity of 180 nm and four different contrasts. When the periodicity is $\simeq 180$ nm the contrast profile shows a clear peak only for the magnetisation inside the DW whereas when the domains are larger, four contrast levels can be observed, as shown in the profile in Fig. 5.61(e). Fig. 5.62 shows a zoom of the image in Fig. 5.61(d). The intensity profile shows the presence

of four contrast levels. The relation between the intensity of the X-ray absorption and the magnetisation direction is explained in the insert.

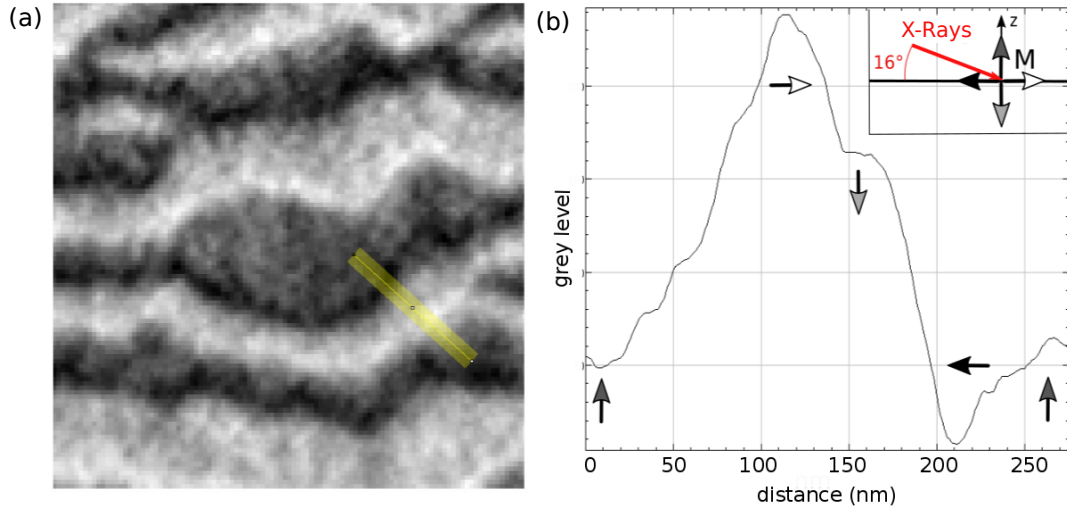


Figure 5.62: (a) XMCD images with the X-Rays parallel to the hard axis (zoom of the image in Fig. 5.61(d)). (b) Profile of the contrast along the yellow line in (a).

The darker and brighter contrasts indicate the presence of DWs with a polarisation partially along the hard axis. It means that the DWs have an important Néel component. A more accurate study and more images with different orientations with respect to the X-ray beam are necessary in order to determine the complete two-dimensional magnetisation map. Unfortunately only four hours of beamtime could be used for these measurements. On the other hand, this result clearly shows that in the W\Co\Au-Pt_{solid solution} sample for this Co thickness the DMI interaction is comparable to, if not stronger than the in-plane anisotropy.

5.8.5 Comments on the search of elliptical skyrmions in a W\Co\Au-Pt solid solution system

The W\Co\Au-Pt_{solid solution} sample shows the presence of strong anisotropic properties. The magnetic properties have been studied as function of the Co thickness. For large thickness the system is demagnetized by the surface dipolar interaction. In this conditions a configuration with stripe domains parallel to the in-plane easy axis is found. The same configuration with a larger periodicity has been found even for thinner Co layer after demagnetisation with an out-of-plane magnetic field. Kerr microscopy studies of the DW dynamics allowed to evidence the origin of this magnetic configuration, which arises from a strong anisotropy in the DW motion.

MFM measurements with the application of a static magnetic field have been performed in order to confine elliptical skyrmionic bubbles but the reduced sensitivity of this technique to thin magnetic films did not allow to display and characterize them.

XMCD-PEEM measurements allowed to reveal the internal structure of the DWs along the in-plane hard axis of the system. They show the presence of a Néel DW component.

More XMCD-PEEM measurements and BLS studies will be performed in order to complete the magnetic characterisation and maps of this system.

5.9 W\Fe\Co\Au

A sample W\Fe\Co\Au has been grown with the aim of stabilizing anti-skyrmionic bubbles at room temperature. The fundamental condition for the stabilisation of these topological solitons is the inversion of DMI sign between two perpendicular in-plane directions $\frac{D_x}{D_y} < 0$. Ab-initio calculations have shown that this condition can be fulfilled at the W(110)\Fe interface [18, 140]. In the calculations a perfect pseudomorphic

bcc (110) Fe on bcc (110) W surface is considered. Experimentally this occurs up to 2 ML of Fe. For thicker layers the Fe structure relaxes and disorder is induced in the crystal. Then the system is not comparable anymore with the calculated one and the conditions for an inversion of DMI may be lost. The problem of studying a system with 2ML of Fe is that the Curie temperature could be close to room temperature and the magnetic moment too small to be measured with microscopy techniques. Moreover the W(110)\Fe interface presents a strong in-plane anisotropy. These problems can be resolved by growing a Co wedge layer on top of the Fe and capping the system with a layer of Au. The Co layer allows to increase the magnetic moment and the Co\Au interface induces a strong out-of-plane anisotropy. Moreover, the DMI induced at this interface is weak. This is fundamental because the presence of a strong DMI at the interface opposite to the W(110)\Fe could shift the total DMI value and avoid the sign inversion.

5.9.1 Growth and crystal characterisation

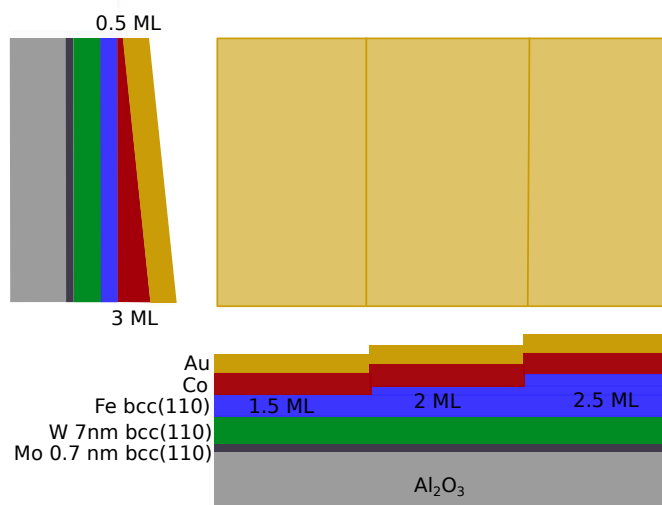


Figure 5.63: Sketch of the W\Fe\Co\Au sample

The W\Fe\Co\Au stack is designed and prepared in order to investigate how the magnetic properties change as a function of the Co and Fe thickness.

The Mo and the W layers are deposited as explained in Sec. 5.2. The mask in the deposition system allows to grow a Fe layer composed by three steps of different thickness (1.5, 2, 2.5 ML) (Fig. 5.63). The Fe layer has been deposited at room temperature and with a moderate laser power (0.8 W). The bulk Fe has a bcc crystal structure with a lattice parameter of 0.286 nm.

RHEED measurements performed on the three steps confirm the expected Fe growth behavior (Fig. 5.64). For 1.5 and 2 ML, along the bcc[001] direction the W and Fe crystals have exactly the same lattice parameters whereas along the bcc[$\bar{1}10$] the Fe is partially relaxed with a small mismatch with respect to the W crystal. For 2.5 ML the Fe crystal relaxes even along the bcc[001], as shown in Fig. 5.64 where the diffraction peak can be fitted with two Lorentzian functions. The first one corresponds to the Fe lattice parameter for 1.5 and 2 ML whereas the second one corresponds to the relaxed lattice parameter ($d = 0.288$ nm). Along the bcc[$\bar{1}10$] direction the Fe RHEED peaks are broader than along bcc[001]. This means that the Fe crystal along this direction is not uniquely defined. The crystal could be stressed and relaxed in different ways as a function of the Fe crystal position with respect to the substrate potential. A high density of crystal defects like dislocations could exist along this direction.

A Co wedge layer is grown with a thickness from 0.5 ML to 3 ML as shown in Fig. 5.63. The Co grows strongly stressed on top of the Fe and assumes the same crystal symmetry. Indeed, along both the main directions the Co peaks are broad. Along bcc[$\bar{1}10$] the Fe and the Co have the same lattice parameter whereas along bcc[001] the Co is partially relaxed.

Finally 1.5 nm of Au is deposited with MBE in order to increase as much as possible the quality of the

Co\Au interface and thus the strength of the out-of-plane anisotropy. The Au crystal grows on the Co bcc (110) surface with a relaxed fcc(111) structure.

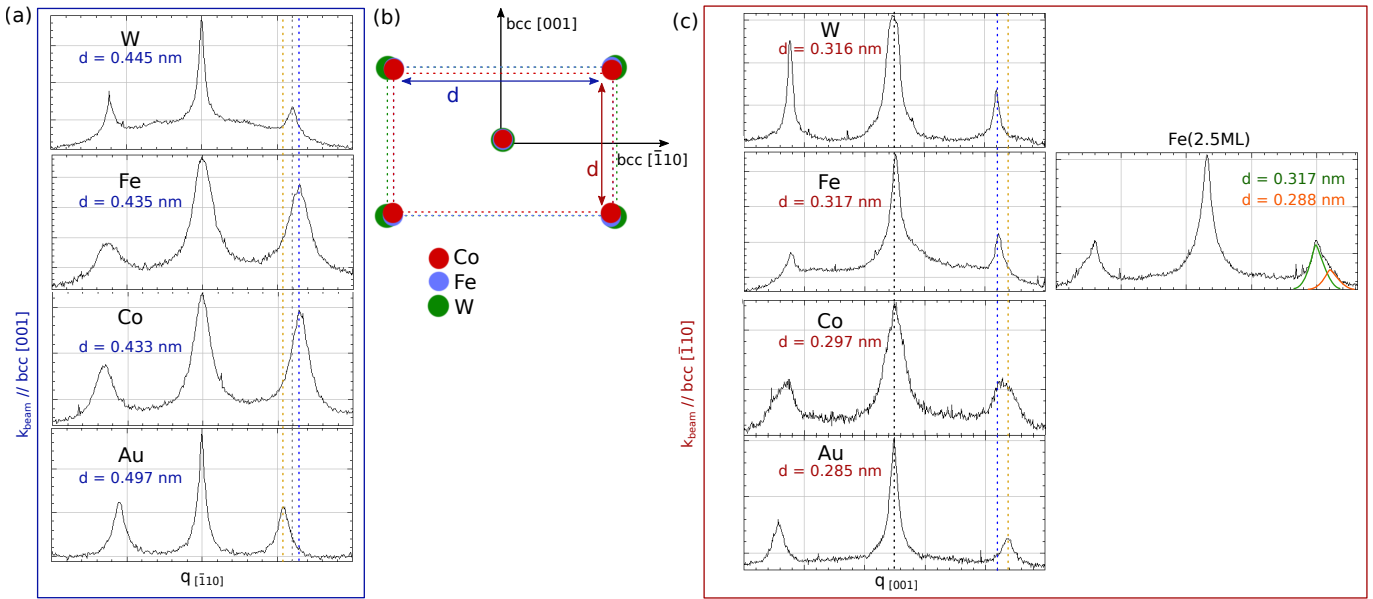


Figure 5.64: (a) RHEED pattern intensity plots for the different materials as a function of the moment $q_{[\bar{1}10]}$ when the electron beam is parallel to the bcc[001] direction. (b) Sketch of the relationship between the W (green), Fe (blue) and Co (red) crystal structures. (c) RHEED pattern intensity plots for the different materials when the electron beam is parallel to the bcc $[\bar{1}10]$ direction

5.9.2 Magnetic characterisation and perspectives

Polar Kerr microscopy has been performed along the Co wedge for each Fe step. The hysteresis loops performed with polar Kerr magnetometry show that the system has an in-plane magnetisation. It means that the W\Fe in-plane anisotropy dominates the Co\Au out-of-plane anisotropy. The Co\Au interface has one of the strongest interface out-of-plane anisotropies between a heavy metal and room temperature magnetic materials [141]. On the other hand, we showed in Sec. 5.3.1 that the interface between the Co and $\text{Co}_x\text{O}_{x-1}$ presents an unexpected strong out-of-plane anisotropy. The hopes for out-of-plane magnetisation in a system with the W\Fe interface are not vanished and a system W\Fe\Co\Co $_x$ O $_{1-x}$ Au will be grown with this aim.

Chapter 6

Conclusions and perspectives

6.1 Conclusions

In this thesis I studied the relationship between the **crystal symmetry**, the **DMI symmetry** and the **topological solitons** in epitaxial magnetic thin films. The particular case of thin films with C_{2v} symmetry has been considered. These systems are particularly interesting for their anisotropic properties that allow to stabilize magnetic solitons with different symmetries and topological numbers. We used theoretical and experimental approaches to investigate this phenomenon:

Micromagnetic approach

An introduction to the magnetic interactions in thin film system is given in the chapter "*Introduction to the magnetism in C_{2v} systems*". The relationship between the atomistic and the micromagnetic formulations of magnetic interactions is studied. This allowed to underline the role of crystal symmetry in the determination of the symmetry of the magnetic interactions and explain the presence of anisotropic interactions in systems with C_{2v} symmetry.

In the chapter "*Magnetic topological solitons*" I studied the effect of the anisotropic magnetic interactions on the configurations of 1D and 2D magnetic solitons. This is done in the continuous magnetisation approximation used in micromagnetism. The discussion starts from the simplest one-dimensional soliton, the domain wall, and step by step new interactions and symmetries are added in order to characterize the stability conditions and the properties of skyrmions and anti-skyrmions.

The study of the DW energy and polarisation in systems with a C_{2v} symmetry is complex and required the analysis of each magnetic interaction.

The effect of the DMI can be studied by two parameters which describe the strength of the interaction along the main axes, $D_s^{(x)}$ and $D_s^{(y)}$:

- If $D_s^{(x)}/D_s^{(y)} > 0$ the DMI promotes Néel DWs with the same chirality along the main axes and mixed Bloch and Néel DWs along the intermediate directions.
- If $D_s^{(x)}/D_s^{(y)} < 0$ the DMI promotes Néel DWs with opposite chirality along the main axes and mixed Bloch and Néel DWs along the intermediate directions. There is always a direction along which the DMI promotes a pure Bloch DW.

In systems with C_{2v} symmetry the magnetic anisotropy has an in-plane easy axis which promotes a DW polarisation along this direction. The exchange interaction is anisotropic and changes the DW energy and width without changing the DW polarisation. Under the studied conditions the volume dipolar interaction is negligible with respect to the in-plane anisotropy.

The competition between these interactions stabilizes DWs with highly anisotropic energy and polarisation. Along the in-plane easy axis the anisotropy and the DMI stabilize a Néel DW with the polarisation set by the DMI chirality. Along the hard axis the interactions are in competition and two degenerate DW polarisations can be found. Along the intermediate directions, if $D_s^{(x)}/D_s^{(y)} > 0$ the DW polarisation

changes smoothly, and if $D_s^{(x)}/D_s^{(y)} < 0$ it changes with abrupt polarisation jumps.

The study of the DW energy and configuration is essential to study 2D topological solitons.

In the section "2D topological solitons" we have developed an analytical topological soliton model. It contains expressions of the long range demagnetizing and exchange curvature energies. These are two key ingredients to stabilize bubbles and skyrmions in ferromagnetic thin films. This allowed us to study systematically topological soliton solutions over a wide range of parameters and explore quantitatively the possible transitions between small and large topological solitons. In the skyrmion-bubble transition a critical point is present above which the transformation between both spin textures becomes continuous. While the distinct characteristics of skyrmion and bubbles remain, their common nature as topological solitons is emphasised. Above the critical (D_{cs}, H_{cs}) point, the topological soliton can not be strictly named a skyrmion or a bubble, as it possesses some characteristics of both objects, and it may be addressed as supercritical skyrmion.

In the second part of the section "2D topological solitons" we have shown that when the dipolar interactions are neglected the ASk energy can be written in a circular symmetric form. The Sk and the ASk in systems with different symmetry but the same strength of magnetic interactions have the same size and stability energy. The presence of dipolar interactions breaks the circular symmetry of the ASk energy. With the support of micromagnetic simulations we have studied the energy and the shape of Sk and ASk as a function of M_s and we explained the role of the dipolar interaction. We can distinguish three different effects. The interaction due to the surface charges does not break the circular symmetry and stabilizes in the same way Sk and ASk. The volume charges depend on the in-plane moment configuration. While the Sk configuration shows homochiral Néel moment rotation, anti-skyrmions show partly Néel and partly Bloch rotations. The latter do not produce magnetic charges. The ASk configuration is therefore more stable and the tendency to favor Bloch rotations induces a square shape. Moreover the presence of Néel rotations with different chiralities induces a partial flux closure effect and further increases the ASk stability. Since both Sk and ASk are stable when all the magnetic energies cancel each other, a small variation of a single parameter like the dipolar energy can have a large influence on the shape and energy of the textures.

Experimental approach

The experimental work is described in the chapter "Experimental results: magnetism in C_{2v} epitaxial systems". It is divided into three main parts, presenting the different magnetic systems that were grown and analysed. For each system I described the growth parameters and crystal symmetry, followed by the results of the magnetic characterisation and finally the results from the magnetic microscopy measurements. This explanation path allowed to understand how the symmetry and quality of the crystals determine the symmetry of the magnetic properties and how the magnetic configurations depend on them. Three different magnetic epitaxial systems with a C_{2v} symmetry are analysed:

- bcc(110) W \ hcp(0001) Co \ fcc(111) Au and bcc(110) W \ hcp(0001) Co \ fcc(111) Pt
- bcc(110) W \ hcp(0001) Co \ fcc(111) Au-Pt_{solid solution}
- bcc(110) W \ bcc(110) Fe \ hcp(0001) Co \ fcc(111) Au

The discussion for each material is divided into three parts according to the main question of this work. First the growth condition and the crystal quality and symmetry are shown. Then the results of the magnetic characterisation are discussed in order to understand the strength and symmetry of the anisotropic interactions. Finally the magnetic microscopy images of the magnetic configurations found on these system are reported.

All the system present C_{2v} crystal symmetry that has been investigated with RHEED and GIXRD. It arises from the bcc W(110) surface that at the interface with the hcp Co(0001) can induce anisotropy in the interface interactions like the DMI and the magneto-crystalline anisotropy. The fcc Pt (111) and the fcc Au (111) do not change the system symmetry. In-situ STM allowed to confirm the layer-by-layer growth and interface quality of the stacks.

The magnetic properties of the systems W\Co\Pt and W\Co\Au are described in section "Magnetic characterisation". Three techniques have been used:

- Polar Kerr magnetometry allowed the acquisition of hysteresis loops along the sample wedges and thus allowed to study the changes of magnetic order as a function of the thickness. I showed that the in-plane Co/W interface anisotropy dominates over the Co/Pt out-of-plane anisotropy for all the thicknesses studied.

The Co/Au out-of-plane anisotropy is larger than the in-plane Co/W interface anisotropy and the system W\Co\Au is magnetized out-of-plane for the thickness range between 1.7 ML and 4.5 ML.

A particular strong out-of-plane has been found at the Co_xO_{1-x}/Co interface. The origin of this effect is not understood and further studies are needed.

- Polar Kerr microscopy has been used to study the magnetic domain expansion. The main aim of this study was to use the dynamics of DWs to determine the DMI parameters in the W\Co\Au sample with a 0.65 nm thick Co layer and an C_{2v} symmetry. The DW propagation along the hard axis did not allow the determination of the DMI, due to the complexity of the DW configuration and its dynamics. Along the easy axis, the in-plane anisotropy and the DMI stabilize a Néel DW and the standard methods have been modified to determine the DMI (D_s^x). The study of the Walker breakdown speed suggests a $D_s^x = 1.1$ pJ/m, whereas the study of the DW motion under the application of an in-plane magnetic field gives $D_s^x = 1.2$ pJ/m. The two values are in agreement showing the validity of the methods used.

The study of the DW speed as a function of an in-plane field along an intermediate angle between the easy and the hard axis shows a particular behavior due to the complexity of the DW dynamics in systems with C_{2v} symmetry. This complexity makes it impossible to describe the DW dynamics in C_{2v} symmetry systems with one-dimensional models along a general in-plane direction.

- We have used BLS spectroscopy in the Damon-Eshbach configuration to investigate the DMI in an out-of-plane magnetized epitaxial Au/Co(0.65 nm)/W(110) trilayer. The asymmetry of the BLS spectra allowed to estimate the presence of a DMI that promotes a clockwise chirality with a DMI strength 2 to 3 times larger along bcc[110] than along bcc[001]. BLS in the Damon-Eshbach configuration allows only the calculation of the DMI parameter for Néel magnetic rotations. In systems with a C_{2v} symmetry the DMI promotes Néel magnetic rotations only along the main crystal axes. A micromagnetic model has been developed to estimate the strength of the DMI along all the in-plane directions and calculate the DW polarisation promoted by DMI in Au/Co(0.65 nm)/W(110) systems.

The DMI values obtained by the study of the DW motion and by BLS are in disagreement:

$$D_s^x(\text{DWmotion}) = 1.1 \text{ pJ/m} \quad D_s^x(\text{BLS}) = 0.29 \text{ pJ/m} \quad (6.1)$$

In the rest of this thesis only the DMI values obtained by BLS have been considered. Indeed the DMI evaluation from the DW dynamics is very complex and the methods used depend on magnetic parameters that have been estimated or calculated by other techniques. Moreover, the DW dynamics has been studied in 2D systems with 1D micromagnetic methods that could neglect relevant effects. Instead the DMI evaluation by BLS needs only the calculation of the magnetic moment per unit surface. Moreover BLS is particularly suited for the study of anisotropic systems because it allows to extract the magnetic properties independently along any direction.

In section "Internal DW configuration and elliptical skyrmions" the results of two microscopy techniques, MFM and XMCD-PEEM, were shown. The W\Co\Au system presents the anisotropic energy environment necessary for the stabilisation of elliptical skyrmions. Skyrmionic bubbles have been stabilized using two different confinements: nanopatterned structures and nanodefects in a continuous film.

The MFM images show the presence of skyrmionic bubbles on the nanopatterned structures. The interaction with the tip and local defects deform the skyrmion bubbles shape, which hides the anisotropic properties. Technical problems during the lithography did not allow to study this system with XMCD-PEEM. However, this technique allowed to show the presence of skyrmionic bubbles stabilized in continuous films without magnetic field, but problems with the XMCD-PEEM set-up did not allow to study the internal configuration of these skyrmionic bubbles.

One possible strategy in order to increase the chance of stabilizing elliptical skyrmions is to increase the DMI interaction and the anisotropic properties. In this way the energy fluctuations induced by the defects should have less impact on the magnetic configuration. From the study of the magnetic properties of the W\Co\Au and W\Co\Pt systems and from literature we knew that Co\Au has a strong out-of-plane anisotropy and a low DMI whereas the Co\Pt induces a strong DMI but its out-of-plane anisotropy is weaker than the in-plane anisotropy of W\Co. Therefore a system with mixed properties between Co\Au and Co\Pt interfaces has been grown with the right energy environment to display elliptical skyrmions.

In section "W\Co\Au-Pt solid solution" the growth conditions, the magnetic characterisation and the results of microscopy techniques have been shown. The W\Co\Au-Pt_{solid solution} sample shows the presence of strong anisotropic properties. The magnetic properties have been studied as function of the Co thickness. For large thickness the system is demagnetized by the surface dipolar interaction. In this conditions a configuration with stripe domains parallel to the in-plane easy axis has been found. The same configuration with a larger periodicity has been found even for thinner Co layer after demagnetisation with an out-of-plane magnetic field. Kerr microscopy studies of the DW dynamics allowed to evidence the origin of this magnetic configuration, which arises from a strong anisotropy in the DW motion.

MFM measurements with the application of a static magnetic field have been performed in order to confine elliptical skyrmionic bubbles but the small sensitivity of this technique to thin magnetic systems did not allow to display and characterize them.

XMCD-PEEM measurements allowed to display the internal structure of the DWs along the in-plane hard axis of the system. They show the presence of a Néel DW component.

In section "W\Fe\Co\Au" the growth conditions and crystal symmetry of a W\Fe\Co\Au system have been shown. This system had been grown with the aim of stabilizing anti-skyrmionic bubbles at room temperature. The fundamental condition for the stabilisation of these topological solitons is the inversion of DMI sign between two perpendicular in-plane directions $\frac{D_x}{D_y} < 0$.

Ab-initio calculations have shown that this condition can be fulfilled at the W(110)\Fe interface [18, 140]. In the calculations a perfect pseudomorphic bcc(110) Fe on bcc(110) W surface is considered. Experimentally it occurs up to 2 ML of Fe. For thicker layers the Fe structure relaxes and disorder is induced in the crystal. Then the system is not comparable anymore with the calculated one and the conditions for an inversion of the DMI may be lost. The problem of studying a system with 2ML of Fe is that the Curie temperature could be close to room temperature and the magnetic moment too small to be measured with microscopy techniques. Moreover the W(110)\Fe presents a strong in-plane anisotropy. These problems can be resolved by growing a Co wedge layer on top of the Fe and capping the system with a layer of Au. The Co layer allows to increase the magnetic moment and the Co\Au interface induces a strong out-of-plane anisotropy. Moreover the DMI induced at this interface is weak. This is fundamental because the presence of a strong DMI at the interface opposite to the W(110)\Fe could shift the total DMI value and avoid the sign inversion. RHEED measurements confirmed the pseudomorphic growth of Fe on W(110) and showed that the Co grows strained with a C_{2v} symmetry on the Fe(110). Polar Kerr microscopy has been performed along the Co wedge for each Fe step. The hysteresis loops performed with polar Kerr magnetometry showed that the system has an in-plane magnetisation. It means that the W\Fe in-plane anisotropy dominates the Co\Au out-of-plane anisotropies.

6.2 Perspectives

This thesis is a pioneering work on the effects of anisotropic energies on the symmetry and topological number of magnetic solitons. The number of questions raised during the work is larger than the number of answers finally obtained.

We were able to develop a micromagnetic approach to study the effect of the breaking of rotational symmetry in the plane of thin films. A complete study of the effect of anisotropic interactions has been developed only for 1D topological solitons. In the case of 2D topological solitons the model has been limited to two particular cases : isotropic magnetic interactions with isotropic DMI and with anisotropic DMI strength with chirality inversion. Both cases are interesting for the study of the skyrmion and anti-skyrmion properties but they are really specific and impossible to obtain in systems with C_{2v} symmetry since more complex anisotropic interactions can be expected. The study of the energy and the configuration of skyrmions and anti-skyrmions in a larger range of anisotropic interactions is of large interest. Indeed, a range of parameters for which both the solitons coexist can be found. Two works in literature [18, 142] show that skyrmions and anti-skyrmions have degenerate energy when the DMI along one direction is zero. The first [18] does not consider the role of the dipolar interactions whereas the second [142] does not study its effect in detail and does not show in which range of magnetic parameters the two solitons are stable. With the intent of understanding that, we started performing micromagnetic simulations that include biaxial magnetic anisotropy, anisotropic exchange, dipolar interactions and anisotropic DMI.

Experimentally we are in parallel completing the study on the systems analysed in this thesis and designing new stacks. These will be grown to obtain the conditions for the stabilisation of anti-skyrmions and the coexistence of skyrmions and anti-skyrmions.

We have patterned nanostrips in $W/Co/Au$ to reduce the complexity of the domain expansion phenomenon and understand better the dynamics of the domain walls. Nitrogen vacancy microscopy and XMCD-PEEM measurements will be used to study the internal configuration of the domain walls.

The magnetic characterisation of $W/Co/Au-Pt_{\text{solid solution}}$ is not complete. We are performing BLS spectroscopy on this system in collaboration with Hans Niembach from NIST in Boulder (USA). XMCD-PEEM measurements will be performed to complete the study on the domain wall configuration and to search for elliptical skyrmions.

Changing the quality of the interface and using new interfaces will allow to change the strength of the magnetic interactions in samples with W/Co or W/Fe . The good conditions for the stabilisation of anti-skyrmions and the coexistence of skyrmions and anti-skyrmions could be found. The realisation of these systems is a crucial step in the understanding of topological magnetic solitons.

Bibliography

- [1] AN Bogdanov and DA YABLONSKII. On the theory of inhomogeneous states of magnetic substances in the region of phase-transitions induced by a magnetic-field the mixed state of antiferromagnets. *ZHURNAL EKSPERIMENTALNOI I TEORETICHESKOI FIZIKI*, 96(1):253–260, 1989.
- [2] B.A. Ivanov, V.A. Stephanovich, and A.A. Zhudskii. *J. Magn. Magn. Mater.*, 88(1-2):116, 1990.
- [3] S. Mühlbauer, B. Binz, F. Jonietz, C. Pfleiderer, A. Rosch, A. Neubauer, R. Georgii, and P. Böni. Skyrmion lattice in a chiral magnet. *Science*, 323(5916):915–919, 2009.
- [4] Niklas Romming, Christian Hanneken, Matthias Menzel, Jessica E. Bickel, Boris Wolter, Kirsten von Bergmann, André Kubetzka, and Roland Wiesendanger. Writing and deleting single magnetic skyrmions. *Science*, 341(6146):636–639, 2013.
- [5] C. Moreau-Luchaire, C. Moutafis, N. Reyren, J. Sampaio, C. A. F. Vaz, N. Van Horne, K. Bouzehouane, K. Garcia, C. Deranlot, P. Warnicke, P. Wohlhuter, J. M. George, M. Weigand, J. Raabe, V. Cros, and A. Fert. Additive interfacial chiral interaction in multilayers for stabilization of small individual skyrmions at room temperature. *Nat. Nanotechnol.*, 11(5):444, MAY 2016.
- [6] Olivier Boulle, Jan Vogel, Hongxin Yang, Stefania Pizzini, Dayane de Souza Chaves, Andrea Locatelli, Tefvik Onur Mentès, Alessandro Sala, Liliana D. Buda-Prejbeanu, Olivier Klein, Mohamed Belmeguenai, Yves Roussigne, Andrey Stashkevich, Salim Mourad Cherif, Lucia Aballe, Michael Förster, Mairbek Chshiev, Stéphane Auffret, Ioan Mihai Miron, and Gilles Gaudin. Room-temperature chiral magnetic skyrmions in ultrathin magnetic nanostructures. *Nat. Nanotechnol.*, 11(5):449, MAY 2016.
- [7] I.E. Dzyaloshinskii. *Sov. Phys. JETP*, 5:1259, 1957.
- [8] Tôru Moriya. Anisotropic superexchange interaction and weak ferromagnetism. *Physical Review*, 120(1):91, 1960.
- [9] A. Fert and Peter M. Levy. Role of anisotropic exchange interactions in determining the properties of spin-glasses. *Phys. Rev. Lett.*, 44:1538–1541, Jun 1980.
- [10] Julian Hagemester, Elena Y. Vedmedenko, and Roland Wiesendanger. Pattern formation in skyrmionic materials with anisotropic environments. *Phys. Rev. B*, 94:104434, Sep 2016.
- [11] Utkan Güngördü, Rabindra Nepal, Oleg A. Tretiakov, Kirill Belashchenko, and Alexey A. Kovalev. Stability of skyrmion lattices and symmetries of quasi-two-dimensional chiral magnets. *Phys. Rev. B*, 93:064428, Feb 2016.
- [12] Pin-Jui Hsu, André Kubetzka, Aurore Finco, Niklas Romming, Kirsten von Bergmann, and Roland Wiesendanger. Electric-field-driven switching of individual magnetic skyrmions. *Nat. Nanotechnol.*, 12:123, 2016.
- [13] K. Shibata, J. Iwasaki, N. Kanazawa, S. Aizawa, T. Tanigaki, M. Shirai, T. Nakajima, M. Kubota, M. Kawasaki, H. S. Park, D. Shindo, N. Nagaosa, and Y. Tokura. Large anisotropic deformation of skyrmions in strained crystal. *Nat. Nanotechnol.*, 10(7):589, JUL 2015.
- [14] B Dupé, C N Kruse, T Dornheim, and S Heinze. How to reveal metastable skyrmionic spin structures by spin-polarized scanning tunneling microscopy. *New J. Phys.*, 18(5):055015, 2016.

- [15] Wataru Koshibae and Naoto Nagaosa. Theory of antiskyrmions in magnets. *Nat. Commun.*, 7:10542, JAN 2016.
- [16] Ajaya K. Nayak, Vivek Kumar, Peter Werner, Eckhard Pippel, Roshnee Sahoo, Françoise Damay, Ulrich K. Rößler, Claudia Felser, and Stuart Parkin. Discovery of magnetic antiskyrmions beyond room temperature in tetragonal heusler materials. 548, 03 2017.
- [17] Lorenzo Camosi, Stanislas Rohart, Olivier Fruchart, Stefania Pizzini, Mohamed Belmeguenai, Yves Roussigné, Andreï Stashkevich, Salim Mourad Cherif, Laurent Ranno, Maurizio de Santis, and Jan Vogel. Anisotropic dzyaloshinskii-moriya interaction in ultrathin epitaxial au/co/w(110). *Phys. Rev. B*, 95:214422, Jun 2017.
- [18] Markus Hoffmann, Bernd Zimmermann, Gideon P. Mueller, Daniel Schuerhoff, Nikolai S. Kiselev, Christof Melcher, and Stefan Blügel. Antiskyrmions stabilized at interfaces by anisotropic Dzyaloshinskii-Moriya interactions. *Nature Comm.*, 8:308, 2017.
- [19] Melvin A Ruderman and Charles Kittel. Indirect exchange coupling of nuclear magnetic moments by conduction electrons. *Phys. Rev.*, 96(1):99, 1954.
- [20] Junjiro Kanamori. Superexchange interaction and symmetry properties of electron orbitals. *Journal of Physics and Chemistry of Solids*, 10(2-3):87–98, 1959.
- [21] John B Goodenough, A Wold, RJ Arnett, and N Menyuk. Relationship between crystal symmetry and magnetic properties of ionic compounds containing mn^{3+} . *Physical Review*, 124(2):373, 1961.
- [22] PW Anderson. Antiferromagnetism. theory of superexchange interaction. *Physical Review*, 79(2):350, 1950.
- [23] XL Wang, MY Ni, Z Zeng, and HQ Lin. Effects of hydrogen impurities on $ge_{1-x}mn_x$ semiconductors. *EPL (Europhysics Letters)*, 87(4):47001, 2009.
- [24] K Sato, W Schweika, PH Dederichs, and H Katayama-Yoshida. Low-temperature ferromagnetism in $(ga, mn)_n$: Ab initio calculations. *Physical Review B*, 70(20):201202, 2004.
- [25] I Turek, J Kudrnovský, G Bihlmayer, and S Blügel. Ab initio theory of exchange interactions and the curie temperature of bulk gd . *Journal of Physics: Condensed Matter*, 15(17):2771, 2003.
- [26] M Etzkorn, PS Anil Kumar, W Tang, Y Zhang, and J Kirschner. High-wave-vector spin waves in ultrathin co films on $w(110)$. *Physical Review B*, 72(18):184420, 2005.
- [27] L Udvardi and L Szunyogh. Chiral asymmetry of the spin-wave spectra in ultrathin magnetic films. *Physical review letters*, 102(20):207204, 2009.
- [28] I.E. Dzyaloshinskii. *J. Phys. Chem. Solids*, 4:241, 1958.
- [29] I Dzyaloshinsky. A thermodynamic theory of “weak” ferromagnetism of antiferromagnetics. *Journal of Physics and Chemistry of Solids*, 4(4):241–255, 1958.
- [30] M Heide, G Bihlmayer, and Stefan Blügel. Dzyaloshinskii-moriya interaction accounting for the orientation of magnetic domains in ultrathin films: $Fe/w(110)$. *Physical Review B*, 78(14):140403, 2008.
- [31] Hongxin Yang, André Thiaville, Stanislas Rohart, Albert Fert, and Mairbek Chshiev. Anatomy of dzyaloshinskii-moriya interaction at co/pt interfaces. *Physical review letters*, 115(26):267210, 2015.
- [32] J Sampaio, V Cros, S Rohart, A Thiaville, and A Fert. Nucleation, stability and current-induced motion of isolated magnetic skyrmions in nanostructures. *Nature nanotechnology*, 8(11):839–844, 2013.
- [33] AN Bogdanov and DA Yablonskii. “Thermodynamically stable” vortices” in magnetically ordered crystals. the mixed state of magnets. *Zh. Eksp. Teor. Fiz*, 95:182, 1989.

- [34] A Crépieux and Claudine Lacroix. Dzyaloshinsky–moriya interactions induced by symmetry breaking at a surface. *Journal of magnetism and magnetic materials*, 182(3):341–349, 1998.
- [35] P Moras, G Bihlmayer, PM Sheverdyaeva, SK Mahatha, M Papagno, J Sánchez-Barriga, O Rader, L Novinec, S Gardonio, and C Carbone. Magnetization-dependent rashba splitting of quantum well states at the Co/W interface. *Phys. Rev. B*, 91(19):195410, 2015.
- [36] U Gradmann and J Müller. Flat ferromagnetic, epitaxial 48ni/52fe (111) films of few atomic layers. *physica status solidi (b)*, 27(1):313–324, 1968.
- [37] Patrick Bruno. Tight-binding approach to the orbital magnetic moment and magnetocrystalline anisotropy of transition-metal monolayers. *Physical Review B*, 39(1):865, 1989.
- [38] Olivier Fruchart. lecture notes on nanomagnetism. <http://fruchart.eu>.
- [39] G Garreau, M Farle, E Beaurepaire, and K Baberschke. Curie temperature and morphology in ultrathin co/w (110) films. *Physical Review B*, 55(1):330, 1997.
- [40] Ulrich Gradmann. Magnetism in ultrathin transition metal films. *Handbook of magnetic materials*, 7:1–96, 1993.
- [41] CM Schneider, P Bressler, P Schuster, J Kirschner, JJ De Miguel, and R Miranda. Curie temperature of ultrathin films of fcc-cobalt epitaxially grown on atomically flat cu (100) surfaces. *Physical review letters*, 64(9):1059, 1990.
- [42] Ch Würsch and D Pescia. Test of scaling theory at a two-dimensional ising-like transition using a monolayer of iron. *Journal of magnetism and magnetic materials*, 177:617–619, 1998.
- [43] V Usov, S Murphy, and IV Shvets. Study of ferromagnetic–paramagnetic phase transition in two-dimensional fe/mo (1 1 0) epitaxial films. *Journal of magnetism and magnetic materials*, 290:764–767, 2005.
- [44] PR Willmott and JR Huber. Pulsed laser vaporization and deposition. *Reviews of Modern Physics*, 72(1):315, 2000.
- [45] T Smausz, B Hopp, Cs Vass, and Z Tóth. Experimental study on droplet generation during excimer laser ablation of polyethylene glycol 1000. *Applied surface science*, 168(1-4):146–149, 2000.
- [46] Tsuyoshi Yoshitake, Gousuke Shiraishi, and Kunihito Nagayama. Elimination of droplets using a vane velocity filter for pulsed laser ablation of fesi2. *Applied surface science*, 197:379–383, 2002.
- [47] Jeffrey T Cheung. Pulsed laser deposition. In *Handbook of Vacuum Science and Technology*, pages 694–710. Elsevier, 1998.
- [48] TN Hansen, Jørgen Schou, and JG Lunney. Angular distributions of silver ions and neutrals emitted in vacuum by laser ablation. *EPL (Europhysics Letters)*, 40(4):441, 1997.
- [49] Olivier Fruchart, Pierre-Olivier Jubert, Mustafa Eleoui, Fabien Cheynis, Bogdana Borca, Philippe David, Valérie Santonacci, Annick Liénard, Manabu Hasegawa, and Claire Meyer. Growth modes of fe (110) revisited: a contribution of self-assembly to magnetic materials. *Journal of Physics: Condensed Matter*, 19(5):053001, 2007.
- [50] Vitaliy A Shchukin and Dieter Bimberg. Spontaneous ordering of nanostructures on crystal surfaces. *Reviews of Modern Physics*, 71(4):1125, 1999.
- [51] Arvind Baskaran and Peter Smereka. Mechanisms of stranski-krastanov growth. *Journal of Applied Physics*, 111(4):044321, 2012.
- [52] MA Grinfeld. The stress driven instability in elastic crystals: Mathematical models and physical manifestations. *Journal of Nonlinear Science*, 3(1):35–83, 1993.

- [53] John E Mahan, Kent M Geib, GY Robinson, and Robert G Long. A review of the geometrical fundamentals of reflection high-energy electron diffraction with application to silicon surfaces. *Journal of Vacuum Science & Technology A*, 8(5):3692–3700, 1990.
- [54] PS Pershan. Magneto-optical effects. *Journal of applied physics*, 38(3):1482–1490, 1967.
- [55] Chun-Yeol You and Sung-Chul Shin. Generalized analytic formulae for magneto-optical kerr effects. *Journal of applied physics*, 84(1):541–546, 1998.
- [56] R.W. Damon and J.R. Eshbach. Magnetostatic modes of a ferromagnet slab. *J. Phys. Chem. Sol.*, 19:308, 1961.
- [57] Daniel D Stancil and Anil Prabhakar. *Spin waves*. Springer, 2009.
- [58] A. N. Bogdanov and U. K. Rößler. Chiral symmetry breaking in magnetic thin films and multilayers. *Phys. Rev. Lett.*, 87:037203, Jun 2001.
- [59] Jung-Hwan Moon, Soo-Man Seo, Kyung-Jin Lee, Kyoung-Whan Kim, Jisu Ryu, Hyun-Woo Lee, Robert D McMichael, and Mark D Stiles. Spin-wave propagation in the presence of interfacial dzyaloshinskii-moriya interaction. *Physical Review B*, 88(18):184404, 2013.
- [60] Kh. Zakeri, Y. Zhang, J. Prokop, T.-H. Chuang, N. Sakr, W. X. Tang, and J. Kirschner. Asymmetric spin-wave dispersion on fe(110): Direct evidence of the dzyaloshinskii-moriya interaction. *Phys. Rev. Lett.*, 104:137203, Mar 2010.
- [61] Mohamed Belmeguenai, Jean-Paul Adam, Yves Roussigné, Sylvain Eimer, Thibaut Devolder, Joo-Von Kim, Salim Mourad Cherif, Andrey Stashkevich, and André Thiaville. Interfacial dzyaloshinskii-moriya interaction in perpendicularly magnetized pt/co/alo x ultrathin films measured by brillouin light spectroscopy. *Physical Review B*, 91(18):180405, 2015.
- [62] Sergej O Demokritov, Burkard Hillebrands, and Andrei N Slavin. Brillouin light scattering studies of confined spin waves: linear and nonlinear confinement. *Physics Reports*, 348(6):441–489, 2001.
- [63] C Mercher. Mathematical framework for topological solitons in chiral magnetism. *48th IFF Spring School 2017 lecture notes*.
- [64] P Gaunt and CK Mylvaganam. Nucleation and pinning at 360° domain walls in smco5 and related alloys. *Journal of Applied Physics*, 48(6):2587–2590, 1977.
- [65] CB Muratov and VV Osipov. Theory of 360 domain walls in thin ferromagnetic films. *Journal of Applied Physics*, 104(5):053908, 2008.
- [66] E Feldtkeller. Coupled walls in multilayer films. *Journal of Applied Physics*, 39(2):1181–1190, 1968.
- [67] Y Mokrousov. Berry phase in quantum mechanics. *48th IFF Spring School 2017 lecture notes*.
- [68] Karin Everschor-Sitte and Matthias Sitte. Real-space berry phases: Skyrmion soccer. *Journal of Applied Physics*, 115(17):172602, 2014.
- [69] Christian Pfleiderer and Achim Rosch. Condensed-matter physics: Single skyrmions spotted. *Nature*, 465(7300):880–881, 2010.
- [70] A Neubauer, C Pfleiderer, B Binz, A Rosch, R Ritz, PG Niklowitz, and P Böni. Topological hall effect in the a phase of mnsi. *Phys. Rev. Lett.*, 102(18):186602, 2009.
- [71] A Hoffmann, W Jiang, X Zhang, Y Zhou, G Yu, KL Wang, X Wang, X Cheng, W Zhang, MB Jungfleisch, et al. Skyrmion hall effect. *Bulletin of the American Physical Society*, 62, 2017.
- [72] Naoto Nagaosa and Yoshinori Tokura. *Nat. Nanotechnol.*, 8:899, 2013.
- [73] A.A. Thiele. Steady-state motion of magnetic domains. *Phys. Rev. Lett.*, 30(6):230, 1973.

- [74] Wanjun Jiang, Pramey Upadhyaya, Wei Zhang, Guoqiang Yu, M. Benjamin Jungfleisch, Frank Y. Fradin, John E. Pearson, Yaroslav Tserkovnyak, Kang L. Wang, Olle Heinonen, Suzanne G. E. te Velthuis, and Axel Hoffmann. Blowing magnetic skyrmion bubbles. *Science*, 349(6245):283–286, 2015.
- [75] Johannes Wild, Thomas NG Meier, Simon Pöllath, Matthias Kronseder, Andreas Bauer, Alfonso Chacon, Marco Halder, Marco Schowalter, Andreas Rosenauer, Josef Zweck, et al. Entropy-limited topological protection of skyrmions. *Science advances*, 3(9):e1701704, 2017.
- [76] S Rohart, J Miltat, and A Thiaville. Path to collapse for an isolated néel skyrmion. *Physical Review B*, 93(21):214412, 2016.
- [77] Igor S Lobanov, Hannes Jónsson, and Valery M Uzdin. Mechanism and activation energy of magnetic skyrmion annihilation obtained from minimum energy path calculations. *Physical Review B*, 94(17):174418, 2016.
- [78] David Corts-Ortuno, Weiwei Wang, Marijan Beg, Ryan A Pepper, Marc-Antonio Bisotti, Rebecca Carey, Mark Vousden, Thomas Kluyver, Ondrej Hovorka, and Hans Fangohr. Thermal stability and topological protection of skyrmions in nanotracks. *Scientific reports*, 7(1):4060, 2017.
- [79] André Thiaville, Stanislas Rohart, Émilie Jué, Vincent Cros, and Albert Fert. Dynamics of dzyaloshinskii domain walls in ultrathin magnetic films. *EPL (Europhysics Letters)*, 100(5):57002, 2012.
- [80] S. Rohart and A. Thiaville. Skyrmion confinement in ultrathin film nanostructures in the presence of dzyaloshinskii-moriya interaction. *Phys. Rev. B*, 88:184422, Nov 2013.
- [81] Lorenzo Camosi, Nicolas Rougemaille, Olivier Fruchart, Jan Vogel, and Stanislas Rohart. Micromagnetics of anti-skyrmions in ultrathin films. *arXiv preprint arXiv:1712.04743*, 2017.
- [82] AA Belavin and AM Polyakov. Metastable states of two-dimensional isotropic ferromagnets. *JETP lett*, 22(10):245–248, 1975.
- [83] A M Kosevich, B A Ivanov, and A S Kovalev. Dynamical and topological solitons in a ferromagnet. *Physica 3D*, 1:363, 1981.
- [84] Ar Abanov and Valery L Pokrovsky. Skyrmion in a real magnetic film. *Physical Review B*, 58(14):R8889, 1998.
- [85] F Waldner. *J. Magn. Magn. Mater.*, 31:1203, 1983.
- [86] F Waldner. *J. Magn. Magn. Mater.*, 54:873, 1986.
- [87] F Waldner. Comment on “Spin correlations of 2D quantum antiferromagnet at low temperatures and a direct comparison with neutron-scattering experiments”. *Phys. Rev. Lett.*, 65:1519, 1990.
- [88] X. Z. Yu, Y. Onose, N. Kanazawa, J. H. Park, J. H. Han, Y. Matsui, N. Nagaosa, and Y. Tokura. Real-space observation of a two-dimensional skyrmion crystal. *Nature*, 465(7300):901–904, 2010.
- [89] Stefan Heinze, Kirsten von Bergmann, Matthias Menzel, Jens Brede, Andre Kubetzka, Roland Wiesendanger, Gustav Bihlmayer, and Stefan Blügel. Spontaneous atomic-scale magnetic skyrmion lattice in two dimensions. *Nature Phys.*, 7(9):713–718, 2011.
- [90] Anne Bernand-Mantel, Lorenzo Camosi, Alexis Wartelle, Nicolas Rougemaille, Michaël Darques, and Laurent Ranno. *arxiv:1712.03154*, (), 2017.
- [91] A A Thiele. The Theory of Cylindrical Magnetic Domains. *Bell System Technical Journal*, 48(10):3287–3335, 1969.
- [92] Yih-O Tu. Determination of magnetization of micromagnetic wall in bubble domains by direct minimization. *J. Appl. Phys.*, 42(13):5704–5709, 1971.

- [93] N S Kiselev, A N Bogdanov, R Schäfer, and U K Rößler. Chiral skyrmions in thin magnetic films: new objects for magnetic storage technologies? *Journal of Physics D: Applied Physics*, 44(39):392001, 2011.
- [94] A O Leonov, T L Monchesky, N Romming, A Kubetzka, A N Bogdanov, and R Wiesendanger. The properties of isolated chiral skyrmions in thin magnetic films. *New J. Phys.*, 18(6):065003, 2016.
- [95] A P Malozemoff and J C Slonczewski. *Magnetic Domain Walls in Bubble Materials*. Academic Press, New York, 1979.
- [96] Felix Büttner, Ivan Lemesh, and Geoffrey SD Beach. Theory of isolated magnetic skyrmions: From fundamentals to room temperature applications. *Scientific Reports*, 8(1):4464, 2018.
- [97] A Bogdanov and A Hubert. The stability of vortex-like structures in uniaxial ferromagnets. *J. Magn. Mater.*, 195:182–192, 1999.
- [98] B. A. Ivanov and A. M. Kosevich. Bound states of a large number of magnons in a ferromagnet with a single-ion anisotropy. *Journal of Experimental and Theoretical Physics*, 45(5):1050, 1977.
- [99] A. M. Kosevich, B. A. Ivanov, and A. S. Kovalev. Magnetic Solitons. *Physics Reports*, 194(3-4):117–238, 1990.
- [100] Y Zhou, E Iacocca, A A Awad, R K Dumas, F C Zhang, H B Braun, and J Åkerman. Dynamically stabilized magnetic skyrmions. *Nature Communications*, 6:8193, sep 2015.
- [101] Karin Everschor-Sitte, Matthias Sitte, Thierry Valet, Artem Abanov, and Jairo Sinova. Skyrmion production on demand by homogeneous dc currents. *New J. Phys.*, 19(9):092001, 2017.
- [102] M Mostovoy and A O Leonov. Multiply periodic states and isolated skyrmions in an anisotropic frustrated magnet. *Nature Communications*, 6:1–8, 2015.
- [103] A. O. Leonov and M. Mostovoy. Edge states and skyrmion dynamics in nanostripes of frustrated magnets. *Nat. Comm.*, 8(May 2016):1–7, 2017.
- [104] The Object Oriented MicroMagnetic Framework (OOMMF) project at ITL/NIST.
- [105] U Rössler, A Bogdanov, and C Pfeleiderer. Spontaneous skyrmion ground states in magnetic metals. 442:797–801, 09 2006.
- [106] Marine Schott, Anne Bernard-Mantel, Laurent Ranno, Stefania Pizzini, Jan Vogel, H el ene B ea, Claire Baraduc, St ephane Auffret, Gilles Gaudin, and Dominique Givord. The skyrmion switch: Turning magnetic skyrmion bubbles on and off with an electric field. *Nano Letters*, 17(5):3006–3012, 2017.
- [107] Konstantin Y Guslienko. Skyrmion state stability in magnetic nanodots with perpendicular anisotropy. *IEEE Magn. Lett.*, 6:1, 2015.
- [108] S. Pizzini, J. Vogel, S. Rohart, L. D. Buda-Prejbeanu, E. Ju e, O. Boulle, I. M. Miron, C. K. Safeer, S. Auffret, G. Gaudin, and A. Thiaville. Chirality-induced asymmetric magnetic nucleation in Pt/Co/alo_x ultrathin microstructures. *Phys. Rev. Lett.*, 113:047203, Jul 2014.
- [109] Pavel F Bessarab, Valery M Uzdin, and Hannes J onsson. Method for finding mechanism and activation energy of magnetic transitions, applied to skyrmion and antivortex annihilation. *Computer Physics Communications*, 196:335–347, 2015.
- [110] PF Bessarab. Comment on “path to collapse for an isolated n el skyrmion”. *Physical Review B*, 95(13):136401, 2017.
- [111] S Rohart, J Miltat, and A Thiaville. Reply to “comment on ‘path to collapse for an isolated n el skyrmion’”. *Physical Review B*, 95(13):136402, 2017.

- [112] R. Sellmann, H. Fritzsche, H. Maletta, V. Leiner, and R. Siebrecht. Spin-reorientation transition and magnetic phase diagrams of thin epitaxial au(111)/co films with w and au overlayers. *Phys. Rev. B*, 64:054418, Jul 2001.
- [113] Thai Ha Pham, J Vogel, J Sampaio, M Vaňatka, J-C Rojas-Sánchez, M Bonfim, DS Chaves, F Choueikani, P Ohresser, E Otero, et al. Very large domain wall velocities in pt/co/gdox and pt/co/gd trilayers with dzyaloshinskii-moriya interaction. *EPL (Europhysics Letters)*, 113(6):67001, 2016.
- [114] Stefania Pizzini, Jan Vogel, Stanislas Rohart, LD Buda-Prejbeanu, E Jué, Olivier Boulle, Ioan Mihai Miron, CK Safeer, Stéphane Auffret, Gilles Gaudin, et al. Chirality-induced asymmetric magnetic nucleation in pt/co/alo x ultrathin microstructures. *Physical review letters*, 113(4):047203, 2014.
- [115] A Hrabec, NA Porter, A Wells, MJ Benitez, G Burnell, S McVitie, D McGrouther, TA Moore, and CH Marrows. Measuring and tailoring the dzyaloshinskii-moriya interaction in perpendicularly magnetized thin films. *Physical Review B*, 90(2):020402, 2014.
- [116] Soong-Geun Je, Duck-Ho Kim, Sang-Cheol Yoo, Byoung-Chul Min, Kyung-Jin Lee, and Sug-Bong Choe. Asymmetric magnetic domain-wall motion by the dzyaloshinskii-moriya interaction. *Physical Review B*, 88(21):214401, 2013.
- [117] F. Robaut O.F.K. MC Grath. Epitaxial growth of w(110) on al by pulsed laser deposition. *Surface Science Letters*, 315:1017, 1994.
- [118] O. Fruchart, S. Jaren, and J. Rothman. Growth modes of w and mo thin epitaxial (110) films on (1120) sapphire. *Appl. Surf. Sci.*, 135:218 – 232, 1998.
- [119] EF Wassermann and HP Jablonski. Epitaxial growth of iron on (100)-and (111)-gold substrates. *Surface Science*, 22(1):69–75, 1970.
- [120] H Fritzsche, J Kohlhepp, and U Gradmann. Epitaxial strain and magnetic anisotropy in ultrathin co films on w (110). *Physical Review B*, 51(22):15933, 1995.
- [121] Patrick Bruno. Magnetic surface anisotropy of cobalt and surface roughness effects within neel’s model. *Journal of Physics F: Metal Physics*, 18(6):1291, 1988.
- [122] Dan Zhang, You Wang, and Yang Gan. Characterization of critically cleaned sapphire single-crystal substrates by atomic force microscopy, xps and contact angle measurements. 274:405–417, 06 2013.
- [123] See Supplemental Material at [URL will be inserted by publisher] for details on the sample growth and calculations.
- [124] S Andrieu, C Chatelain, M Lemine, B Berche, and Ph Bauer. Size effect on magnetism of fe thin films in fe/ir superlattices. *Physical review letters*, 86(17):3883, 2001.
- [125] Yoko Yoshimura, Kab-Jin Kim, Takuya Taniguchi, Takayuki Tono, Kohei Ueda, Ryo Hiramatsu, Takahiro Moriyama, Keisuke Yamada, Yoshinobu Nakatani, and Teruo Ono. Soliton-like magnetic domain wall motion induced by the interfacial dzyaloshinskii-moriya interaction. *Nature Physics*, 12(2):157–161, 2016.
- [126] S Lemerle, J Ferré, C Chappert, V Mathet, T Giamarchi, and P Le Doussal. Domain wall creep in an ising ultrathin magnetic film. *Physical review letters*, 80(4):849, 1998.
- [127] Daniel S Fisher and David A Huse. Directed paths in a random potential. *Physical Review B*, 43(13):10728, 1991.
- [128] Kab-Jin Kim, Jae-Chul Lee, Sung-Min Ahn, Kang-Soo Lee, Chang-Won Lee, Young Jin Cho, Sunae Seo, Kyung-Ho Shin, Sug-Bong Choe, and Hyun-Woo Lee. Interdimensional universality of dynamic interfaces. *Nature*, 458(7239):740, 2009.

- [129] M Vaňatka, Juan-Carlos Rojas-Sánchez, Jan Vogel, Marlio Bonfim, M Belmeguenai, Y Roussigné, A Stashkevich, A Thiaville, and S Pizzini. Velocity asymmetry of dzyaloshinskii domain walls in the creep and flow regimes. *Journal of Physics: Condensed Matter*, 27(32):326002, 2015.
- [130] Reinoud Lavrijsen, DMF Hartmann, A Van Den Brink, Yuxiang Yin, Beatriz Barcones, RA Duine, MA Verheijen, HJM Swagten, and Bert Koopmans. Asymmetric magnetic bubble expansion under in-plane field in pt/co/pt: Effect of interface engineering. *Physical Review B*, 91(10):104414, 2015.
- [131] Satoru Emori, Eduardo Martinez, Kyung-Jin Lee, Hyun-Woo Lee, Uwe Bauer, Sung-Min Ahn, Parnika Agrawal, David C Bono, and Geoffrey SD Beach. Spin hall torque magnetometry of dzyaloshinskii domain walls. *Physical Review B*, 90(18):184427, 2014.
- [132] B Astie, J Degauque, J Porteseil, and R Vergne. Influence of the dislocation structures on the magnetic and magnetomechanical properties of high-purity iron. *IEEE Transactions on Magnetics*, 17(6):2929–2931, 1981.
- [133] Georg Woltersdorf and B Heinrich. Two-magnon scattering in a self-assembled nanoscale network of misfit dislocations. *Physical Review B*, 69(18):184417, 2004.
- [134] L. Baselgia, M. Warden, F. Waldner, Stuart L. Hutton, John E. Drumheller, Y. Q. He, P. E. Wigen, and M. Maryško. Derivation of the resonance frequency from the free energy of ferromagnets. *Phys. Rev. B*, 38:2237–2242, Aug 1988.
- [135] A. A. Stashkevich, M. Belmeguenai, Y. Roussigné, S. M. Cherif, M. Kostylev, M. Gabor, D. Lacour, C. Tiusan, and M. Hehn. Experimental study of spin-wave dispersion in py/pt film structures in the presence of an interface dzyaloshinskii-moriya interaction. *Phys. Rev. B*, 91:214409, 2015.
- [136] L. Udvardi and L. Szunyogh. Chiral asymmetry of the spin-wave spectra in ultrathin magnetic films. *Phys. Rev. Lett.*, 102:207204, May 2009.
- [137] Jacob Torrejon, Junyeon Kim, Jaivardhan Sinha, Seiji Mitani, Masamitsu Hayashi, Michihiko Yamanouchi, and Hideo Ohno. Interface control of the magnetic chirality in CoFeB/MgO heterostructures with heavy-metal underlayers. *Nat. Commun.*, 5, AUG 2014.
- [138] Kwang-Su Ryu, See-Hun Yang, Luc Thomas, and Stuart SP Parkin. Chiral spin torque arising from proximity-induced magnetization. *Nature communications*, 5:3910, 2014.
- [139] Alex Hubert and Rudolf Schäfer. Magnetic domains: the analysis of magnetic microstructures. 2008.
- [140] Bernd Zimmermann, Marcus Heide, Gustav Bihlmayer, and Stefan Blügel. First-principles analysis of a homochiral cycloidal magnetic structure in a monolayer cr on w(110). *Phys. Rev. B*, 90:115427, Sep 2014.
- [141] MT Johnson, PJH Bloemen, FJA Den Broeder, and JJ De Vries. Magnetic anisotropy in metallic multilayers. *Reports on Progress in Physics*, 59(11):1409, 1996.
- [142] Siying Huang, Chao Zhou, Gong Chen, Hongyi Shen, Andreas K. Schmid, Kai Liu, and Yizheng Wu. Stabilization and current-induced motion of antiskyrmion in the presence of anisotropic dzyaloshinskii-moriya interaction. *Phys. Rev. B*, 96:144412, Oct 2017.